UNIVERSITY OF SOUTHAMPTON

FACULTY OF ENGINEERING AND THE ENVIRONMENT

National Centre for Advanced Tribology

Development of Detection Techniques for Investigating Scuffing Mechanisms of Automotive Diesel Cast Irons

By

Timothy James Anthony Kamps

Thesis for the degree of Doctor of Philosophy

July 2017

UNIVERSITY OF SOUTHAMPTON

ABSTRACT

FACULTY OF ENGINEERING AND THE ENVIRONMENT

Tribology

Thesis for the degree of Doctor of Philosophy

DEVELOPMENT OF DETECTION TECHNIQUES FOR INVESTIGATING SCUFFING MECHANISMS OF AUTOMOTIVE DIESEL CAST IRONS

Timothy James Anthony Kamps

Increasingly stringent environmental legislation has led automotive manufacturers to focus engine development on achieving greater fuel efficiency by friction reduction. Engine friction losses between 4 and 15 % are typical for diesel engines, with approximately 50 % occurring at the piston assembly. Viscous losses associated with shearing lubricant films may be reduced by using oil with a lower viscosity, however this also results in the contact surfaces being separated by thinner lubricant films, which makes them more susceptible to scuffing. Improving the scuffing resistance of engine materials requires a detailed understanding of the contact conditions that lead to scuffing. However this is a complicated process that is often characterised by a rapid progression and therefore it is difficult to detect accurately and repeatedly the onset of scuffing failure.

This thesis explores the possibility of using deviations in the instantaneous friction force measured using a laboratory tribometer to assess whether the onset and progression of scuffing can be repeatedly determined for cast iron diesel cylinder liner materials. Two techniques were developed that assessed the deviation in spatially resolved friction signal as a function of stroke length as well as the level of disorder in the instantaneous root mean squared friction force. This enabled transitions in scuffing behaviour to be assessed for a Grade 250 flake graphite and a designation 400-15 nodular cast iron cylinder liner materials under lubricated reciprocating sliding at increasing contact pressure.

The detection techniques allowed tests to be interrupted during scuffing transitions for the analysis of surfaces using a combination of profilometry, scanning electron microscopy, energy dispersive X-ray spectroscopy and focused ion beam microscopy. The results showed that once sufficient energy was available for the sliding contact to degrade the lubricant, progression to mild scuffing occurred. This was characterised for Grade 250 cast iron by surface platelet formation and subsurface crack networks associated with the de-cohesion of the flake graphite phase from the pearlitic matrix. Progression to severe scuffing was characterised by adhesive transfer and back transfer of these platelets resulting in catastrophic wear of the cast iron surface.

Compared to flake graphite cast iron, nodular cast iron transitioned to mild scuffing at lower contact pressures, but exhibited an intermediate scuffing stage that prolonged the transition to severe scuffing. This was due to the formation of a comprehensive oxide film associated with the ferritic matrix, but also because the adhesive removal of material was associated with angular dross inclusions from the nodularisation process.

The techniques were applied to a conformal ring liner geometry that exhibited velocity dependant friction behaviour and therefore the detection techniques were adapted to include contact potential and disorderly friction data to detect scuffing transitions. The failure mechanisms were confirmed to be similar to that observed for both line contact and fired engine scuffing tests and showed that these techniques could be used to repeatedly detect scuffing transitions within 18 % maximum absolute deviation. Recommendations for testing of future engine materials for scuffing resistance are discussed as well as potential areas of further research.

Table of Contents

Table of Figures

Table of Tables

Nomenclature

α	Pressure viscosity coefficient	Pa^{-1}
B	Contact width	M
d	Stroke position	Mm
E	Elastic Modulus	GPa
E'	Reduced Modulus	GPa
F	Normal Load	N
F_f	Friction force	N
F_n	Friction noise	
F_p	Friction power	W
h	Film thickness	m
L	Profile length	µm
l	Contact length	m
λ	Oil film parameter	
ν	Poisson's ratio	
N	Angular speed	$Rads^{-1}$
P	Pressure	Pa
R	Cylinder radius	M
R_a	Average roughness	µm
R_q	Root mean square roughness	µm
R'	Reduced radius	m
U	Entrainment velocity	ms^{-1}
µ	Friction coefficient	
Z	Oil viscosity	Pas

DECLARATION OF AUTHORSHIP

I, Timothy James Anthony Kamps declare that this thesis and the work presented in it are my own and has been generated by me as the result of my own original research.

Development of detection techniques for investigating scuffing mechanisms of automotive diesel cast irons.

I confirm that:

This work was done wholly or mainly while in candidature for a research degree at this University;

Where any part of this thesis has previously been submitted for a degree or any other qualification at this University or any other institution, this has been clearly stated;

Where I have consulted the published work of others, this is always clearly attributed;

Where I have quoted from the work of others, the source is always given. With the exception of such quotations, this thesis is entirely my own work;

I have acknowledged all main sources of help;

Where the thesis is based on work done by myself jointly with others, I have made clear exactly what was done by others and what I have contributed myself;

Parts of this work have been published as:

- Kamps, T.J., Walker, J.C., Wood, R.J., Lee, P.M., Plint, A.G., Reproducing automotive engine scuffing using a lubricated reciprocating contact, Wear, 332, 2014, 1193-1199.
- Kamps, T.J., Walker, J.C., Wood, R.J., Lee, P.M., Plint, A.G., Scuffing mechanisms of EN-GJS 400-15 spheroidal graphite cast iron against a 52100 bearing steel in a PAO lubricated reciprocating contact, Wear, 376-377, 2017, 1542-1551.

Signed: .....

Date: .....

Acknowledgements

My supervision team have provided continued support and encouragement during my post graduate studies. Their combined knowledge and insight has been invaluable during this early stage of my career in tribology. I'm indebted to Dr Walker for introducing the subject to me during my undergraduate degree and creating this opportunity to research tribology. His guidance, patience and enthusiasm have been essential for my academic and professional development.

I'd like to thank Mr Plint and Mr Harris for their generous support of my foray into the topic. Mr Plint's passion for the subject and extensive tribological knowledge has be a constant source of inspiration. I'm very much obliged to Dr Lee for his unique industrial insight into the topic which was crucial to ensuring the success of this research. I am grateful for Professor Wood's comments and leadership of the National Centre for Advanced Tribology during my studies.

I would also like to acknowledge the very helpful technical assistance I received from Mr Favede, Mr Willmont, Mr Moneer, Dr Harvey and Dr Kucita. I have enjoyed being part of the research community at the National Centre for Advanced Tribology which has been very supportive of my perambulations in tribology and for this I am very grateful.

I'd like to thank my fiancée for her patience during writing of this thesis and my family for their enduring support, especially my parents, who kindled my initial interest in engineering and encourage me in all my endeavours.

Strenuis Ardua Cedunt

1 Introduction

1.1 Motivation

High fuel prices and increased environmental awareness cause consumers to demand vehicles with higher fuel economy, lower emissions and a longer working life than ever before. These demands arise from a harsh economic situation which stimulates increasingly intense competition in both the consumer car market and commercial trucking fleets. In September 2011 the Environmental Protection agency (EPA) and the National Highway Traffic Safety Administration (NHTSA) on behalf of the Department of Transport of the United States of America promulgated new rules under the title: Greenhouse gas emissions standards and fuel efficiency standards for medium and heavy-duty engines and vehicles [1]. The final rules detail up to a 23 % reduction in CO_2 emissions and fuel consumption for heavy duty engines manufactured to the 2017 model year standards over the 2010 baseline.

In an effort to meet the new specification and increase fuel economy, frictional losses in the engine were minimised by reducing the viscosity of new lubricants. Engine friction losses differ between combustion cycles and individual engine design, however between 4 % and 15 % is typical for diesel engines with 50 % of losses occurring at the piston rings, piston skirt and rod bearing [2]. 80 % of these tribocontacts operate in hydrodynamic and elastohydrodynamic regimes, and therefore the viscous losses associated with shearing lubricant films may be reduced by using oil with a lower viscosity [3]. However this also results in the contact surfaces being separated by thinner lubricant films which provides them with less wear protection [4].

Lower emissions may also be achieved by reducing the engine mass whilst maintaining the same power output, known a downsizing. This minimises the excess energy used to accelerate the drive-train leaving a larger proportion available for useful work. However, increasing an engine's specific output (power output per unit displacement) leads to high combustion pressures and temperatures which are detrimental to the tribological performance of lubricated interfaces in the engine [4].

1.2 Scuffing in automotive engines

Contemporary engine designs seek to exploit these two design methodologies by operating on the periphery of the load carrying capacity of thin lubricant films at high temperatures to achieve increased efficiency. This makes them susceptible to occasional adverse changes in operating conditions, which may lead to lubricant film collapse and premature mechanical failure.

The piston ring-liner interface endures a particularly harsh lubrication environment, as although the contact pressures are typically not greater than 70 MPa [4], the temperature, lubricant

supply, range of speeds and loading profile can promote lubricant starvation [5].Wear that occurs during starvation, characterised by macroscopically observable directional modification of the surface morphology may be classified as scuffing, according to the ASTM terminology standard G40 [6]. In many cases scuffing wear is sufficiently severe to modify the surface geometry such that oil consumption and blow-by increase to an unacceptable level resulting in piston seizure [7].

1.3 Scuffing detection

Scuffing is a complex multi-stage process with many interdependent variables [8]. Techniques that investigate the onset and progression of scuffing need to be highly sensitive as the transition from mild wear to seizure occurs in a couple of minutes [9]. Acoustic emissions [10–12], electrostatic sensors [8,13,14] and high speed friction data [15] have been used to detect the onset of scuffing however the repeatability and understanding of the physical phenomenon which are detected by these techniques have yet to be fully investigated.

1.4 Aim and objectives

The purpose of this work was to developing new and novel bench test capabilities to understand the fundamental causes and events leading to piston ring and liner scuffing for two cast iron materials used for heavy duty diesel engines.

1. Undertake a thorough literature search of 'Scuffing', looking at the range of definitions and uses of the word, analysing current definitions of scuffing, with supporting evidence and literature.
2. Review literature assessing existing terminology and methods to identify limitations of current scuffing detection techniques.
3. Produce a repeatable and reliable test methodology to produce a scuff on cast iron liner material using an idealised line contact using a laboratory tribometer.
4. Develop a novel technique based on high speed friction data to detect scuffing and assess their repeatability.
5. Investigate the fundamental causes and events that lead to scuffing for two cast iron materials used for heavy duty diesel engines.
6. Assess the applicability of the detection techniques to conformal piston ring on liner geometry.
7. Develop recommendations for a laboratory standard scuffing test to enable subsequent screening of materials pairs and lubricants.

1.5 Methods and techniques

Scuffing was investigated using a bench-top laboratory tribometer and a variety of surface analytical techniques to understand the onset of scuffing according to the contact conditions and lubrication regimes. It is challenging to produce a ring on liner or line contact in a bench tribometer test that replicates failure observed in operating engines, not least due to the large number of variables involved and their interdependence. There are many different parameters that cause a material to scuff e.g. load, temperature, and velocity. There exists also a number of ways to detect scuffing, including measuring friction force and acoustic emissions. It was the purpose of the literature review to assess existing terminology and methods to produce a reliable test methodology and detection techniques to investigate scuffing.

The literature was used to develop a methodology that induced scuffing by increasing the energy input into the contact. Two techniques to detect and differentiate between the onset and progression of scuffing were developed. They were alternatives for quantifying the characteristic friction behaviour which accompanied each stage of the scuffing mechanism.

1) Local changes in friction force was compared to the average friction force to produce a new parameter describing the disorderly nature of the signal (friction noise).
2) The friction force magnitude at specific locations was compared to empirical determined thresholds.

These two techniques were applied to the scuffing test methodology and evaluated for their accuracy and repeatability. The scuffing mechanisms of two cast iron liner materials with different micro-structures were compared: Flake BS145 grade 250 and Nodular BS2789 grade 400-15. The reciprocating piston ring was simulated using a 52100 G5 steel roller bearing element. The experiments were lubricated using a base polyalphaolefin oil which had a viscosity of 4 cSt at 100 ^{o}C, deliberately chosen to increase the propensity for scuffing due to the absence of chemical additives. The surface topography and material micro-structure of the scuffed surfaces was investigated using: 2D stylus profilometery, 3D optical microscopy, scanning electron microscopy, energy dispersive x-ray spectroscopy and focused ion beam microscopy.

The project was a collaboration between the University of Southampton; Southwest Research Institute an independent not for profit research facility; and Phoenix Tribology Ltd manufacturer of tribology test equipment. It was supervised by Dr John Walker and Professor Robert Wood at the University of Southampton, Dr Peter Lee, Principal Engineer and Tribologist at Southwest Research Institute and Mr George Plint, owner of Phoenix Tribology.

2 Literature review

2.1 Surface topography

2.1.1 Average roughness R_a

Surfaces which appear smooth by superficial observation, consist of varied distribution of surface heights. When two surface come into contact it is usually the high spots, termed asperities, where contact usually occurs. The average surface roughness Ra is a measure of the deviation in height of the surface with reference to the mean overall height. It is defined in Equation 2.1 [16].

$$R_a = \frac{1}{L}\int_0^L |y(x)|\, dx \qquad \textit{Equation 2.1}$$

Where y is the surface height above the mean line at position x along the length of the profile L. It has its limitations: there is no indication of the spacing of the height deviations neither is there an indication of the probability of finding a deviation at a specific position. It is only capable of measuring roughness along a plane intersecting the surface i.e. 2D. This means that the value of R_a varies depending on the orientation of the profile line across the face of the surface.

2.1.2 RMS roughness R_q

Another measurement of surface roughness is the root mean square roughness which has a greater sensitivity to outlying surface heights compared to R_a. It is the standard deviation of the amplitude density function discussed in the next section and defined in Equation 2.2 [16].

$$R_q^2 = \frac{1}{L}\int_0^L y^2(x)\, dx \qquad \textit{Equation 2.2}$$

2.1.3 Bearing area curve

Considering the profile in Figure 2.1, the probability of finding a point at a height of y from mean is $p(y)$. This can be drawn as a graph such the quantity $p(y)\Delta y$ is the proportion of the surface with heights between y and Δy.

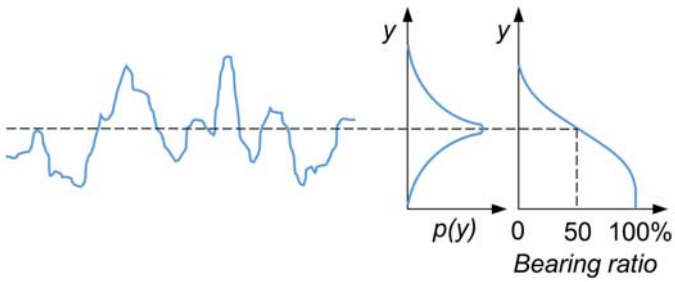

Figure 2.1: Amplitude density function and bearing area curve, adapted from Hutchings [16].

The bearing area curve may be obtained by discretely integrating the amplitude density function at specific heights h, Equation 2.3 [17].

$$Number\ of\ points\ (y \geq h) = \int_h^\infty p(y)\,dy \qquad \textit{Equation 2.3}$$

The curve provides the ratio between void and the material, the bearing area, at a specific height h from the maximum peak, Figure 2.1. It is used in EN ISO 13565-2 [18] to calculate the following parameters, shown graphically in Figure 2.2.

R_k is the depth of the roughness core profile, which excludes high peaks and deep valleys. $Mr1$ and $Mr2$ are respectively, the material level in percent that separates the high peaks from the roughness core profile and the deep valleys from the roughness core profile. For a cylinder liner to be considered plateau honed $Mr2 - Mr1\ > 60\ \%$ [19]. R_{pk} is the average height of the high peaks above the roughness core profile, it provides information on running in behaviour [20]. R_{vk} is the average depth of the profile valleys projecting through the roughness core profile, it indicates lubricant retention volume [20].

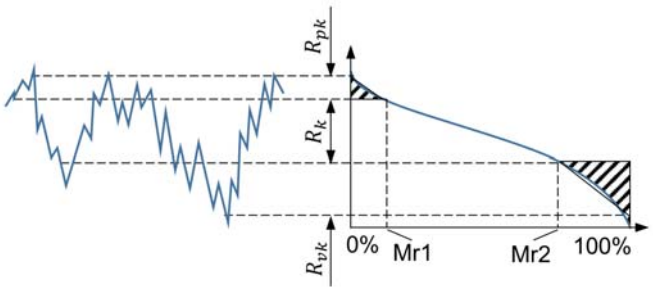

Figure 2.2: Graphical representation of surface texture parameters defined by EN ISO 13565-2 adapted from Andersson [20].

2.2 Hertzian pressure distribution

When the curved edge of a cylinder is loaded against a flat surface the area of contact between them depends on the load they support and therefore their elastic deformation. The calculation of the pressure in such a contact was first calculated by Heinrich Rudoloph Hertz who gave his name to the analysis [21]. It relies on three assumptions: 1) only elastic not plastic deformation

occurs, 2) the absolute geometry of the contacting bodies does not limit stresses developed below the surfaces, 3) Only normal forces are considered as the surfaces are frictionless. An annotated schematic of the generic geometry that results in a line contact is shown in Figure 2.3. Where R = cylinder radius, b = half the contact width and l = contact length. The mean contact pressure (p_m) may be calculated by using Equation 2.4 and Equation 2.5 [21].

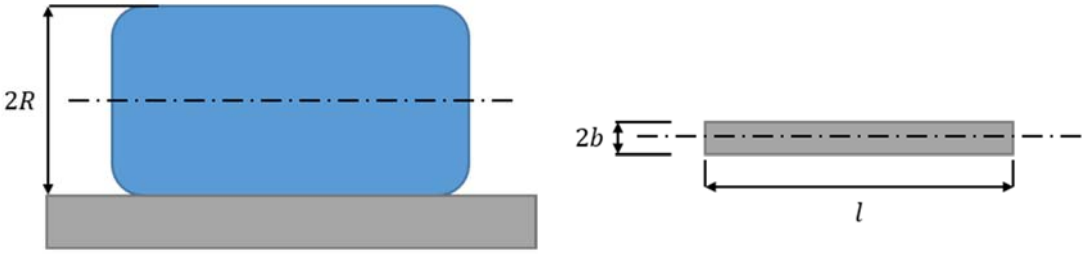

a) b)

Figure 2.3: Hertzian line contact schematic of a cylinder on a flat plane (a) and contact area (b), adapted from Beek [21].

$$p_m = \frac{F}{2bl} \qquad \textit{Equation 2.4}$$

Where

$$b = 2\left(\frac{2}{\pi}\right)^{\frac{1}{2}}\left(\frac{F}{l}\right)^{\frac{1}{2}}\left(\frac{R'}{E'}\right)^{\frac{1}{2}} \qquad \textit{Equation 2.5}$$

$$\frac{1}{R'} = \frac{1}{R_1} + \frac{1}{R_2} \qquad \textit{Equation 2.6}$$

$$\frac{1}{E'} = \frac{1-\nu_1}{2E_1} + \frac{1-\nu_2}{2E_2} \qquad \textit{Equation 2.7}$$

Where: F is the normal load (N), R' is the reduced radius (m), $E'$is the reduced modulus of elasticity (GPa). R_1 is the radius (m), E_1 is the modulus of elasticity (GPa) and ν_1 is the poisson's ratio of the cylinder and R_2 is the radius (m), E_2 is the modulus of elasticity (GPa) and ν_2 is the poisson's ratio of the flat plane.

2.3 Friction

Friction is the reactive force which opposes the relative motion of two surfaces in contact [22]. In the case of dry sliding, the magnitude of the friction force depends on the normal load, surface finish and material properties of the surfaces in contact. Dry sliding in air is also affected by the level of contamination on the surfaces of the materials which significantly impacts on the interaction of the surfaces. Despite the complex nature of a dry sliding contact the friction force F_f is generally found to be proportional to the normal force N, Equation 2.8. This observation was first made by Leonardo Da Vinci in the fifteenth century [23,24], although he suggested that they were directly proportional.

$$F_f = \mu \, . \, N \qquad \textit{Equation 2.8}$$

The empirical relationship in Equation 2.8 was later attributed to work by Guillaume Amontons in 1699 and Charles Coulomb in 1781 [21] and subsequently became known as the first law of friction. This was an improvement on Leonardo da Vinci's work, approximately 200 years before, which had noted that the friction force was directly proportional to the normal force [25]. He had also noted that the friction coefficient was independent of contact area, with which both Amontons and Coulomb concurred and which became known as the second law of friction. Coulomb also concluded that the friction coefficient was independent of velocity and this has been presented as the third law of friction. However in 1883 Beauchamp Tower disputed this, reporting that load and speed had an effect on the friction coefficient [21].

Until the 20th Century the understanding of the mechanisms which caused friction was still in its infancy. The laws of friction had remained unchanged and were based on empirical relationships. Bowden and Tabor were first to offer a physical explanation for why friction force was proportional to load and independent of contact area in 1943 [21]. They explained that friction was due to asperities on the contact surfaces being elastically and plastically deformed. The sum of the area of each asperity interaction was called the real contact area, differentiating it from the macroscopic or projected contact area referred to previously.

When the contact load was increased, the pressure at each asperity increased. This caused them to elastically deform which increased the real contact area until it was able support the load without further deformation [26]. Consequently as the real contact area had increased, the friction force which was required to further deform the asperities during sliding also increased. Similarly when the projected contact area was increased, the pressure seen by each asperity was less. This resulted in less deformation of the asperities and consequently reduced the real contact area, such that it remained the same for a given load.

Since the publication of Bowden and Tabor's work [27] the interaction mechanisms of the surface asperities has been the subject of investigation. Current understanding broadly categorises friction mechanisms for lubricated sliding into three categories, abrasion, adhesion and fatigue, which will be discussed later.

Equation 2.6 suggests that only one friction coefficient exists for a given set of conditions. However often the friction force measured during an experiment varies considerably. This can be caused by fluctuations in the contact conditions or an inherent instability associated with the contact [28]. Coulomb was the first to distinguish between the force required to commence motion, static friction and the force required to sustain motion, kinetic friction. Consequently at the beginning of sliding the surfaces remain stationary until the force applied exceeds the static friction force. If the static friction of a contact is significantly higher than the dynamic friction it

is probable that the sliding contact may exhibit stick slip behaviour. In this case during stick, when the surface is stationary, the material compliance permits it to deform until the force at the interface overcomes the static friction force and slip occurs. The force then reduces and the contact is arrested by the static friction and the cycle repeats itself [21]. It is also possible for stick slip to be extrinsic, where compliance in the test apparatus friction measurement assembly permits the contact to vibrate. This is known to affect wear mechanisms and consequently friction measurement apparatus are designed minimise these effects [29]. Variation in friction force may still occur during a test as a direct consequence of a cyclic wear mechanism however generally a well-designed test should achieve stable friction coefficient [30].

2.4 Lubrication

Friction can be reduced between sliding surfaces by separating them with a lubricant. Most tribological contacts are accidentally or deliberately separated by a solid, liquid or gas lubricant, the function of which is to reduce the interfacial sliding friction force. The following section will briefly review the main variables that influence the type of lubrication that occurs between sliding metallic surfaces lubricated by an oil film.

2.4.1 Film thickness

Lubricant film thickness is controlled by the entrainment velocity of the contact. In converging geometry contacts the elastic deformation of the surfaces result in an asymmetric pressure distribution. This contact condition is called the elasto-hydrodynamic lubrication regime. In order to calculate the elasto-hydrodynamic film thickness the Reynolds equation is required to be solved numerically. A good approximation can however be achieved using the relationship in, Equation 2.7 [21].

$$\frac{h_c}{R'} = 1.19 \left(\frac{\alpha U}{R'}\right)^{\frac{8}{11}} \left(\frac{E'R'}{F/L}\right)^{\frac{1}{11}} \qquad \textit{Equation 2.9}$$

Where α= pressure viscosity coefficient (Pa^{-1}), U= entrainment velocity (ms^{-1})

The ratio of the lubricating film thickness between two contacting bodies and their composite surface roughness differentiates between the lubricant categories detailed below and is referred to as the oil film parameter λ_s [9].

$$\lambda_S = \frac{h_{min}}{\sqrt{R_{q1}^2 + R_{q2}^2}} \qquad \textit{Equation 2.10}$$

Where h_{min} is the minimum film thickness separating the surfaces and R_{q1} and R_{q2} are the respective root mean square roughness of the two bodies.

2.4.2 Lubrication regimes

The nature of a contact's lubrication can be described by four main regimes: hydrodynamic, elasto-hydrodynamic (or EHL), mixed and boundary; schematics of each are shown in Figure 2.4.

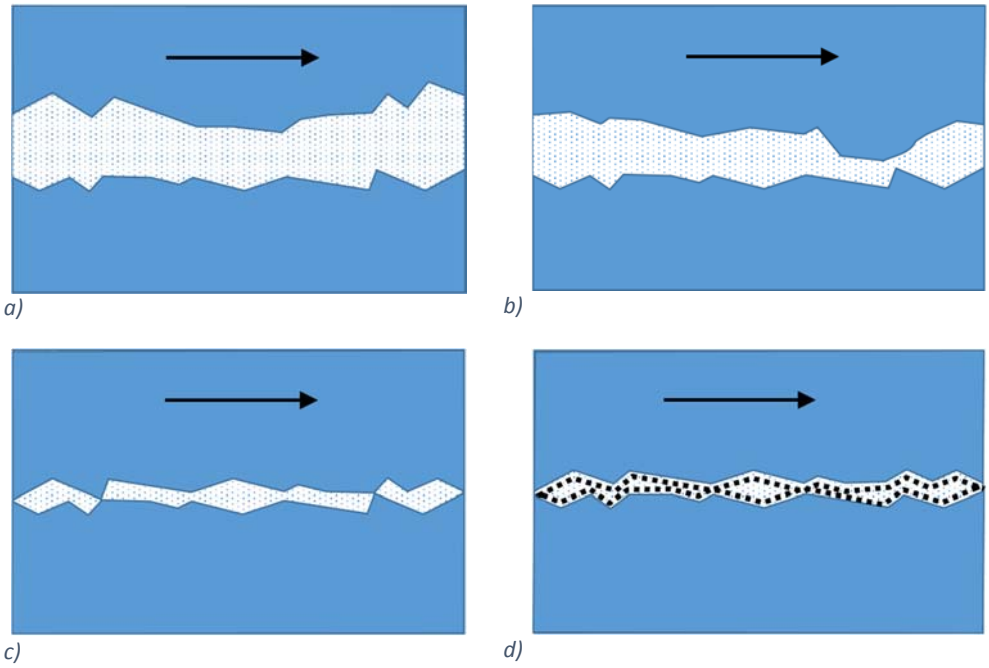

Figure 2.4: Lubricant regime schematics adapted from Bhushan [31] *a) hydrodynamic, b) elastohydrodynamic, c) mixed, d) boundary.*

2.4.2.1 Hydrodynamic

In the case of hydrodynamic lubrication h_{min} is much larger than the surface roughness. A wide tolerance in surface roughness is permitted providing h_{min} is always much larger as there is no contact between the surfaces. The lubricant bears the load by being externally pressurized in the case of hydrostatic bearing or by the relative motion and converging geometry in a hydrodynamic bearing [32]. No wear can occur due to asperity interaction in this regime due to the thickness of the film however surface fatigue, cavitation wear or fluid erosion can all occur [33].

2.4.2.2 Elasto-hydrodynamic

The local pressure in an elasto-hydrodynamic (EHL) contact is sufficient to cause the lubricant viscosity to increase significantly. This phenomena allows pressures large enough to elastically deform the contact surfaces to be supported by the lubricant film. An elastically deformed EHL contact surface has a characteristic narrowing step (approximately 80 % of h, shown in Figure 2.5) at the trailing edge which causes a significant pressure increase, this is often larger than the Hertzian maximum pressure (shown as dotted line) [34]. The lubricant film is still thick enough

to keep the contact faces separated due to the relative velocity of the contact's surfaces to entrain fluid and separate the surfaces (entrainment velocity) [32] and so consequently the wear processes are similar for hydrodynamic lubrication. The significant deformation of the contact surfaces promotes fatigue wear, which is often more severe and usually the most common type of failure [17].

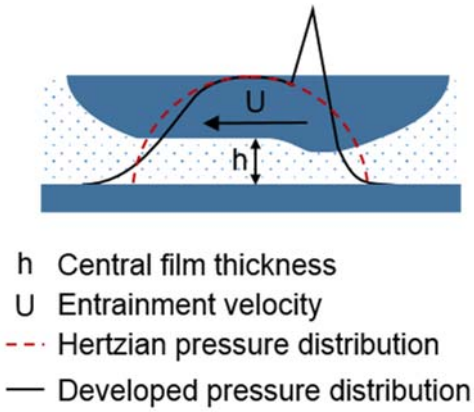

Figure 2.5: Schematic of an EHL line contact showing the film shape and pressure distribution adapted from Dowson [34].

2.4.2.3 Mixed

The mixed lubrication regime occurs during the transition from hydrodynamic to boundary lubrication. Increasing the contact load reduces the lubricant film thickness and consequently the contact load is distributed between increasing numbers of asperities and less lubricant [32]. The friction associated with the asperity interactions and viscous drag of the lubricant both contribute to the friction coefficient in this regime. Compared with the hydrodynamic regime the asperity contact causes increased wear and as a result the friction coefficient increases, this can be limited by the action of boundary lubricants [35].

2.4.2.4 Boundary

When a contact is operating in the boundary regime nearly all of the load is carried by surface asperities [32]. Boundary lubrication is often caused by inadequate lubricant supply during start-stop operation for contacts that are normally hydrodynamic or elasto-hydrodynamic [31]. In this regime the friction coefficient and level of wear is controlled chemically by surface films produced by the lubricant [33]. Surface films are typically formed when polar long chain molecules such as carboxylic acids (present in the lubricant) are adsorbed by metal oxide layers on the contact surfaces. Intermolecular forces cause the perpendicular orientation of carboxylic acid molecules to the surface, shown in Figure 2.6. This mutual repulsion also stabilises the film of adsorbed molecular chains, which are typically 2 to 3 nm long [16]. Hutchings [16] comments that in boundary lubrication ``*there are small areas of asperity contact*'' and therefore wear does occur, however to much less of a degree compared to an unprotected surface. The dominant

failure mechanisms in this regime are adhesive wear and enhanced corrosion due to aggressive film formation [31].

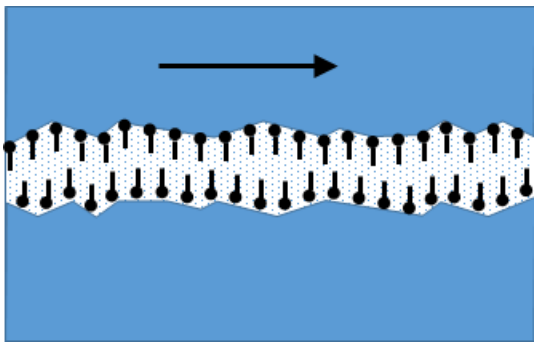

Figure 2.6: The operation of a boundary lubricant adapted from Hutchings [16].

2.4.3 The Stribeck curve

On 5th December 1901 Richard Stribeck presented his work on sliding lubricated surfaces, which was subsequently published on 6th September 1902 [36]. It described the relationship between friction and lubricant entrainment speed and presented the information as a graph which was later to become known as the Stribeck Curve, Figure 2.7. Adolf Martens and Robert Thursten both produced similar results considerably earlier, roughly 15 years in the case of Martens [37]. However, it is suspected that Stribeck's journal choice: Zeitschrift des Vereins Deutscher Ingenieure, was key to the eponymous naming, as it was the most important contemporary technical journal in Germany [37].

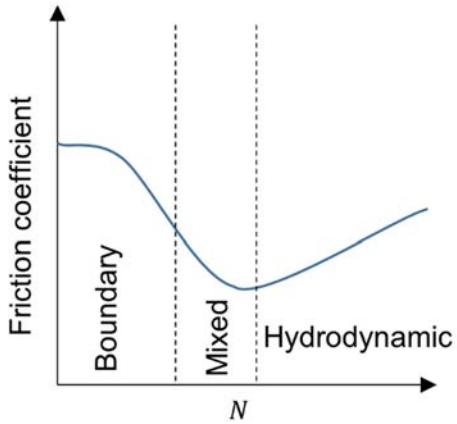

Figure 2.7: Friction regimes adapted from Caines and Haycock [38].

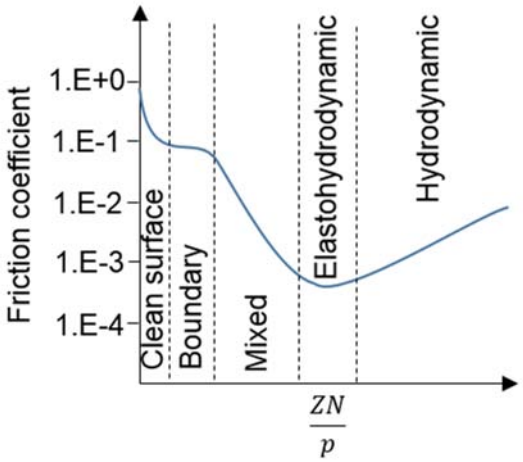

Figure 2.8: Modern classification of Lubrication regimes adapted from Bhushan [31].

Ten years after Stribeck's publication, Gümbel plotted Stribeck's data in the form of friction coefficient against the dimensionless lubrication parameter $\frac{ZN}{p}$; where Z is oil viscosity (Pas), N is angular speed (rads^{-1}) and P is pressure (Pa) [39]. In America, Mayo Dyer Hersey simultaneously discovered the same relations, known as the Hersey number [40]. Sometimes $\frac{ZN}{p}$

is substituted for λ the oil film parameter allowing cleaner quantitative analysis; as for a given contact of constant roughness, λ is only affected by the film thickness. The Stribeck curve was originally split into three lubrication categories: boundary, mixed and hydrodynamic lubrication, Figure 2.7 [37]. Considering the hydrodynamic region, as the lubrication film thickness increases the coefficient of friction increases. This is due to viscous shear within the lubricant [33]. As the velocity decreases the contact quickly moves through the mixed regime, leading to an increase in friction as asperity contact becomes the main load bearing mechanism.

Lubrication theory was developed throughout the 20th Century resulting in modifications to the original three regimes, a modern Stribeck curve can be seen in Figure 2.8. A detailed account of lubrication theory development can be found in Dowson's History of Tribology [41]. The graph in Figure 2.9 shows λ plotted on the y axis, with the λ range for each lubrication regime highlighted. This demonstrates the importance of λ as a design parameter, especially for surfaces that experience wear through running-in, described below.

The graph presented in Figure 2.10 shows `relative' contact life against λ (although the author does not quote units of life). It is unsurprising to observe that the maximum component life is concurrent with the hydrodynamic regime. The life of the contact increases with λ until it reaches a maximum once operating in the hydrodynamic regime. Comparing this to Figure 2.8, the increase in product life time is inversely proportional to the decrease in the contacts friction coefficient.

As λ increases, the friction coefficient passes its minimum and begins to increase due to viscous losses associated with shear within the lubricant. The development of lower viscosity lubricants seek to minimise these shear losses and there is a clear trend within the automotive sector in this direction. It is clear therefore that the most efficient and effective working point is around $\lambda = 2.5$. It should be noted that if the film thickness decreases further the coefficient of friction increases very rapidly and the contact lifetime dramatically decreases. As a result best design practice should if possible operate close to the hydrodynamic lubrication regime. This demonstrates the importance of λ as a design parameter.

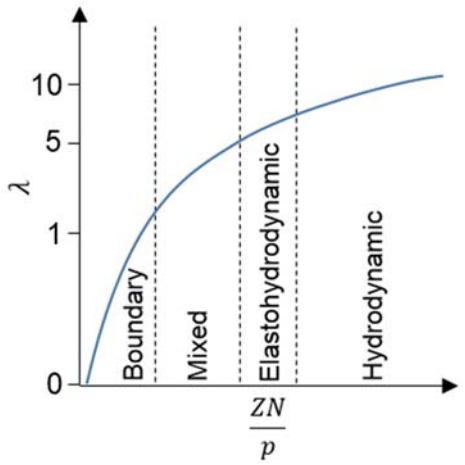

Figure 2.9: λ plotted against $\frac{ZN}{P}$ demonstrating how it can be used a tool to identify the operating lubrication regime of a contact adapted from Bhushan [31].

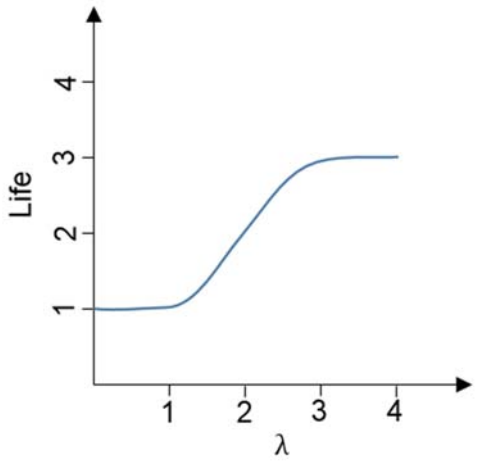

Figure 2.10: The life of highly stressed components plotted against λ adapted from Dowson [34].

2.4.4 Oil base stock and formulated additive function

Lubricated sliding contacts associated with automotive combustion engines are lubricated by oil. Oils can be classified in to mineral oils and synthetic oils. Mineral oils are obtained from the fractional distillation of crude oil and consist of a wide variety of hydrocarbons and hydrocarbon derivatives containing nitrogen, oxygen and sulphur [42]. Pure mineral oils have become increasingly insufficient for modern internal combustion engine applications due to increasingly harsh operating conditions. Consequently additives are required to modify mineral oils to achieve the required performance or used to blend with a pure synthetic oil.

Synthetic oils have been made from the synthesis of CO and H_2 via the Fischer-Tropsch process which created oil with a wide composition and so was best suited to combustion [38]. This process was developed during the Second World War to supply Germany's hydrocarbon requirement and was later utilised by South Africa while suffering crude oil embargoes. However, modern synthesised lubricants are produced by polymerisation and therefore have very limited composition which give the advantage of either just being light or heavy in composition [38].

Of most interest are olefin oligomers, a family of moderate molecular weight polymers which include polyalphaolefins. Polyalphaolefins are created from polymerizing C_{10} to C_{14} (olefins) acquired from wax cracking. Polyalphaolefins are very commonly hydrogenated to produce very stable and pure paraffin hydrocarbons. Since the late 1980's they have been used as low viscosity blending agents for multi-grade oils as they do not increase volatility of the blend as much as conventional petroleum stock [38].

2.4.4.1 Additives

Lubricant additives are chemicals which improve the performance of a base oil. Originally developed to modify the properties of refined mineral oils, they were also included in fully formulated synthetic oils. Additives are grouped depending on their effect, the most common are: Pour point depressants, viscosity modifiers, dispersants, detergents, anti wear, friction modifiers, corrosion and oxidation inhibitors, demulsifiers and antifoam. A detailed discussion of their function and mechanism can be found in the 'Automotive lubricants reference book' [38].

Due to the complex nature of additive compounds and the intellectual property surrounding them, interchanging additives from different companies is unlikely to produce identical results, even when their superficial inspection technical data is identical (e.g. metal content and total base number (TBN)). The significant cost of retesting, seeking accreditation and approvals usually provides a prohibitive barrier for an alternative blend. Therefore an oil formulation is fixed at the time of development and the oil blender is committed to the original additive suppliers for the duration of the product lifetime [38].

2.5 Wear

Wear is the process of surface topography modification which occurs when two surfaces in relative motion come into contact, it may result in the removal or redistribution of material across the surface [43]. Sliding contacts are susceptible to three main wear mechanisms; adhesion, abrasion and fatigue. In a lubricated sliding contact it is the role of the lubricant to separate the surfaces preventing wear. However when the lubricant film breaks down several different asperity interactions are possible.

2.5.1 Adhesive wear

Pure metals are homogenous and strongly adhere to one another when they are 'clean' as the availability of free electrons in the atomic structure of a metal allows them to readily bond to each other [25]. The presence of a thin oxide layer which forms in air on all but the noble metals will however significantly reduces this effect. Surface finish (smoothness or roughness) and the properties of the mating metals such as their crystal structure and hardness also affect the strength of mutual adhesion [42]. The presence of non-metallic inclusions in heterogeneous microstructures reduces the strength of adhesive bonding compared to pure metals.

If the adhesive force between two asperities in relative motion is strong, one of which is usually significantly harder than the other, wear debris or a transfer film will be formed. The adhered asperity junction can have a higher strength than the yield strength of the softer of the two materials. Consequently as the shear strain increases the softer asperity fractures at a point

away from the interface. The distance from the interface depends on the work hardening which has occurred due to the plastic deformation of the asperity and also the geometry of the asperity itself. The result of this process is transfer of material from the soft to the hard surface with no wear particles necessarily ejected from the system. The adhesive wear site on the softer material may exhibit brittle or ductile features depending on the geometry of the asperity as well as the material properties [25].

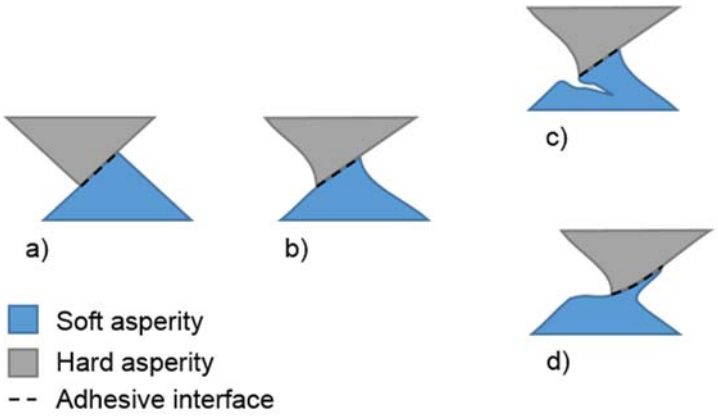

Figure 2.11: a) Asperities adhere together, b) asperities plastically deform due to shear stress, c) asperity fracture, d) ductile yield of asperity, adapted from [25].

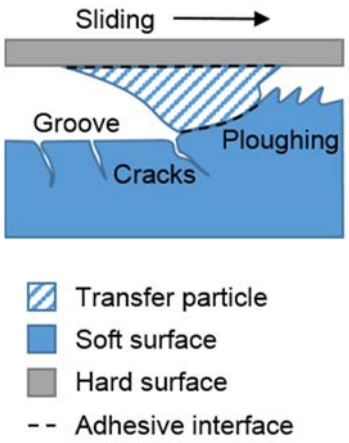

Figure 2.12: Transfer particle forming grooves by ploughing soft surface, which initiates cracks due to high tensile stress adapted from [25].

Bowden and Tabor presented a model of adhesive wear which predicted that the maximum friction coefficient attributed to adhesive wear was 0.2 [27]. The ratio of the yield strength to the shear strength was assumed to be the same at an asperity as in the bulk material. However adhesive wear often results in a friction coefficient in excess of this, which may be explained by the mechanism of asperity junction growth [44]. If the protective oxide film is removed from the surface of the asperities in this interaction then it is possible that an adhesive junction will form [43].

The model for junction growth assumes that the normal pressure applied to an asperity has exceeded its plastic limit, consequently the material is free to flow and negligible shear force is required for relative motion of the surfaces. However as the surfaces move the asperity junction width increases which increases the contact area and reduces the pressure [43]. The reduced contact pressure is not sufficient for the asperity to continue to deform plastically, consequently the shear stress must increase for plastic deformation to continue. This increase in shear stress at the interface is measured as an increase in the friction coefficient. Work hardening of asperities also increases the friction coefficient however compared to the force required for junction growth it is negligible [25]. Providing that the asperity surfaces are not inhibited from adhering by contamination on the surface such as oxides or lubricant, the junction width

continues to grow increasing the friction coefficient [43]. This process produces a positive feedback loop which can result in the seizure of the contact [25]. The ductility of the metal is a measure of its ability to plastically deform, which is key to asperity junction growth and consequently adhesive wear.

If the process of junction growth is interrupted by the presence of contaminants on the surface then the asperity junction will yield resulting in a transfer film on the surface of the hard surface. The presence of a transfer film on one of the contact surfaces distinguishes adhesive wear from any other mechanism [25]. It can be identified as it is in relief on the hard surface which has little or no wear observable in places where the film is not present.

Further asperity interactions with the transfer film may cause it to transfer back to the softer surface or to separate to form a transfer particle. Transfer particles grow in size as they collect more wear debris during sliding. The contact pressure deforms the agglomeration of wear particles producing a work hardened transfer particle with a lamellar structure [25] which adheres to the hard surface. During continued sliding these work hardened transfer particles can plough grooves into the softer surface, known as two body abrasion. This ploughing action can produce high tensile stresses which initiate cracks in the softer surface which appear similar to those observed in surface crack initiated fatigue wear, Figure 2.12.

Adhesive wear of load bearing surfaces is mitigated by separating asperities using a lubricant film. However in real applications contacts can become starved of lubricant resulting in the surface asperities coming into contact increasing the friction coefficient. The increased friction force is required for the deformation of asperities, which can lead to fatigue wear discussed in the next section, as the surfaces slide past one another.

2.5.2 Fatigue wear

Fatigue wear is often associated with rolling contact fatigue however it also occurs in dry and lubricated reciprocating sliding contacts. Fatigue wear of a surface occurs due to the propagation of cracks in the material caused by the repetitive interaction of asperities causing plastic deformation of the surface and subsurface microstructure. The asperities transmit shear forces which results in the material grains breaking down in to dislocation cells. The plastic deformation of the dislocation cells causes them to elongate parallel to the direction of sliding [25].

Crack initiation may occur at the surface or below the surface depending on the severity of the shear force acting on it. Surface initiated crack fatigue wear occurs when the shear force is large such as during dry sliding wear. Cracks initiate at weak points in the matrix perpendicular to the direction of sliding, such as grain, dislocation or phase boundaries. The cracks then follow the

boundaries until they return to the surface, forming a wear particle [25]. The introduction of a lubricant into the contact reduces the shear stress on the material therefore favouring subsurface crack initiation fatigue wear [25].

In a lubricated sliding contact where the transmitted shear stress is not great enough to initiate cracking, fatigue may still occur by a process called plastic ratcheting. In this process incremental plastic deformation of soft surface asperities in the direction of sliding occurs during each pass of the harder sliding surface. This forms thin filmy platelets of the softer material until the plastic limit is reached, at which point the platelets detached from the surface [45].

2.5.3 Abrasive wear

Abrasive wear may be classified as either two or three body abrasive wear which are readily identifiable from their respective wear scars. Two body abrasion produces wear tracks in the direction of sliding and is caused by an asperity on the harder surface ploughing through the softer counter surface [43]. There is direct transfer of the contact load through the two body abrasive particles. It is also caused by work hardened transfer particles which adhere to the reciprocating surface and then subsequently plough the surface [46].

Three body abrasion produces wear tracks with a dimpled surface with no directionality and has a lower wear rate than two body abrasion [25]. This is caused by third body particles which are entrained between the two surfaces under test [16]. These particles may be from the environment such as silica [43] or soot, or they could be spalled coatings or hard particles liberated from the matrix of one of the bulk surfaces, they are typically smaller than the h_{min}.

In a lubricated sliding contact abrasive particles are often larger than the film thickness and consequently the contact load is transferred through them instead of the lubricant [16]. Depending on the material properties of the surfaces and the particles, wear usually occurs by a combination of plastic deformation and brittle fracture [16]. Several parameters pertaining to the particles influence the wear rate, these include: hardness, shape, and size in relation to microstructural features such as hard phases in the abraded surface [16].

2.6 Scuffing of automotive piston ring-liner contacts

2.6.1 Cast iron as diesel engine material

Alloys of iron with typically more than 2 % carbon are classified as cast irons and they lend themselves to the eponymous manufacturing process due to their low melting points, good fluidity and low solidification shrinkage. Cast irons are often chosen as engine block material as they are inexpensive, can be readily cast into intricate moulds and have high resistance to wear. Aluminium alloys have been used in the automotive industry as engine block material to achieve weight saving, however the increased pressure and temperature in the combustion chambers

of high specific output diesel engines precludes their use [47]. Cast irons typically contain 2.0 - 4.5 wt% C [48] as well as other alloying elements, such as silicon (1.0-3.0 wt%) which modifies the eutectic and encourages cementite (Fe_3C) to decompose into α-ferrite, pearlite and graphite upon slow cooling. The exact composition and heat treatment of the alloy dictates the shape of the graphite, its micro-structure and therefore its mechanical properties. The three main types of cast iron are based on the morphology of the graphite phase and therefore termed: flake, nodular or compacted.

Flake cast iron has been commonly used as a cylinder liner material due to its good mechanical properties, tribological performance and low cost [49]; however the increased stress placed on the piston ring cylinder liner contact by engine downsizing requires better performance than it offers. Therefore potential alternative materials including nodular cast iron, compacted cast iron and steels are currently being investigated [50]. Nodular cast iron has better tensile and fatigue strengths than flake cast iron whilst retaining good machinability and low manufacturing costs [50–52]. The enhancement in material properties are realised by changing the graphite morphology from flakes (angular high aspect ratio inclusions which act as stress raisers) to nodules which reduce the propensity of cracking in the matrix [53,54]. Consequently specific output can be increased by achieving weight saving through manufacturing cylinder liners with thinner wall thickness.

2.6.2 Grey cast iron

Traditionally both gasoline and diesel engine blocks were cast from grey cast iron which contains flake graphite in a pearlitic micro-structure. Graphitic flakes, shown in Figure 2.13a, act as a solid lubricant to aid machining of the casting and also prevent scuffing when the engine is in service. The pearlitic micro-structure is harder than the alternative ferritic micro-structure and enhances wear resistance [55]. Increased wear resistance can also be achieved by adding phosphorous (<0.3 wt%) to the alloy which upon cooling forms a hard steadite phase, Fe_3P. The increased hardness reduces the machinability of the alloy, consequently only cylinder liners and not a whole block are cast from hard grey cast iron. The composition of a typical engine alloy such as EN-GJL-250 grey cast iron containing graphite of the form I can be specified by the manufacturer providing the tensile strength of a sample is a minimum of 250 MPa, according to EN 1561:2011 [56] . The hardness is not specified for the grade although it is generally in the range of 168 - 252 Hv depending on the relative tensile strength of the material [56].

2.6.3 Nodular cast iron

The addition of magnesium during the casting process causes the graphite to form a spheroidal shape, Figure 2.13b. Cerium is also added as a nodularising agent to prevent impurities such as bismuth, lead, titanium and antimony from stabilising flake formation [57]. The individual nodules appear in a variety of sizes but are generally larger and have a wider spacing than the

flakes in grey cast iron. The nodules grow surrounded by austenite, therefore inoculation with ferrosilicon ensures short carbon diffusion distances thus preventing the formation of white iron (cementite). The matrix can either be pearlitic or ferritic depending on heat treatment. Nodular cast iron has a lower thermal conductivity than grey cast iron. It is however stronger and more ductile than grey cast iron as the nodules of graphite do not cause stress concentrations to the same degree as the graphite flakes. The composition of a typical engine grade nodular graphite cast iron such as EN-GJS 400-15, can be specified by the manufacturer providing the minimum sample tensile strength exceeds 400 MPa according to EN 1563:2011 [58]. The hardness is not specified however it is typically between 135-180 Hv [58] and has graphite in the form V and VI according to EN ISO 945-1 [59].

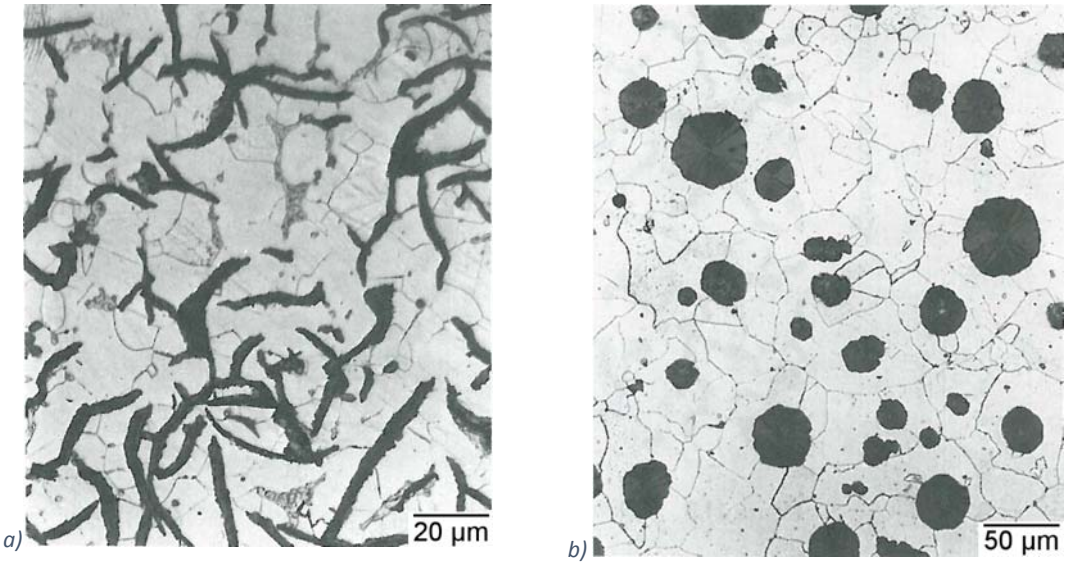

Figure 2.13: Optical images of a) Grey cast iron and b) Nodular cast iron reprinted from [48] *with permission from Wiley & Sons Ltd* [1].

2.7 Diesel engine piston ring materials

Piston rings are manufactured from cast irons and steels and may also be coated to improve their tribological performance. In the past nodular cast iron rings were found to give acceptable performance [60–62], but as specific power output increased, chrome coating of the piston rings provided enhanced scuffing resistance [63]. Modern environmental requirements have seen manufacturers greatly increase engine specific output by using forced induction, whilst at the same time using thinner piston rings to reduce friction losses in the ring pack [61]. Nodular cast

[1] Original figure numbers Figures 11.3a and 11.3 b. The following copyright statement applies: No part of this publication may be reproduced, stored in a retrieval system or transmitted in any form or by any means, electronic, mechanical, photocopying, recording, scanning or otherwise, except as permitted under Sections 107 or 108 of the 1976 United States Copyright Act, without either the prior written permission of the Publisher, or authorization through payment of the appropriate per-copy fee to the Copyright Clearance Centre, 222 Rosewood Drive, Danvers, MA 01923, (508)750-8400, fax (508)750-470. Requests to the Publisher for permission should be addressed to the Permissions Department, John Wiley & Sons, Inc., 605 Third Avenue, New York, NY 10158-0012, (212) 850-6011, fax (212) 850-6008, E-Mail: PERMREQ@WILEY.COM.

iron no longer has the required mechanical performance [62] and the temperature of the interface often exceeds the working limit of chrome [19]. Consequently nitrided steel rings have been used for heavy duty diesel engines due to their superior mechanical properties. These rings have a CrMoV or CrSi composition with a martensitic structure [64] and have a hardness of between 360 and 480 HV [65].

2.8 Historical perspective on automotive scuffing

The Ramsbottom ring for steam engines was developed in the nineteenth century. It was so effective at sealing the ring-liner contact that it has been incorporated in the design of internal combustion engines ever since [41]. As engine development progressed the piston ring-liner contact was identified by Ricardo in 1922 as responsible for the majority of engine frictional losses [66]. A more recent study by Holmberg et al [67] has shown this still to be the case. A significant failure mechanism of this contact is scuffing and occurs when the friction between the piston ring and cylinder liner reaches a critical value, it can be terminal. 16 years after Ricardo, Teetor explained the importance of metallurgical considerations in relation to scuffing [68]. Dowson explained how prior to the late 1940s and the 1950s little work on the fundamentals of the piston ring function had been developed until the 1960s when a "concerted attack" on ring dynamics, lubrication and wear occurred [41].

2.9 The definition of scuffing

During the 1960s research interest in tribology grew rapidly and was brought centre stage by the Jost report in 1966 [69] which highlighted the cost of poor tribological practices for British industry. In 1969 the Organisation for Economic Co-operation and Development (OECD) met in Paris to define tribological terminology, including scuffing, as "local damage caused by the occurrence of solid-phase welding between sliding surfaces without local surface melting" [70]. However despite the publication of this definition, the word scuffing was used vaguely. Eyre and Dutta [71] commented in 1975 that "Many definitions of scuffing appear in the literature and one which would appear to receive the most universal acceptance is" the OECD definition adding that "Experimental evidence to support this statement is however extremely sparse". The research community continued to use a vague definition of scuffing as Bushan highlighted when he commented in 1999 that "Severe types of adhesive wear are often called galling, scuffing, welding or smearing, although these terms are sometimes used loosely to describe other types of wear" [31]. In 2007 a `Guide to Friction, Wear and Erosion testing' was published by Budinski in which he implied that scoring and scuffing are the same form of `sliding wear characterized by localised macroscopic "scratches" or "furrows" in the direction of motion" and stated that "scoring is really galling" [72]. The OECD defines galling as "A severe form of scuffing associated with gross damage to the surfaces or failure." [70]. It interprets a different relationship between

these terms stating that galling could describe both scoring and scuffing and suggests that these more detailed descriptive terms be used instead.

The confusion over the definition of scuffing is compounded by differing usage on either side of the Atlantic. Hutchings [16] explains that in the UK scuffing is associated with the OECD definition, however in the US scoring is sometimes used to describe the same definition. More significantly scuffing and scoring can be used in the US to “imply scratching by abrasive particles” [16].

In recent years there has been a resurgence in interest in scuffing caused due to its increased occurrence resulting from engine downsizing and lower viscosity lubricants being adopted in order to reduce emissions. Consequently in 2015 the ASTM terminology committee sought to clarify the definition of scuffing so as to focus the research effort. The definition included a reference to lubrication and a description of the scuffed surface topography: “A form of wear occurring in inadequately lubricated tribosystems that is characterized by macroscopically observable changes in texture, with features relating to the direction of motion” [6]. This definition permits any form of wear to constitute scuffing and this reflects the complicated nature of scuffing, however additional terms such as adhesive and abrasive wear provide further clarification when analysing failure modes. Considering the confusion surrounding ‘the’ scuffing mechanism it is perhaps unsurprising that the definition describes the result of scuffing in terms of surface damage rather than the mechanism by which it occurs. This definition of scuffing therefore appears to seek only to separate lubricated sliding failure scuffing from galling which is dry sliding failure.

2.10 Scuffing severity

One of the problems in providing a comprehensive definition of scuffing is that it appears to be a complicated process involving a number of initiating variables [73] that can often cause rapid progression from initiation to seizure, in a matter of minutes [9]. However in order to understand and control scuffing, a detailed knowledge of its initiation is needed now more than ever before, given the tighter tolerances, low viscosity lubricants and harsher conditions imposed on the piston ring cylinder liner contact.

According to Nilsson [74], Ludema [75] considers the OECD definition to be a final stage in the process of scuffing events. However Ludema's definition does differ from the OECD to say that a general definition of scuffing is “a roughening of surfaces by plastic flow whether or not there is material loss or transfer” [75]. This suggests that adhesive wear defined by OECD as “wear transference of material from one surface to another during relative motion, due to a process of solid-phase welding” [70] is not required for scuffing. Lacey agrees with the OECD that scuffing

failure is “ultimately, severe adhesive wear” [76]. When Neale defined scuffing in 1970, he considered the OECD definition to be the beginning of scuffing, initial “adhesion between the high spots as a result of local welding, which gives rise on further movement to tearing or dragging of the surfaces”. While Neale describes a detailed explanation of the OECD definition, Ludema's definition occurring 14 years later is much more complex and reflects the advances in knowledge during that time.

He suggested a possible clarification of terminology, when he defines scuffing “in terms of microscopic aspect of surface failure. Perhaps this leaves the term `scoring' for the macroscopic manifestations of failure” [75]. Summers-Smith [77] also made a distinction between microscopic and macroscopic wear and then uses the terms `mild’ and `severe'. “In the former, the wear particles are very fine (0.01-0.02 μm) and there is comparatively little roughening of the worn surface. In `severe' wear the wear particles are much larger and the surface becomes rough and torn in appearance, giving rise to what is usually termed scuffing or galling”; unfortunately he does not comment on how much larger the wear particles are. Where severe-scuffing is mainly concerned with the OECD definition, mild-scuffing attempts to explain the process leading up to severe-scuffing.

Munro also reported “minor and severe forms”[78] of scuffing. He observed streaky wear patterns on the bores and rings during minor scuffing and reported the formation of white layers on the surface of cast iron accompanied by a local temperature increase [78]. He reported that severe wear follows as the hard layer spalls from the surface; it is probably caused by abrasion or the wear debris collapsing the lubricant film leading to adhesive wear.

In contrast to other authors, Morris et al [14] and Tasbaz et al [13] discussed the scuffing mechanisms in terms of first and second transition scuffing. These are different from the mild and severe scuffing proposed by Ludema. In the first scuffing transition, martensitic white layers can be formed by localised heating caused by asperity contact while a lubricating film exists. Morris et al commented that the formation of the white layer is not accompanied by an increase in wear rate and could be used as an indicator of imminent scuffing. The second transition scuffing causes “catastrophic failure” by “severe adhesive wear”. The lubricating film has “totally collapsed” and a sharp increase in friction force is observed with the transition [14].

Aue et al [79] also suggested that severe scuffing of ferrous materials forms a hard ‘white’ surface layer which spalls to result in severe scaring. Munro [78] supports Aue's analysis that scuffing wear quickly accelerates to abrasive wear during spalling of the hard ‘white’ surface layer. Munro also agrees with the OECD's definition of scuffing when he comments “Gross damage characterised by the formation of local welds between sliding surfaces' as described by Barwell is typically shown in minor and severe forms” [78]. Murray [73] also described the final

stage of scuffing as “the local welding of portions of the ‘interacting surfaces in relative motion’”. It therefore appears that many authors have agreed with the OECD definition of scuffing as Eyre and Dutta noted [71], however only as the final stage of the scuffing process. Slightly confusingly a few authors chose not to explicitly separate severe wear caused by spalling of the hard ‘white’ surface layers formed during severe scuffing from the rest of the scuffing system. However it is considered that scoring is a better terminology for this [79].

As the process leading to severe scuffing is cumulative, it appears it can be interrupted in various ways [73,75]. If the lubricant is running too hot, improving cooling can halt the scuffing process and allow the lubricant film to reform. Friction modifier additives form absorbed chemical films of low shear strength which interrupt the progression of plastic fatigue as the energy is dissipated in shearing the films instead of deforming the contact surface [80]. Oil filtration removes debris that have been formed preventing them from being reintroduced into the contact and causing the lubricating film to collapse due to high local pressures [75]. It must therefore be decided at which stage in this process scuffing is said to have occurred: in the case of Ludema's model is it when wear debris have been formed and cause “severe plastic flow and heating, which propagates the damage at an ever-increasing rate."[75]. It is clear that two separate definitions for mild and severe scuffing are required.

2.11 Empirical scuffing models

Scuffing is often associated with a temperature increase due to extreme loading and speed conditions and many of the initial scuffing models were focused on a mathematical definition of a critical scuffing temperature. Bowmann and Stachowiak [80] noted that Dyson [81,82] gave an excellent review of scuffing related research before 1975 based on Block's critical temperature theory which has been used extensively for design, specifically for gears [83]. In the second part of the review Dyson discussed scuffing mechanisms however he concluded that “neither the survey of empirical criteria nor that of the scuffing mechanisms proposed by various authors seems to offer much of a clue about what is really happening” [82]. Matveevsky also developed the concept of `critical frictional power intensity' [84], with Alliston-Greiner et al having also discussed the heat generation in a contact in terms of an `Energy Pulse'[85]. Bowmann and Stachowiak explain that one of the disadvantages of the temperature models is that they use the friction coefficient which is notoriously difficult to measure and completely system dependent. Probably the biggest weakness however is that very large assumptions are required for the calculation and as a consequence the different models produce a ``large range of critical scuffing temperatures'' [80].

Several authors [80,81,86] have considered unexpected scuffing processes to be triggered by lubricant film collapse which is controlled by a large number of variables such that they focus on

what happens once the film collapses. Indeed it was found by Lee and Cheng [87] that scuffing was not guaranteed to occur even if EHL and micro EHL films collapsed. Bowmann and Stachowiak present a review of such scuffing models in their 1996 paper [80] consisting of various different temperature and physical models and offer their own definition as the sudden failure of protecting films in mechanical equipment operating under extreme conditions of load and speed. The order of reported scuffing events however exist in various concatenations. Whether contact occurs which generates heat and causes scuffing or whether scuffing occurs and significant heat is generated is discussed by Ajayi et al [88] who propose that scuffing is “accompanied by a large amount of heat generation” when “the rate of thermal softening exceeds the rate of work hardening'' [88].

Desorption models consider the effect of EHL film collapse on the chemical films adsorbed on the surfaces of the contact. Lee and Chen considered desorption in terms of critical temperature-pressure theory shown in Figure 2.14 [89]. It can be seen that polar additive molecules are absorbed on the surfaces of the contact at low temperatures and pressure. However as the temperature and pressure increase the percentage of absorbed molecules on the surfaces decreases until a critical value is reached causing film failure. This occurs at higher temperatures because the surface films are thermally excited and therefore have greater probably of detaching from the surface [80]. Desorption has been found to occur circa 150^{o}C [90,91].

Lubricant decomposition models have been considered to explain the events that initiate scuffing [92]. At temperatures exceeding 150^{o}C, higher temperatures and longer service durations increase the probability of the lubricant oxidising to produce low molecular weight products [92]. These either evaporate or polymerise to form sludge [80] which can physically disrupt the supply and formation of lubricant.

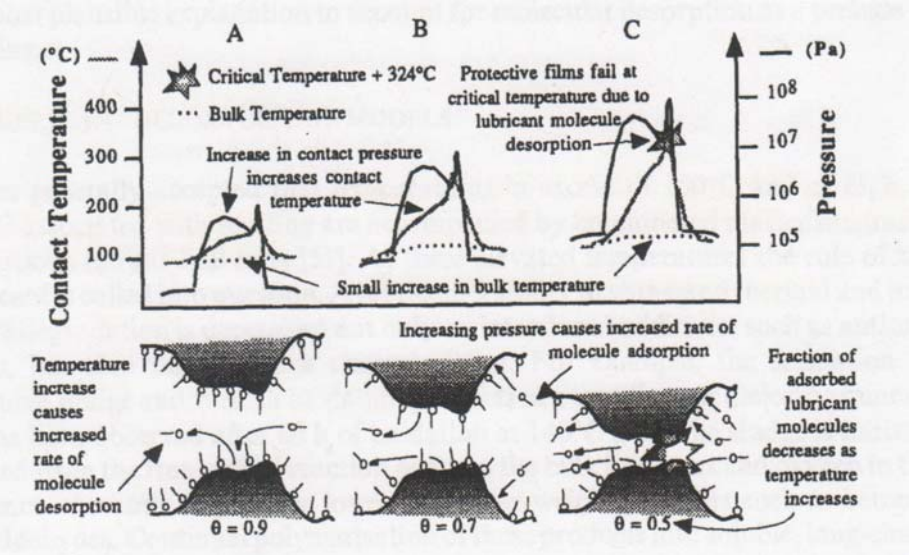

Figure 2.14: The chemical desorption model of Lee and Chen, reprinted from [80] *with permission of Springer* [2].

At elevated temperatures oxygen can dissolve and diffuse through oil which enables oxide films to form on surfaces of lubricated contacts [93]. The oxide films sacrificially protect the surfaces from scuffing by preferentially shearing [94]. Summers-Smith discusses how protective oxide films can form allowing a transition from severe back to mild wear as well as the formation of chemical additive film to maintain mild wear even when boundary lubricant fails [77]. It should be noted that the base stocks containing sulphur have the ability to form surface films albeit to a lesser extent than a dedicated additive. Although Ludema discusses fatigue as a scuffing initiation process he also agrees that the "break down of surface films is considered to be related to the initiation of scuffing, either due to the breakdown of elasto-hydrodynamic films, or desorption of physical or chemically adsorbed films, or penetration or removal of oxide films" [74].

In Aue's review of scuffing he carefully describes the `thermal bump' scuffing mechanism, a term first coined by NASA [79]. Aue agrees with Neale that a random event is required to increase the friction locally causing a rise in temperature and expansion called a 'thermal bump'. Aue then elaborates on the heating process explaining that the thermal bump, "rubs harder, becomes hotter, grows higher and so on in a vicious circle". Two outcomes are now possible, in the first instance the wear rate matches the bump growth and on return of the lubricant supply the bump shrinks on cooling, consequently the contact remains stable. In the second instance the wear rate is not sufficient for stability, therefore the thermal bump grows and the contact temperature rises, collapsing the oil film. At this stage mild welding occurs due to the increased

[2] Original: "Figure 2. Schematic illustration of critical lubricant temperature criterion. (A) Low temperatures and pressures, molecules absorbed on contacting surfaces, (B) temperature and pressure increases, the fraction of lubricant molecules absorbing/desorbing from surfaces decreases (θ), (C) at the critical temperature the fraction of absorbed molecules falls below 0.5 resulting in film failure." Tribology Letters, A review of scuffing models, 2, 1996, 119, W.F. Bowman, G.W. Stachowiak, © J.C. Baltzer AG, Science Publishers 1996 with permission of Springer.

friction coefficient. If the process continues the formation of hard white layers occurs. Aue suspects the white layers to be martensite formed by “temporary rapid heating and immediate cooling by the cold surroundings” and comments that if the “heating action continues, severe scoring will result” [79]. The severe scoring Aue refers to is possibly due to the debris formed by the white layer as it spalls from the surface as a result of the shear force transmitted through the contact, due to the high coefficient of friction.

Batchelor and Stachowiak recently published an empirical scuffing mechanism [95]. It is called the `Lubricant catalytic decomposition model' and amalgamates all of the mechanisms discussed. In this way the mechanism takes into account many of the interdependent variables associated with scuffing whilst remaining suitably material and lubricant nonspecific; consequently it provides a very convincing qualitative explanation of the scuffing process. The mechanism proposes that plastic deformation caused by high lubricant pressures causes flash temperatures which result in the surface oxide layer catalysing the thermal decomposition of the lubricant. This involves the removal of physical and chemical films from the surface and also the breakdown of the lubricant molecules such that a protective lubricant film can no longer be formed. In the absence of a lubricating film the oxide layer is removed, exposing the contact surface resulting in asperity adhesion and mild scuffing.

It is clear from most of the models reviewed above that scuffing is a thermally driven process caused by frictional heating. Heat is either generated by dissipating kinetic energy of the contact via viscous drag of the lubricant or in collisions of asperities [95]. The balance between heat generation and cooling is important in determining the lubricant behaviour and the local properties of the contact surfaces. Both Shuster et al [12] and Lacey et al [76] concurred that the failure of the boundary lubricant film due to thermal feedback ultimately accelerated scuffing by allowing an increase in friction from asperity contact that ultimately led to severe adhesive wear.

2.12 Piston ring – cylinder liner scuffing

Neale detailed a probable mechanism of scuffing specific to a combustion engine, in which he commented that scuffing is likely to occur just after TDC (Top Dead Centre) on the top compression ring during a power stroke. Scuffing occurs here because the oil film is the thinnest due to the low ring velocity, the temperature is high from combustion and it is furthest away from the oil supply. He hypothesised that at a critical film thickness the “interaction between the surface asperities becomes sufficiently severe” to generate a temperature increase that when coupled with the rubbing speed “cause escalating surface damage” [96]. It is clear that for severe-scuffing to occur ultimately the lubricating film has to break down. Ludema argued however that before the film breaks down the scuffing process has already begun by the load

transfer through the lubricating film causing plastic fatigue [75]. A visual interpretation of the scuffing model proposed by Ludema is shown in Figure 2.15. It can be seen how plastic fatigue causes the formation of debris which compromise the EHL film leading to scuffing [80]. Staph et al [84] also noted that wear can take place without the lubricating film collapsing. They explained that cyclic stresses are still transmitted through a full EHL film and can cause pitting. These two reports are important in explaining scuffing which occurs towards the end of a components life under standard operating conditions. While this may offer a deeper understanding which can be used to improve the design of such a concentrated contact, it does not help explain unexpected scuffing events during the contact's working life.

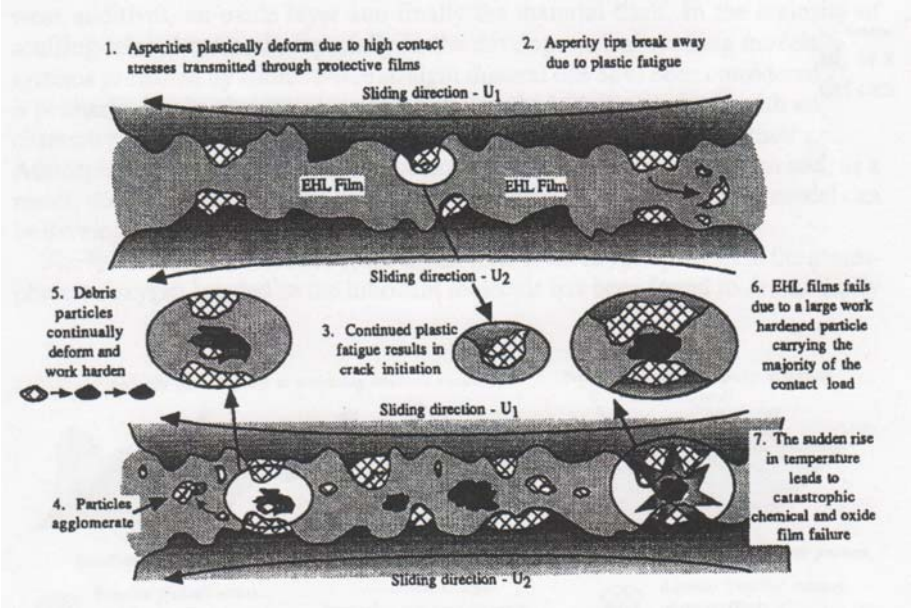

Figure 2.15: A visual interpretation of the scuffing model Ludema proposed, reprinted from [80] *with permission of Springer* [3].

When discussing scuffing Dyson [81] commented that “the two most influential factors appear to be piston speed and bore surface finish”. Lacey [76] agreed that surface finish is important. He has suggested the role asperities play in collapsing the lubricating film, whilst noting that the probability of a scuffing event occurring increases when the surfaces have not completed running in and still have a significant roughness. This is due to the influence of the surface roughness on the lubricant regime as previously discussed in Section 2.4.1. The incidence of scuffing during running in can be traced to the surface machining process, usually honing. Torn or folded metal (TFM) is created during machining. It is intuitive that a surface with a large amount of TFM will have an increased roughness. The term TFM was first proposed by Hesling

[3] Original: “Figure 3. Schematic illustration of the asperity interaction model proposed by Ludema [75]. Agglomerated debris formed from plastically deformed asperities work harden and carry the majority of the contact load. This in turn causes EHL and micro-EHL film failure, resulting in uncontrolled temperature rises and complete film failure.” Tribology Letters, A review of scuffing models, 2, 1996, 122, W.F. Bowman, G.W. Stachowiak, © J.C. Baltzer AG, Science Publishers 1996 with permission of Springer.

in 1963 [97] and defined by Gupte et al [98] as “microscopically smeared metallic debris attached to a machined surface, particularly on honed bore surfaces”. Gupte et al proposed a surface index parameter which rates surfaces according to the amount of TFM present. In their work a set of surfaces were first qualitatively ranked using a SEM and then optical profilometery was used to measure various surface parameters in order to calculate the surface index. It was found that the surface index parameter ranked the samples in the same order as the qualitative SEM technique. The ranked surfaces were then tested for their scuff resistance by increasing the normal load exerted on the contact in a vertical reciprocating rig. The results showed that increasing amounts of TFM decreased the normal load required for scuffing. This agrees with Lacey's observation as a poor finish give a large amount of TFM and a higher roughness.

2.13 Scuffing damage in cast iron engines

In 1970 Neale offered a comprehensive description of scuffed components from a ring-liner contact in his survey of piston ring scuffing. The surfaces of scuffed components exhibit smeared lines in the direction of sliding, shown in Figure 2.16 a) and b). On closer inspection with the naked eye or a low power microscope the surfaces appear ``torn and smeared'' [96]. Often scuffing occurs locally on the ring and liner, however it always occurs across the whole width of the ring shown in Figure 2.16 b). The scuff lines are distinguished from ``sharper scratch lines'' caused by ``small particles of abrasive dirt'' shown in Figure 2.16 b) [96]. The fact that both the liner and ring have a smeared appearance suggests material transfer between the liner and the ring. The phenomenon tends to be local lines on the surface suggesting localised regions subject to plastic deformation.

Carver and Johnson performed a detailed investigation of scuffing in a turbocharged diesel 855 cu.in. 6 in line engine [99]. Using a laboratory dynamometer, scuffing was induced by increasing engine coolant and intake charge temperatures to 100 ^{o}C and 66 ^{o}C respectively. The tests were run at the rated speed (2100 rpm) at full power (335 horsepower) until failure or 500 hours had elapsed. Scuffing was detected by an increase in oil consumption and increased blow-by. A severely scuffed liner from the investigation looks similar to work by Neale, with scratch lines in the direction of motion, Figure 2.17 a). Scanning electron microscope images of the scuffed surfaces show the surface topography in detail. The mildly scuffed liner condition, was still present outside the scores and consisted of smeared material forming a smooth surface. Severe scuffing occurred inside the scores, Figure 2.17 b). Here the severe adhesive wear has resulted in a surface constructed of adhesive wear particles with large topographic relief.

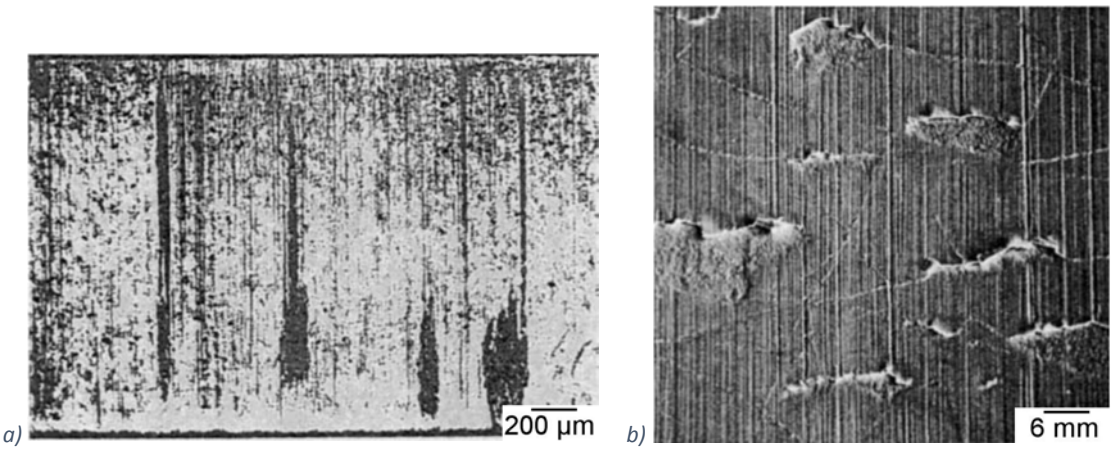

Figure 2.16: Scuffed and scored components from the piston ring liner contact: a) Major scuffing of cast iron ring, b) Scuffed chrome liner, republished from Neale [42] *with permission from Elsevier* [4].

During the initiation of scuffing the surface topography of the cast iron reduced in roughness compared to the original honed surface, as can be observed in Figure 2.17 c), this was also observed by Wojciechowski et al [100]. Plastic deformation of peaks into valleys occurred forming a surface which consisted mainly of a plateau [101], typically cracks in the surface were observed to be of the same order as the graphite flakes [102].

The graphite in the cast iron microstructure is referred to in literature as providing a solid lubricant which in the event of lubricant starvation provides a limited resistance to scuffing [20,103]. The beneficial effect is balanced against the weakness of the graphite/matrix interface, which can be crack initiation sites [54]. The plastic deformation of the surface has been found to extrude graphite from the microstructure to the surface [103]. The size and distribution of the graphite has been observed to affect the continuity of graphite films formed on the surface during sliding [104]. Nodular cast iron, despite its improved ductility, has been found to produce discontinuous graphitic films which have been attributed to its poor scuffing resistance compared with flake cast iron [105].

Humidity, sliding directionality, load, speed and surface preparation have been identified as variables which affect the formation of graphitic films. Sugishita et al [103] observed that high shear rates were effective in removing graphitic films from the surface of the cast iron. They also reported that the addition of small amounts of lubricant (0.006 cm^3 of light oil) removed the graphitic films and resulted in lower friction coefficient for similar materials [103]. The formation of a graphite film on the surface of the cast iron has been reported to only occur at specific sliding conditions [54]. Montgomery [105] observed the localised formation of graphitic films on

[4] Republished with permission of Elsevier Science and Technology Journals, from Tribology Handbook, M.J. Neale, ed., 2nd ed., 1995; permission conveyed through Copyright Clearance Center, Inc.

nodular cast iron and concluded that the scuffing resistance was not enhanced as only some of the asperity interactions were protected by the graphite film.

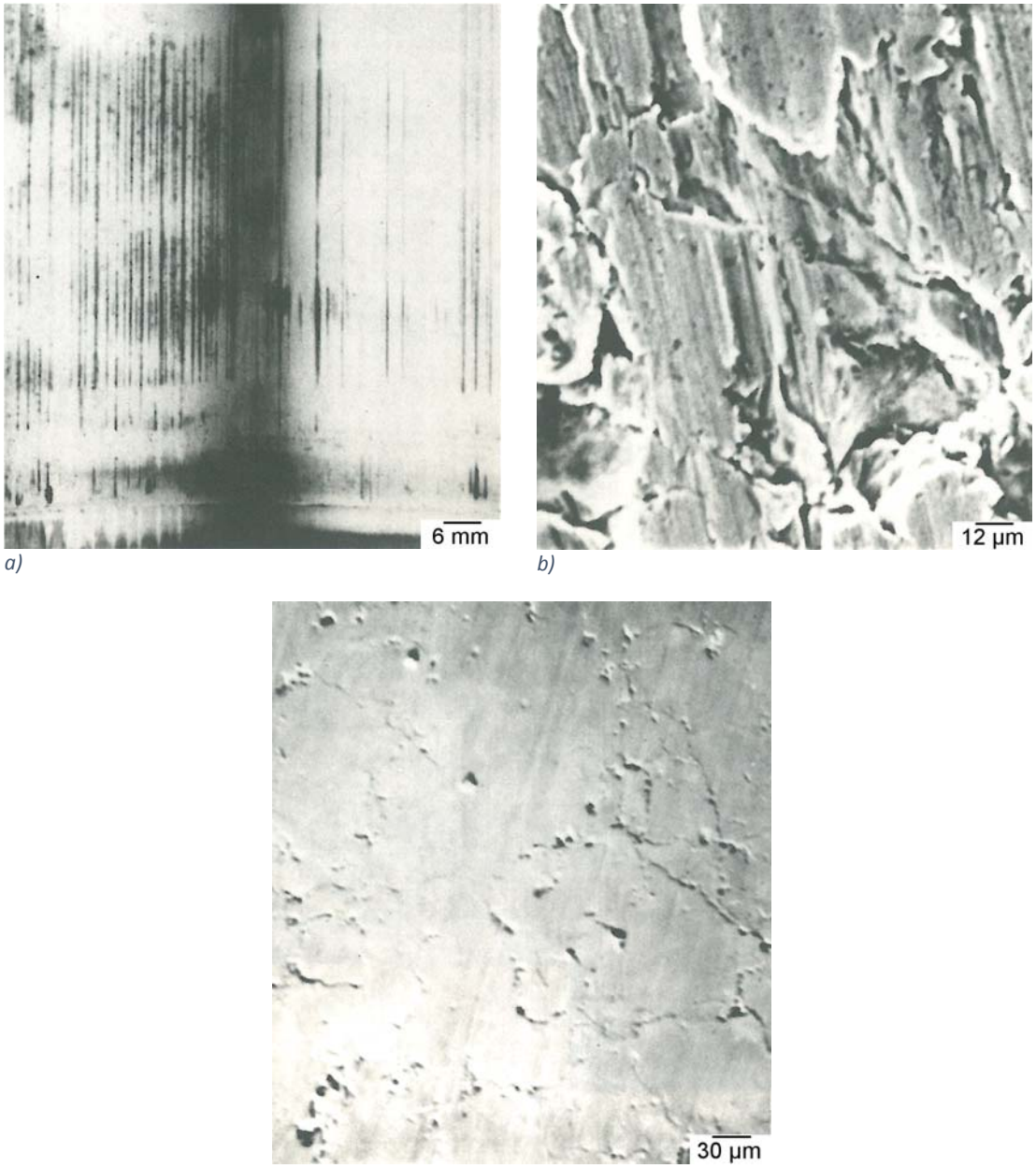

a) *b)* *c)*

Figure 2.17: Scanning electron microscope images of a scuffed bore from a fired dynamometer test reprinted from [99] *with permission of IMechE, a) Scuffed cast iron liner, b) Severe adhesive damage inside scoring marks, c) Mild adhesive smearing outside scoring marks.*

Flake cast iron has been reported to fail under sliding contact due to the removal of wear particles caused by the initiation and propagation of cracks along the graphite matrix interface [49,54,106–108]. The rate of crack propagation has been reported to be increased with reciprocating sliding compared with unidirectional sliding [107]. The reversing shear stress causes the graphite/matrix interface to fatigue and cracks to propagate. The high aspect ratio of

the graphite flakes creates stress raisers at the interface with the matrix. The wear particles have been observed to be smeared across the surface [54]. These fracture and produce filmy wear debris [101]. The size of the platelets has been observed to be similar to the spacing between the graphite flakes in the original microstructure [102].

The nodular structure of the graphite in the cast iron is known to enhance is ductility. The nodular shape does not form stress raisers to precipitate cracking. However it has been observed that the graphite nodules deform due to the shear stress transmitted through the matrix [106,52,51]. The deformed nodules have an increased aspect ratio leading to stress concentration and crack propagation through the interface with the matrix. Montgomery [105] observed that during mild wear cracks were propagated through the matrix to the graphite nodules and then around the graphite/matrix interface. This then liberated relatively large wear particles which were considered likely scuffing initiators and was why cast iron has been considered to have poor scuffing resistance.

Prasad [54] observed that grooves in the surface were formed by hard chips ploughing the cast iron surface, an abrasive mechanism. This mechanism was secondary to the formation of iron platelets which indicated adhesive wear. He observed that abrasive wear dominated during dry sliding and adhesive wear during lubricated sliding. The lubricant is likely to have controlled the formation of transfer particles and reduced the contact temperature favouring the formation of adhesive platelets over work hardening of the particles.

2.14 Methodologies for investigating scuffing of ring liner contacts

2.14.1 Scuffing test levels

Within tribological testing there are several different scales of test, ranging from expensive full scale engine tests in the field to comparatively low cost bench apparatus. Blau [109] summarises publications investigating the piston ring liner contact, and defines 5 categories based on the German standard DIN 50 322 [110], Table 2.1:

Table 2.1: Complexity levels for tribological automotive testing.

Level	Description
A	Vehicle on- and/or off-road tests
B	Full-size dynamometer test stand
C	Full-scale engine tests
D	Sub-assembly tests
E	Coupon tests

Each of these tests performs a different function and is integral to the development of new materials and lubricants. Blau comments that descending the list (Level A-E) cost decreases and control over the variables increase. However the main consideration is to “establish a direct

engineering linkage to Level A performance" [109]. Woydt and Kelling noted that Level E tests should use genuine real world parts "in order to increase the transferability...to engines tests on an acceptable level" [111].

Level B and C automotive industry standard tests for scuffing resistance are usually based on methodologies for the evaluation of engine oils in high speed single cylinder diesel engines. These are based on the ASTM D6750-10b or D6681-10a standards [112,113]. ASTM D6750-10b details two tests: 1K (0.4 % fuel sulphur) and 1N (0.04 % fuel sulphur). Both tests measure piston ring on liner scuffing as well as oil consumption and the tendency for deposits to form in the ring groves. They are used for API performance categorisation. The 1K is a historic test and is used to correlate with direct injection heavy duty high speed engines before 1989, that had aluminium pistons and 0.4 % mass fraction of sulphur. It is used for API CI-4 and CH-4 classification [114]. The 1N is a more recent test used to correlate with four stroke direct injection diesel engines that meet 1994 US federal exhaust emission requirements when using fuel with less than 0.05 % mass fraction of sulphur. It is used for API CJ-4, CI-4 and CG-4 classification [114]. ASTM D6681-10a is a single cylinder diesel engine Caterpillar 1P accelerated test procedure that measures piston, ring and liner scuffing as well as oil consumption and the tendency for deposits to form in the ring groves. It is used for API CH-4 classification [114].

2.14.2 Laboratory bench tests

For a level D or E bench test to have a good linkage to level A tests, it is crucial that the test geometry represents the real world application. Han et al [107] conducted work using both reciprocating and revolving geometry and found that the scuffing resistance of 1080 steel and grey cast iron was ranked in an opposite manner for each machine. It would seem that a reciprocating geometry would be most suitable for testing scuffing of a ring-on-liner contact, however many of the papers concerned have used pin-on-disk and/or block-on-ring type tribometers. Wang [115] noted that "The nominal maximum contact stress in (these tribometers) is usually much higher than the contact stress between the piston skirt and cylinder bore" and concluded that a reciprocating tribometer was required. While Wang was concerned in this instance with the piston skirts, a similar conclusion can be applied to piston rings.

There are two main types of Hertzian contact used for this geometry: point contact and line contact. Scuffing tests are often conducted using a point contact as this allows very high contact pressures to be generated, and consequently rapidly accelerated testing [13,14,107]. However the nature of the point contact is fundamentally different in the way it stresses the surface and the way the lubricant film can be formed such that it behaves very differently from a line contact, which is more representative of a conformal ring-liner contact.

Laboratory tribometers by their nature are limited in their operating envelope, often being outside that of a Level B or C engine test. Lee and Chittenden [116] provide an excellent appreciation of factors that need to be considered in this regard when designing tribometer tests to replicate engine conditions. In terms of scuffing tests, there is a difference in the discrete line contact produced in the tribometer and the (almost) continuous contact around a liner in an engine. In the engine, lubricant can only flow through the ring-liner interface however in the tribometer the lubricant can be forced to the edges of the contact and thus care is required with lubricant feed rates in tribometer scuffing tests. Matching the position of maximum acceleration to simulate the TDC position where scuffing occurs is achievable with most reciprocating tribometers due to the shortened stroke length of a tribometer compared to an engine stroke, although at the expense of representative mid-stroke lubricant film conditions. The transient load profile of a fired engine is also difficult to simulate on a tribometer, with the contact pressure at TDC again usually being selected to be representative.

2.14.3 Running in

Beginning of life scuffing often occurs during running-in if the roughness is not reduced to a sufficient level before the contact is subjected to its maximum designed load [76]. During running-in the texture and micro-structure of the surface are modified before scuffing occurs, typically work hardened by the repetitive micro plastic deformation of the contact [88]. The deformation is either caused by direct contact of the asperities or by the shear stress transmitted through lubricant [75], previously discussed. The material and the lubricant scuffing performance will be affected, due to the coupled nature of the contact. Thus a controlled running in period that accurately replicates the changes found in the real world application is required to produce a representative surface for scuffing.

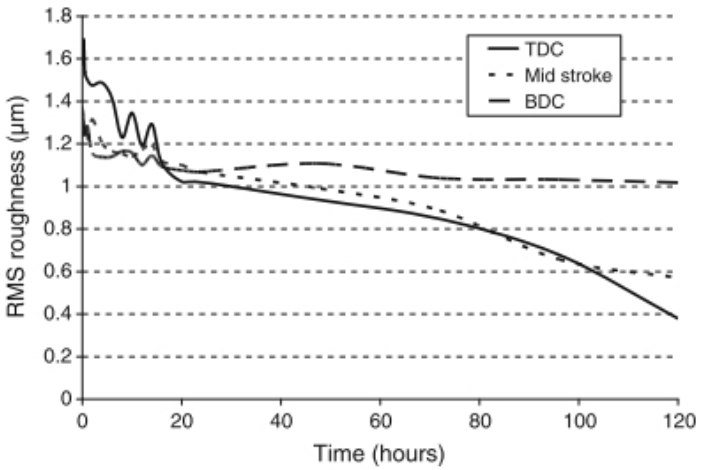

Figure 2.18: A graph of cylinder liner RMS roughness against engine operating time [117]*, reprinted from* [116] *with permission of Springer* [5]*.*

Figure 2.20 shows the decrease in RMS roughness of the cylinder liner with respect to engine operating time. Examining the TDC position the graph presents in 3 stages. The first stage, 0-20 hours shows erratic roughness changes with a significant decrease overall, 1.7 to 1 µm. The second stage exhibits an almost linear decrease in roughness 1-0.8 µm between 22 and 78 hours. In the third stage a larger gradient of decreasing roughness is seen. The time taken to achieve the change in roughness is clearly far too long for run-in to occur in a bench test at operating conditions, although Lee and Chittenden [116] note that a high tribostroke ratio (tribometer to engine stroke ratio) will increase the speed of running in. When run-in is accelerated care must be taken to ensure that the run-in surface and wear mechanism are representative of that seen in an engine.

As previously discussed the roughness plays an important part in the lubrication mechanism of the contact. After over 120 hours of operation the TDC roughness drops from 1.7 to 0.4 µm. This raises the issues of the appropriate roughness to start a scuffing test, with literature values for roughness of honed cylinder liners varying between 0.375 - 1.1 µm [19,78,118,119]. Much published work in this area uses a fixed load for a fixed duration in order to condition a well run-in sample [13,14,120]. This allows wear rates to be calculated more easily as the running-in duration is the same for each test. The rate of wear should stabilise by the end of the run-in and before the test progresses to scuff initiation. Indicating that any surface morphology or subsurface micro-structural changes occurring during run-in have reached a steady state. This should ensure that the samples can be repeatability conditioned to give repeatable results. The running in phase of a scuffing test must also allow time in the correct temperature range for a

[5] Original: “Figure 15. Change in cylinder liner surface roughness with respect to engine operating time [117].” Tribology Letters, Consideration of Test Parameters in Reciprocating Tribometers Used to Replicate Ring-On-Liner Contact, 39, 2010, 81-89, P.M. Lee, R.J. Chittenden, © Springer Science+Business Media, LLC 2010, with permission of Springer.

representative tribofilm to form before scuffing is initiated. The time period and temperature required depends on the type of lubricant and any formulated additive chemistry.

In order to investigate the onset of mild-scuffing and progression to severe-scuffing, a test must be designed that repeatability produces a scuff. This task is very difficult, considering the ambiguity in defining the cause and growth of a scuff as previously discussed. However, two popular methods used in literature to initiate scuffing are load based and temperature based tests, which shall now be discussed.

2.14.4 Load based tests

In load based tests the independent variable is the contact load which is increased until the lubricant protection fails resulting in scuffing. This however does not represent the range and fluctuation of loads experienced by the piston ring inside an engine. Many tests [13,14,107] use contact pressures one to two orders of magnitude larger than those published for the ring liner contact which has been reported as 1.4-5.7 MPa [121], 7 MPa [122], 7-11 MPa [123], 13.5 MPa [124], 70 MPa [4]. The high loads restrict the majority of lubrication to the boundary regime however this is “supported by a small but not always insignificant contribution from elastohydrodynamic effects” [86]. This does not represent the ring liner contact which only experiences boundary at TDC and Bottom Dead Center (BDC), which quickly changes to mixed then hydrodynamic as the entrainment speed increases with a sinusoidal profile [125]. Consequently careful thought is required in designing the tribometer test to ensure that scuffing produced is representative of fired engine scuffing. Considering the loading profile, which when coupled with the velocity profile results in the lubrication regime change, El-Sherbiny [126] designed a `force follower guide' which is capable of imparting a particular load shape over the stroke.

Scuffing is known to start just after TDC when the oil film is thinnest and the temperature is greatest [96]. Often scuffing occurring here does not cause failure of the contact as the oil film recovers throughout the stroke. However repeated scuffing events disrupt the honed surface and are likely to prevent the oil film recovering, allowing the damage to propagate down the cylinder liner [19]. For a test to cause scuffing propagation with a representative mechanism of the ring-on-liner contact, it should replicate the lubricant regime changes. Applying a constant load does not allow any lubricant or surface recovery and therefore may not produce a representative scuff. In order to determine if this is the case detailed examination of the micro-structure throughout the test especially during the scuffing event is required.

2.14.5 Temperature based tests

Scuffing can be initiated by increasing the contact temperature, two main approaches have been taken in the past. The first category looks at the scuffing resistance of materials pairs, this is sometimes achieved by using kerosene as a lubricant [115,127]. During testing after the running in phase, the temperature is increased sufficiently for the kerosene or oil to evaporate at a predictable rate to give a starved contact and subsequently scuffing occurs. This test has the obvious limitation that it cannot be used to test the scuffing resistance of lubricants and can result in significant scuffing failure variation [128].

The second category operates a contact in boundary lubrication, either by a large load or by a very slow entrainment speed, and then the temperature increase is used to breakdown additive packages so that the boundary film fails [86,129]. This method allows the testing of lubricants but careful consideration of the stroke, frequency and load is required to control the surface temperature to prevent flash temperatures significantly different from the bulk temperatures [85].

2.14.6 Scuff detection

There are a variety of different techniques that can be used to detect scuffing, ranging in complexity, expense and accuracy. Methods which analyse friction force and acoustic emissions arising from the contact dominate the literature. The sensitivity of the specific methods classify them into two categories. The low sensitivity techniques detect severe scuffing whereas the high sensitive techniques can detect the onset of scuffing and differentiate between scuffing severity.

Fundamental investigation into scuffing is frequently carried out using laboratory tribometers equipped with friction transducers. Consequently friction coefficient has commonly been used to detect scuffing. Reciprocating tribometers which measure friction in two directions employ a root mean square average which rectifies friction measurement and averages it across several strokes, It is common practice to define scuffing by a sharp rise in the average friction coefficient [98,107,115,120,127,130] as shown in Figure 2.21. This indicates a step change in the energy dissipated into the contact, signalling the transition from a mild to a severe wear regime.

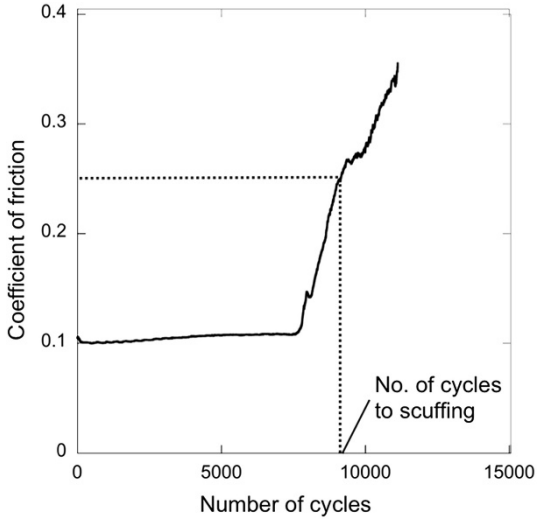

Figure 2.19: A graph of typical friction coefficient behaviour during scuffing, reprinted from Olander et al [128] *with permission from Elsevier* [6].

Root mean square averaging is suitable for measuring the friction signal from reciprocating tribometers as it accurately averages an amplitude symmetrical square wave, compared with calculating an arithmetic average which results in an error of 11 % [131]. As is the case with all averaging techniques in the time domain the time constant specified is a balance between signal stability and response. The time constant associated with the RMS average produces a delay between the increase in friction at the contact and the observed change in friction coefficient, typically in the order of seconds. This is suitable for contacts operating in quasi steady state conditions, such as the reduction in friction force during running in, as the average responds to gradual changes however is less than satisfactory for measuring rapidly occurring wear transitions. Therefore stopping the test when a sharp rise in friction coefficient occurs results in a surface with a severely modified topography which gives little indication as to the onset of the scuffing.

Jensen et al [102] noticed that by stopping the test before the rapid increase, information about the scuffing mechanism could be obtained. They comment that this is difficult to achieve as the window of opportunity is very small. Cooper and Moore [86] overcame this by observing the friction force using a high sample rate (high speed data). They attributed brief increases in friction force to local scuffing events and noticed that these events had "more modest" effects on the time average friction coefficient [86].

Local increases in friction force can be seen in Figure 2.22, however the resulting differences in friction force are hidden by the relatively long time constant used for the RMS averaging. In the

[6] Reprinted from Wear, 340–341, P. Olander, S.S. Eskildsen, J.W. Fogh, P. Hollman, S. Jacobson, Testing scuffing resistance of materials for marine 2-stroke engines - Difficulties with lab scale testing of a complex phenomenon, 9-18, Copyright (2015), with permission from Elsevier.

case of the Phoenix Tribology TE-77 reciprocating tribometer, the friction force true RMS to DC converter has a time constant of 1.4 seconds. Therefore at reciprocating speeds of 10 Hz, the friction force is an average of 14 cycles or 28 strokes. The RMS signal consequently has low sensitivity to local difference in friction force, responding only to severe scuffing damage where an increase in friction force is often an order of magnitude across the whole stroke.

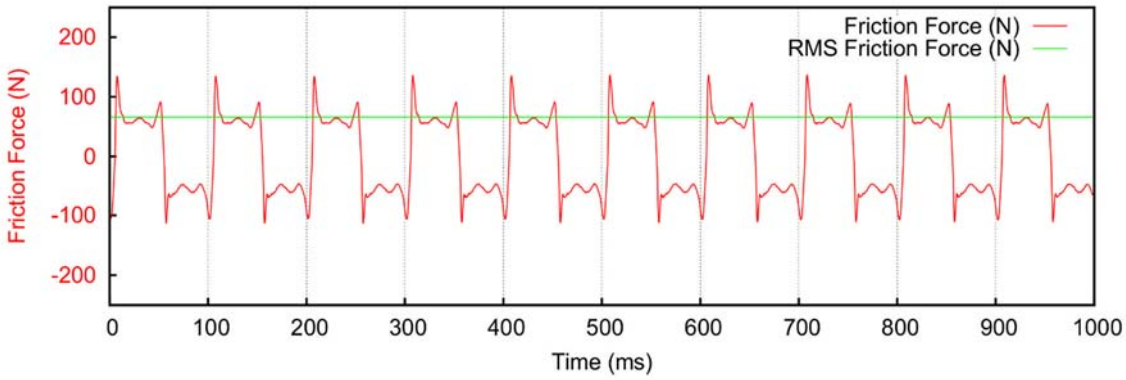

Figure 2.20: Comparison of instantaneous and RMS friction force measurements adapted from [132].

High speed data acquisition requires that the friction transducer has a suitable bandwidth to provide a sensing resolution to match the acquisition frequency. This usually requires the use of piezoelectric transducers rather than strain gauges and may explain why the technique has not been adopted more widely. When high speed sampling is analysed the investigator has be aware of apparatus effects and limitations of the measurement system, which will be discussed for the present study in the methodology section.

Qu et al [15] used a similar technique to evaluate the performance of fuel injector materials using a reciprocating crossed cylinder (pin-on-twin) arrangement. It involved monitoring the relative change in the high speed friction data to detect the local onset and progression of scuffing. This technique proved successful in discriminating between three different stages of scuffing wear. Despite the success of this work many scuffing tests continue to use the "rapid increase in friction coefficient" method, in recent work by Hershberger et al [133] for example, the onset of scuffing was determined by listening! Recently in 2005, Ajayi [49] detected the onset of scuffing in a block on ring machine and developed an explanation of the mechanism. The results are informative however the repeatability is questionable as the methodology used for detecting scuffing initiation involved the operator listening for a change in noise of the test apparatus. This elementary technique demonstrates the need for development of detection technologies to repeatedly stop experiments during the initiation of scuffing.

A more robust methodology for detecting scuffing using acoustic emission condition monitoring has been developed by Saeidi et al [10]. They observed that a Fourier transform analysis of the contact's acoustic emission was not sufficient to identify the onset of scuffing. Instead sub-band energies of wavelet packet transform were used to identify the onset of scuffing. This technique had an accuracy of 65 % for recognising pre-scuffing [10]. This technique was then used to instigate the scuffing progression of flake cast iron in a lubricated reciprocating contact [108].

2.15 Summary

2016 was the 50th anniversary year of the Jost report [29] and much experimental work investigating scuffed surfaces occurred in the interim. It is curious however that after 50 years, the different definitions discussed in this chapter are so greatly varied in their description of scuffing mechanisms. Each description is accompanied by empirical evidence, often optical micrographs, which validates each definition. The difference between the reported mechanisms is genuine, however all the mechanisms are described by the authors as scuffing. For this to be true the definition of scuffing must be broad to include a variety of wear mechanisms, as reflected in the most recent ASTM definition.

Scuffing has become a research topic of interest once again as the limit of current materials are approached and exceeded by modern engine design. Increasing stringent environmental legislation has encouraged engine manufacturers to increase engine specific output by forced induction and reduce frictional losses. Consequently the piston ring liner contact experiences higher pressure and temperature than ever before whilst being lubricated by oils of decreasing viscosity. The result is an increased occurrence of scuffing events at this interface, which due to their catastrophic nature, are extremely undesirable.

In all the literature reviewed scuffing did undoubtedly occur. However, in many instances the wear process examined was the final most severe condition, whether adhesive or abrasive. Examination of a severely scuffed sample is informative, although investigation of samples that have experienced macroscopic changes in their geometry is of perhaps less use as in a real life application the part would have failed or been taken out of service long before this point.

The most interesting part of the mechanism is its initiation and progression to severe scuffing, as being able to alter or prevent either process is a significant advantage for designers in selecting materials and lubricants. Initiation for cast iron engine block materials is thought to involve plastic and elastic deformation as well as mild polishing wear adversely altering the surface topography. There can be many triggers for progression of the scuffing mechanism to severe wear, which is the onset of severe adhesive wear as discussed by Morris [62] and the pivotal role that energy dissipation in the contact plays in initiating scuffing has been examined.

However, detecting this transition reliably has been shown to be difficult with existing methodologies. The current provision of scuffing detection techniques have yet to provide sufficient detail and repeatability to fully understand the onset and progression of scuffing of automotive engine materials. Such an approach is crucial for assessing the scuffing mechanisms of future engine materials.

This thesis explored the development and use of two friction force techniques to detect scuffing initiation and discriminate between different stages of scuffing progression. The work looked at characteristic friction force signals arising from severe scuffing of flake graphite cast iron in an idealised lubricated line contact and developed precursor thresholds that determined when the sliding contact was transitioning. This information was then used to repeat and then interrupt testing at the transition boundaries such that the surface microstructure could be examined and scuffing mechanisms determined. Comparison between flake and nodular graphite cast iron was then assessed using the same criteria before the applicability of the technique to a conformal ring liner contact was evaluated. Recommendations regarding the use of the techniques developed in this thesis as a potential scuffing test standard was summarised and presented as conclusions.

3 Experimental methodology

3.1 Overview and approach

In order to reproduce and detect the onset of scuffing that occurs between a piston ring and cylinder liner in a fired combustion engine using a reciprocating laboratory bench top apparatus, it was necessary to first simplify the geometry to a line contact (cylinder on flat) that would ensure scuffing test repeatability.

As discussed previously, the onset of scuffing is controlled by a number of interdependent variables [109] which were considered simultaneously with reference to real world conditions (level A: fired engine test) to replicate scuffing as seen in service [116]. This allowed the development of a test protocol that would ensure repeated scuffing of flat cast iron plate (simulating the cylinder liner in a diesel combustion engine) sliding against bearing steel cylinders (representing high performance steel piston rings). Observation of the instantaneous friction signal characteristic behaviour led to the development of an autonomous scuffing detection method and the creation of a 'disorderly friction' parameter that allowed detailed assessment of frictional changes to the contact that were otherwise masked by the average friction coefficient. Finally, the methodology was extended to a conformal ring-liner contact using real engine components to assess how the approach worked at a component test level.

3.2 Development of a scuffing test on a reciprocating tribometer

This investigation focused on the scuffing mechanisms of the liner surfaces, therefore a synthetic base stock lubricant was used as it did not contain any antiwear or friction additives that may have concealed the material response. Similarly abrasive particles such as sand or soot were not introduced as this would have forced an abrasive wear mode to cause scuffing potentially masking the material mechanism. Therefore scuffing was induced in a lubricated reciprocating sliding contact by increasing the dissipated frictional power.

The initial approach adopted was to increase either the temperature or the normal load supported by the contact until scuffing occurred. Increasing the normal load was considered superior in terms of differentiating between similar surfaces and therefore the method considered the effect of continuously increasing the contact pressure or increasing the normal load in discrete increments. The frictional power dissipated in the contact could be controlled more precisely using the latter methodology and was consequently used for the line contact tests. It was subsequently applied to assess the scuffing performance of a ring on liner geometry.

3.2.1 Cylinder on flat test materials

The reciprocating contact chosen to simulate ring-liner scuffing was a cylinder on flat geometry. The cylinders were made from 52100 steel and had a specified G5 tolerance, obtained from

Bearing Boys Ltd, UK. They had dimensions of 6 mm diameter and 10 mm long with a 0.5 mm radius at each end. This type of countersurface was chosen to simulate the ring surface for a number of reasons: 1) The steel composition was similar to class 60 ring materials according to ISO 6621-3 [65]; 2) The G5 surface finish required no additional preparation; 3) There was security of supply; 4) Other scuffing related studies had also used this material, enabling a direct comparison [86,107,134,135]. The flat test plates of dimensions 58 mm x 38 mm x 4 mm were made from two different grades of cast iron: 1) Flake BS1452 Grade 250; 2) Nodular BS2789 Grade 400-15. The flake cast iron was chosen as a standard cast iron that would be used in lower specific power diesel engines, whilst the spheroidal cast iron was chosen as a comparison material that might be used in higher specification engines, both were supplied by West Yorkshire Steel Co Ltd, UK.

3.2.2 Surface topography

In order to reproduce scuffing mechanisms that occur in fired engines using a benchtop tribometer, the surface topography of the cast iron flat samples was required to be similar to that of a honed cylinder liner. Cylinder liner honing uses a cylindrical tool which slides axially inside a bore whilst rotating. As the tribometer required flat samples this technique could not be used, instead the cast iron samples were ground at 45^{o} to the direction of sliding to simulate a honed surface. The surface roughness, kurtosis, reduced peak and valley heights of both samples were subsequently measured using a Taylor Hobson Talysurf equipped with a standard 2 µm diamond tip. The samples were orientated such that the grinding marks (lay) were perpendicular to the profile direction. A profile measurement length of 13 mm and a filter data length of 4 mm with L_c=0.8 mm and L_s=0.0025 mm was used. This gave a bandwidth of 320:1 complying with ISO 4288:1996. Six profiles were measured at 4 mm intervals. The 52100 countersurface cylinders were measured in a similar manner, orientated so that the profile was measured about their circumference. A profile length of 4 mm was used with a filter L_c=0.25 and L_s=0.0025 with a bandwidth of 100:1. Four profiles were measured at 2 mm intervals. Their cylindrical form was subtracted from this measurement by the software package 'Ultra' and Abbott-Firestone curves were generated for each surface to facilitate comparison of surface peak and valley parameters (R_{pk} and R_{vk}) compared at 5 % and 90 % of the bearing area ratio.

3.2.3 Vickers hardness

The Vickers hardness of the DD13 liner sections used in the conformal ring-liner contact, ground flake and spheroidal plates were measured using an indentation force of 10 kgf. 30 indents arranged in three lines of 10, separated by 3.5 mm intervals were recorded for flake cast iron. Five collinear indents separated by 2 mm intervals were recorded for spheroidal and compacted

cast iron. Average and standard deviation Vickers hardness values were subsequently calculated.

3.2.4 Optical microscopy

Transverse sections were taken from a DD13 liner, flake plate and spheroidal plate and mounted in Bakelite prior to grinding with SiC paper down to grade 1200 and polished with diamond paste to a finish of 1 µm. Surfaces were then imaged with an optical microscope (BX51 Olympus for the plates and Alicona Infinite Focus for the liner) to identify the presence and morphology of the graphite phases in the microstructure.

3.2.5 Friction force measurement and acquisition

The steel cylinders were clamped in the reciprocating assembly of a Phoenix Tribology TE-77 reciprocating tribometer, with their axis perpendicular to the direction of reciprocation to form a line contact with the cast iron plates, Figure 3.1.

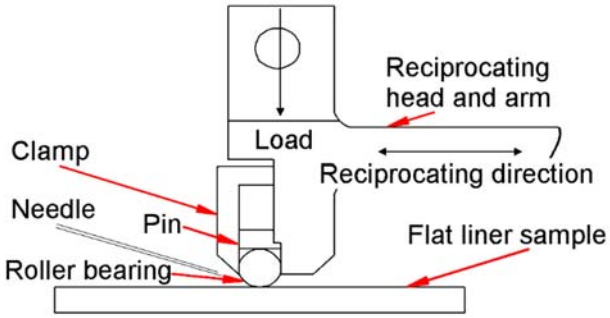

Figure 3.1: TE-77 line contact configuration adapted from Phoenix Tribology Ltd [136].

The stationary plate specimens were supported on knife edges, Figure 3.2, which withstood the normal load applied to the contact but provided no resistance to shear resulting from the reciprocation of the counter surface. The restoring force was proved by a piezo crystal transducer (Kistler 9203) which was used to measure the friction force. The transducer was intrinsically stiff, 40 N/µm which was required for measuring high forces occurring during scuffing with negligible displacement [137]. The small extension and compression of the transducer resulting from the friction force produced an alternating charge. A charge amplifier, Kistler 5011, was used to convert the signal to an AC voltage. The amplifier time constant which is defined as the time for a step input to be reduced to 37 % of its original value [138] was set to 1 s. This operated the amplifier in AC coupled mode removing the effect of DC drift during high frequency reciprocation [139].

The specimen bath assembly had a mass of approximately 1 kg and consequently according to Equation 3.2 had a resonant frequency of 1 kHz, naturally lower than the natural frequency of the transducer 27 kHz. Consequently a 300 Hz low pass filter was applied on the charge amplifier

to remove any components of the friction signal which were mechanical responses from the friction measurement assembly.

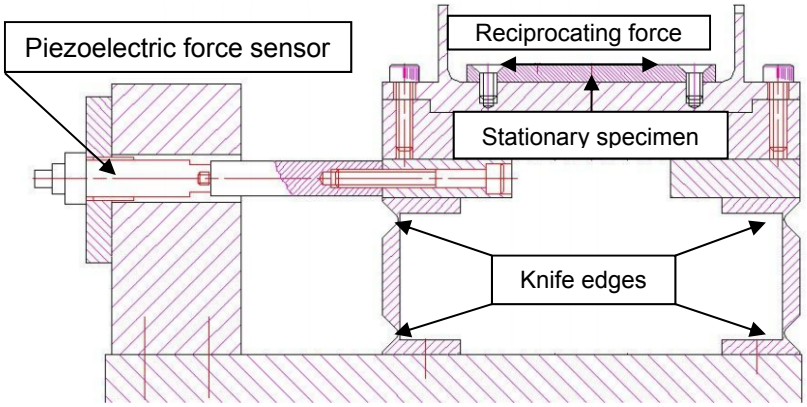

Figure 3.2: Schematic diagram of the TE-77 friction measurement assembly.

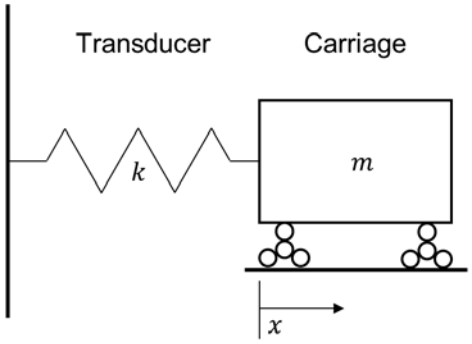

Figure 3.3: Free body diagram of the TE-77 friction measurement assembly.

Undamped, unforced system equation of motion

$$\ddot{x} + \frac{k}{m}x = 0 \qquad \textit{Equation 3.1}$$

Natural frequency of this system

$$\frac{1}{2\pi}\sqrt{\frac{k}{m}} \qquad \textit{Equation 3.2}$$

Where: x is displacement (m), m is the specimen bath assembly mass (kg), k is the spring constant of the piezo crystal transducer (N/m).

The root mean square average of the amplified signal was calculated by a true RMS to DC converter. The converter is an analogue integrated circuit with a configurable time constant which was set by the manufacturer to 1.4 s. The resulting DC signal was then acquired at a sample rate of 1 Hz. The instantaneous friction force was acquired by sampling the amplified signal at 10 kHz using a PCI data acquisition card with a filter of 1 kHz.

The stroke position was simultaneously recorded using a linearly variable differential transformer attached to the reciprocating arm of the tribometer. The signal conditioning applied

to the friction data was more extensive than that applied to the LVDT, consequently there was a slight offset between the two acquired signals. However at the speeds used for the reported experiments this effect was insignificant.

3.2.6 Contact potential measurement

Bowden and Tabor noted that a relative measure of the fluid lubrication in a tribological contact can be achieved by measuring the electrical resistance across it [27]. This technique is called electric contact resistance (ECR) and is widely used on test apparatus as it is a very cost effective and robust solution for providing a relative measure of asperity contact. A variation of this technique is called contact potential (CP) which measures of the electric potential across the contact. The Lunn-Furey contact potential circuit used in the TE-77 is shown in Figure 3.4.

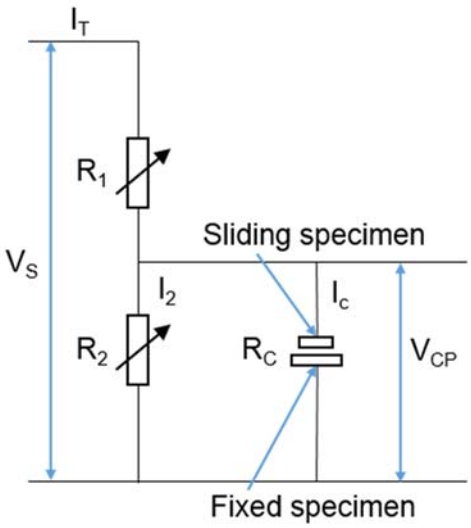

Figure 3.4: Lunn-Furey contact potential circuit used in the TE-77 ECP system adapted from Plint [140].

The contact potential measurement was made by connecting the contact in parallel with one side of a potential divider circuit. The potential divider controlled the open circuit voltage applied across the contact when an insulating film was present and also limited the closed circuit current flow through the contact during metallic contact. Furey demonstrated that a voltage above 1500 mV was required to induce measurable effects in the contact [141]. The potential difference applied by the TE-77 contact potential circuit was 50 mV to minimise the formation of films or oxides at the contact interface [141]. The resistor values were selected such that the closed contact current was limited to 100 mA [139].

High speed friction and contact potential data can be compared against the contact velocity to reveal information about the contact lubrication regime. Considering a lubricated metal on metal contact, if the friction force is found to be independent of sliding speed then no hydrodynamic effects are occurring. If a contact potential also exists then an insulating film,

either an oxide film or layer of boundary additive, will likely have formed. The contact will be operating in boundary or starved lubrication regime depending on the chemistry of the lubricant [86]. If however there is no contact potential then metal on metal contact will be occurring which will likely result in a very high coefficient of friction (>0.2). If the friction force is inversely proportional to the velocity [101] and the contact potential is proportional to sliding speed then the contact is in the mixed lubrication regime. This happens because the increasing velocity causes increasing separation and reduction in the number and size of asperity contacts reducing the friction and increasing the contact potential.

3.3 Development scuffing detection techniques

3.3.1 Design of bespoke software to detect mild and severe scuffing

High speed friction data obtained during the continuous load ramp tests revealed characteristic deviations from the RMS average at the stroke reversal positions, which were indicative of different stages of the scuffing process. During the onset of scuffing the friction force increased in accelerating and decelerating directions, Figure 3.5. Friction force increases in the accelerating direction were hypothesized to be caused by adhesive wear occurring locally at the stroke reversal position. Subsequently an increase in the decelerating direction was observed which was attributed to the force required to deform adhesive wear debris trapped in the contact. It was proposed that the presence of local increases in friction force at stroke reversal positions could therefore be used to measure the onset and severity of scuffing wear.

A software plug-in for the TE-77 high speed data acquisition software was written with assistance from Phoenix Tribology Ltd. The software independently evaluated the difference between the magnitude of the friction force at the stroke reversal position in both the accelerating and decelerating directions and the RMS of the high speed friction signal, Figure 3.5. The software had three input parameters: the percentage increase in the stroke decelerating direction; the percentage increase in stroke accelerating direction and the distance inside the stroke reversal position to be analysed, Figure 3.6. The software displayed a visual warning when scuffing had onset and terminated the test once mild scuffing had established, preserving the mildly scuffed surface.

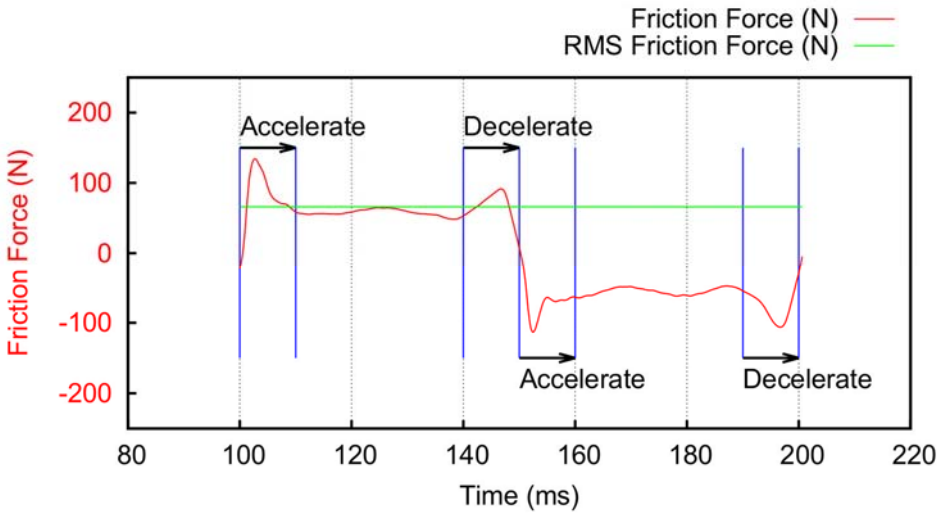

Figure 3.5: Local increases in friction force in both the accelerating and decelerating directions during mild scuffing.

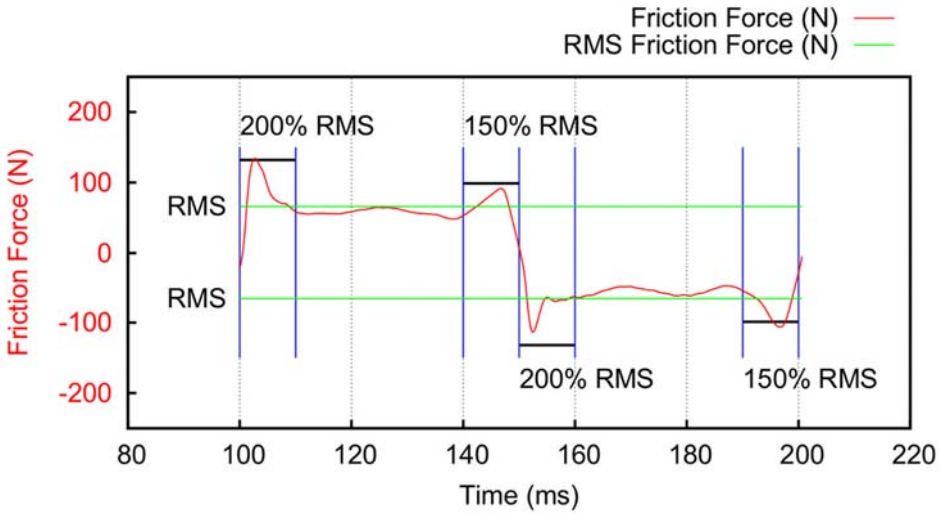

Figure 3.6: Independent accelerating and decelerating scuffing software thresholds with respect to the RMS friction force.

The software only evaluated a window of data at the reversal positions, which could be adjusted to ensure the software only evaluated increases in friction associated with the stroke reversal positions. This parameter was dictated by the material properties which can dampen the friction force slew from positive to negative and also the reciprocating speed as the rise time on the friction force amplifier can displace the signal in the time domain.

3.3.2 Development of friction noise parameter

Analysis of high speed friction data from the continuous load ramp tests suggested that the magnitude and frequency of friction perturbations occurring across the entire stroke, not only at the stroke reversal positions, gave an indication of the presence and severity of scuffing in the contact. In the case of the boundary lubricated contact prior to the onset of scuffing, the friction force was independent of sliding velocity and had low magnitude deviations from the RMS value, Figure 3.7. The onset of adhesive wear during mild scuffing significantly increased the magnitude

and frequency of the friction perturbations (Figure 3.8), these however decreased with the progression to severe scuffing, Figure 3.9.

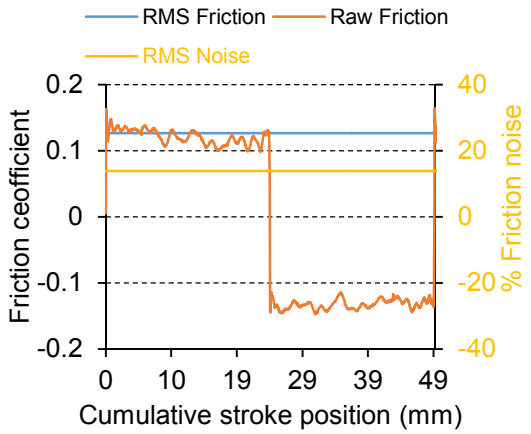

Figure 3.7: Running in 50N load, 0.127 RMS friction, 14 percent friction noise.

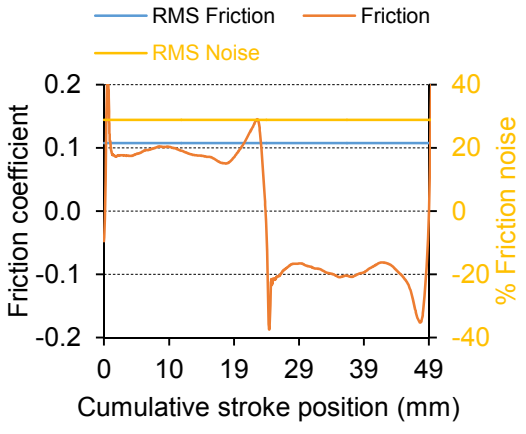

Figure 3.8: Mild scuffing 615N load, 0.107 RMS friction, 29 percent friction noise.

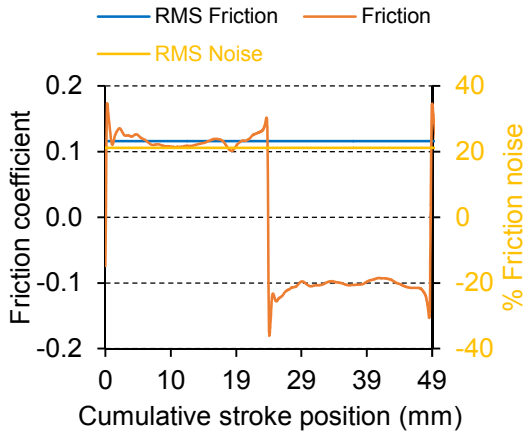

Figure 3.9: Severe scuffing 1kN load, 0.116 RMS friction, 21 percent friction noise.

This characteristic behaviour had to be condensed into a single metric, so that different stages of scuffing damage could be automatically identified by the tribometer during a test. The metric was called the friction noise parameter as it measured the average instantaneous friction force deviation from the RMS of the friction force signal. Considering the irregularly of the perturbations, and that in some instances the magnitude exceeded 100 % of the average value, the RMS average was used [131].

The friction noise parameter was defined in Equation 3.3, where c_x = RMS time constant. It was calculated at any time t by measuring the RMS of the difference between the instantaneous friction signal at time t and the RMS value, calculated from the proceeding c_2 s of friction data, between time t and $t - c_1$.

$$f_{noise}(t) = \underbrace{\sqrt{\frac{1}{c}\int_{t-c_1}^{t} \underbrace{\left(|f(t)| - \sqrt{\frac{1}{c}\int_{t-c_2}^{t} f(t)^2\,dt}\right)^2}_{2}\,dt}}_{3}$$

1a 1b

Equation 3.3

The friction noise parameter, Equation 3.3 was separated into three stages so that it could be implemented as an analogue circuit with assistance from Phoenix Tribology Ltd.

1. The AC signal from the charge amplifier was split into two identical channels, Figure 3.10:
    a. Channel a was full wave rectified
    b. Channel b passed through an RMS to DC converter (time constant c_2)
2. The difference between the two signals, instantaneous friction noise, was calculated using operational amplifier, Figure 3.11.
3. The friction noise parameter was then calculated by averaging the instantaneous friction noise using an RMS to DC converter (time constant c_1), Figure 3.12.
4. The non-dimensional friction noise parameter was reported as a percentage of the RMS friction, this calculation was done by the TE-77 control software, Equation 3.4.

$$f_{\%\,noise}(t) = \frac{\sqrt{\frac{1}{c}\int_{t-c_1}^{t}\left(|f(t)| - \sqrt{\frac{1}{c}\int_{t-c_2}^{t} f(t)^2\,dt}\right)^2\,dt}}{\sqrt{\frac{1}{c}\int_{t-c_2}^{t} f(t)^2\,dt}}$$

Equation 3.4

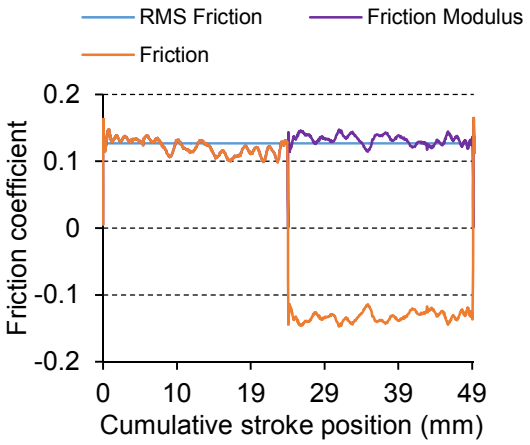

Figure 3.10: Stage 1, RMS friction is calculated and the instantaneous friction signal is rectified.

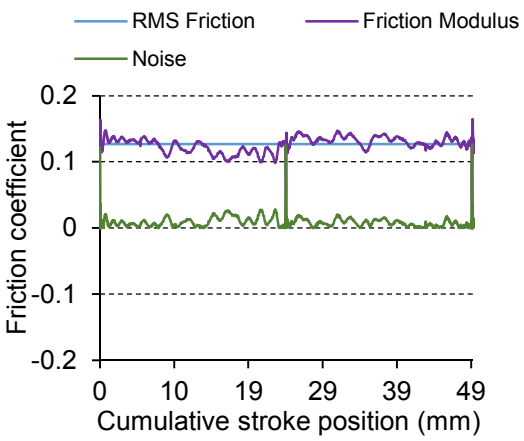

Figure 3.11: Stage 2, The instantaneous noise is calculated by subtracting the rectified instantaneous friction signal from the RMS friction.

The friction noise parameter quantified the instantaneous friction force disorder. It could not discern between signal noise arising from perturbations caused by the contact frictional characteristics or artefacts arising from the measurement system. There were two sources of

error specific to the friction noise calculation, aside from those associated with the friction signal measurement which have been previously discussed.

The first source of error was caused by the asymmetry of the instantaneous friction signal. When a signal was asymmetric there was an offset between the RMS average friction and the average friction in each direction. As the friction noise calculation used a full wave rectification which resulted in the instantaneous friction from both reciprocating directions being compared with the RMS across both directions, the level of friction noise increased with respect to the signal asymmetry, Figure 3.12 and Figure 3.13.

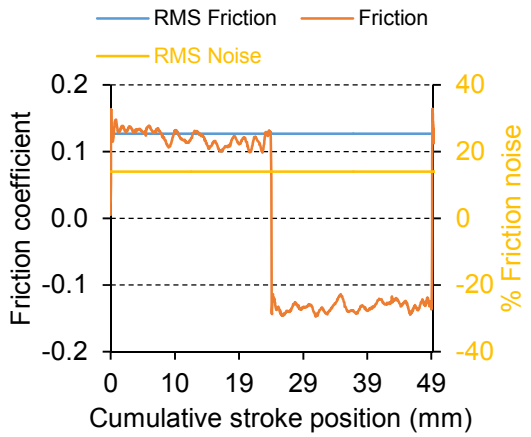

Figure 3.12: The effect of symmetric friction on friction noise percentage.

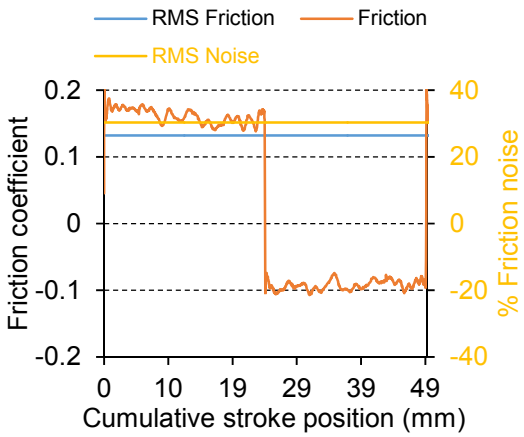

Figure 3.13: The effect of asymmetric friction on friction noise percentage.

There were several reasons for an asymmetric friction signal, these may have genuinely arisen from the contact and occurred due to directional properties of the surface such as texturing or specimen misalignment. It was however more common for the asymmetry to be caused by an asymmetric response of the piezo transducer in compression and tension. This error was minimised by calibrating the friction noise circuit for the piezo transducer by selecting an appropriate offset.

The second error was caused by the instantaneous friction force discontinuity at the stroke reversal position. When the reciprocating sample changed direction the friction signal changed polarity e.g. from positive to negative. The physical friction force reversal happened instantaneously, however the slewing of the amplifier coupled with the low pass filter took a finite amount of time, 3 ms. At the discontinuity the friction force passed through zero, which resulted in the largest possible deviation from the RMS. As the reciprocating velocity increased, the discontinuity accounted for a greater proportion of the friction force measured over the stroke and consequently caused the friction noise level to increase, Figure 3.14 and Figure 3.15.

This source of error was constant throughout the tests as they were conducted at a constant reciprocating frequency. It could therefore be easily identified and disregarded from the interpretation of the friction noise, so than only noise arising from the contact was analysed.

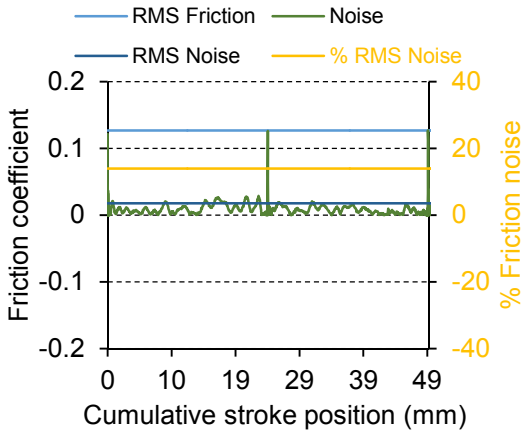

Figure 3.14: Stage 3, The RMS friction noise percentage is calculated from the instantaneous noise and the RMS friction.

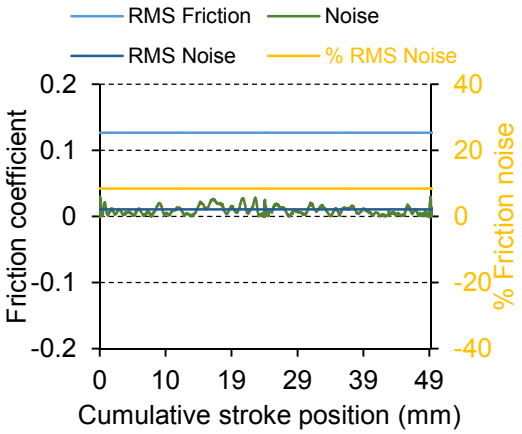

Figure 3.15: The effect of removing stroke reversal discontinuities on friction noise percentage.

The friction noise parameter increased in magnitude when mild scuffing was about to develop into severe scuffing, Figure 3.8. This was because at the point of transition there were sporadic high energy adhesive events occurring on the surface resulting in severe local increases in friction force. Once the transition to severe scuffing had occurred the friction force increased across the entire stroke resulting in an increase in the RMS friction coefficient and a decrease in friction noise, Figure 3.9.

Friction noise had high sensitivity to local differences in friction force which quantified the onset and magnitude of mild-scuffing before it progressed to severe scuffing. Therefore by combining friction noise and the time averaged friction coefficient information, it was possible to identify when scuffing was occurring and differentiate between the severity of mild-scuffing and severe-scuffing, Figure 3.16.

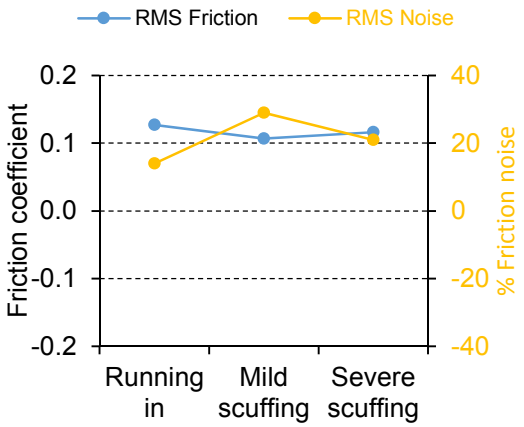

Figure 3.16: RMS friction and RMS noise characteristics of a scuffing wear mechanism.

3.3.3 Continuous load ramp test

The maximum stroke length of the tribometer was restricted to 25 mm, which was 16 % of the stroke of a EPA Detroit Deisel 13 (156 mm) [142]. This stroke length was selected to obtain the

lowest tribostroke ratio, in this case 9.8:1 [116], which gave the longest wear track possible to facilitate the observation of scuffing initiation and progression across the wear scar.

Two continuous load ramp scuffing tests were conducted with a common stroke of 25 mm and a frequency of 10 Hz. Lubricant was drip fed at a constant rate into the contact, to try to simulate the oil splashed on to the bores in the engine. The test used a PAO 4 (4 cSt at 100 ^{o}C) base oil which was supplied at 5 ml/h by a glass syringe through a metal needle located at the stroke reversal position on the cast iron sample. A synthetic base stock of this viscosity was chosen as the trend within the automotive industry is towards thinner lubricants with lower shear and churning losses. The lubricant was unformulated without an additive package in order to facilitate scuffing. The test sequence is shown in Figure 3.17. The test started with a run-in period which lasted for 30 min with a load of 50 N at ambient temperature, which corresponded to an initial Hertzian contact pressure of 110 MPa and which was of the order found in a harsh ring on liner engine contact [4]. This was followed by a temperature ramp from ambient to 150 ^{o}C over 30 min, measured using a K-type thermocouple located on the cast iron contact surface. The load was then continuously ramped from 50 to 1000 N over 30 min, at a rate of 31.6 N/min. The test finished at steady state conditions of 150 ^{o}C and 1000 N. The tests were manually terminated after a rapid increase in the average friction force was detected defining a scuffing event. The time averaged contact potential was sampled at 1Hz.

The test was repeated but interrupted at the onset of mild-scuffing, based on the high speed friction values. Instantaneous high speed friction and contact potential measurements were sampled synchronously with displacement, at 10 kHz for 1 s every 60 s throughout the experiment. In the pre-scuffed condition the high speed friction force signal plotted against displacement formed a square shape, Figure 3.18. When mild-scuffing occurred the friction force at the stroke reversal positions increased to approximately 100 % greater than the mid stroke, at which point the test was terminated, Figure 3.19.

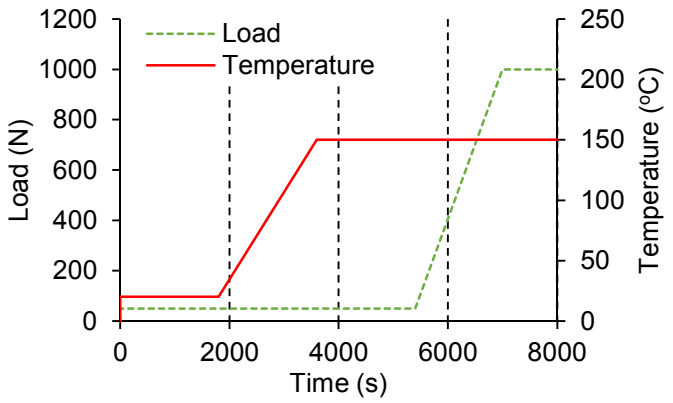

Figure 3.17: Continuous load ramp test procedure schematic.

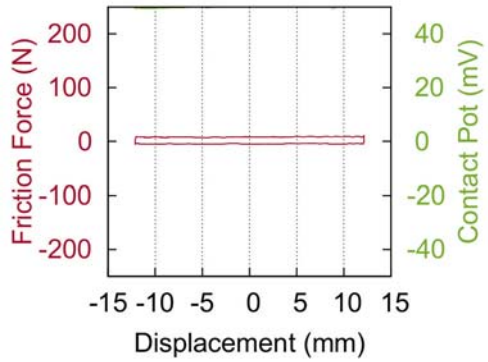

Figure 3.18: Pre-Scuff, High speed friction and contact potential plotted against displacement captured at 10kHz for 1s.

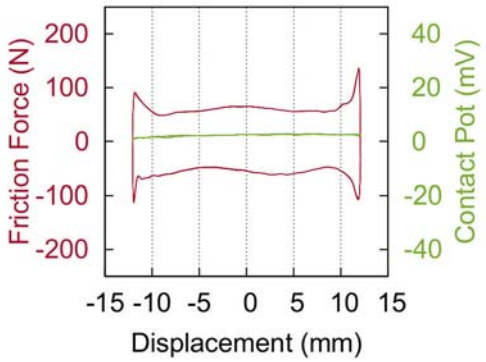

Figure 3.19: Mild-Scuff, High speed friction and contact potential plotted against displacement captured at 10 kHz for 1s.

3.3.4 Discrete load step test

The test procedure was modified to improve the repeatability of scuffing of the cast iron plate samples. As the stroke length had been prescribed, the tribometer reciprocating velocity was chosen to match the maximum acceleration seen in an engine which required a frequency of 15 Hz. At this speed the maximum velocity was not fast enough to accurately represent the mid-stroke engine conditions, however this was of little consequence as from literature scuffing was known to initiate just after the TDC position where maximum acceleration occurs and contact conditions were most severe. The increase in frequency also allowed an increase in frictional energy input into the system, without exciting resonant machine frequencies that would have led to excessive vibration.

The lubricant used for these tests was a fresh batch of synthetic PAO 4 base stock of the same viscosity previously used in the continuous load ramp tests and supplied by ExxonMobil (Spectrasyn 4). It was found during testing that despite being an identical lubricant, it exhibited superior scuffing resistance leading to the conclusion that the preliminary batch may have been degraded. Consequently, the test temperature was raised to 180 ˚C in order to allow sufficient frictional energy increase from discrete load increments to induce scuffing. To further assist scuffing occurring at a lower load than 1000 N, the lubricant feed rate was reduced to 1 ml/h for the first group of tests and 0.5 ml/h for the second group of tests, with both supplying the contact by a glass syringe through a metal needle located at the edge of stroke reversal position.

The aim of the discrete load step tests was to compare the scuffing resistance of the two different cast iron materials (flake and spheroidal) as detected by the two novel scuff detection techniques outlined above. The two techniques were integrated into the main tribometer control software, allowing the experiments to be stopped automatically when scuffing occurred. During the first group of tests both techniques were operated in display mode and the tests

were manually terminated after a rapid increase in average friction force was detected defining a scuffing event, the same criteria had been used for the continuous load tests.

The second group of tests were automatically terminated when severe scuffing occurred indicated by the RMS friction coefficient exceeding 0.2. This threshold was chosen as an indicator of severe scuffing as it has been proposed in literature as the magnitude at which adhesive junction growth occurs [27]. Criteria of similar magnitude have also been used in literature to indicate scuffing [128]. However some authors only qualitatively describe the threshold for scuffing as a rapid rise in friction coefficient [107,51,115,133]. It was observed that a rate of change of friction coefficient above 0.04 s^{-1} was the characteristic behaviour that indicated severe scuffing in these tests. The time averaged contact potential was sampled at 1 Hz for both groups of tests. Friction noise was sampled at 1 Hz and the instantaneous high speed friction and contact potential were sampled at 10 kHz for 1 s every other second.

The instantaneous friction and contact potential data from the severe scuffing tests were analysed to determine the thresholds for the increases in the accelerating and decelerating directions that indicated the onset set of scuffing. It was observed that thresholds of 140 % in the accelerating direction and 110 % the decelerating direction constituted a lowest identifiable criteria that occurred after the run-in period and before friction perturbations occurred across the stroke. Analysis of the wear scars from repeat tests using this criteria confirmed that it successfully indicated the onset of scuffing. Consequently it was used as the threshold for detecting the onset of scuffing for both types of cast iron material.

Before and after testing, each sample and counter surface was ultrasonically cleaned in isopropanol for the first group of tests however this process frequently had to be repeated as residue was often present after cleaning. Petroleum ether was found not to leave residue on the surface and consequently was used for the second group of tests. Gravimetric mass loss of both plate and cylinder countersurface was performed using a precision balance. A schematic of the discrete load step tests program can be seen in Figure 3.20. After each test, the surfaces of the plate and cylinder counter surface were examined using the surface analysis methods outlined in Section 3.4.

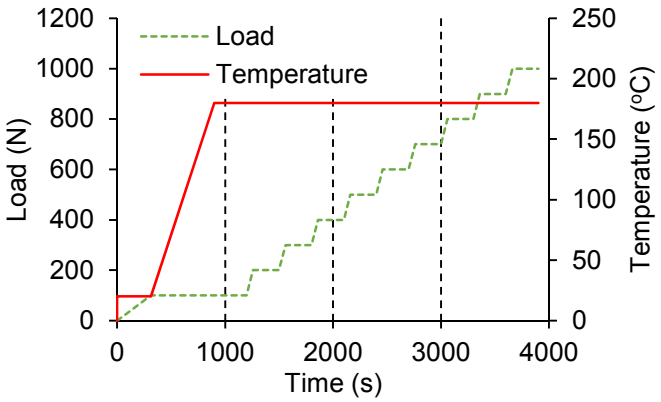

Figure 3.20: Discrete load step test procedure schematic.

3.3.5 Ring liner load step test

In order to assess the viability of these methods to detect scuffing transitions at a component level, the discrete load step test program and methodology was applied to a piston ring on cylinder liner configuration on the TE-77, Figure 3.21. Oversize martensitic chromium steel piston rings of 138 mm diameter and flake graphite cylinder liners OEM parts from a EPA 2010 Detroit Diesel 13, 12.8L engine, as used in the ASTM D8074 engine sequence test [143], were sectioned to fit the TE-77 ring holder, Figure 3.21. The ring had a 3.35 mm wide barrel face and a keystone profile which formed a line contact, 30 mm in length, across the entire width of the liner segment. The ring extended beyond each side of the liner and was held between the green and red plates, it formed a conformal contact without being tensioned. The liner samples were machined to fit in the sample bath and secured using counter sunk screws. Identical lubricant to the discrete load ramp tests above was supplied in the same manner at a feed rate of 0.5 ml/h.

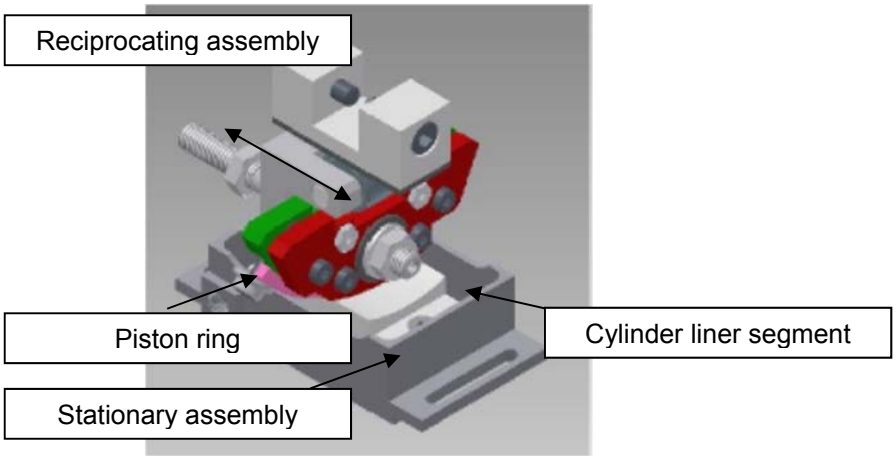

Figure 3.21: TE-77 piston ring and cylinder liner configuration.

3.3.6 Test Summary

The experimental details of the tests presented in the following chapters, are summarised in Tables 3.1, 3.2 and 3.3. Table 3.1 pertains to tests using the continuous load ramp methodology which was applied solely to investigate the scuffing mechanisms of flake graphite cast iron.

Tables 3.2 and 3.3 show details of the tests used to investigate the scuffing mechanisms of both flake and nodular graphite cast irons using the discrete load step methodology.

Table 3.1 Experiment details of the flake graphite cast iron continuous load ramp tests, 10 Hz.

Test ID	Contact	Scuffing severity	Load step duration	Temperature °C	Lubricant feed rate ml/h
CLS	Coupon	Severe	31.6 N/min	150	5.00
CLMS	Coupon	Severe	31.6 N/min	150	5.00

Table 3.2 Experiment details of the flake graphite cast iron discrete load step tests, 15 Hz.

Test ID	Contact	Scuffing severity	Load step duration	Temperature °C	Lubricant feed rate ml/h
DLS	Coupon	Severe	600	150	0.05
S1	Coupon	Severe	600	180	0.05
S2	Coupon	Severe	600	180	0.05
MS1	Coupon	Mild	600	180	0.05
MS2	Coupon	Mild	600	180	0.05
RLS1	Component	Severe	600	180	0.05
RLS2	Component	Severe	600	180	0.05
RLMS1	Component	Mild	600	180	0.05

Table 3.3 Experiment details of the nodular graphite cast iron discrete load step tests, 15 Hz.

Test ID	Contact	Scuffing severity	Load step duration	Temperature °C	Lubricant feed rate ml/h
NS1	Coupon	Severe	300	180	0.05
NS2	Coupon	Severe	300	180	0.05
NS3	Coupon	Severe	600	180	0.05
NS4	Coupon	Severe	600	180	0.05
NIS1	Coupon	Intermediate	600	180	0.05
NIS2	Coupon	Intermediate	600	150	1.00
NMS1	Coupon	Mild	600	180	0.05
NMS2	Coupon	Mild	600	180	0.05

3.4 Surface analysis

3.4.1 Variable focus optical profilometry

Topographies of the scuffed flake and nodular cast iron wear scars were examined using a non-contact, focal plane variation microscope, Alicona Infinite Focus. A 3D dataset of the surface was constructed by measuring the reflected intensity of a beam of light at different distances from the surface. The reflected light is most intense when the surface is in focus, therefore all the 2D intensity images can be stacked on top of each other to provide 3D topographical information. The microscope was also used to take 2D images of the surfaces. The whole wear scar of the flake cast iron sample was imaged in 2D but only the centre was scanned in 3D. The 3D data was laid over the 2D image as a colour map. The Alicona software was used to compress, by averaging in the y direction a 500 µm wide form profile in 3D into 2D. The average profile was

aligned with the 2D image and 3D topographical map of the surface to present the information coherently.

3.4.2 Stylus profilometry

The surface roughness, kurtosis, reduced peak and valley heights of the scuffed cast iron surfaces were measured using a Taylor Hobson Talysurf equipped with a standard 2 µm diamond tip. The samples were orientated such that the grinding marks (lay) were perpendicular to the profile direction. Although the grinding marks were not present in the wear scars of the severely scuffed surfaces, the orientation remained at 45^{o} to the wear scar. This enabled a profile of sufficient length to fulfil the ISO 4288:1996 criteria for rougher surfaces to be measured. As the scuffed samples were of differing roughness, the profile measurement length, data filter length and cut-off lengths were selected depending on the individual sample surface roughness to comply with ISO 4288:1996. The reported surface parameters were averaged from at least three measured profiles.

3.4.3 Scanning electron microscopy and energy dispersive X-Ray spectroscopy

The cast iron surfaces were examined under a scanning electron microscope (SEM) to investigate the scuffing wear mechanism. The microscope was a JEOL JSM-6500F with an energy dispersive X-ray detector (Oxford Inca 300) attached. Detailed topographical secondary electron images (SEI) were captured as well as compositional back scattered electron images (BSI) at accelerating voltages of 15 and 20 keV. Material differences identified in the BSE images were investigated further by using EDX on selected points.

3.4.4 Focused ion beam microscopy

To further investigate the material response to scuffing, focused ion beam cross-sections and microscopy images were taken perpendicular and additionally in the case of nodular parallel to the sliding direction to analyse the change in the subsurface micro-structure, using a Zeiss NVision 40 dual beam FIB. A voltage of 30 kV was used to accelerate a beam of Ga^{+} ions into the material surface between 3 nA and 80 pA, in order to selectively remove (sputter) material from the surface. Secondary electrons emitted from the interaction of the Ga^{+} ions with the sample material were collected using an in lens detector. The amount of electrons emitted from the sample depended on how far into the material the ion travelled. This was directly affected by the angle of the incident beam and the crystallographic orientation of the material. The further into the sample the ion travelled the fewer electrons escaped from the surface producing low contrast, conversely if an ion travelled a short distance more electrons escaped producing a high contrast. This phenomenon is called ion channelling and results in high contrast images of the material micro-structure [144].

4 Scuffing mechanisms of flake graphite cast iron

4.1 Microstructure and hardness

The EN-GJL0250 flake graphite cast iron microstructure is shown in the optical image of the cross sectioned sample, Figure 4.1 a). It was observed that the graphite morphology tended to have a high aspect ratio consistent with flakes, 1-2 µm in width and 40-100 µm in length, with occasional morphologies that were more equiaxed. The graphite morphology was classified as form I, distribution D, size 7 according to EN ISO 945-1:2008 [59]. The graphite colonies were observed to surround areas of ferrous matrix which were shown from high magnification SEM images to be areas of pearlite Figure 4.1 b). These observations agreed with the microstructures documented in literature for flake graphite cast iron according to BS EN 1561:2011 [56]. The nominal composition supplied by the manufacturer is shown in Table 4.1.

Table 4.1: Nominal composition (wt%) of EN-GJL0250 flake cast iron plate [145].

C (wt%)	Mn (wt%)	Si (wt%)	P (wt%)	S (wt%)	Mg	Fe
2.90-3.65	0.40-0.70	1.80-2.90	0.30	0.10	None	balance

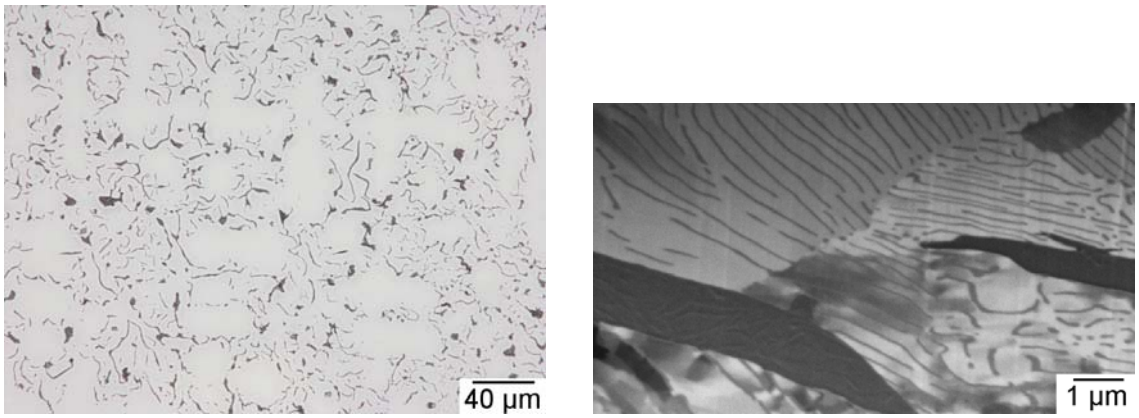

a) *b)*

Figure 4.1: Optical microscope image (a) of transversely sectioned flake graphite cast iron plate and SEM image (b) of pearlitic matrix.

The Vickers hardness of the flake cast iron samples and the 52100 cylinders were 209 ± 9 H_v and 845 ± 4 H_v, respectively, Table 4.2. The hardness ranking of these materials agreed with the properties quoted in literature, Section 2.6.2.

Table 4.2: Flake cast iron and roller bearing properties: Vickers hardness (Hv), average surface roughness (R_a), kurtosis (R_k), reduced peak height (R_{pk}) and reduced valley depth (R_{vk}) from a Talysurf contact profilometer (standard deviation error (σ).

Sample	Hv	σ	R_a	σ	R_k	σ	R_{pk}	σ	R_{vk}	σ
Roller bearing	845	4	0.041	0.009	0.088	0.012	0.066	0.054	0.139	0.074
Mild CLMS ground	209	9	0.413	0.011	1.215	0.029	0.513	0.063	0.887	0.066
Severe CLS ground	209	9	0.566	0.013	1.838	0.057	0.597	0.089	0.925	0.089

4.2 Ground flake cast iron surface roughness

Surface finish is known to be crucial to scuffing performance [98,146–148], therefore the topography of the ground surface finish was analysed to verify that it was representative of a honed cylinder liner [76,96,98]. Honing is a multistep process where each successive operation deforms the surface to a lesser depth than the previous step. The first steps correct for geometric out of roundness after the boring process. Following this, the honing step is used to cut a cross-hatch pattern in the surface which acts to retain lubricant and trap debris particles. Peaks on the surface created during the formation of the cross hatch pattern are removed during plateau honing, which forms a smooth plateau surface above the deeper honing marks, facilitating a greater load bearing area. This distribution of surface heights is said to have a negative skew and can be visualised using a bearing area curve which plots surface height in descending order, discussed previously in Section 2.1.3.

The flake graphite cast iron samples were surface ground, as a flat surface could not be readily honed and this process achieved a surface similar to the honing process. This resulted in an R_a = 0.490 µm, R_{pk} = 0.555 ± 0.076 µm, R_{vk} = 0.906 ± 0.078 µm and 77 ± 2 % plateau (average), Table 4.2. This is at the lower end of the average surface roughness range published in literature of 0.38 - 1.1 µm for honed cast iron liners [19,78,118,119]. The R_{vk} = 0.906 was almost twice the R_{pk} = 0.555, showing that the ground surface had a negative skew. The plateau created by the grinding process can be seen between $Mr1$ and $Mr2$ on the bearing area curve, Figure 4.2. The ground flake cast iron sample had a plateau of approximately 77 % of the surface which was higher than the minimum of 60 % required for a plateau honed surface [19]. The roughness of the roller bearing samples, measured in the direction of reciprocation, had an R_a = 0.041 ± 0.009 µm.

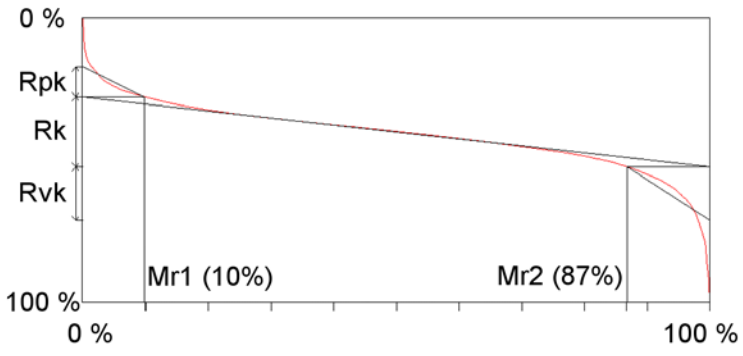

Figure 4.2: Bearing area curve for the ground flake cast iron surface from a Talysurf profilometer (2 µm tip).

The topographical analysis above showed that the grinding process repeatedly produced a surface finish similar to a plateau honed cylinder liner. This was important as it has been reported in literature that topography variation influences the scuffing wear mechanism and failure load [98,146–148].

4.3 Preliminary flake cast iron scuffing tests

4.3.1 Continuous loading tests

The continuous load methodology was used to investigate the flake graphite material scuffing mechanism which changed the ground surface into a severely scuffed wear scar. The friction force, normal load, contact potential and cast iron temperature were plotted against the time elapsed for the mild and severe continuous load tests, Figure 4.3.

As can be seen from the graphs the average friction force was similar in magnitude and behaviour for both tests. Whilst the friction force was unaffected by increasing the contact temperature to 150 ^{o}C, the contact potential was affected. In the severe scuffing test the temperature increase appeared to cause the formation of an insulating film on the surface, evidenced by an increase in contact potential, which was removed by increasing the load to 400 N. This effect was not observed in the mild scuffing test where a brief increase in contact potential occurred around 80 ^{o}C. However, this decreased to a negligible amount once the temperature had reached 150 ^{o}C. High speed friction force data from the running in period (Figure 4.4a) exhibited a square wave geometry, indicating this effect was not due to a change in the lubrication regime between tests, but a surface phenomenon. The tests appeared consistent with each other in terms of the mild and severe transition and as the lubricant was additive free, it was thought that such an insulating tribo-layer did not significantly affect the scuffing failure mechanism of the flake cast iron surface.

The mild scuff test was stopped at 620 N, the load at which the friction force stabilised during the severe scuffing test which coincided with an increase in friction force at the stroke reversal positions, Figure 4.4b. The severe scuff test was stopped when a rapid increase in average friction force was detected at a load of 1 kN indicating severe-scuffing was occurring.

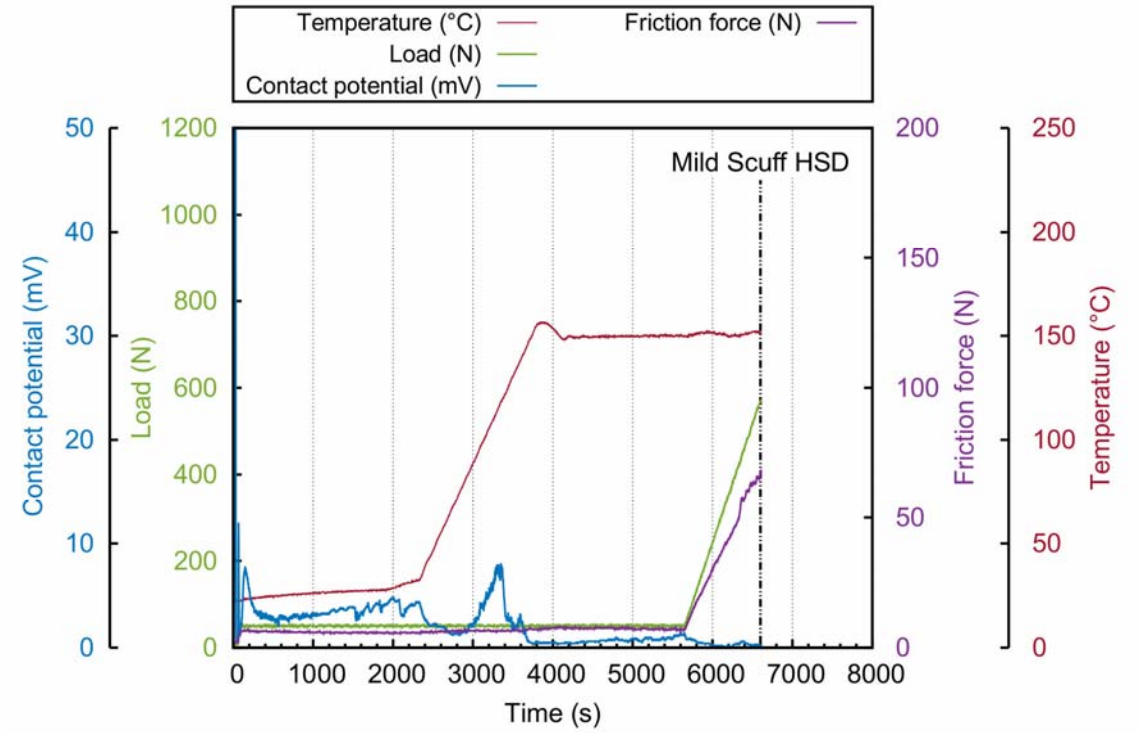

(a)

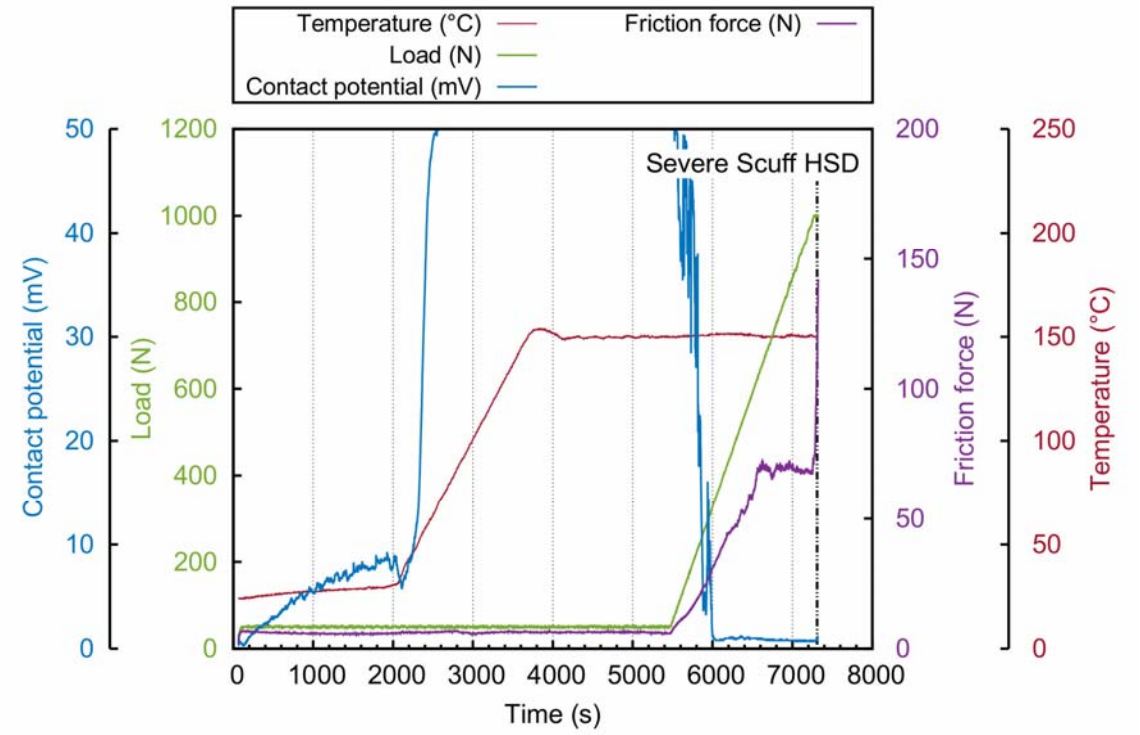

(b)

Figure 4.3: Continuous load flake cast iron (a) mild CLMS and (b) severe CLS scuffing test data graph.

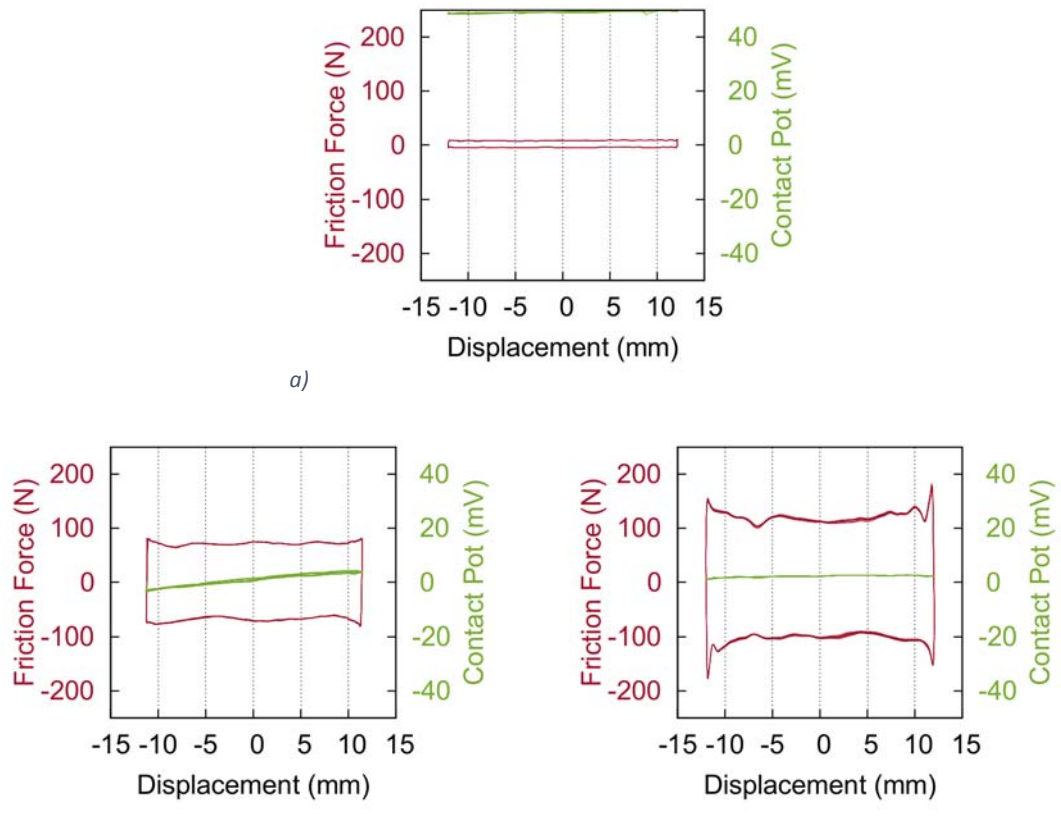

Figure 4.4: High speed friction and contact potential data for flake cast iron tests: (a) continuous load running in (b) Continuous load mild scuff, (c) Continuous load severe scuff.

High speed friction and contact potential data was sampled for 1 s prior to scuffing, during mild and severe scuffing, and plotted against stroke displacement in Figure 4.4. The friction data recorded before the onset of scuffing presented as a regular square wave which was symmetrical about 0 N. This indicated that the friction force was independent from sliding velocity, suggesting both a boundary lubrication regime but also that adhesive wear was not occurring at the reversal positions, Figure 4.4 a). The contact potential indicated the presence of a continuous electrically insulating film over the entire stroke.

Figure 4.4 b) showed that at the onset of mild-scuffing, the friction force remained constant over the stroke apart from at the stroke reversal positions. Here, the friction force deviated from the standard square wave and was approximately 10 % greater than over the rests of the stroke. The continuous electrically insulating film previously observed was not present during mild-scuffing .The area encompassed by the graph which represented the friction power dissipated in the contact (F_P), also increased from the pre-scuff condition 3 W to 35 W. F_P was calculated from the high speed friction data acquired at 10 kHz for 1 s using Equation 4.1, where at data point i: F_i is the friction force and d_i is the stroke position.

Upon severe-scuffing, Figure 4.4 c), the friction force was disordered across the entire stroke. The friction power dissipated in the contact increased from 35 W during the mild-scuff condition

to 57 W during severe scuffing due to the increased load. The magnitude of the friction force at the stroke reversal positions compared with stroke average increased 50 %. The contact potential shows that no electrically insulating film was present during severe-scuffing.

$$F_P = \sum_{i=1}^{10^4} \left| F_{f(i-1)} . \left(d_i - d_{(i-1)} \right) \right| \qquad \textit{Equation 4.1}$$

One of the most obvious trends in the continuous loading test was the increase in friction force during the load ramp, from approximately 6 N during the running in phase to around 70 N at a normal load of around 620 N. The friction force then stabilised until severe scuffing occurred, despite the continuously increasing contact pressure. During this period the surface yields due to the applied shear stress as the asperities are unable to resist the increasing load and consequently deform. This mechanism has been reported to occur in the early stages of scuffing [101,102]. Consequently when the test was repeated to produce a mild scuff surface, the test was stopped at the contact load which was thought to indicate the deformation of surface asperities.

This method of detecting mild scuffing had two disadvantages. The first was that the onset of scuffing could only be detected after it had occurred due to the time for enough data to be collected to notice a change in trend. Secondly it relied on the repeat test behaving in an identical manner to the severe test, which can be challenging for a tribological experiment. Despite these limitations the methodology did facilitate initial discrimination between a mild and severely scuffed surface.

The scuffing test was designed to identify the progression of scuffing in flake cast iron but also to compare the relative scuffing resistance with nodular cast iron. The latter will be quantified by comparing the severe scuffing contact pressure for both materials. However, severe scuffing of the flake cast iron occurred at the maximum load of the tribometer, which left no room to discriminate if the nodular cast iron had a higher scuffing resistance. Plastic deformation of surface asperities has been reported as an attrition process and consequently it is possible for the surface to wear into a condition that will facilitate scuffing at one contact pressure [15]. Consequently it was hypothesised that if the contact was given time to respond to the change in load before increasing the load further it may scuff at a lower load. Therefore continuous load ramp methodology was changed to a discrete load step methodology, which is also more common in the literature [98,106,107,120,133,146,149,150]. Failure within a load increment would then facilitate improved discrimination between materials that might otherwise respond differently to a dynamic load increase.

4.3.2 Discrete loading profile

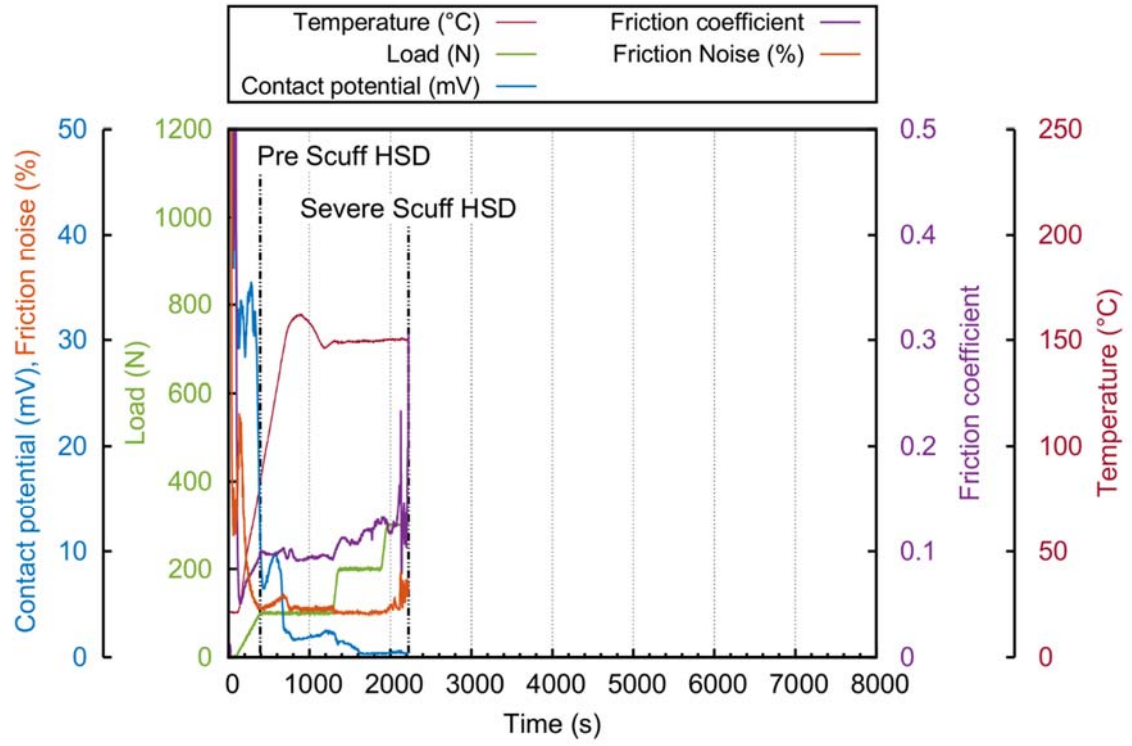

Figure 4.5: Discrete load flake cast iron severe scuffing test data graph.

During the initial load ramp the contact was separated by an insulating film indicated by the contact potential value being above 30 mV. Consequently the friction force was proportional to the sliding speed and this was reflected by the friction noise exceeding 20 %. At the end of the initial load ramp the increased load caused the contact to transition into boundary lubrication. The friction force was then independent of the sliding velocity and consequently deviated very little from the RMS friction, resulting in a decrease in the friction noise.

As the surface wore-in the roughness decreased and the contact transitioned back into the mixed regime. The hydrodynamic effects of the lubricant in this regime allow partial separation at the higher velocities experienced near the middle of the stroke. This effect was reflected by the increase in contact potential and friction at 500 s. During this period the contact temperature was increased which reduced the viscosity of the lubricant present in the contact. It could then no longer support the 100 N load and the contact transitioned back to the boundary regime, which was accompanied by a decrease in friction noise and contact potential at 700 s. All hydrodynamic effects were prevented by the increases in contact load to 200 N, indicated by a slight decrease in friction noise and contact potential.

Severe scuffing occurred during the 300 N load step. The friction noise increased from 5 to 6 % prior to the increase in friction coefficient above 0.2. The increase in friction noise was caused by substantial deviation from the RMS friction due to local increases in friction force arising from adhesive wear. Once the friction coefficient had exceeded 0.2, indicating severe scuffing, the

friction noise increased to 8 % as damage spread across the stroke resulting in large friction fluctuations. The friction noise measurement provided an indicator of the local friction events providing that the contact potential was close to 0 mV indicating that the contact was operating in the boundary lubrication regime.

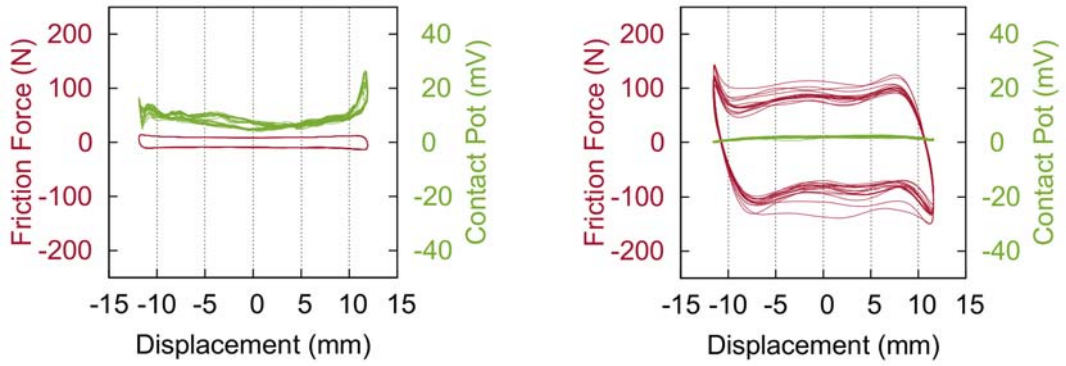

a) *b)*

Figure 4.6: High speed friction and contact potential data for discrete load flake cast iron test: (a) pre scuff, (b) severe scuff.

The high speed friction data for the discrete load method was inadvertently filtered using 100 Hz low pass filter rather than a 300 Hz low pass filter which was used for the rest of the high speed data acquisition, Figure 4.6. Consequently the time taken for the friction signal to slew polarity at the stroke reversal positions manifested as a gradual change and caused the friction data to present as rhombus rather than the square form which it was in reality. It also smoothed the friction fluctuations occurring across the stroke. Despite this filtering, the progression of adhesive wear from the stroke reversal positions to the centre of the scar could still be determined from the instantaneous friction signal, indicative of severe scuffing and consistent with the rise in average friction coefficient above 0.2 observed in Figure 4.5.

The main difference between a discrete and continuous load ramp was that the friction behaviour at constant load could be evaluated. The coefficient of friction was constant around 0.1 during running-in. During the 200 N load step the friction coefficient increased which showed friction force increased independently from the contact load. This demonstrated the benefit of using a discrete load profile which allowed the contact response to an increase in the contact pressure to be observed.

Scuffing failure of the surfaces occurred during the 300 N load step due to an increased sliding frequency and simultaneous initiation of both load and temperature ramps. It was beneficial to have induced scuffing failure at lower loads compared to the continuous ramp tests, as failure at a maximum load of 1 kN would not allow comparison with other materials (e.g. Nodular cast iron) that may exhibit superior scuffing resistance. Subsequent discrete load tests were conducted with the temperature ramp occurring after the load ramp to running in load in order

to allow the surface to be conditioned conformally without both friction and external energy supplied to the contact.

4.4 Detecting scuffing transitions using high speed data

In order to detect the earliest stages of scuffing a sensitive and robust detection method was required. Two scuffing detection techniques, disorderly friction (friction noise) and the scuffing detection software, were therefore developed based on quantitative analyses of the characteristic behaviour of the instantaneous friction force observed at the different stages of scuffing, as outlined in Section 3.3. The following experiments were conducted using both techniques to gain further understanding of the flake cast iron scuffing mechanism.

4.4.1 Severe scuffing tests

The flake cast iron test data for the two severe scuffing tests is presented in Figure 4.7. Comparing both tests, the friction coefficient magnitude and response was similar. The criteria prescribed for severe scuffing was when the friction coefficient exceeded 0.2, which was set on the tribometer control software to automatically terminate the tests. Both tests failed within 125 s of each other at a load of 300 N after the contact had experienced a period at steady state, Table 4.3.

During running-in the contact potential decreased as the load increased indicating that the lubricant film, caused by the reciprocation of the counter face, had exceeded its pressure limit. The presence of a velocity dependant lubricant film caused the instantaneous friction to deviate from a velocity independent square wave, increasing the friction noise. As the film thickness decreased, the friction force became independent from the velocity and consequently uniform over the stroke, reducing friction noise. In both tests the film did not fully collapse until the temperature was elevated above 50 ^{o}C due to the subsequent reduction in lubrication viscosity.

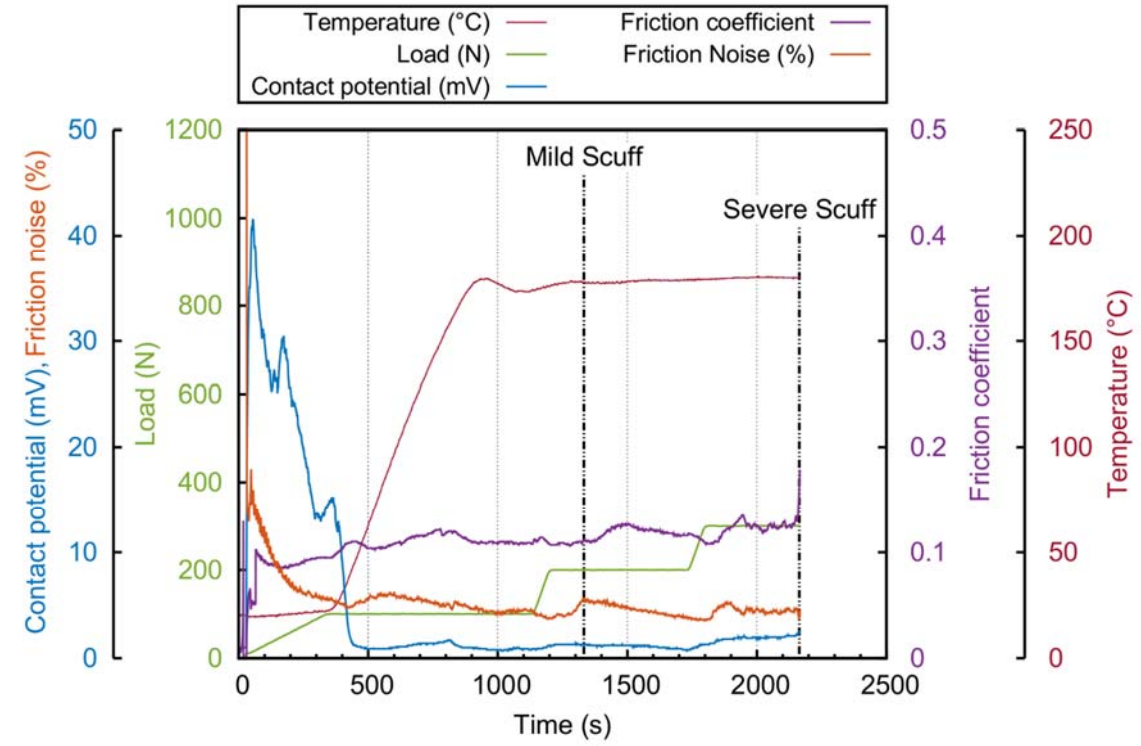

(a)

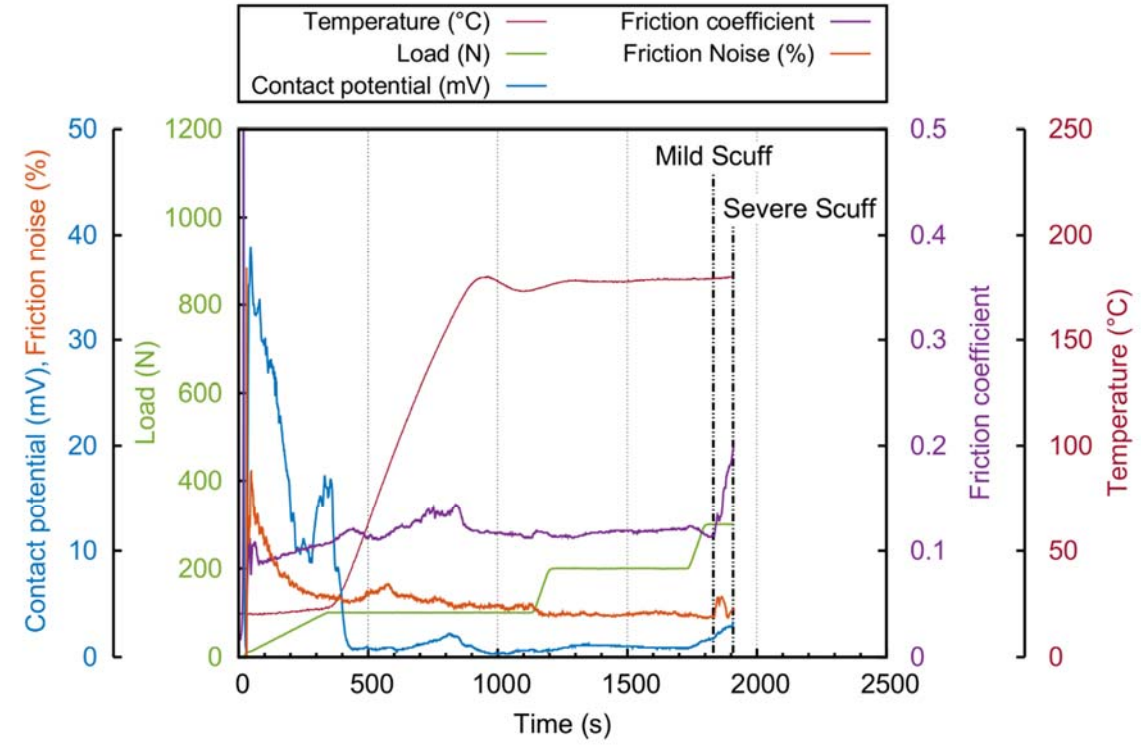

(b)

Figure 4.7: Flake cast iron severe scuffing test data graph (a) S1 and (b) S2.

Subsequent increases in friction noise occurred independently from increases in contact potential and therefore indicated the presence of local variations in friction force across the stroke which could be attributed to asperity interactions on the surface.

An insulating film developed during the 300 N load step in both tests. As the lubricant film had already collapsed and there were no additives present in the lubricant this film is likely to have been an oxide layer caused by the friction energy dissipated in the action of mild scuffing, which has been reported by Saeidi et al and also Han et al [107,108].

Although both tests failed at the same condition the failure mechanism was slightly different. In the case of second severe scuffing test (S2), the onset of severe scuffing occurred gradually over approximately 50 s, in contrast to all the other severe scuffing tests presented where the transition took 1-2 s. It was thought that a degraded lubricant film formed on the surface of this test which was resistant to scuffing, consequently scuffing damage required time to wear the film away in the transition from mild to severe scuffing.

The criteria that indicated the onset of mild scuffing was determined from analysis of the high speed friction data recorded during the severe scuffing tests S1 and S2, Figure 4.8 and Appendix flake Figure 10.1. The criteria consisted of two thresholds, the first was the maximum friction force in the accelerating direction at the stroke reversal positions before fluctuations developed across the stroke. This was chosen as it was hypothesised that a local increase in friction force at the reversal positions in the accelerating direction was caused by the energy required to initiate adhesive wear. It was thought that this threshold would be suitable to indicate the onset of scuffing, as the reversal positions had been identified in previous tests as the location for scuffing initiation [15].

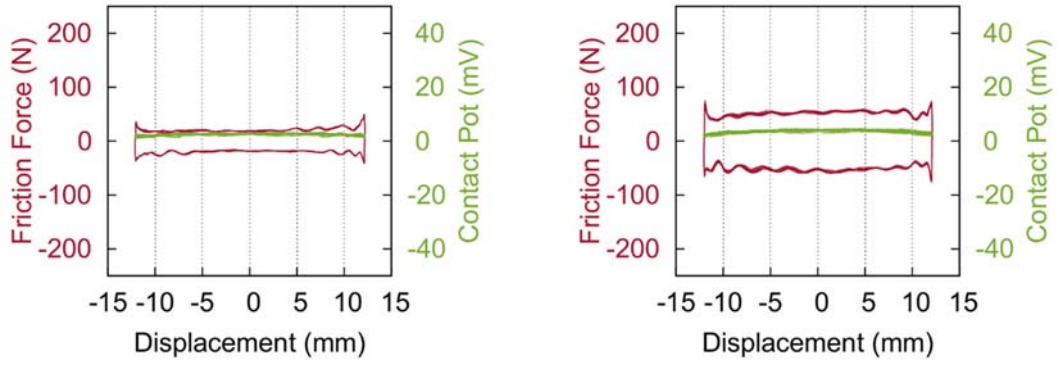

(a) *(b)*

Figure 4.8: High speed friction and contact potential data from (a) mild and (b) severe scuffing of scuffed flake test S1.

It was observed however that increases in friction force in the accelerating direction occurred before adhesive wear initiated. The additional force was probably required during mild wear, which involved micro ploughing of the surface to plastically deform asperities into the grinding marks. In order to distinguish between mild wear and the onset of adhesive wear, the criteria also specified that the friction force increased in the decelerating direction. This was thought to verify the presence of adhesive wear, as the increase in friction force was hypothesised to be

required to deform cast iron adhesive wear particles that had become trapped between the end of the wear scar and the counter face as it reciprocated.

Applying the mild scuff criteria to tests S1 and S2, the lowest identifiable thresholds for the friction force magnitude at the stroke reversal positions were 140 % of the RMS value in the accelerating direction and 110 % in the decelerating direction. The location and occurrence of mild scuffing was labelled in Figure 4.7 by retrospectively applying these thresholds to the severe scuffing tests S1 and S2.

The shape of the instantaneous friction signal, where mild scuffing was identified, was similar in characteristic for both tests which consisted of uniform friction force across the stroke with the criteria specified increase at the stroke reversal positions. The presence of the local increases in friction force at the stroke reversal positions which satisfied the mild scuffing criteria also caused an increase in friction noise of approximately 2 %, Figure 4.7. This magnitude of friction noise was not unique to the onset of scuffing, it also occurred during running-in due to hydrodynamic lubricant effects. Consequently although the friction noise quantified friction force disorder it relied on the contact operating in the boundary lubricant regime to detect scuffing which was indicated by the contact potential. However the rate of change of friction noise was an indication of the onset of severe adhesive wear, in the same way that a rapid increase in friction force has been used as an indicator that scuffing is occurring. As the friction noise parameter was a measure of deviation from the RMS, it has a much higher sensitivity to changing friction force than the RMS friction coefficient and consequently provided an earlier indication of the onset of scuffing. Therefore it can be concluded at this stage that the friction noise parameter provided an indication of the onset of severe scuffing although cannot solely be used to identify mild scuffing.

4.4.2 Mild scuffing tests

Both mild scuffing tests (MS1 and MS2) behaved in a very similar manner and were terminated within 275 s of each other (Table 4.3) when the high speed data mild scuff criteria had been exceeded, Figure 4.9. The behaviour was similar to the second severe scuffing test where the friction coefficient reached a peak during running-in at 800 s. This behaviour did occur during the first severe scuffing tests however it had a much lower magnitude. Possible reasons for this difference could include local variations in the cast iron microstructure, where graphite colonies may be inhomogeneously distributed at the contact surface.

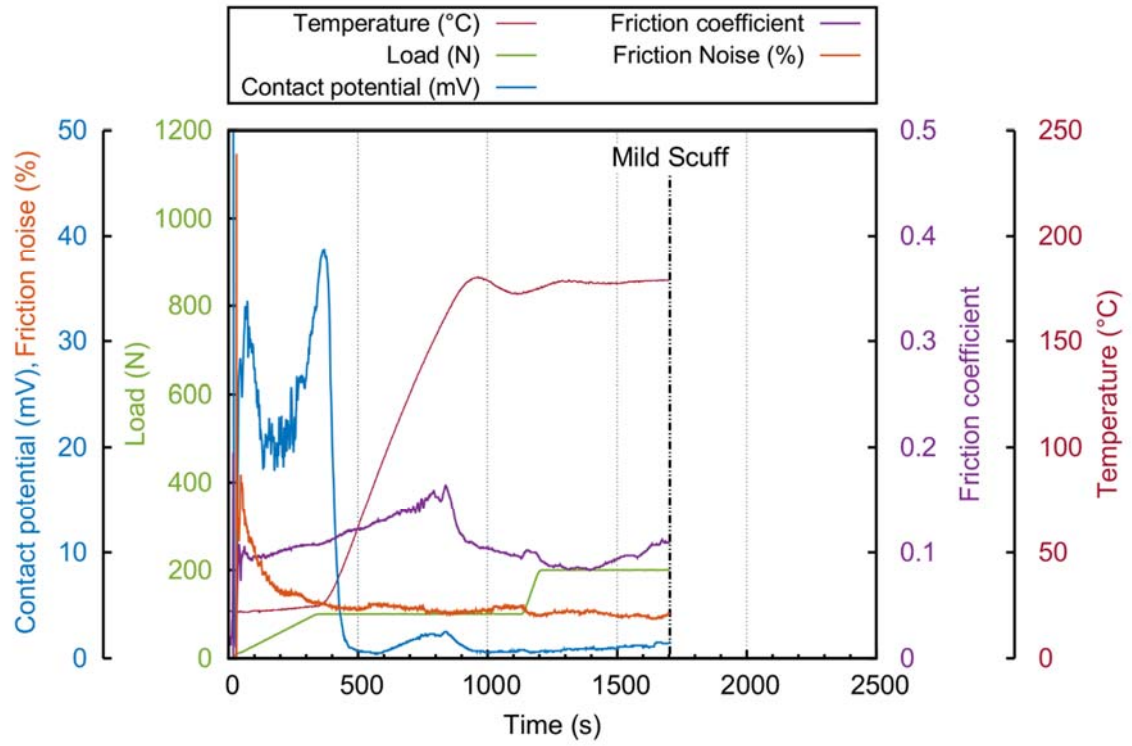

(a)

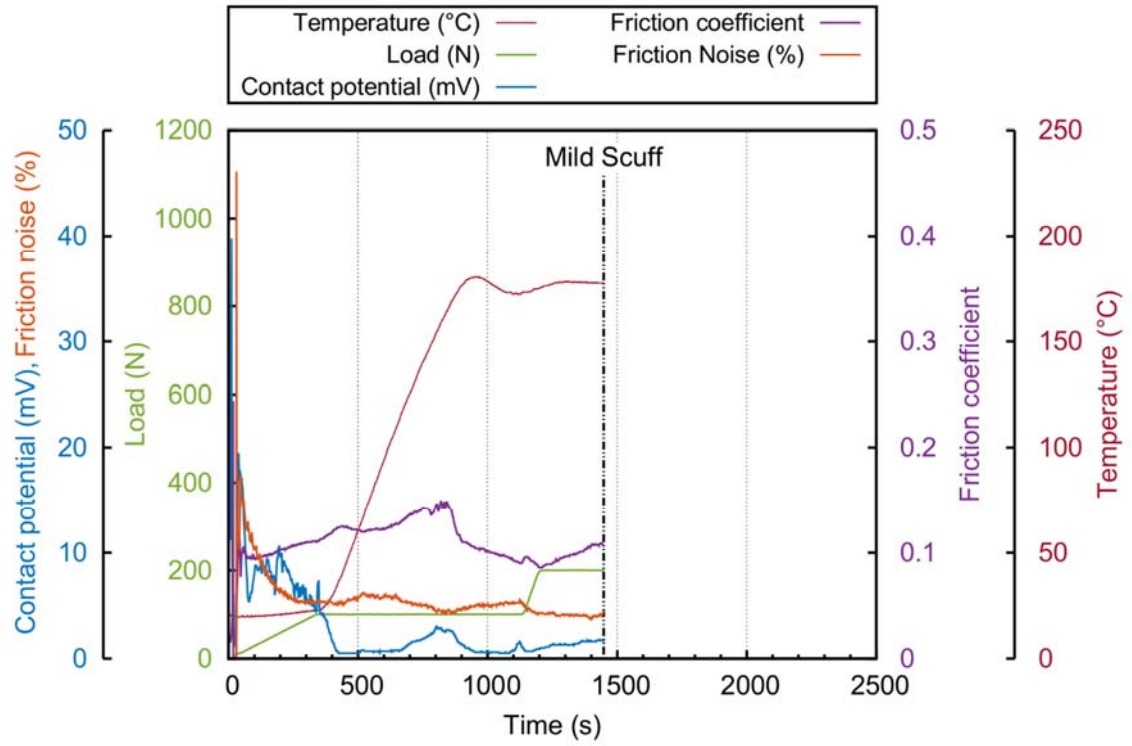

(b)

Figure 4.9: Mild scuffing test data graph (a) MS1 (b) MS2.

There was no discernible difference between the high speed friction and contact potential data from each mild scuffing test, shown in Figure 4.10. Local increases in friction force only occurred at the stroke reversal positions and the rest of the stroke had a uniform friction value. Consequently the friction noise did not exhibit any characteristic change to indicate the onset

of mild scuffing, which was consistent with observations for the severe tests S1 and S2. The friction force behaviour indicated that the experimental conditions were well controlled and that the test sequence did not induce unstable wear transitions. The high speed friction scuffing methodology provided a repeatable indicator that mild scuffing was occurring within 18 % absolute deviation, Table 4.3.

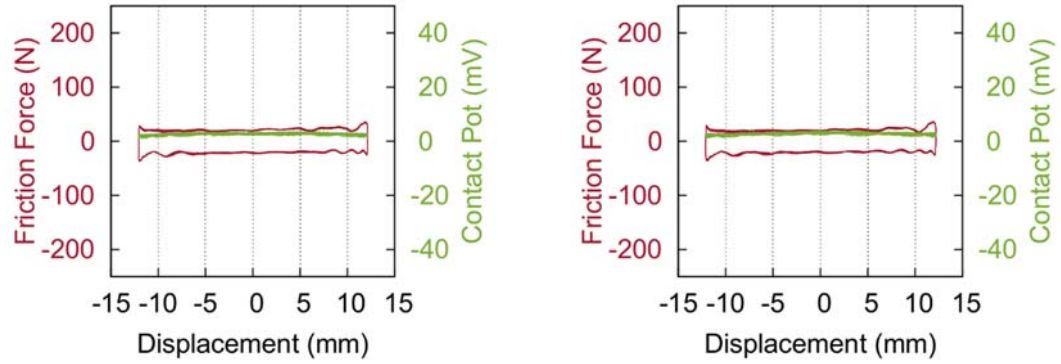

(a) *(b)*

Figure 4.10: High speed friction and contact potential data (a) MS1 and (b) MS2.

Table 4.3: Comparison of test duration and scuffing load for mild and severe flake cast iron.

Test Name	Mild		Severe scuffing	
	Test time (s)	Load (N)	Test time (s)	Load (N)
Severe S1	1320	200	2160	300
Severe S2	1820	300	1910	300
Mild MS1	1600	200		
Mild MS2	1440	200		
Max absolute Deviation	275	75	125	0
Max absolute Deviation (%)	18	33	6	0

4.5 Surface analysis

4.5.1 Scuffed surface profilometry

Three dimensional colour depth maps and surface profiles of the continuous load mild and severe scuffed wear scars are shown in Figure 4.11. The wear scars were rectangular with no evidence of edge loading, indicating a good line contact had formed between the 52100 cylinder and the cast iron plate. Both wear scars had a similar wear depth of approximately 20 µm in the middle of the stroke, however material up to 30 µm deep had been removed just before the stroke reversal positions on the severely scuffed surface. This was consistent with the onset of adhesive wear initiating at the stroke reversal positions as shown by the instantaneous friction signal in Figure 4.8 b).

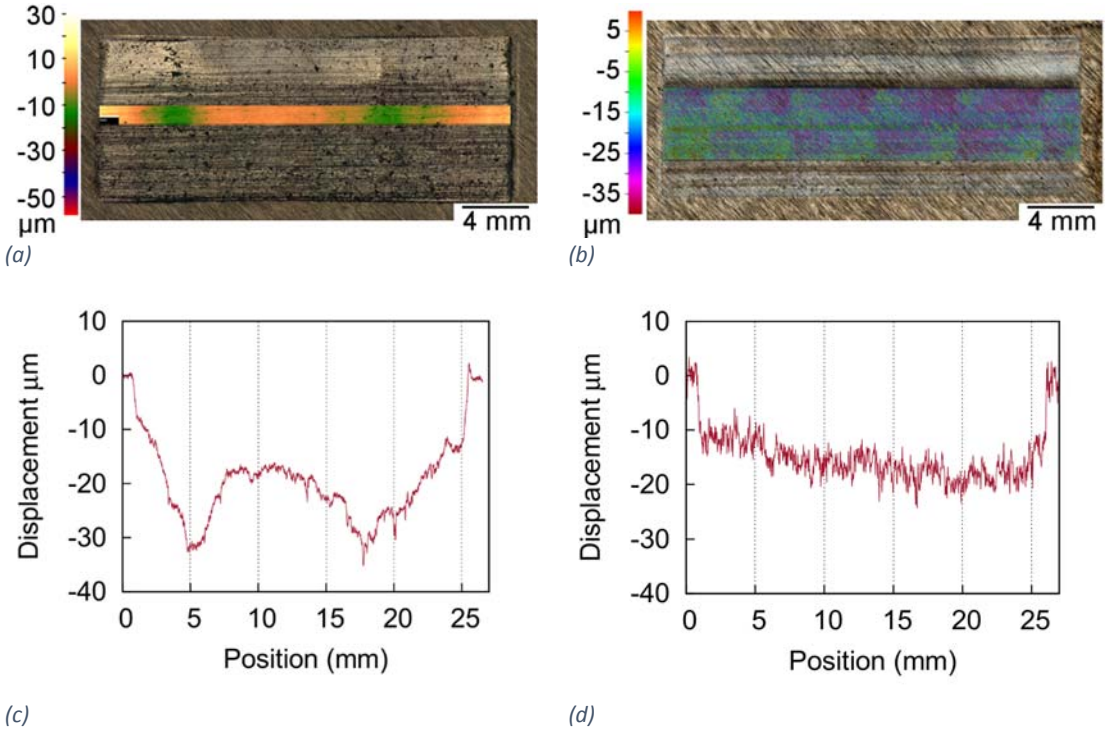

Figure 4.11: Optical images, 3D colour maps and surface profiles of the (a & c) severe CLS and (b & d) mild CLMS scuffed flake cast iron wear scars.

Higher magnification optical images of the continuous load tests revealed their contrasting topographical features. The continuous load severe scuffing test wear scar contained surface craters of the order of 100 µm in length and up to 35 µm in depth, Figure 4.12 a). This was direct evidence of the adhesive wear mechanism being the dominant failure mode for severe scuffing and was wholly consistent with previous studies from the literature on scuffing failure of metallic surfaces [108]. There was no evidence of the ground surface finish (at 45˚) outside the craters, instead scratches in the direction of reciprocating were observed. Grinding marks, up to a depth of 2 µm, were however present on the mild-scuffed surface and were the deepest surface defects present, Figure 4.12 b). Thus the transition from a pre-scuffed surface to a mild scuff is characterised by a change in surface topography that results in the disappearance of the surface lay (ground at 45˚). Further, the transition from a mild scuffed surface to a severely scuffed surface is likewise characterised by the formation of surface craters consistent with an adhesive wear mechanism. These observations were consistent with the data in Table 4.4, where it was observed that the mild scuffed surface decreases in average surface roughness compared to the unworn ground surface, whilst the severely scuffed surface increases in average surface roughness.

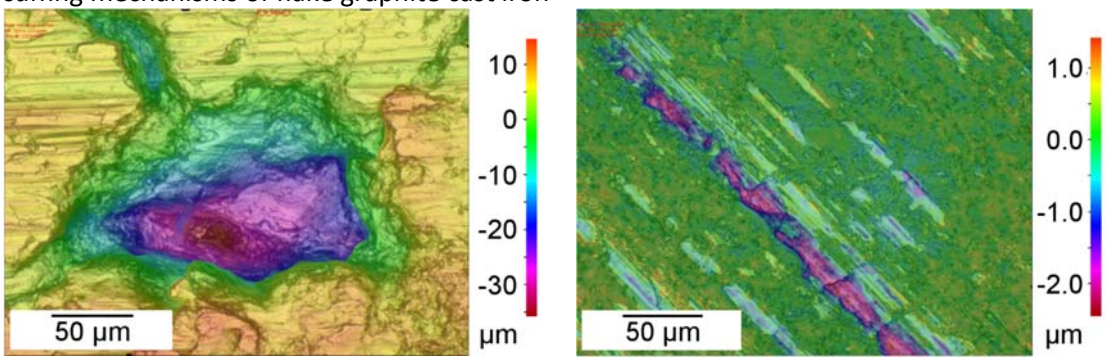

(a) *(b)*

Figure 4.12: Optical images blended with 3D colour maps of the (a) severe CLS and (b) mild CLMS scuffed continuous load flake cast iron surfaces.

The ground surface finish of the flake cast iron surfaces was modified by the scuffing process during testing with the continuous load ramp test sequence. The mild-scuffed flake cast iron surface had a decreased surface roughness compared to the as ground surface of R_a = 0.222 µm, R_{pk} = 0.116 µm and R_{vk} = 0.824 µm, Table 4.4. This increased the bearing area at the expense of the lubricant retention volume which can be seen in Figure 4.13 b). In contrast the severe scuffed flake cast iron surface had an increased surface roughness compared to both the mild-scuffed and ground surface of R_a = 2.197 µm, R_{pk} = 1.952 µm and R_{vk} = 6.873 µm, Figure 4.13 a).

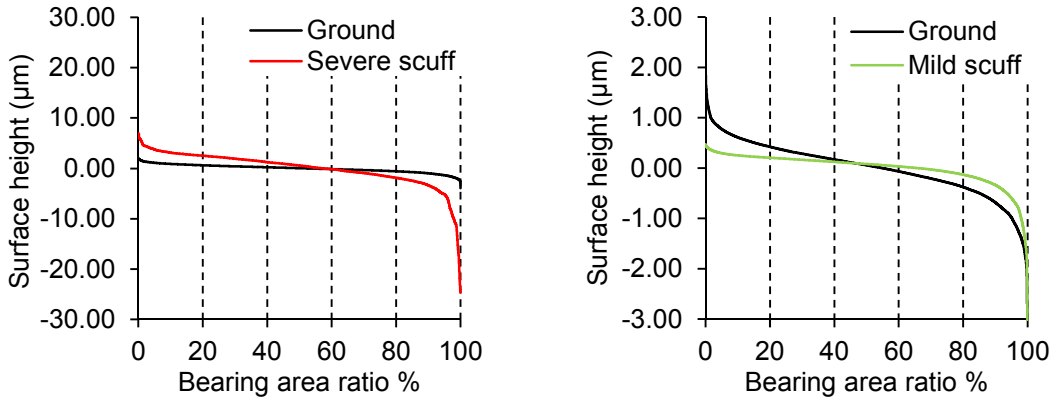

a) *b)*

Figure 4.13: Bearing area curves for the a) severe CLS scuff and b) mild CLMS scuff surface from a Talysurf prolfiometer (2 µm tip).

Table 4.4: Flake cast iron and roller bearing properties: Vickers hardness (Hv), average surface roughness (R_a), kurtosis (R_k), reduced peak height (R_{pk}) and reduced valley depth (R_{vk}) from a Talysurf contact profilometer (standard deviation error (σ).

Sample	R_a	σ	R_k	σ	R_{pk}	σ	R_{vk}	σ
Roller bearing	0.041	0.009	0.088	0.012	0.066	0.054	0.139	0.074
Mild CLMS ground	0.413	0.011	1.215	0.029	0.513	0.063	0.887	0.066
Mild CLMS scuffed	0.222	0.020	0.442	0.014	0.116	0.023	0.824	0.128
Severe CLS ground	0.566	0.013	1.838	0.057	0.597	0.089	0.925	0.089
Severe CLS scuffed	2.197	0.251	6.200	0.789	1.952	1.121	6.873	2..121

4.5.2 Evolution of a mild scuffed surface

The optical images will now be discussed considering the progression of damage starting with the mildly scuffed surfaces. The optical images of the two mildly scuffed surfaces were very similar, which agrees with the similarly of the measured variables previously discussed. Evidence of surface asperity smearing was present as bands running the length of the wear scar. The bands obscured the grinding marks which were present across the rest of the wear scar.

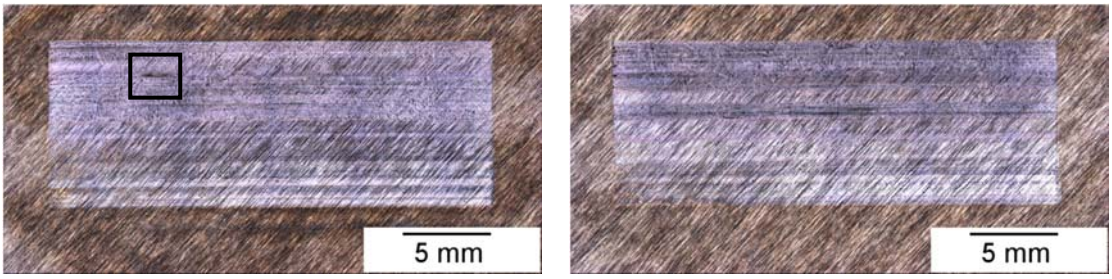

(a) (b)

Figure 4.14: Optical images of mildly scuffed flake cast iron surfaces (a) MS1 and (b) MS2.

Scuffing initiation was observed to have occurred on MS1, 5 mm inside the left stroke reversal position, Figure 4.14 a). The scuff was located on the upper edge of the second band of smearing from the top of the image. It appeared to have a smooth texture and was dark in colour, Figure 4.15. The initiation was aligned with the direction of sliding as were other features in the scuffed area. Most notably the area is in relief (4 µm) with a small local crater in the centre, approximately 7 µm in depth.

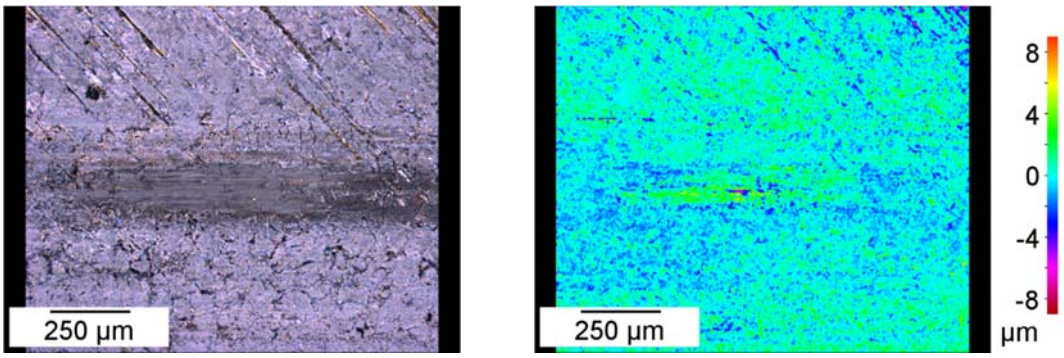

(a) (b)

Figure 4.15: (a) Optical image and (b) colour map of scuffing initiation site on MS1.

This feature is likely to have developed when cast iron surface platelets were transferred onto the reciprocating counter face. Figure 4.16 a) and b), show the interface between the smeared region of the wear scar and the mild wear region where grinding marks were still present. It is clear from the image that the transition between the ground surface and the smeared region is not discrete but a continuous transition characterised by the amount of plastic deformation.

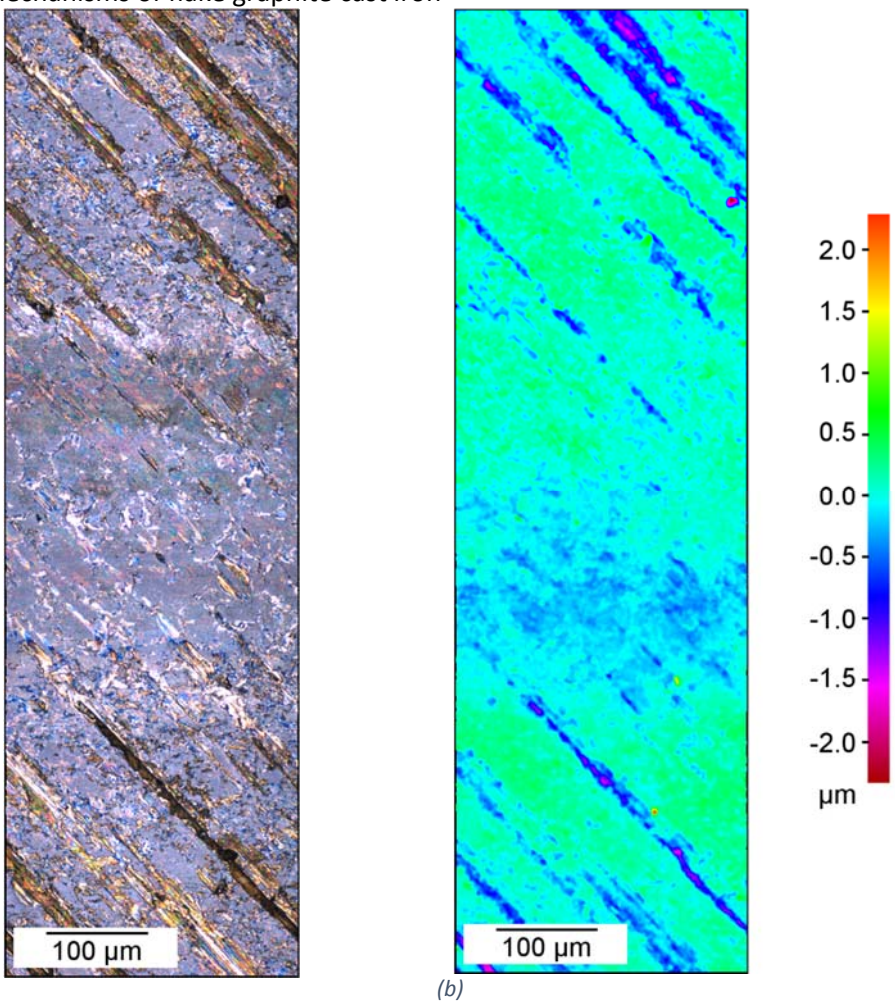

(a) (b)

Figure 4.16: Optical images and colour maps of mildly scuffed flake cast iron surfaces MS2.

The wear occurring across both mildly scuffed wear scars was very similar. However, the onset of adhesive wear was observed at one of the stroke reversal positions of the MS2 wear scar, Figure 4.17. In this image the interface between the stroke reversal position and the ground surface can be seen. At the very edge of the stroke is the development of a wear crater which was up to 100 µm long and 9 µm in depth. There were also smaller craters which had begun to form inside the stroke reversal position collinearly with the large crater. This observation supported the hypothesis that the rise in friction force at the stroke reversal positions in the accelerating direction may be attributed to the onset of adhesive wear. However it also showed that whilst it was possible to detect this transition, the onset of localised adhesive wear did not lead immediately to severe scuffing, but that a cumulative effect of transfer and back transfer was required prior to a rapid rise in the average coefficient of friction.

The surface surrounding the craters had a morphology characteristic of that found in the mild scuffing which was the presence of clearly defined platelets on the surface without either wear tracks in the direction of sliding or grinding marks.

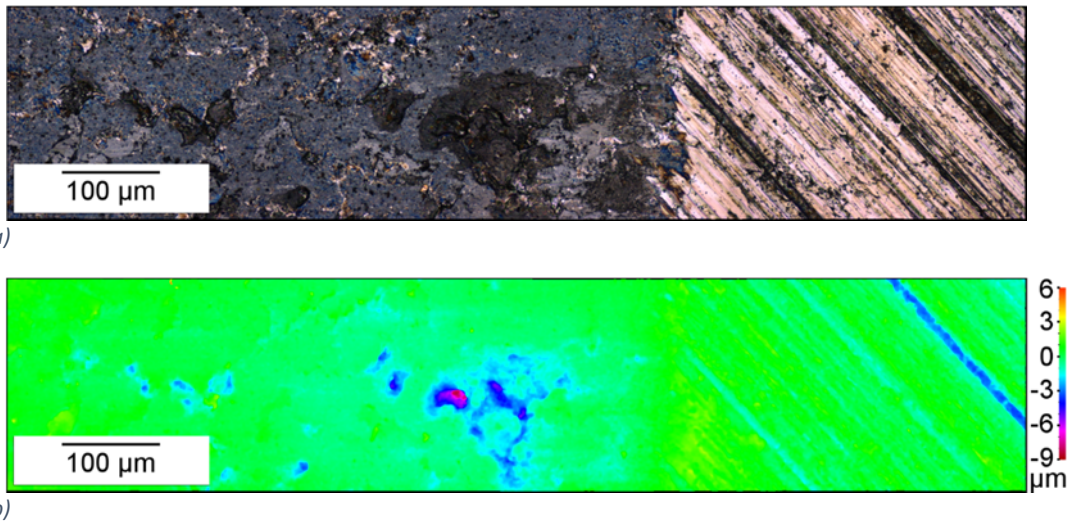

Figure 4.17: (a) Optical images and (b) colour maps of the onset of adhesive wear at the stroke reversal positions MS2.

4.5.2.1 Scanning electron microscopy

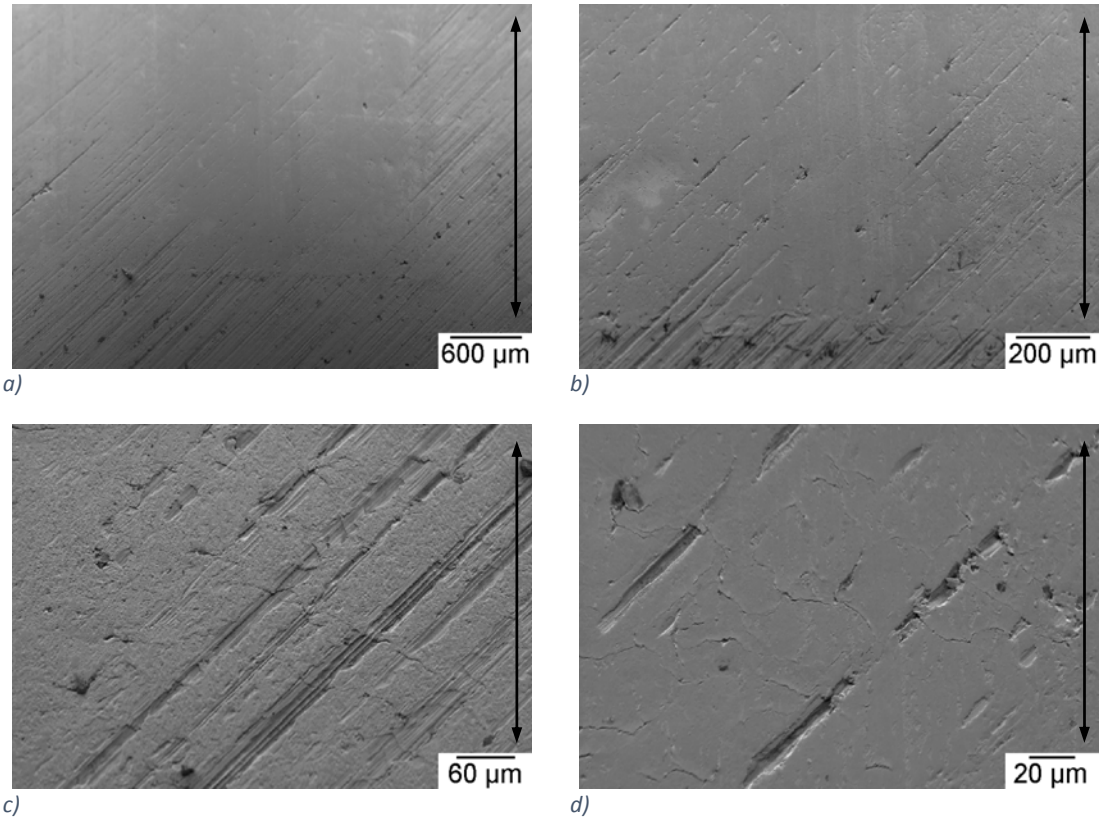

Figure 4.18: Secondary electron images from surface of the mild scuffed continuous load ramp test CLMS: a) Corner of the wear scar; b) Stroke reversal position; c) & d) Magnified regions near stroke reversal position.

SEM images from the continuous load mild scuffed surface wear scar are shown in Figure 4.18. The interface between the wear scar and the ground surface, Figure 4.18 a) and b), confirmed that the onset of mild scuffing resulted in the discontinuity of the ground surface topography. Higher magnification images in Figure 4.18 c) and d), revealed an interesting micro-topography, with wear debris either compacted at the top of peaks between grinding marks, or smeared into

the grinding valleys. Regions in-between the ground valleys exhibited what appeared to be deformed regions with surface cracks resembling smeared iron platelets.

4.5.2.2 Focused ion beam microscopy

A FIB cross section was made through the continuous load mild scuff sample transverse to the direction of reciprocation, to further investigate the platelet formation, Figure 4.19. Surface cracks forming the platelet boundaries were observed to originate at the intersection between the lamellar graphite flakes and the free surface, which has been similarly observed in the literature [49,54,106–108].

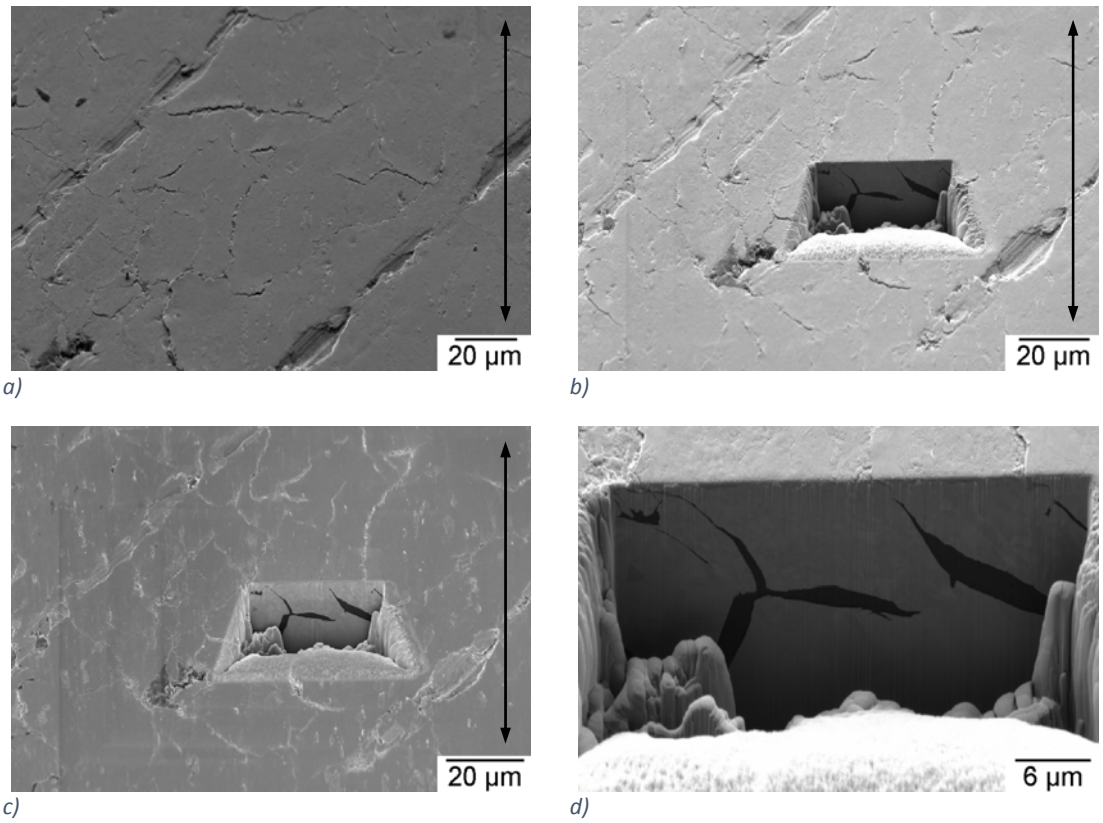

Figure 4.19: SEM images from test CLMS of a) FIB area of interest; b) Secondary and c) Backscattered images of cross-section; d) Higher magnification secondary image of cross-section.

The secondary ion images of the FIB cross section showed that the cast iron had a pearlitic microstructure separated by graphite flakes, Figure 4.20. There was a subsurface deformed layer present which had been strain induced, approximately 2 µm deep, containing a substantially work hardened microstructure with sub-micron grain sizes. It was difficult to determine from these images if this was a change to a martensitic structure, reported to occurring during mild scuffing [13,14] or a refinement of the pearlite matrix formed from fractured Fe_3C lamellas mixed with the ferrite. The image does confirm that the platelet formation is associated with the graphite flakes and that their size is defined by the spacing between flakes intersecting the surface which was also observed by Jensen et al [102].

There was little evidence that the graphite flakes had been deformed or extruded to form a lubricating film which has been reported by Andersson et al [20]. Sugishita et al [103] also reported the formation of a graphitic film. However, a point contact was used with significantly higher contact pressures and consequently the magnitude and depth of the shear stress are likely to have been sufficient to extrude graphite from the matrix.

a)

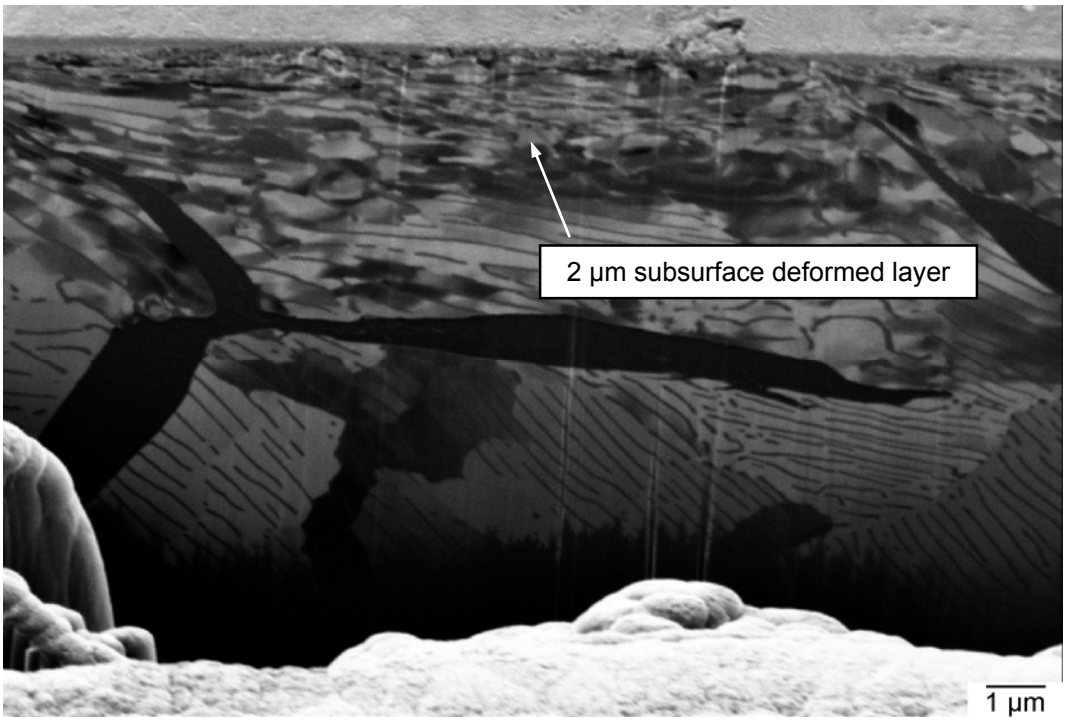

b)

Figure 4.20: Secondary ion images of the mild scuffed flake graphite cast iron surface from the continuous load test CLMS, a) cracks at the interface between the lamellar graphite flakes and the free surface, b) strain induced subsurface microstructurally deformed layer and pearlitic matrix.

4.5.3 Evolution of a severe scuffed surface

Optical images of the wear scars from the severely scuffed surfaces from tests S1 and S2 are shown in Figure 4.21. The first severe test, S1, exhibited two distinct dark regions along the length of the stroke where catastrophic severe scuffing had led to a significant increase in the average coefficient of friction. The second severe test S2 showed the onset of surface transition which occurred between mild and severe scuffing, Figure 4.21 b).

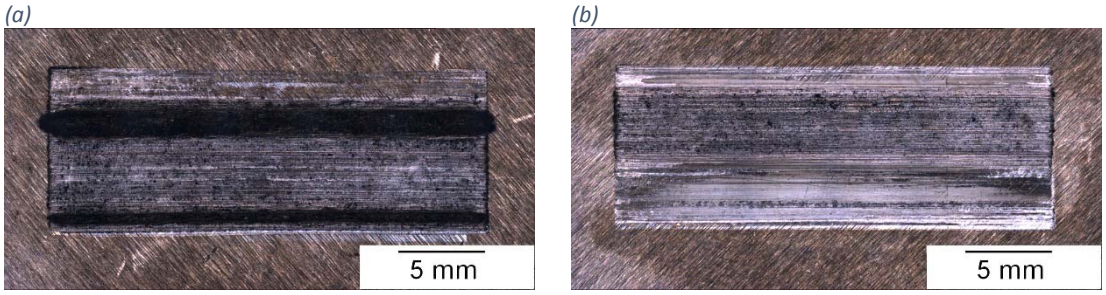

Figure 4.21: Optical images of severely scuffed flake cast iron surfaces (a) S1 and (b) S2.

The severe scuffed surface from test S1 contained two distinct regions, Figure 4.21 a). The largest region was that of severe scuffing which was similar to the region of the onset of adhesive wear observed in MS2. However this region contained wear tracks in the direction of sliding and the wear craters had enlarged from 9 to 25 µm in depth, Figure 4.22 a) and b).

The second region had severe topographical relief of ± 25 µm which was caused by gross material removal during significant adhesive wear, Figure 4.22 c) and d). Evidence for this was the 3 mg mass loss of the liner, Table 4.5, and the agglomeration of wear debris outside the wear scar at each stroke reversal position Figure 4.21 b). The surface was very different from the original ground surface and similar to the severe scuffing observed using the continuous load method in Section 4.3.1.

Table 4.5: Mass loss for tests S2, MS1 and MS2 (standard deviator error, σ).

Sample	Cast iron mass loss (mg)	σ	52100 mass loss (mg)	σ
S2	2.96	0.10	0.07	0.04
MS1	1.15	0.05	-0.02	0.05
MS2	0.13	0.04	-0.03	0.04

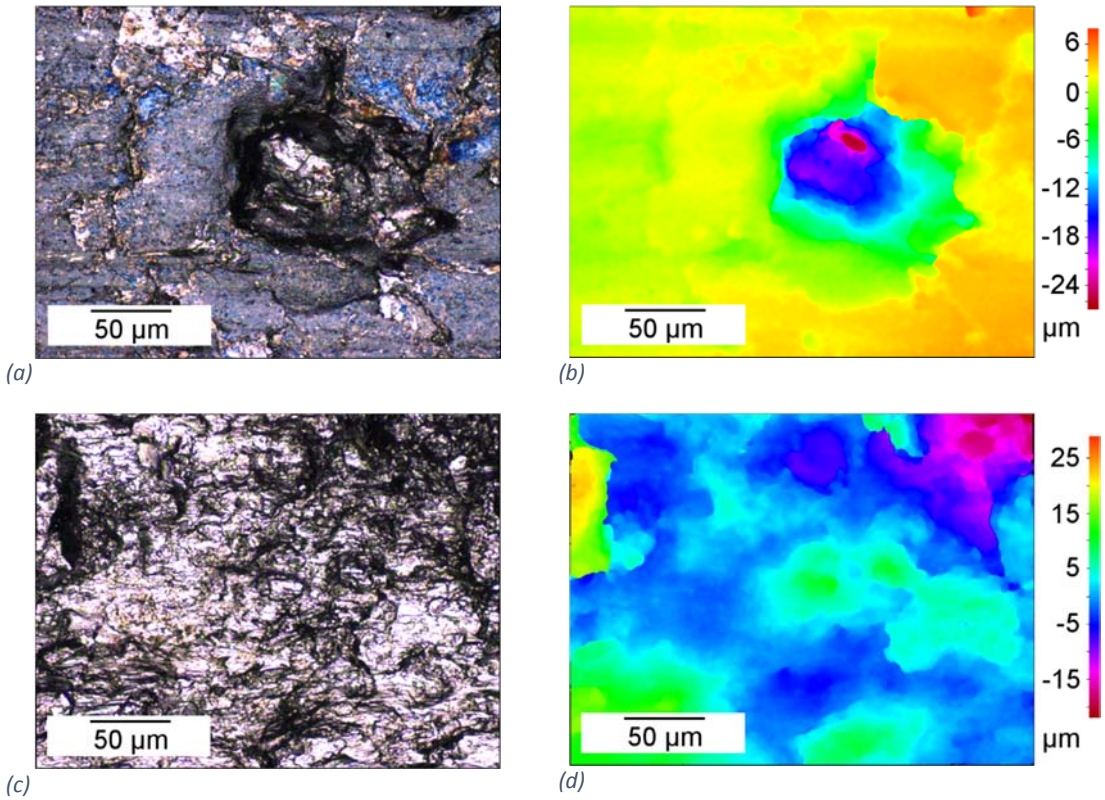

Figure 4.22: Optical images and colour maps of severe adhesive wear and gross material removal during severe scuffing S1.

There was evidence of the formation of a smooth tribolfilm approximately 1 µm in depth across a substantial proportion of the wear track on the surface of the S2 test specimen, bottom of Figure 4.23 a) and b). Outside these regions adhesive craters up to 10 µm deep were present, Appendix flake Figure 4.23 c) and d). It was likely that the tribofilm formed during the progression from the mildly scuffed surface to a severe scuffed surface, which occurred when the lubricant film had broken down as a result of the increased normal load. The presence of small adhesive craters in the gaps in the tribofilm provided evidence for this as the craters had a similar form and magnitude to those found mild scuffing MS2. Ultrasonically cleaning the samples using petroleum ether was unlikely to have removed sections of the tribofilm as it was only observed on parts of the wear scar with similar topographies which were different from the rest of the wear track, Figure 4.24.

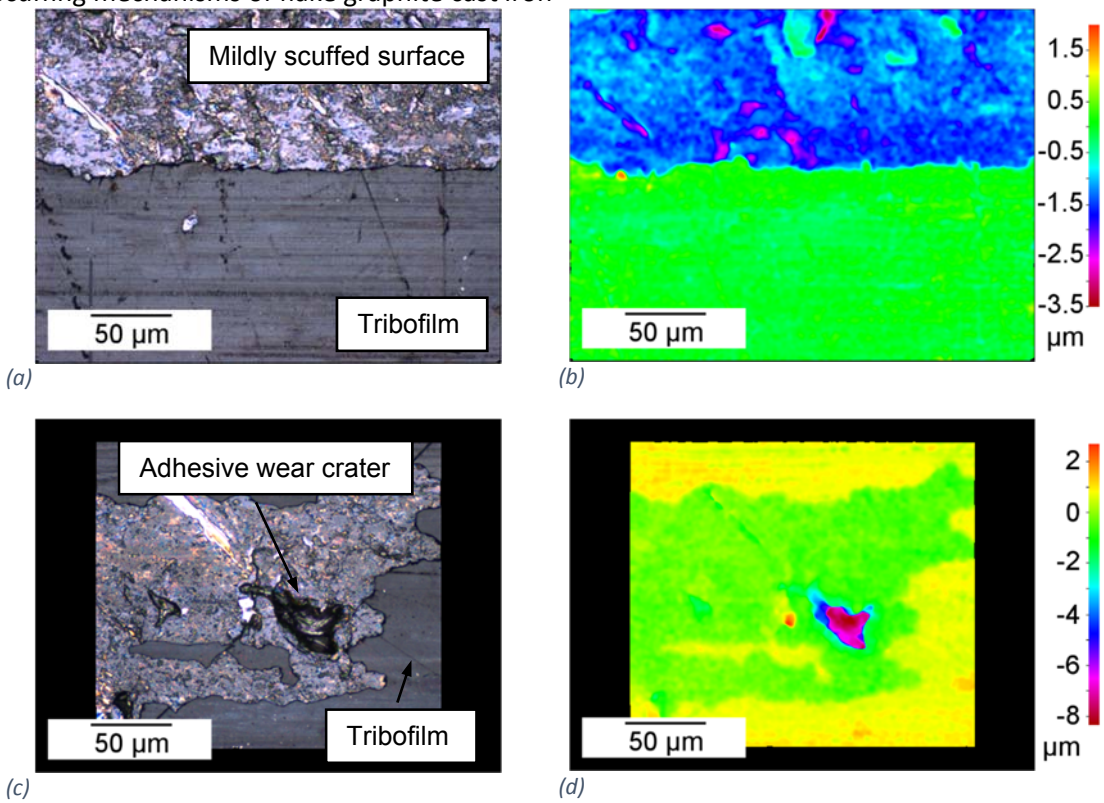

Figure 4.23: Optical images and colour maps after adhesive wear had spread across the stroke S2.

4.5.3.1 Scanning electron microscopy

It was observed that the oil in S2 began to discolour shortly before the test stopped and thus the tribofilm was likely to have consisted of a mix of very fine wear debris and decomposed lubricant. The tribofilm would explain the small increase in contact potential observed prior to the severe scuffing failure, although its presence does not seem to inhibit the onset of severe scuffing. Scanning electron microscopy of the surface, Figure 4.24, showed how the tribofilm was associated with the removal of the grinding marks in the centre of the image allowing the progression to a mild scuffed surface, as can be seen at the top of the image in a). EDX spectra from the dark surface tribofilm, Figure 4.24 b) indicated a high amount of carbon on the surface compared to the mildly scuffed region c), or indeed the unworn ground surface d).

The contact potential signal exhibited a similar trend for test S1; it was thought that the tribofilm may have formed in the absence of localised adhesive wear along a narrow wear track, as observed in test S1, Figure 4.21 a). The tribofilm was therefore the product of wear debris incorporated into the degraded lubricant, but still consistent with the severe scuffing failure mechanism.

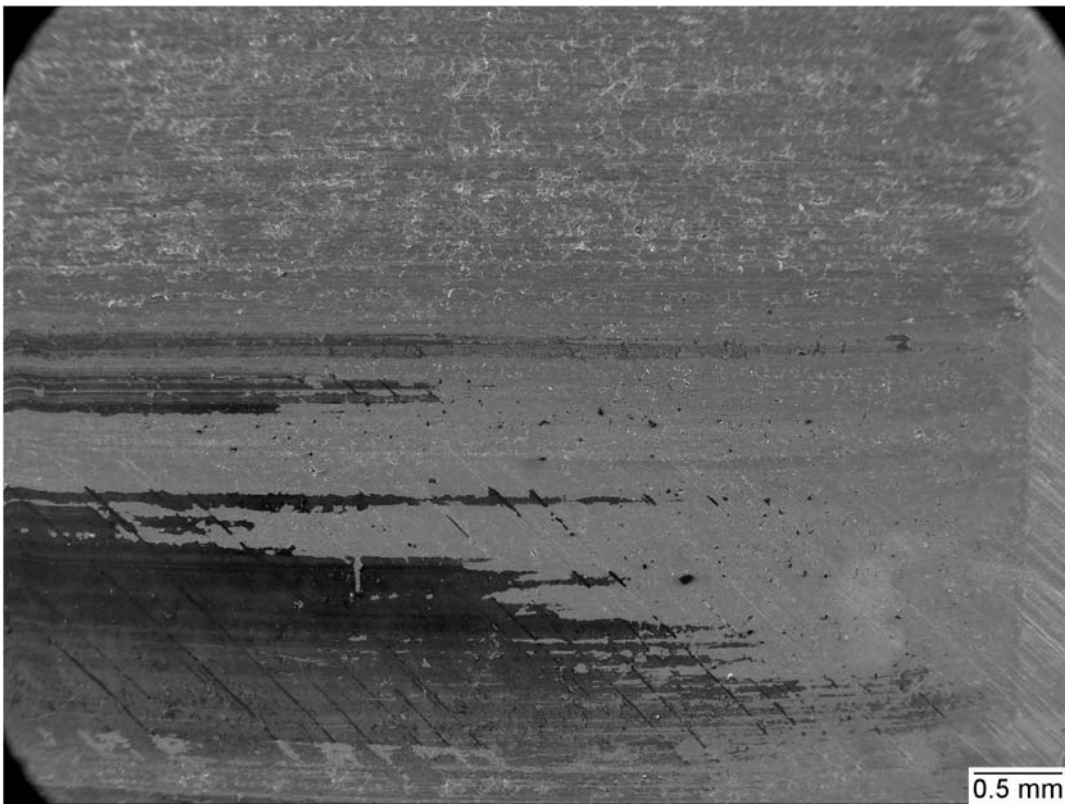

a)

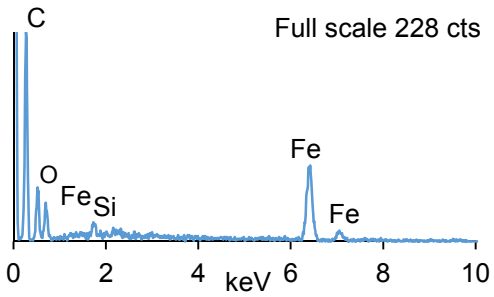

b)

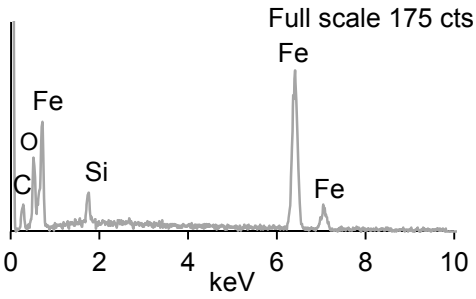

c)

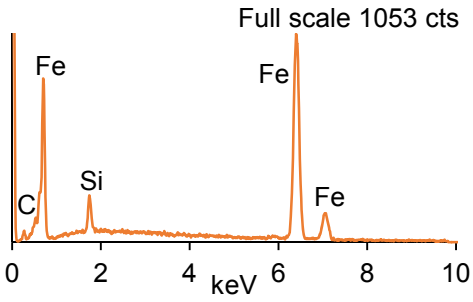

d)

Figure 4.24. Secondary electron image (a) of stroke reversal position from severe scuffed Flake S2. EDX spectra of dark film (b), mild scuffed area (c) and un-worn ground area (d).

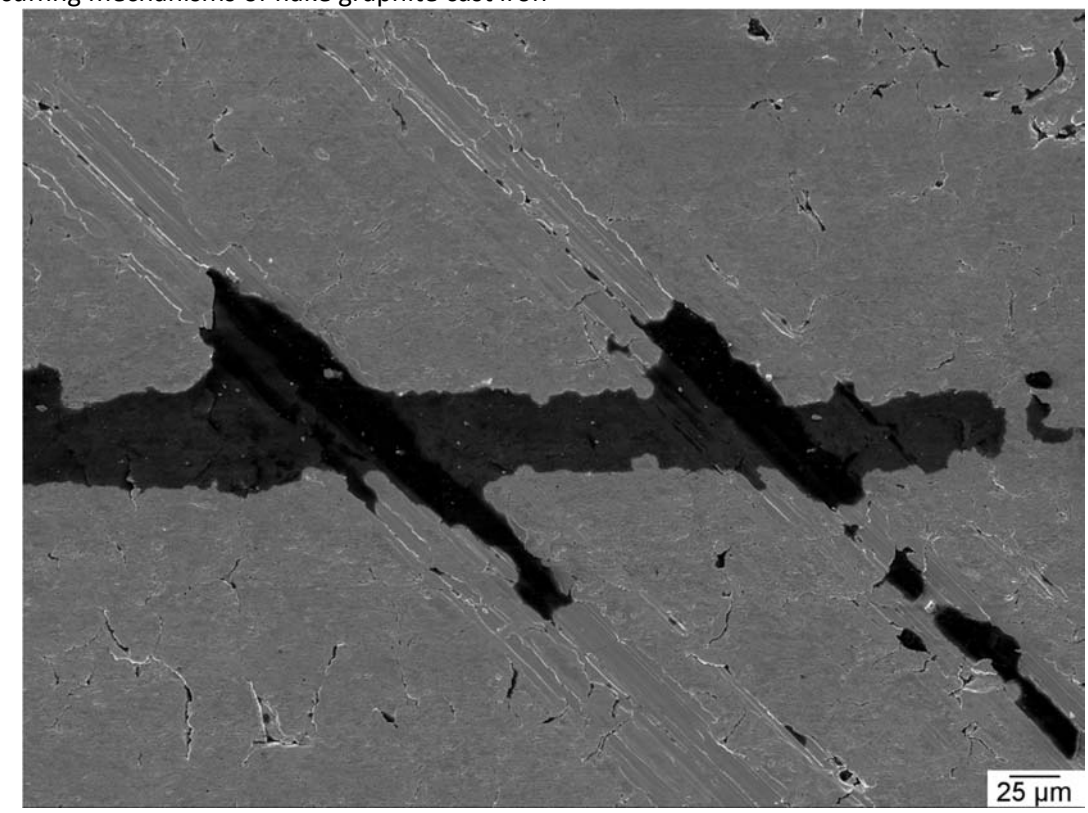

a)

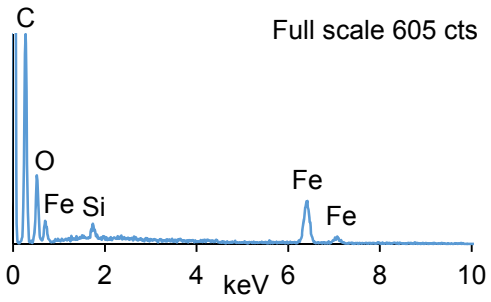

b)

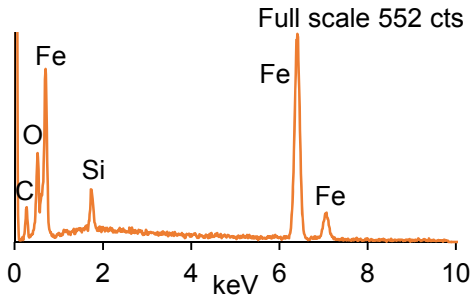

c)

Figure 4.25: Secondary electron image (a) of surface film from severe scuffed Flake S2. EDX spectra of dark film (b) and mild scuffed area (c).

A higher magnification image of this region where the tribofilm was in the process of being removed, Figure 4.25 a), showed that the cast iron surface was transitioning to a mildly scuffed surface, consistent with the 3D topography images above and the high speed friction data, indicating the onset of this transition. EDX spectra of the film again confirmed a strong carbon signal, Figure 4.25 b), which confirms the tribofilm to be the product of lubricant degradation rather than smeared graphite, due to the volume fraction present on the surface. Interestingly an oxygen peak was observed on the mildly scuffed cast iron surface, Figure 4.25 c), suggesting that once the tribofilm was removed, the asperity flash temperatures are sufficient to form a surface oxide, however this appears unable to mitigate the transition to a mildly scuffed surface.

Examination of the severely scuffed surface from the continuous load ramp test, Figure 4.26 a), again showed evidence of platelets, along with the craters observed in the 3D profilometery images in Figure 4.12 a) above. It appeared that these craters had formed around lamellar graphite structures in the cast iron, which was confirmed using EDX. Spectrum 1 located in the crater counted significantly more carbon and less iron compared with spectrum 2 located on one of the plates, Figure 4.26 b). The EDX counts were normalised by feature scaling the results around the element with the most counts in each spectrum.

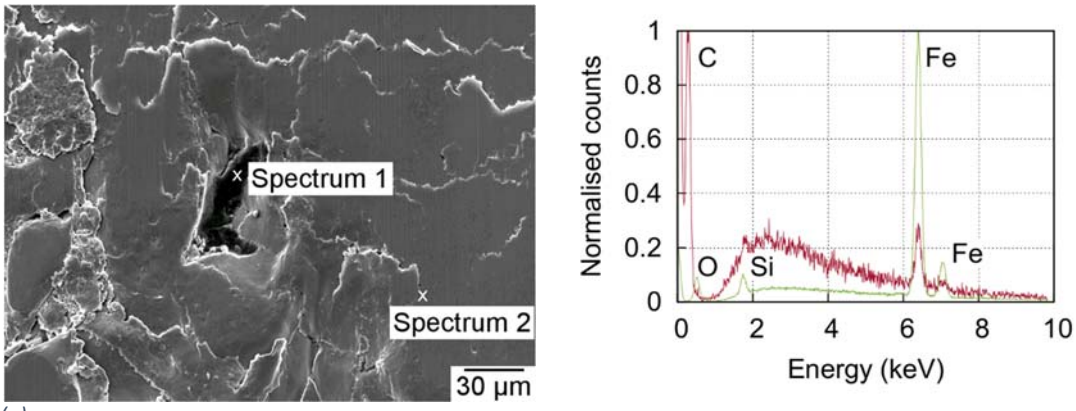

(a) *(b)*

Figure 4.26: (a) Secondary electron image and (b) EDX spectra of a surface crater present on the severely scuffed flake cast iron surface from test CLS.

The severely scuffed discrete load surface was also comprised of platelets smeared across the surface, Figure 4.27 c), although both the severely scuffed surfaces clearly had more extensive damage compared to the mild scuff wear scar. The platelets on the severely scuffed surfaces had defined edges and there was evidence that some of the platelets had been removed from the surface. In contrast the mildly scuffed surface, platelets were loosely defined by the surface cracks which were developing in the surface. The severely scuffed surface exhibited wear tracks parallel to the direction of sliding, although it was clear from Figure 4.27 b) below that this was clearly an adhesive rather than an abrasive wear mechanism.

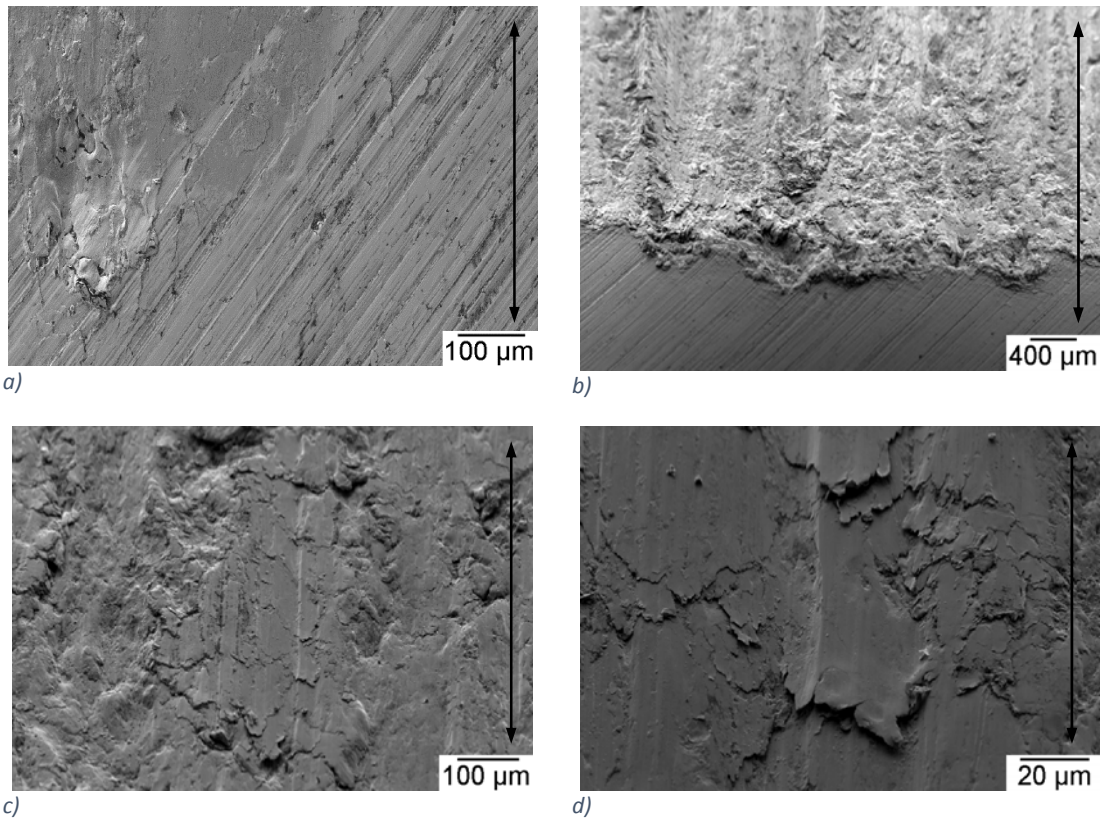

Figure 4.27: Scanning electron microscope images of the discrete load ramp severe scuffed flake cast iron surfaces from test DLS (a) Interface between wear scar and ground surface; (b) Tilted image of stroke reversal position; (c) & (d) Magnified tilted images of wear scar near stroke reversal position.

4.5.3.2 Focused ion beam microscopy

Figure 4.28 a) shows the area of interest for FIB cross sectioning from the severely scuffed flake graphite cast iron surface subject to a discrete load ramp test, which closely resembles the severely scuffed cylinder liner surface observed by Carver and Johnson [99]. The central horizontal line was a deposition of carbon performed in-situ in the FIB, designed to improve the quality of cross sectional polishing by eliminating differential sputter rates. In contrast to the mild scuffed above, the FIB cross section revealed a substantial amount of cracking below the surface but the absence of flake graphite. The cracks appeared to be the boundary between a severely work hardened surface layer approximately 4 µm thick and an inhomogenously deformed bulk, with a large distribution of grain sizes, Figure 4.28 d). The inhomogeneity of the bulk microstructure suggests it had been subjected to local compressive and shear stresses. The work hardened layer was separated from the bulk by significantly large cracks which indicated that it was likely to be formed from severely deformed platelets which had been removed and back transferred, also observed by Prasad [54]. Fracture and extrusion of platelets during the back transfer process are thought to have formed filmy wear debris observed on the surface, Figure 4.28 a), this mechanism was also observed by Papadopoulos et al [101].

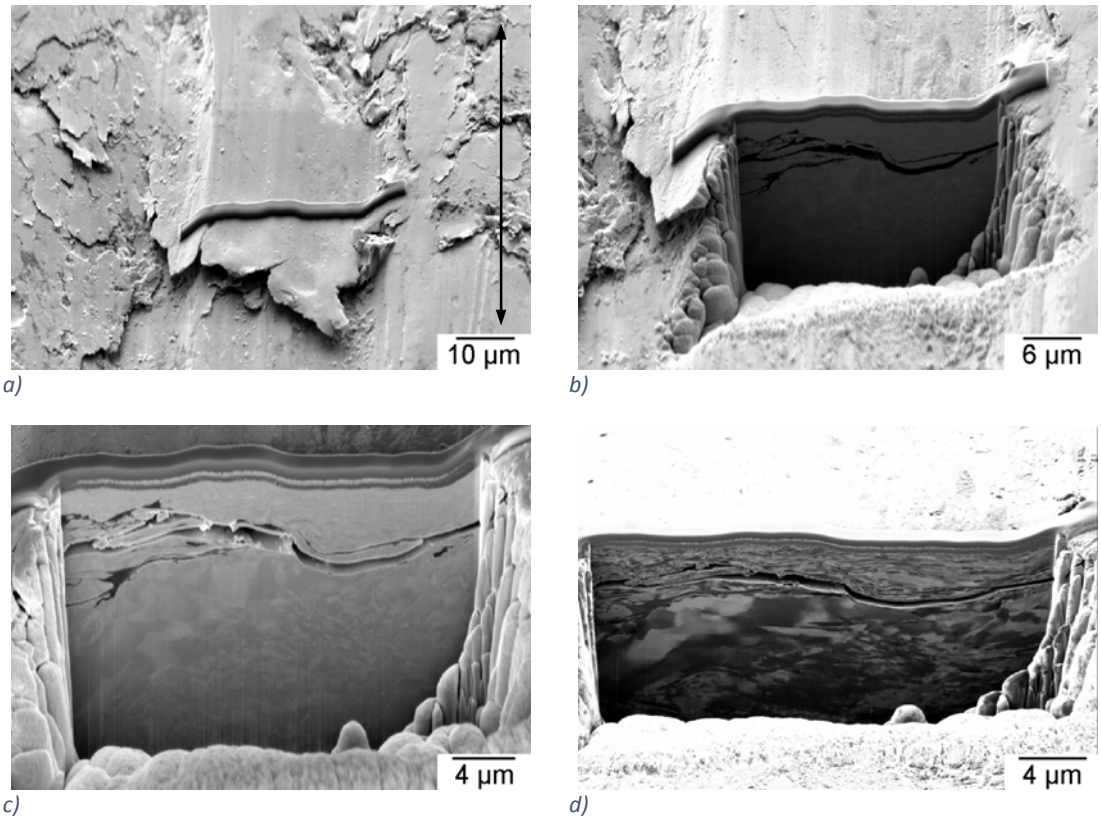

a) b) c) d)

Figure 4.28: Secondary electron (a & b) of the FIB area of interest and cross section from the severely scuffed surface subject to discrete load ramp from test DLS. c) Backscattered electron image and d) Secondary ion image of the cross section.

4.6 Scuffing mechanisms

4.6.1 Onset of mild scuffing

Increasing the normal load after the running-in period resulted in lubricant film collapse across the entire stroke for both continuous and discrete tests, evident from the decrease in contact potential between the pre-scuff and mild-scuff conditions, Figure 4.3. Once the contact was operating in the boundary regime, the further increase in load resulted in the onset of mild scuffing. The friction force remained constant after the normal load exceeded 620 N which indicated that the load was sufficient to plastically deform the peaks on the ground surface. The deformed material was then smeared into the valleys by the reciprocating action of the counter face, Figure 4.12 a). As a result the valleys were filled whilst the surrounding surface reduced in height, producing a polished appearance, Figure 4.18 d).

During mild scuffing, wear occurred evenly across the entire wear scar with smeared debris ejected at the interface between the wear track and the ground finish, Figure 4.18 b). The high speed data indicated an increased friction force at the reversal positions compared to the middle of the stroke. This was evidence of the onset of adhesion between the roller bearing and the cast iron at high loads that initiated mild scuffing, Figure 4.4 b). It confirmed that the

methodology of matching the maximum engine acceleration with the tribometer could produce scuffing at the reversal positions if the other variables of load, reciprocating frequency and lubricant feed rate were carefully controlled. Qu et al [151] also observed a rise in high speed friction force and similarly concluded from this that scuffing started at the reversal positions. The same behaviour was observed in the scuffing of piston ring and cylinder liners of fire engines as reported by Neale [96].

4.6.2 Transition to severe scuffing

During the mild scuffing process cracks began to develop in the surface of the cast iron along lamellar graphite-pearlite boundaries, Figure 4.19 a). In the progression to severe scuffing the cracks grew to form three dimensional networks which defined the size of the platelets that would adhere to the counterface. The polishing process increased the actual surface area of the contact and also reduced the lubricant retention volume, Table 4.4. Therefore as the load was increased the cast iron was subjected to greater adhesive shear forces. Once the adhesive force between the deformed pearlite and the roller bearing was greater than the interfacial strength between the graphite and pearlite, fracture occurred along the lamellar graphite crack networks, Figure 4.20. Han et al [107] noticed cracking along lamellar graphite at much larger magnification. Although a point contact was used in this experiment and resulted in much higher pressure facilitating deep subsurface cracking of the graphite, this result did show that cast iron was susceptible to failure along lamellar graphite-pearlite boundaries, a well known reason that flake cast iron is not very ductile [152].

When cracks occurred along the lamellar graphite-pearlite boundaries, severe scuffing initiated and the platelets transferred to the reciprocating roller bearing, precipitating scuffing across the entire stroke. Qu et al [151] also noticed that scuffing initiated at the reversal positions and spread throughout the stroke, the presented work is therefore consistent with the literature in terms of scuffing progression. Scuffing precipitation over the stroke can be seen in the high speed data which manifests as local increases in friction force, resulting in a highly disordered signal with an increased mean friction value, Figure 4.4 b) & c). The frictional energy dissipated also increased by 22 W, shown by the increase in area under the friction force curve, and indicates the additional work done fracturing, transferring and smearing the platelets from the surface.

It was interesting to note the sub-surface cracks beneath the severely scuffed surface were not always associated with flake graphite, but rather separated a highly work hardened surface layer to a less deformed bulk substrate. This suggests that once severe scuffing has initiated and material has been transferred to the counterface, it is this adhesively transferred material that causes catastrophic adhesive wear to propagate along the entire stroke.

4.6.3 The scuffed surface

The resulting surface was constructed from platelets which were quite brittle having undergone work hardening, confirmed by the FIB cross section Figure 4.28. Previously Han et al [107] had reported that scuffing of a very similar grey cast iron involved little or no plastic deformation of the surface, however with the benefit of high magnification SEM and FIB cross sectioning it was observed that plastic deformation of the pearlitic microstructure does occur even during mild scuffing to a depth of 2 µm.

Surface work hardened platelets were easily fractured at the graphite flake interface forming large craters, Figure 4.12 a). Ajayi et al [88] also found that work hardening of the surface caused by the repetitive micro plastic deformation was a prerequisite for scuffing. The craters were of the same order of magnitude as the length scale of the lamellar graphite structures found in the original cast iron microstructure, Figure 4.1 a). This suggests that the graphite-pearlite boundaries continued to be the site of fracture.

The scuffed cast iron wear scars and associated high speed friction data appeared consistent with other investigations in the literature [107,151]. This showed that high speed friction data analysis could be used successfully to detect the onset of scuffing. The lamellar graphite flakes appeared to be the material initiators for scuffing after analysing microstructural information from the FIB cross section and EDX analysis. This suggested that scuffing resistance was a system property that was heavily dependent on the microstructure once the lubricant had broken down.

4.7 Summary of flake cast iron scuffing mechanisms

Following an initial investigation into scuffing failure of flake graphite cast iron using an idealised line contact geometry to represent a ring liner contact from a fired diesel engine, it was possible to reproduce mild and serve scuffing of the cast iron surface using a bench top tribometer. The methodology was refined to facilitate conditions that would allow repeatable scuffing experiments to be performed .The duration of the severe scuffing tests had a deviation of 6 % and all occurred at the same load of 300 N.

Using surface analysis techniques, it was possible to identify the major scuffing mechanisms responsible for transition from mild to severe scuffing in flake graphite cast iron. Increasing energy input from increased contact pressure caused wear of surface asperities, reducing the roughness of the surface compared to the initial ground surface, Figure 4.29 and Figure 4.30. Material was plastically deformed into the valleys of the ground surface, resulting in both a thin (2 µm) strain induced work hardened surface layer but also crack nucleation at the graphitic flake pearlite interfaces, Figure 4.31.

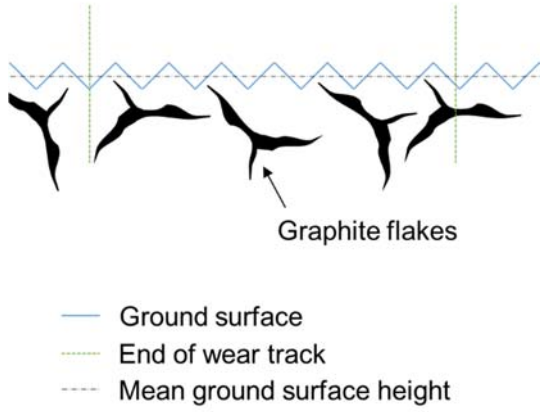

Figure 4.29: Ground flake cast iron suface schematic.

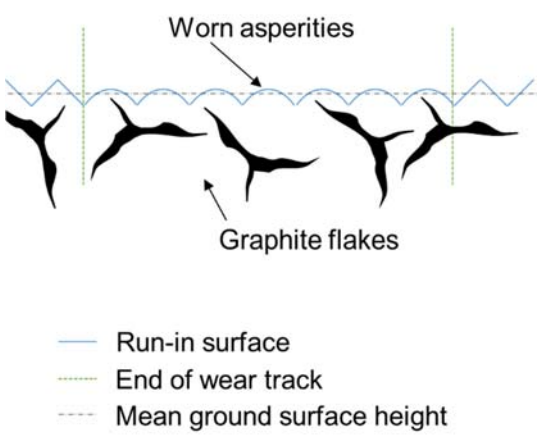

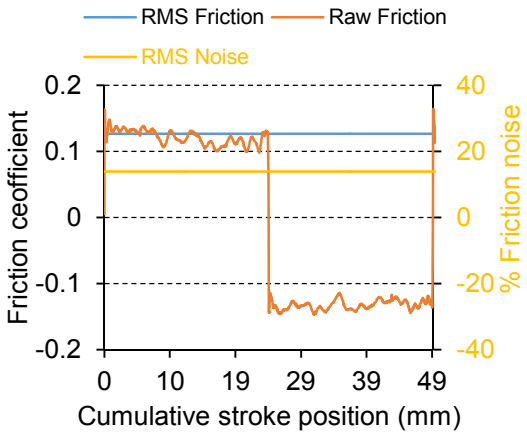

a) *b)*

Figure 4.30: Flake cast iron run-in surface schematic (a) and associated high speed friction data (b).

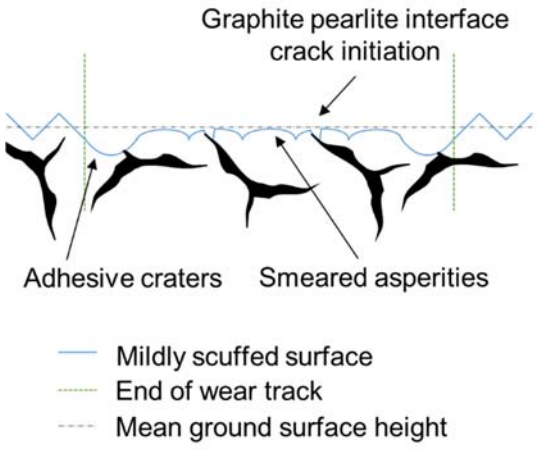

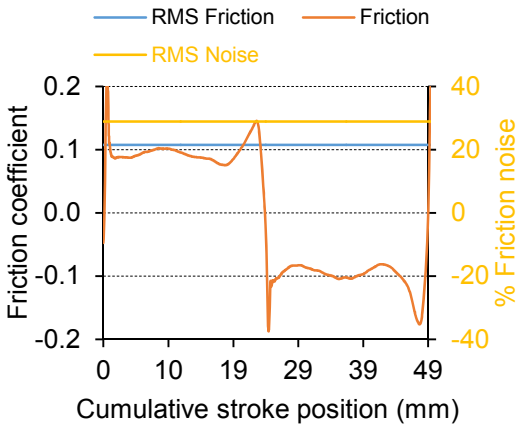

a) *b)*

Figure 4.31: Flake cast iron mildly scuffed surface schematic (a) and associated high speed friction data (b).

The mild scuffed surface had a reduced lubricant retention volume which limited the supply of lubricant into the contact. Therefore by increasing the contact pressure, the lubricant was degraded forming a tribofilm and consequently more energy was dissipated into the cast iron surface which caused the formation and oxidation of cast iron platelets, Figure 4.32. The oxide layer was too thin to be observed by the FIB cross section and unable to interrupt the progression to severe scuffing. The platelets detached from the surface at the graphite-pearlite interface and adhered to the countersurface. Material was transferred and back transferred between the cast iron and counterface until such a point that catastrophic adhesive wear resulted in a significant increase in the average friction coefficient and severe scuffing, Figure 4.33 and Figure 4.34.

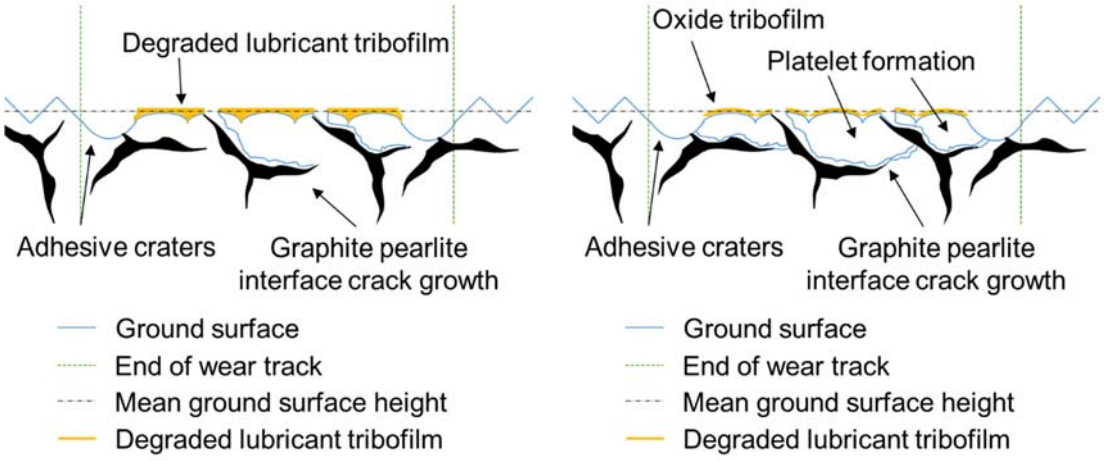

a) *b)*

Figure 4.32: Flake cast iron mild to severe scuffing transition schematics, a) lubircant degredation and b) oxide tribofilm formation.

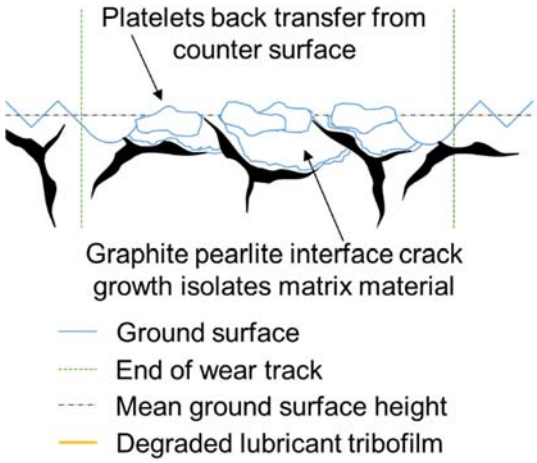

Figure 4.33: Flake cast iron platelet back transfer schematic.

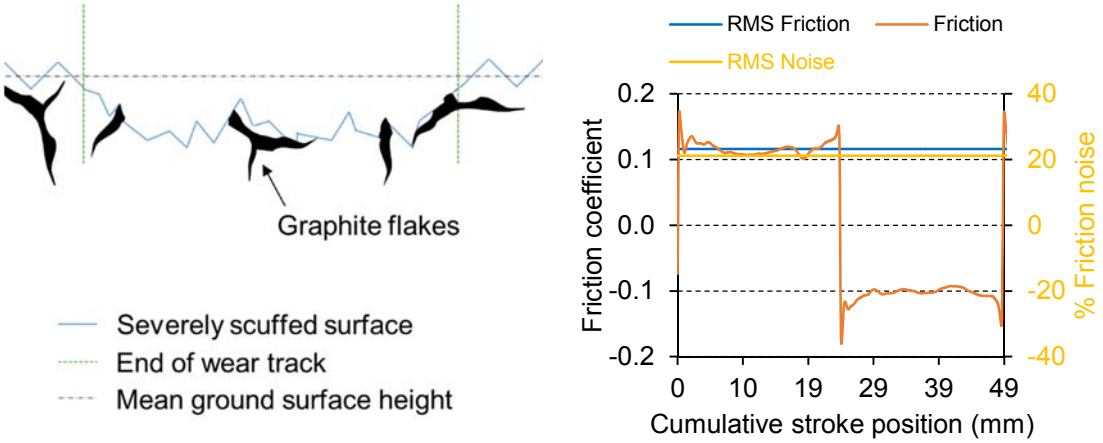

a) *b)*

Figure 4.34: Flake cast iron severely scuffed surface schematic (a) and associated high speed data (b).

Differentiation between the scuffing stages was achieved during the tests by analysing high speed friction data. It was demonstrated that by observing the high speed friction data, thresholds could be determined that were indicative of the transition between scuffing modes. Once these values had been tuned, it was possible to repeat the experiments to gain consistency in failure point. Local deviations in the microstructure were thought to be one source of potential error in the results, however overall the onset of mild scuffing was determined within 18 % maximum absolute deviation of the test time Table 4.3, thereby enabling investigation of the mild scuffed surface topography and sub-surface microstructure.

This section suggested that in the absence of a fully formulated lubricant, the scuffing mechanism was largely determined by the material response to localised plastic deformation, fracture at graphite-pearlite interfaces followed by adhesive transfer between the sliding surfaces leading to scuffing failure. The next section investigates the applicability of the technique to a different type of cast iron, nodular (spheroidal) graphite or ductile cast iron, which could exhibit a different failure mode due to the change in graphite morphology from flake to spheroids.

5 Scuffing mechanisms of nodular graphite cast iron

In order to assess the applicability of the two detection techniques to detect scuffing in other material systems, the discrete load methodology was broadened to investigate nodular cast iron. Nodular (also known as spheroidal or ductile cast iron) is a type of cast iron where the graphite morphology has been modified by the introduction of a nodularising agent (such as magnesium or cerium) such that the carbon atoms form spheres of graphite. As the name suggests, this results in a much more ductile type of cast iron as crack propagation along flake graphite boundaries is suppressed. This material was therefore chosen as a comparative material to flake graphite cast iron as the ferrous matrix would likely result in an adhesive scuffing (rather than, for example an abrasive failure) but potentially via a different mechanism than cracking at the flake interface. Nodular cylinder liners are also used in more demanding automotive applications and thus comparison of failure modes would be useful to interpret from an industrial application point of view. Analysis of the initial nodular microstructure and pre-test roughness was compared to the surface topography and subsurface microstructural evolution of two tests terminated during the transition to severe scuffing (NS). Further tests terminated during mild scuffing (NMS) as well as during intermediate scuffing (NIS) which occurred between mild and severe scuffing was then discussed with a view to explaining the mechanism of scuffing progression.

5.1 Microstructure and hardness

A polished cross section from a EN-GJS 400-15 nodular cast iron plate, obtained from West Yorkshire Steel Co, UK, is shown in Figure 5.1 and exhibited a homogenous distribution of graphite colonies spaced throughout a ferrous matrix, conforming to BS EN 1563:2011 which states that the matrix should be predominantly ferrite with a maximum pearlite content of 5 %. This was confirmed by the higher magnification SEM image in Figure 5.1 b), which showed the absence of pearlite grains, in contrast to the flake graphite cast iron. The contrast between ferritic grains with different crystallographic orientations was caused by ion channelling, previously discussed in Section 3.4.4. The form of the graphite was predominantly equiaxed and whilst not always nodular, conformed to the group V-VI designation for nodularity [59]. The size of the graphite spheroids were analysed by counting particles with a size greater than 10 μm^2 using ImageJ software [153]. Particles that crossed the boundary of the image were excluded. 10 % of the image was covered by 32 graphite spheroids with a mean particle area of 303 +/- 287 μm^2, corresponding to size range 7 (EN ISO 945-1:2008). The nominal composition supplied by the manufacturer is shown in Table 5.1.

Table 5.1: Nominal composition (wt%) of EN-GJS-400-15 nodular cast iron plate [154].

Cast iron type	C (wt%)	Mn (wt%)	Si (wt%)	P (wt%)	S (wt%)	Mg (wt%)	Fe
EN-GJS 400-15	3.40-3.85	0.10-0.30	2.3-3.10	0.10	0.02	0.07	balance

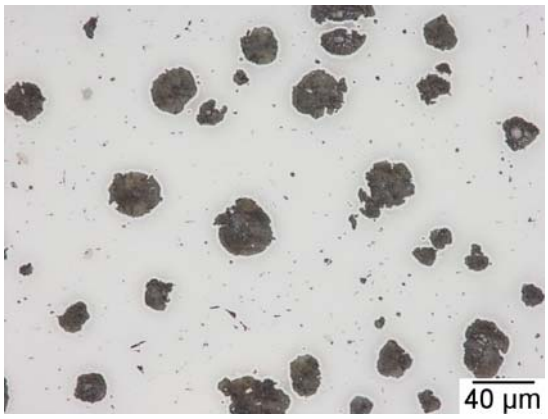

a)

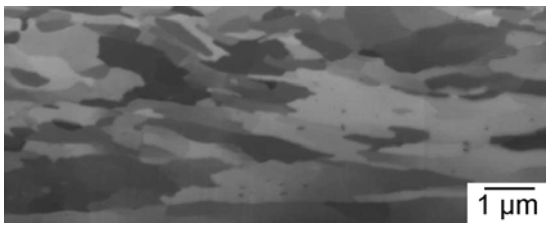

b)

Figure 5.1: Optical microscope image of transversely sectioned nodular graphite cast iron plates and SEM image b) of ferritic matrix.

The ground nodular cast iron plate exhibited a Vickers hardness of 172 ± 3 H_V, conforming to the upper range specified in BS EN 1563:2011 (140-190 H_V). This was slightly lower than the Grade 250 flake graphite cast iron (209 ± 9 H_V) and was attributed to the absence of pearlite in a predominantly ferritic matrix, Figure 5.1 b). The hardness of the 52100 roller bearing counterfaces was as for the flake graphite sliding tests, at a value of 845 ± 4 H_V.

The nodular cast iron samples were surface ground using the same process as the flake graphite cast iron samples. This resulted in an R_a = 0.343 µm which was comparable with flake cast iron which had an R_a = 0.490 µm. The ground nodular cast iron surface also had a negative skew as the R_{vk} = 0.592 was almost twice the R_{pk} = 0.326 (average), Table 5.2. The roughness of the roller bearing samples was the same as for the flak cast iron tests and measured in the direction of reciprocation, had an R_a = 0.041 ± 0.009 µm.

Table 5.2: Specimen properties prior to test: average surface roughness (R_a), kurtosis (R_k), reduced peak height (R_{pk}) and reduced valley depth (R_{vk}) from a Talysurf contact profilometer (standard deviation error, σ).

Sample	Surface	R_a	σ	R_k	σ	R_{pk}	σ	R_{vk}	σ
Roller bearing	-	0.041	0.009	0.088	0.012	0.066	0.054	0.139	0.074
Nodular CI NS1	Ground	0.346	0.013	1.149	0.064	0.350	0.043	0.503	0.022
Nodular CI NS2	Ground	0.340	0.030	0.940	0.059	0.302	0.036	0.681	0.062

5.2 Severe scuffing tests

5.2.1 Friction behaviour

Discrete load ramp tests were conducted using the same conditions developed for the flake graphite cast iron: 15 Hz reciprocating frequency over a stroke length of 25 mm, an initial load to 100 N followed by a temperature ramp to 180 ˚C as a running in period of 1200 s. Following

this a discrete load profile in 100 N increments at 5 minute intervals was initiated until severe scuffing occurred indicated by a rapid rise in average coefficient of friction above 0.2. Friction coefficient, contact potential and load data were plotted against time for two tests (NS1 and NS2) terminated during the transition to severe scuffing, Figure 5.2 and Figure 5.3.

For severe test NS1, at a running-in load of 100 N, the friction coefficient averaged around 0.10, although there were fluctuations during the temperature ramp, with the increase to 180 °C at a constant load of 100 N resulting in the average friction coefficient increasing to a test peak value (apart from the severe scuff). Apart from an increase during the 300 N step, the average friction coefficient trend was to gradually decrease to 0.08 before it increased rapidly to more than 0.18 during severe scuffing. The repeat severe test NS2, Figure 5.3, exhibited similar behaviour except for the second half of the running-in period where the friction coefficient decreased for a period of 300 s before returning to the same trend as the initial test, Figure 5.2. Both tests severely scuffed at a load of 700 N, within 70 s of each other, a sliding distance of 46.5 m, 2 % of the total siding distance of NS2.

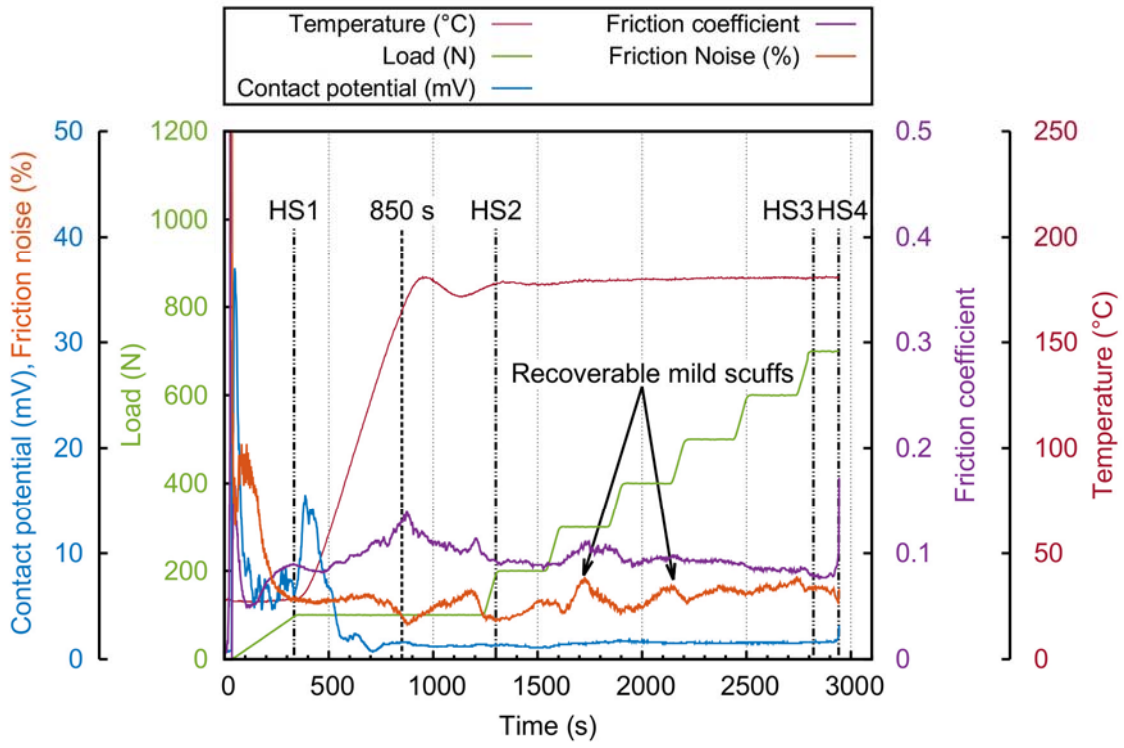

Figure 5.2: Average friction, normal load, temperature and contact potential plotted against time NS1. HS1: running in, HS2: mild scuffing, HS3: intermediate scuffing, HS4: severe scuffing.

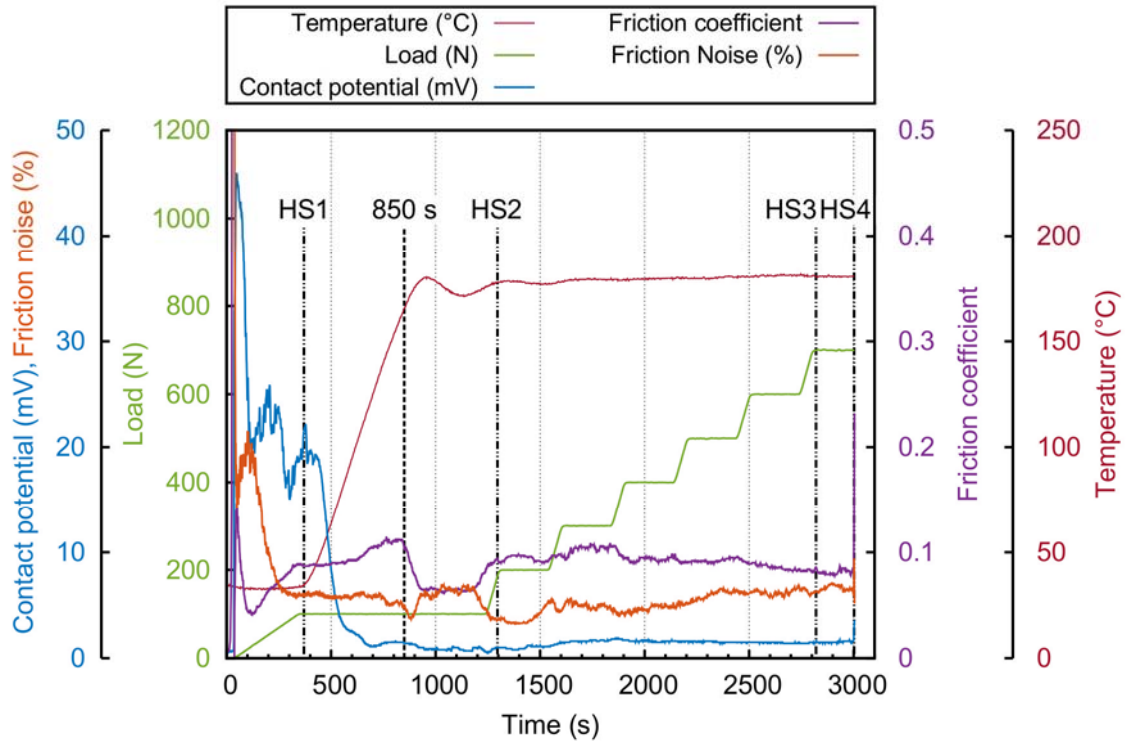

Figure 5.3: Average friction, normal load, temperature and contact potential plotted against time NS2. HS1: running in, HS2: mild scuffing, HS3: intermediate scuffing, HS4: severe scuffing.

5.2.2 Running in

At the start of the tests the contact potential rose as asperities were quickly worn away producing a lubricated conformal contact. As the temperature increased to 100 °C the lubricant viscosity decreased and the load carrying capacity of the film decreased. This was observed as a decrease in contact potential as more asperities came into contact and was also reflected by an increase in the average friction coefficient, Figure 5.2.

The maximum friction coefficient occurred at 850 s for both tests, shortly before the contact reached the operating temperature of 180 °C, two different behaviours were subsequently observed, Figure 5.2 and Figure 5.3. In NS1 the friction coefficient slowly decreased until the 200 N load step (Figure 5.2), however in NS2 it dropped rapidly to a local minimum of 0.07 before increasing up to a similar value to NS1 before the 200 N load step (Figure 5.3). It is thought that a temporary lubricious graphite tribofilm may have been formed on the surface of the cast iron in NS2, which did not form during NS1. The difference may be due to the variations in the relative distribution of graphite in the cast iron samples which caused incomplete formation, as observed by Montgomery [105].

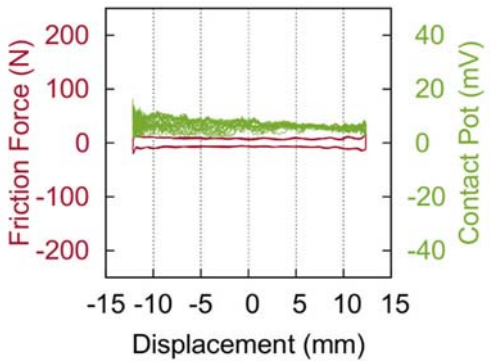

Figure 5.4: (HS1) Friction force and contact potential data at start of the running in period NS1.

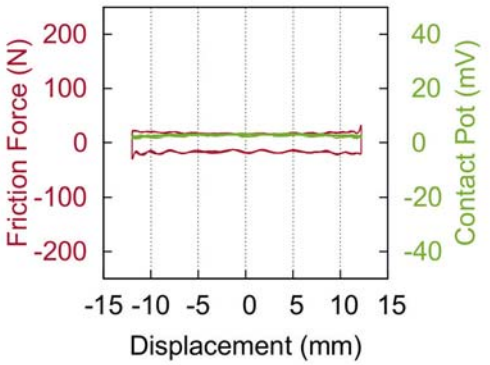

Figure 5.5: (HS2) Friction force and contact potential data during mild scuffing NS1.

High speed friction and contact potential data recorded at the beginning of the 100 N running in period (HS1) for the first test (NS1) was plotted against displacement for 15 sequential cycles, Figure 5.4. The instantaneous friction force had the general form of a square wave and little cyclic variation suggesting that the contact was steadily operating in the boundary lubrication regime even before the onset of the temperature ramp. This would ensure even running in across the entire stroke length rather than an inhomogeneous wear pattern that could be caused by velocity dependent film formation. The contact potential fluctuated between each cycle due to the running in process which gradually wore surface asperities to create a conformal contact. It also varied with stroke position and was initially greater magnitude at one end. This was thought to be due to the position of the fine bore needle that injected lubricant to one end of the stroke, representative of oil supplied from the sump/crankcase to the ring pack from the base of the cylinder bore in a combustion engine.

Interestingly, the same mild scuffing high speed friction criteria that had been developed for the flake graphite tests (140 % accelerating, 110 % decelerating) was achieved during the 200 N load step (HS2), as is plotted in Figure 5.5. However unlike the flake cast iron which severely scuffed shortly after the onset of mild scuffing the nodular cast iron required a contact load above 600 N to severely scuff.

The friction noise sharply increased during the 300N load step accompanied by a more gradual increase in friction coefficient, Figure 5.2. This probably indicated a recoverable mild scuffing event which occurred locally as subsequently the friction noise and coefficient decreased. A similar event occurred in the transition between the 400 N and 500 N load step however there was only a slight change in friction coefficient. The increase in friction noise and decrease in friction coefficient that followed indicated the development of a characteristic friction behaviour specific to the nodular cast iron.

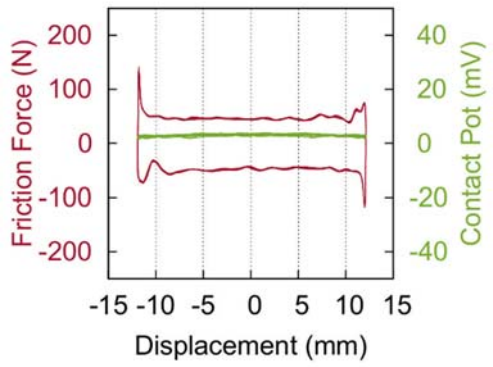

Figure 5.6: (HS3) Friction force and contact potential data during mild scuffing at the start of the failure load step NS1.

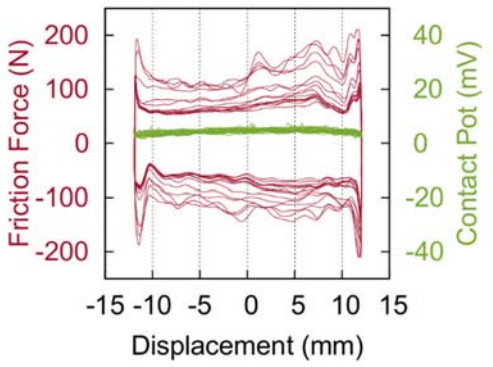

Figure 5.7: (HS4) Friction force and contact potential data during severe scuffing failure NS1.

During the subsequent load steps, this behaviour was observed as a progressive change in the instantaneous high speed friction data, Figure 5.6. The friction force in the decelerating direction (top left/bottom right corner of the graph) increased, exceeding the magnitude in the accelerating direction (top right/bottom left corner of the graph), which was indicated by the gradually increasing friction noise. The contact potential remained close to zero across the entire stroke confirming the increase in friction noise was due to asperity contact. When the magnitude in the decelerating direction exceeded 200 % of the RMS, it defined a change in the wear regime which will be called “intermediate” scuffing. During this period mild scuffing progressed to severe scuffing by accumulated adhesive and abrasive wear.

During severe scuffing, which occurred over the period of 1 second captured by the high speed data in Figure 5.7, the friction force increased during each stroke across the entirety of the stroke length. At the onset of severe scuffing, the increase in friction force occurred locally on the accelerating side of the stroke reversal position which increased to match the decelerating side. The dissipated friction power increased from 13 W during mild scuffing to 66 W during severe scuffing. During the last cycles the friction force signal became very disordered, confirmed by the rapid increase in friction noise, in particular at stroke position 7 mm the friction force increased 100 % in the accelerating direction during 1 s of sliding. The contact potential remained close to zero in both directions, with small variations.

Similar characteristic behaviour of the high speed friction and contact potential data was also observed throughout the severe scuff NS2 test, Appendix nodular Figure 11.1.

5.2.3 Repeat severe tests

Following the two initial severe scuffing tests NS1 and NS2, which scuffed at 700 N, two more severe scuffing tests were carried out NS3 and NS4, Figure 5.8 and Figure 5.9. The friction noise fluctuations that occurred during both NS1 and NS2 indicated that the contact had not reached a steady state condition between each load step. It was an important requirement of the

methodology that the contact did reach steady state to ensure that any load step specific run-in effects that might influence scuffing had occurred during the respective load step. Consequently the load step duration was increased from 300 s to 600 s. If the scuffing failure mechanism was only dependent on the topography evolution rather than the energy input, then severe scuffing would have occurred at a lower contact pressures now that the duration of the loads steps had increase. However this was not the case and severe scuffing was observed at a load of 700 N for NS3 and 600 N for NS4, Table 5.4, confirming that scuffing was dependent on the energy dissipated in the contact, Figure 5.8 and Figure 5.9.

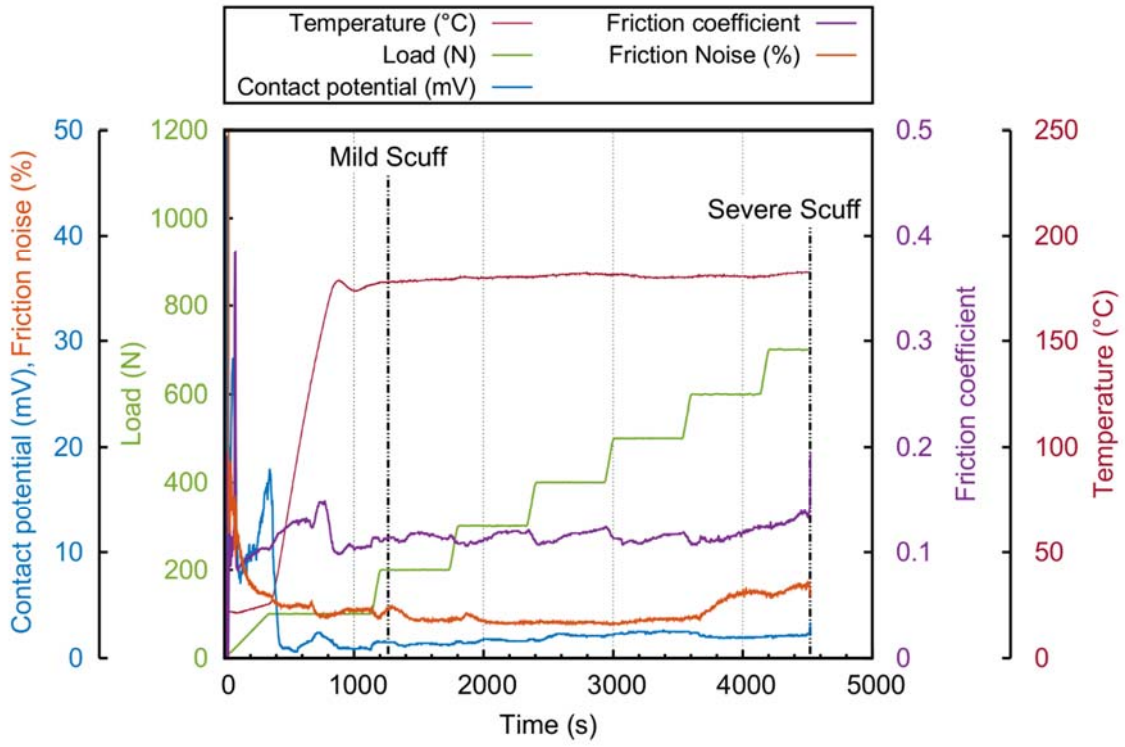

Figure 5.8: Average friction, normal load, temperature and contact potential plotted against time NS3.

NS4 failed at 600 N without a period of increased friction noise which was observed to occur at the same load step for NS3, Table 5.3. This period was also observed for NS1 and NS2 however the trend was less distinct as the friction noise increased gradually throughout the entire duration of these tests to a maximum of 5 %. The increase in friction noise occurred without a corresponding increase in contact potential indicating local variation in friction caused by asperity contact caused by intermediate scuffing. The friction coefficient also increased during this period as scuffing damage propagated from the reversal position across the stroke.

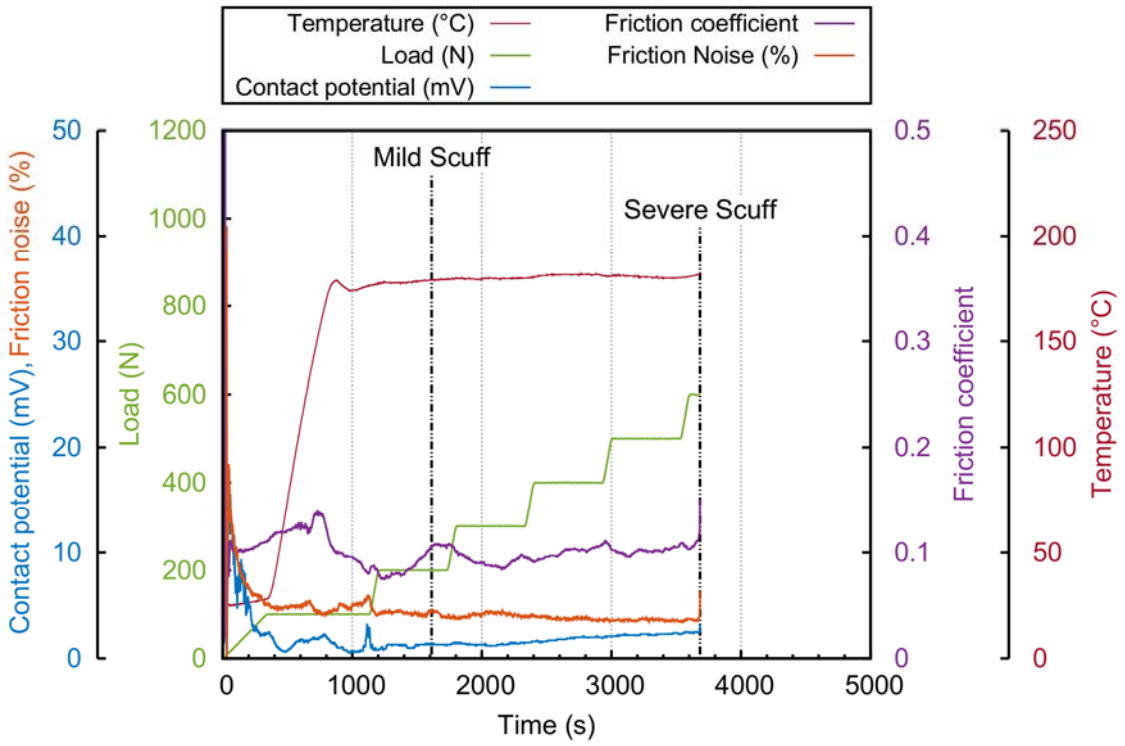

Figure 5.9: Average friction, normal load, temperature and contact potential plotted against time NS4.

Mild scuffing was detected during the 200 N load step for both NS3 and NS4 as well as NS1 and NS2, Table 5.3, Figure 5.8 and Figure 5.9. The software identification of mild scuffing occurred with a simultaneous friction noise local maximum which was similarly observed for the flake cast iron. The high speed friction for severe test NS3 during mild scuffing was similar to mild scuffing tests NMS1 & NMS2, Figure 5.10, however the friction force fluctuated across the central stroke region for severe scuffing test NS4, Appendix nodular Figure 11.2. The fluctuations were thought to be due to hasher contact conditions across the stroke caused by the increased contact pressure arising from misalignment of the counter face as shown in Figure 5.37 b), where grinding marks are still present despite severe scuffing occurring across the rest of the wear scar.

The misalignment was likely to have occurred during the tightening of the clamp retaining the counter face. It is possible that in the latter stages of tightening the torque applied to one of the screws may have been sufficient to cause the clamp to rotate against the other screw. The counter face would have been gripped in the clamp at this stage of tightening and therefore also rotated, resulting in the line contact becoming edge loaded. The increased contact pressure resulting from the misalignment offers an explanation for the reduced failure load (600 N) for this test, Table 5.3.

The onset of severe scuffing in test NS3 was captured with high speed data in Figure 5.11. The magnitude and disorder of the friction force increased with each successive stroke. The friction noise only increased during severe scuffing of NS4 indicating a more aggressive failure, this is reflected in the shape of the high speed friction force in Appendix nodular Figure 11.3. The

difference in behaviour is also thought to be due to the misalignment of the contact Figure 5.37 b).

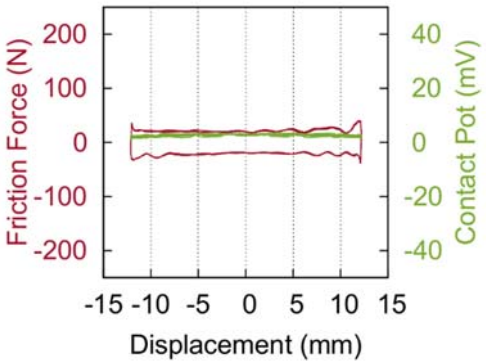

Figure 5.10: Friction force and contact potential data during mild scuffing NS3.

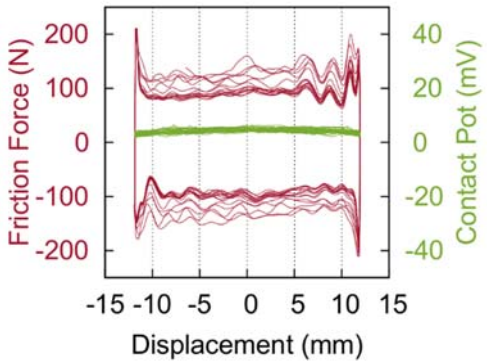

Figure 5.11: Friction force and contact potential data during severe scuffing failure NS3.

As shown in Table 5.3, the repeatability of severe tests NS1 and NS2 was within a few seconds of each other as was the identification of mild scuffing, corresponding to very small maximum absolute deviations of 1 % or less. This demonstrated the potential of the high speed friction detection technique to accurately determine transitions in scuffing regimes, however as shown in Table 5.3 and Table 5.4 such repeatability was not always the case, being up to 13 % of the maximum absolute deviation.

Table 5.3: Comparison of test duration and scuffing load for severe nodular cast iron tests NS1 and NS2 (300 s load step).

Test Name	Mild		Severe scuffing	
	Test time (s)	Load (N)	Test time (s)	Load (N)
NS1	1300	200	2930	700
NS2	1290	200	3000	700
Max absolute Deviation	5	0	35	0
Max absolute Deviation (%)	0.4	0	1	0

Table 5.4: Comparison of test duration and scuffing load for severe nodular cast iron tests NS3 and NS4 (600 s load step).

Test Name	Mild		Severe scuffing	
	Test time (s)	Load (N)	Test time (s)	Load (N)
NS3	1230	200	4550	700
NS4	1610	200	3680	600
Max absolute Deviation	190	0	435	50
Max absolute Deviation (%)	13.4	0	11	8

5.3 Intermediate scuffing tests

5.3.1 Friction behaviour

The evolution from mild to severe scuffing occurred as a distinct progression for flake graphite cast iron, however an intermediate stage was observed for nodular cast iron. This was because the mild scuffing criteria was met early in the test, during the first load ramp, yet there was still a distinct change later on in the test, prior to severe scuffing. In order to investigate this behaviour further, a test was conducted (NIS1) that was interrupted during the onset of this transition, defined as intermediate scuffing. As shown in Figure 5.12, the intermediate stage occurred halfway through the 500 N load step, which was 100 N lower than in severe scuffing test NS3, and was indicated by a rapid increase in friction noise, from 3 to 5 %, although no change in average friction coefficient was observed.

The magnitude of the local increase in friction force which occurred during intermediate scuffing was thought to be a measure of surface wear, Figure 5.13. A magnitude in excess of 200 % of the RMS friction value in the decelerating direction observed to occur with the increase in friction noise during the transition to intermediate scuffing. During intermediate scuffing there was little evidence of high friction force due to adhesive wear during the accelerating phase of the stroke reversal. The contact potential was close to zero across the whole stroke indicating continuous asperity contact.

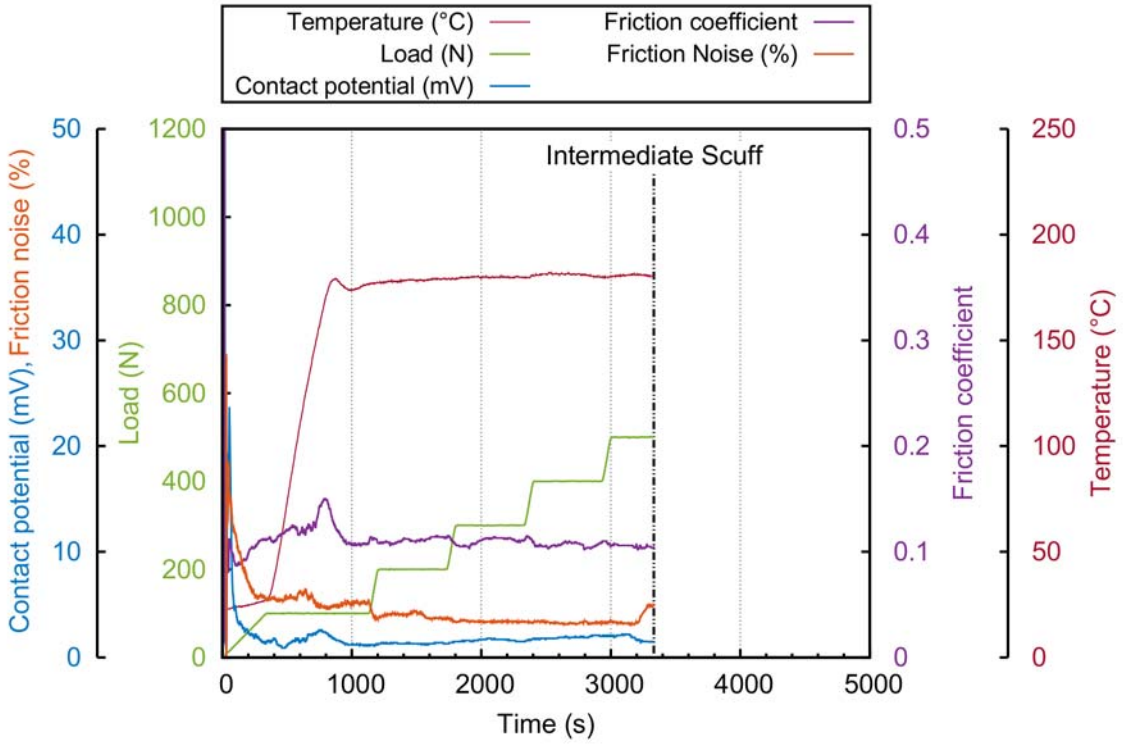

Figure 5.12: Average friction, normal load, temperature and contact potential plotted against time NIS1.

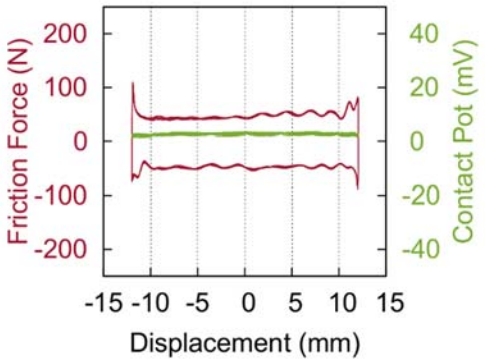

Figure 5.13: Friction force and contact potential data during intermediate scuffing NIS1.

5.4 Mild scuffing tests

5.4.1 Friction behaviour

Using high speed data (HSD), the developed scuffing detection software was used to terminate the tests during mild scuffing. The termination threshold limits were keep the same as the flake cast iron: 140 % increase RMS friction force signal in the accelerating direction and 110 % increase in the decelerating direction.

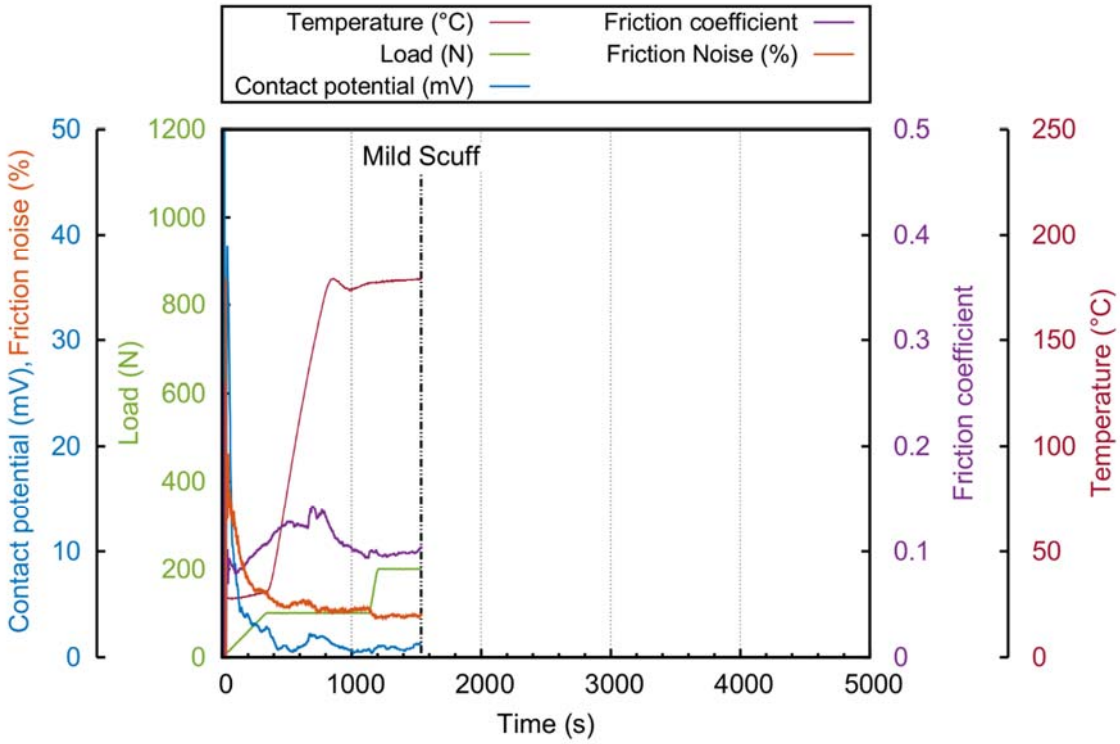

Figure 5.14: Average friction, normal load, temperature and contact potential plotted against time NMS1.

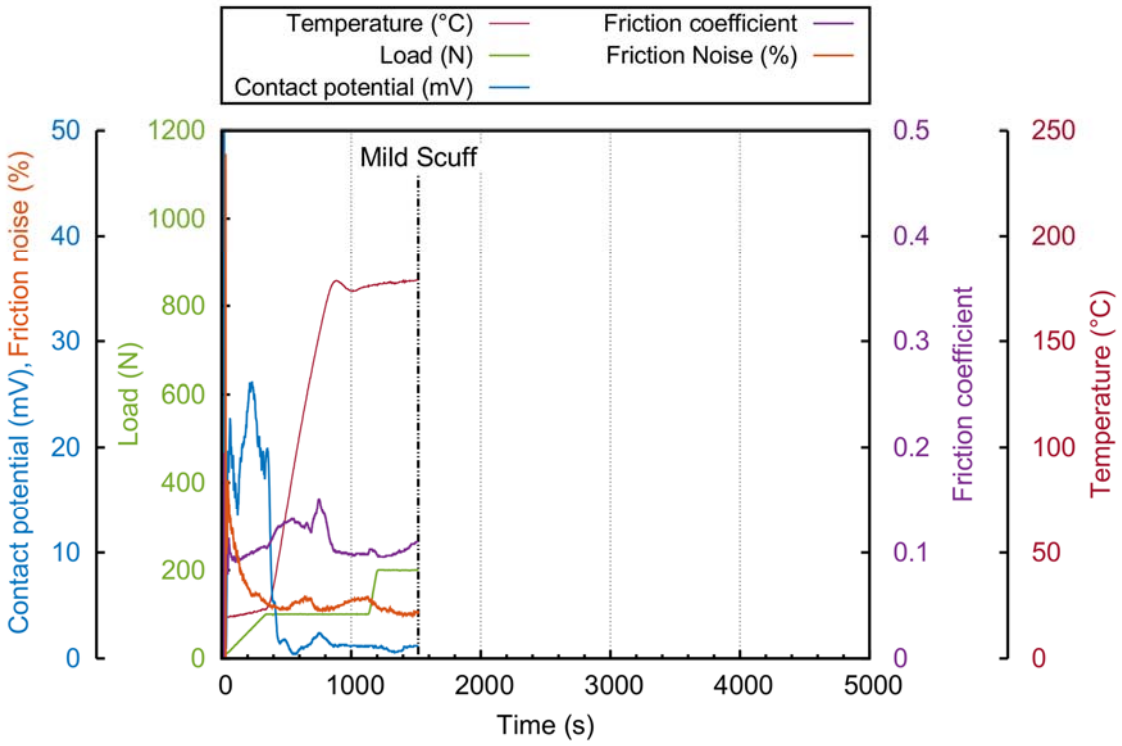

Figure 5.15: Average friction, normal load, temperature and contact potential plotted against time NMS2.

The criteria were consistently achieved during the 200N load step for both tests, with NMS2 terminated within 20 s, 1 % sliding distance of NMS1, Table 5.5. The behaviour of the contact potential, friction coefficient and friction noise were similar for both tests, Figure 5.14 and Figure 5.15. The friction coefficient increased from the start for the tests as the normal load was increased to 100 N. It continued to increase during the temperature ramp reaching a maximum at 100 °C. This was caused by an increasing number of asperity interactions as the lubricant film thickness was reduced first by increasing the contact load and then by decreasing the lubricant viscosity by a temperature increase. The friction coefficient then decreased to approximately 0.1 for the remainder of the running-in period, once the asperities had worn sufficiently that the real area of contact could support the contact load. The average friction coefficient slightly increased before mild scuffing occurred however no increase in friction noise was observed.

Table 5.5: Comparison of test duration and scuffing load for mild and severe nodular cast iron.

Test Name	Mild		Severe scuffing	
	Test time (s)	Load (N)	Test time (s)	Load (N)
NS3	1230	200	4550	700
NS4	1610	200	3680	600
NMS1	1509	200		
NMS2	1519	200		
Max absolute Deviation	237	0	435	50
Max absolute Deviation (%)	16	0	11	8

Comparing the time at which the progression to mild scuffing occurred for the test shown in Table 5.5, it was observed that this occurred within 17 % repeatability for all tests, comparable to the flake graphite repeatability summarised in Table 4.3.

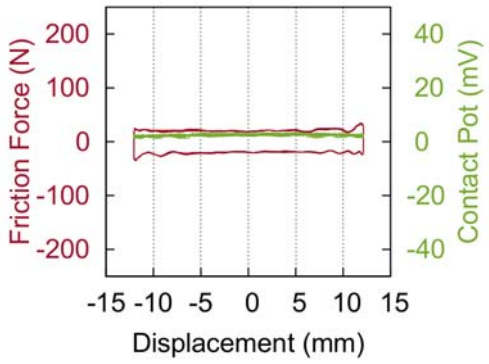

Figure 5.16: Friction force and contact potential data during mild scuffing NMS1.

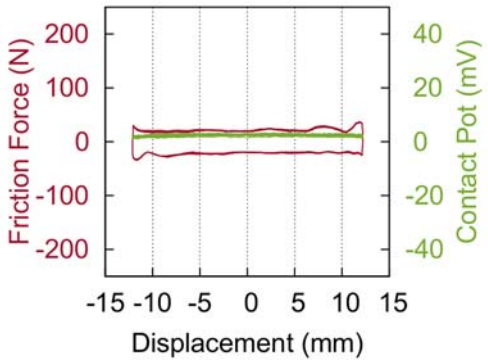

Figure 5.17: Friction force and contact potential data during mild scuffing NMS2.

The high speed data just prior to the end of the tests, Figure 5.16 and Figure 5.17, showed that the contact potential was close to zero across the stroke which indicated the absence of an insulating film. The friction force was constant across the central 12 mm of the stroke but disordered in the 6.5 mm before each end. The maximum friction force occurred at the stroke reversal positions in the accelerating directions, again suggesting the onset of adhesive wear. There was only a slight increase in friction in the decelerating direction as specified in the mild scuffing criteria. Both high speed data graphs exhibited very similar trends.

5.5 Surface analysis

5.5.1 Mild scuff surface topography

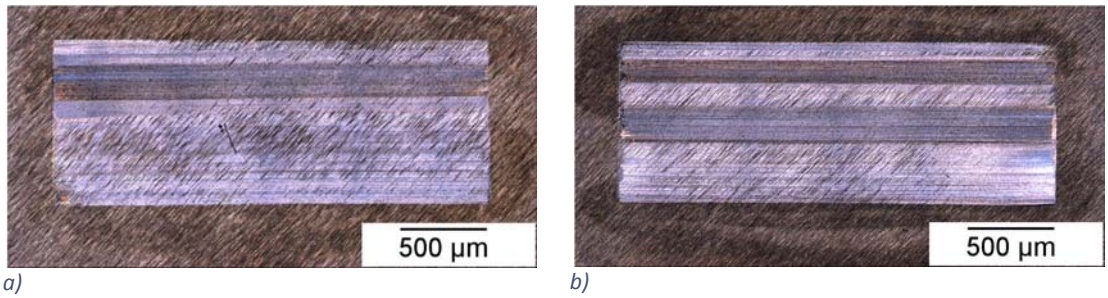

a) *b)*

Figure 5.18 Optical images of mildly scuffed nodular cast iron surfaces (a) NMS1 and (b) NMS2.

The mildly scuffed cast iron surfaces from NMS1 and NMS2 are shown in Figure 5.18. The wear scars contain areas which were worn by different amounts. Three categories of increasing wear severity were identified. The first was defined by the presence of grinding marks; here surface asperities had been plastically deformed into the grinding marks on the surface, however only the first 1 µm was deformed, Figure 5.19. The resulting surface had an increased bearing area and still contained recesses suitable for retaining lubricant.

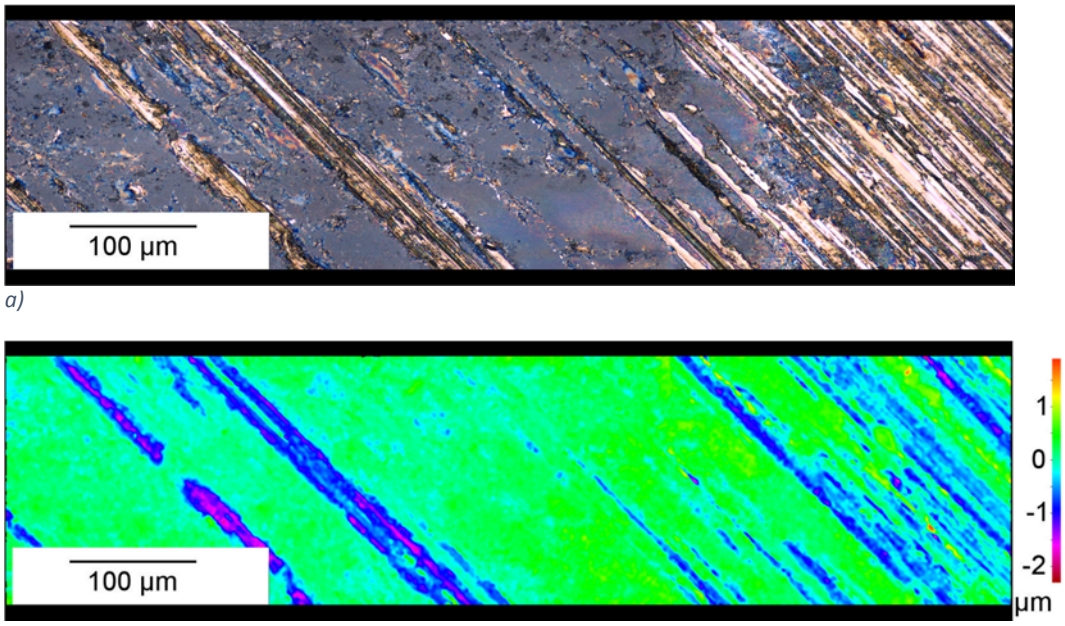

Figure 5.19: Optical image of the mildly scuffed nodular cast iron from test NMS2, showing first category plastic deformation of the surface a) and 3D colour map b).

The second category included surfaces which had worn a further 1 µm below the asperities peaks on the original surface. The resulting 2 µm of wear almost completely removed the grinding marks and produced a smooth surface. The first two categories described the cumulative wear process which changed the surface topography to facilitate lubricant starvation at the reversal positions encouraging the onset of adhesive wear. The continuous nature of this transition is captured in Figure 5.20, which shows the interface between the first (bottom) and second (top) category regions.

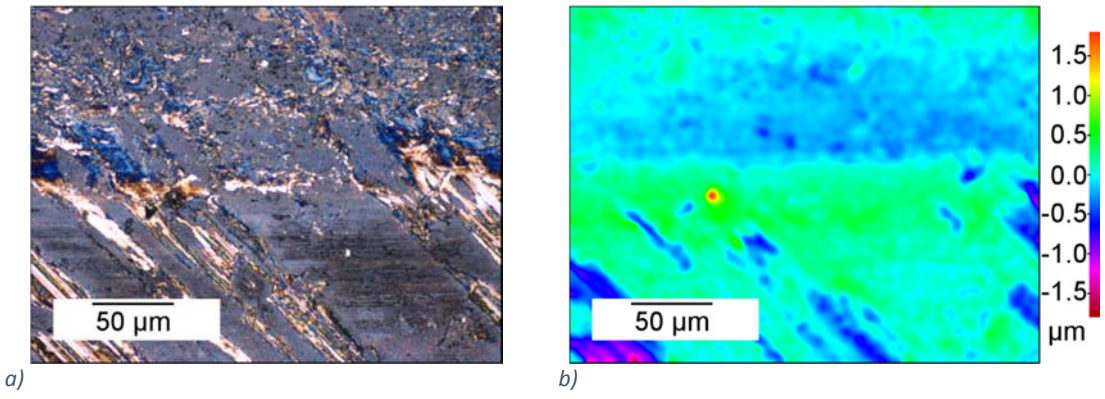

Figure 5.20: Optical image of the mildly scuffed nodular cast iron from test NMS2, showing the transition between first and second category wear a) and 3D colour map b).

The third category was mild scuffing which was defined by the onset of adhesive wear. Adhesive wear craters 3-4 µm in depth could be seen at the stroke reversal positions in Figure 5.21. Debris were also observed in the wear track, Figure 5.20. Plastic deformation of material at the edge of the wear scar was observed and provided evidence that material had transferred to the counterface. This was confirmed in Figure 5.22 which showed the cast iron transfer film which

developed on the surface of the 52100 roller element and an adhesive wear particle which had transferred to the counter face during this process, which was similarly observed by Saeidi et al for flake cast iron [108].

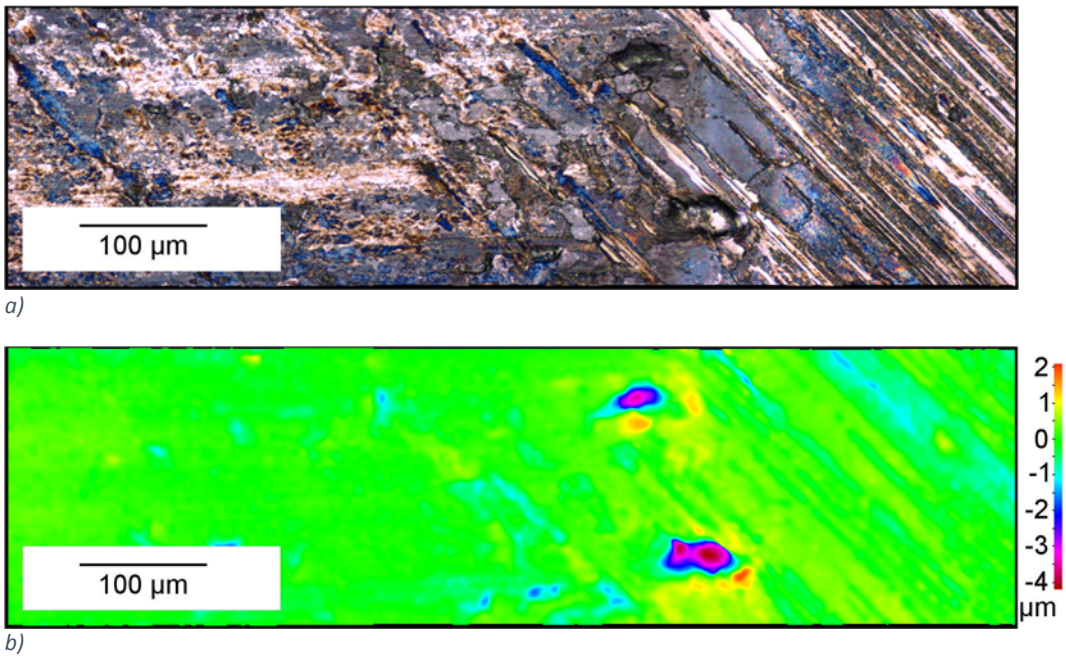

Figure 5.21: Optical image of the mildly scuffed nodular cast iron from test NMS2, surface showing adhesive wear craters and plastically deformed ferrite a) and 3D wear map b).

These observations agree with the assumption that the friction force increase at the stroke reversal position in the accelerating direction was caused by adhesive wear events concurrent with the flake graphite failure mechanism. They also support the assumption that the rise in friction force in the decelerating direction was due to the plastic deformation of wear debris between the counterface and the edge of the wear scar.

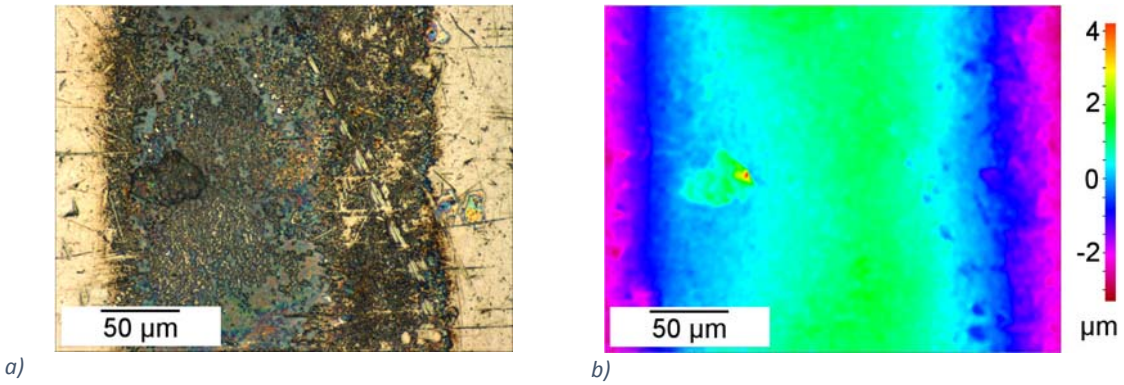

Figure 5.22: Optical image of the 52100 roller bearing element from test NMS1, showing a cast iron transfer film and an adhesive wear particle a) and 3D colour map b).

5.5.1.1 Scanning electron microscopy

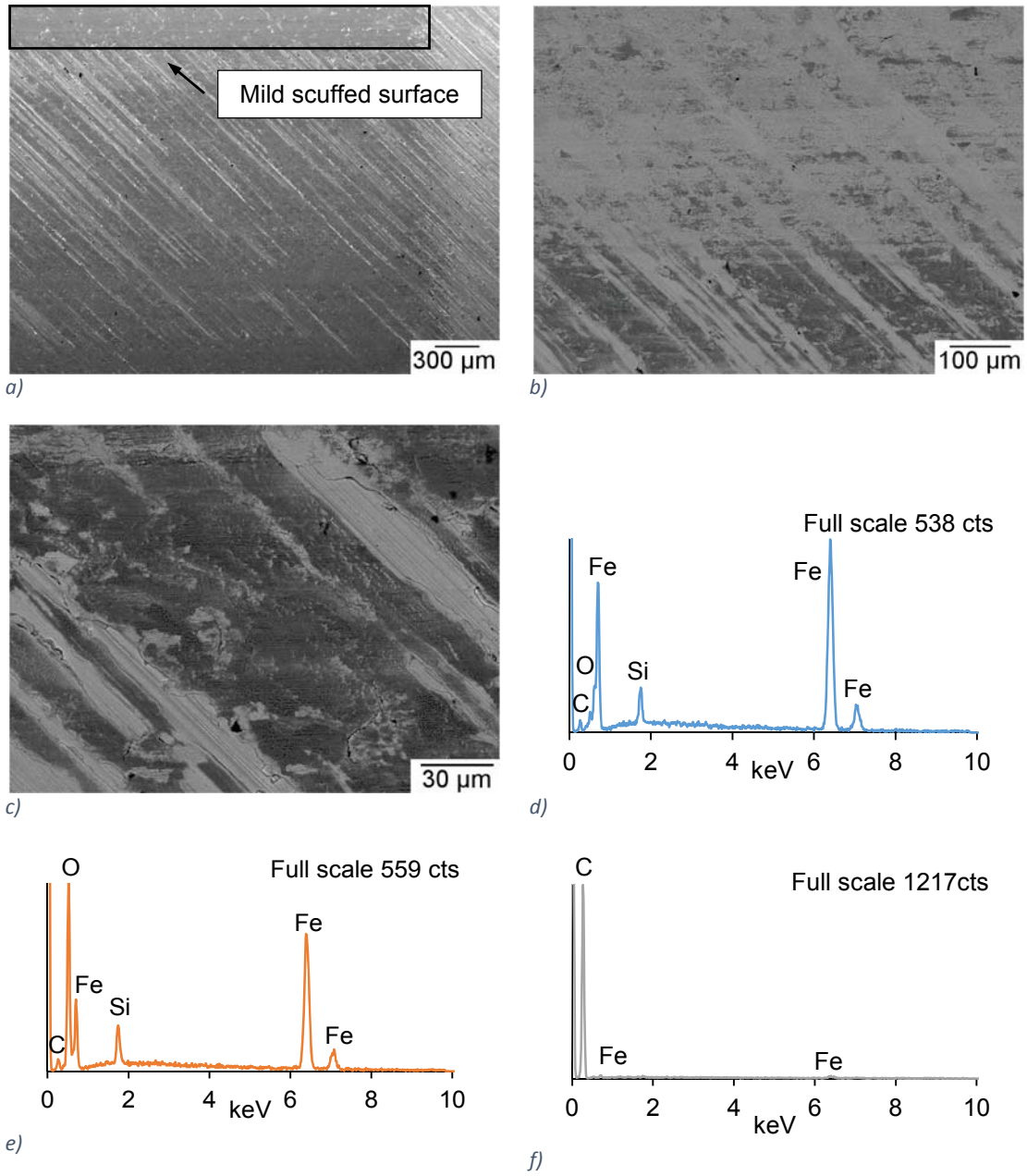

Figure 5.23. Secondary electron (a) and backscattered (b & c) of the wear scar from mild nodular test NMS2. EDX spectra from (c) of light grey grinding mark (d), the dark grey surface film (e) and the lower middle black particle (f).

Figure 5.23 a) is a secondary electron imageof one stroke reversal position from test NMS2 and shows the transition to the mild scuffed surface (top) where the grinding marks are removed, similar to the flake graphite transition in Figure 4.24. The boundary between the mild scuffed surface and the region that still exhibited grinding marks is shown in a backscattered image in Figure 5.23 b). A surface tribofilm of different composition to cast iron was observed as a darker contrast, again similar to the mildly scuffed flake cast iron surface. However higher magnification images and EDX spectra in c) - f) suggested that the surface film was rich in oxygen rather than carbon. This was in contrast to the mildly scuffed flake graphite surface and whilst a tribofilm formed from the lubricant degradation may have previously been present, it appeared that

significantly more surface oxidation arising from asperity flash temperatures had occurred on the nodular cast iron surface. This may be due to the ferritic composition of the nodular cast iron, which may facilitate enhanced surface oxidation compared a pearlitic structure present in flake cast iron. This corroborates the work by several authors [75,108] who cite the formation of an oxide tribofilm as a precursor to the onset of scuffing.

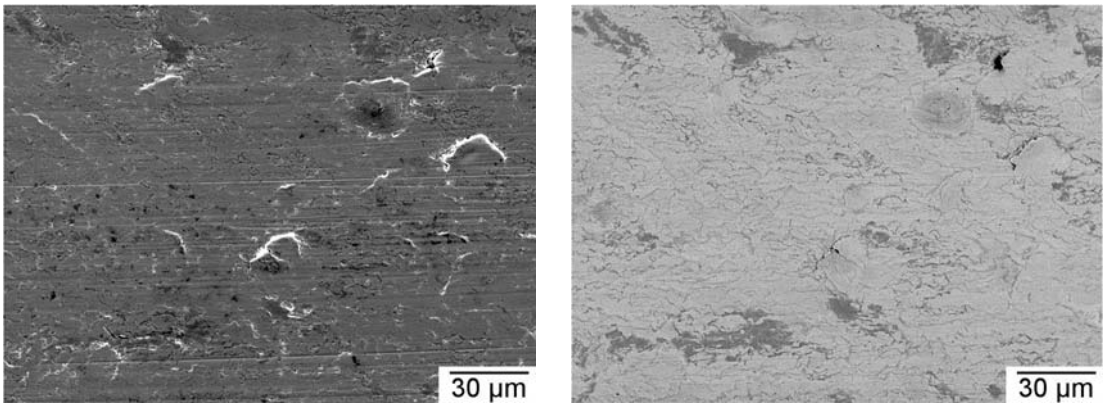

a) b)

Figure 5.24. Secondary (a) and backscattered (b) electron images from the mild scuffed region of the nodular test NMS2.

Higher magnification secondary and backscattered images of the mildly scuffed surfaces, Figure 5.24, suggested both the onset of adhesive wear through the formation of surface platelets but also occurrence of two body abrasion. The backscattered compositional image in b) suggests significant attrition of the surface resulting in fragmentation of particles around 10 µm or less. It is believed that the liberation of these work hardened debris particles were responsible for this two body abrasive behaviour, however the presence of larger surface platelets 20-30 µm in size was also noted and likely to be the source of the transition from mild to severe scuffing. This therefore concurs with the ASTM definition of scuffing which is nonspecific to the dominant wear mechanism but facilitates multiple wear mechanisms contributing to the final scuffing failure. It also offers an explanation as to why the terms scoring, referring to grooves caused by two body abrasion, and scuffing have been used interchangeably [16].

5.5.2 Intermediate scuff surface topography

The optical image of the intermediately scuffed wear scar showed a homogeneous topography characterised by wear tracks in the direction of sliding, Figure 5.25, with no evidence of the original grinding marks in the wear scar. These observations agree with the SEM analysis showing that the oxide debris formed during mild scuffing cause a transition to abrasive wear. This mechanism efficiently removed material resulting in an increased wear rate, evidenced by the mass loss which increased by 5.6 mg, Table 5.9. The wear tracks were approximately 2 µm in depth and were in close proximity to adhesive wear craters 4 µm in depth, as shown in the higher magnification image and colour depth map in Figure 5.26. The adhesive craters were also

observed for the flake progression to severe scuffing. However, due to the absence of abrasive wear, junction growth resulted in craters which were up to 25 µm deeper.

Figure 5.25: Optical image of intermediate scuffed nodular cast iron surfaces NIS1.

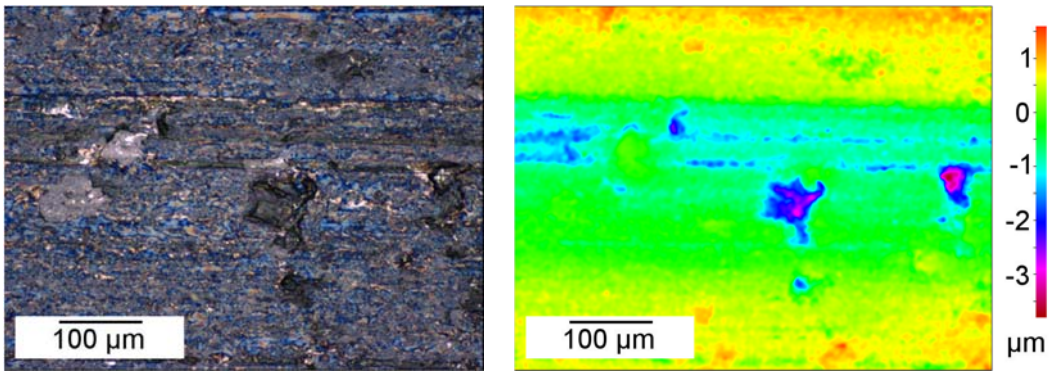

a) *b)*

Figure 5.26: Optical image (a) and 3D colour map (b) of intermediate scuffed nodular cast

5.5.2.1 Scuffed surface profilometery

The ground cast iron surfaces had a bearing surface greater than 60 % and an R_a = 0.34 ± 0.03 µm which agrees with published cylinder liner data of 0.38-1.1 µm [98,155–157]. The ground surface had an initial average surface roughness of R_a = 0.346 ± 0.013 µm which decreased to 0.294 ± 0.014 µm during intermediate scuffing and then increased to 3.247 ± 0.324 µm upon severe scuffing, Table 5.6. The surface texture evolution for each stage of scuffing was therefore similar to the flake cast iron response. The cast iron surface topography evolution associated with intermediate scuffing can be seen by comparing the bearing area curves of the ground and intermediately scuffed surfaces, Figure 5.27. The bearing area curves show that material was removed from the asperity peaks and filled in some of the material valleys. This process was observed as precursor to severe scuffing by Suh et al, [132,158]. Filmy wear debris formed during this process, thought to be responsible for the increase in friction force in the decelerating direction, were observed by Akagaki et al [155].

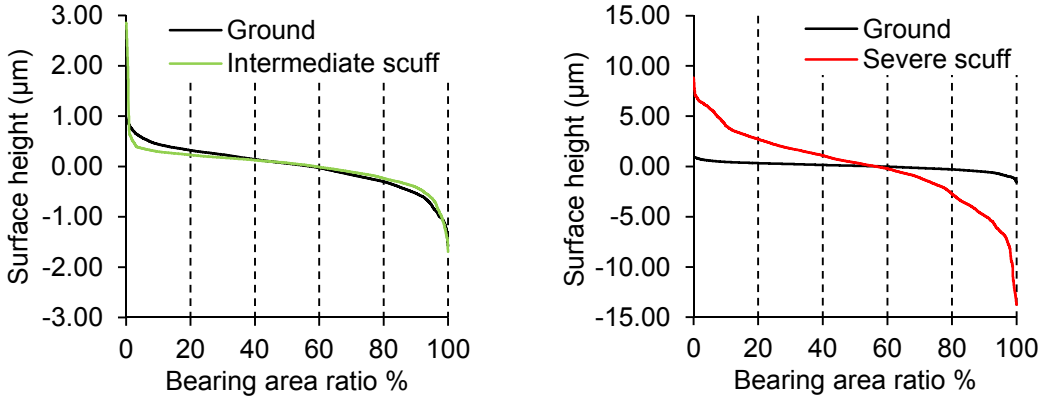

(a) *(b)*

Figure 5.27: Bearing area curves for (a) intermediate and (b) severe scuff surfaces from a Talysurf profilometer (2 µm tip).

Table 5.6: Specimen properties: average surface roughness (R_a), kurtosis (R_k), reduced peak height (R_{pk}) and reduced valley depth (R_{vk}) from a Talysurf contact profilometer (standard deviation error, σ).

Sample	Surface	R_a	σ	R_k	σ	R_{pk}	σ	R_{vk}	σ
Roller bearing	-	0.041	0.009	0.088	0.012	0.066	0.054	0.139	0.074
NS1 cast iron	Ground	0.346	0.013	1.149	0.064	0.350	0.043	0.503	0.022
	Intermediate	0.294	0.014	0.668	0.029	0.323	0.080	0.905	0.137
	Severe	3.247	0.324	8.429	1.041	3.200	0.538	5.007	1.570
NS2 cast iron	Ground	0.340	0.030	0.940	0.059	0.302	0.036	0.681	0.062
	Intermediate	0.297	0.056	0.656	0.090	0.564	0.129	0.876	0.228
	Severe	2.602	0.186	7.822	0.731	3.114	0.788	5.095	0.425

Higher magnification optical and SEM images of the reversal position, Figure 5.28 and Figure 5.29, exhibited evidence of adhesive wear craters up to 12 µm in depth, again noticeably shallower than the flake graphite adhesive craters that were of the order 25 µm in depth. There was also a significant accumulation of wear debris at the stroke reversal position, which is thought to have contributed to the 100 % increase in friction force in the decelerating direction, caused by plastic deformation of adhered wear debris by the leading edge of the counterface as it approached the end of the recessed wear scar. The scanning electron images of the surface away from the stroke reversal position showed a smooth surface with wear tracks in the reciprocating direction which agreed with the stylus profilometery, Figure 5.30. It was noticeable from the SEM images taken in the longitudinal orientation, Figure 5.31, that the intermediate wear scar was composed of two types of surface morphology. There were regions of platelets of various sizes some of which were joined into large sheets approximately 50 µm across, with cracks separating some of the platelets, Figure 5.31 a). These platelets existed alongside wear tracks that exhibited multiple sites of adhesive wear, where craters remained after matrix material had been transferred to the countersurface, Figure 5.31 b). It is likely that the wear debris from the craters work hardened as they were transferred to the counter face, where they

subsequently ploughed the surface, leading to the increase in friction force at the stroke reversal positions.

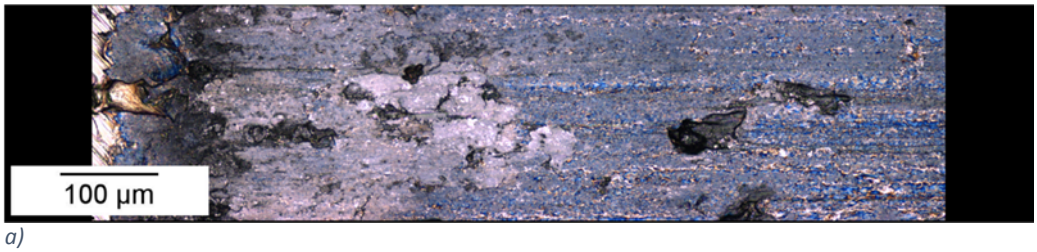

a)

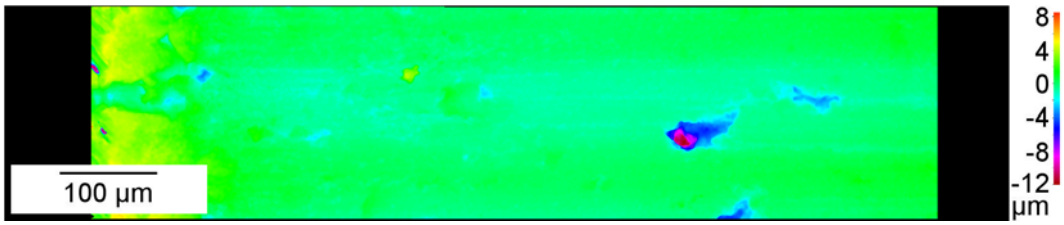

b)

Figure 5.28: Optical image of the intermediate to severe transition nodular cast iron surface from test NTS1, showing a wear particle and adhesive wear craters inside the stroke reversal position a) and 3D colour map b).

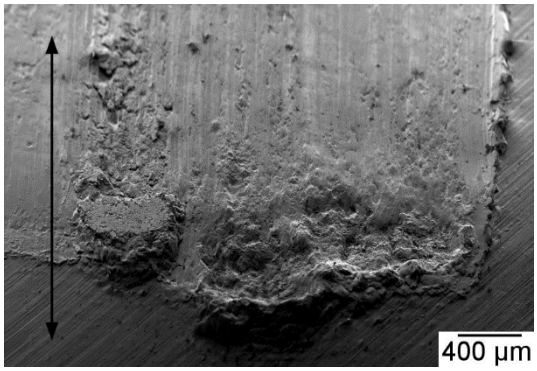

Figure 5.29: Debris agglomeration at the edge of the wear scar.

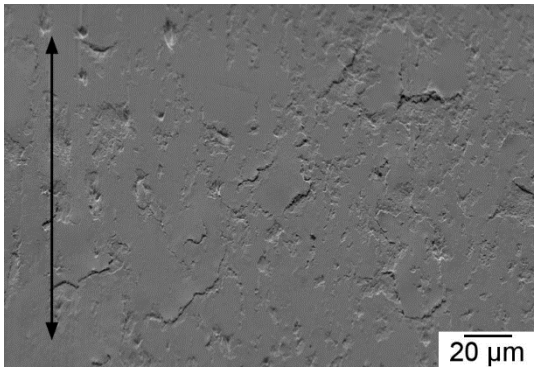

Figure 5.30: Intermediate scuff surface.

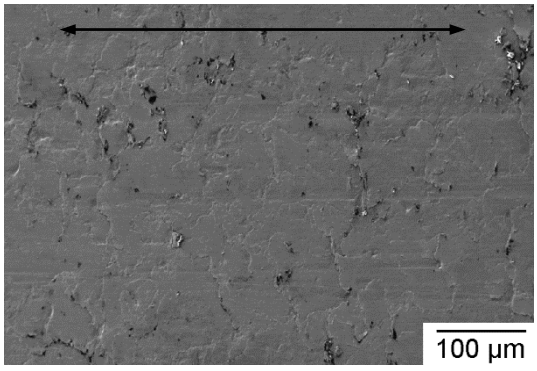

a)

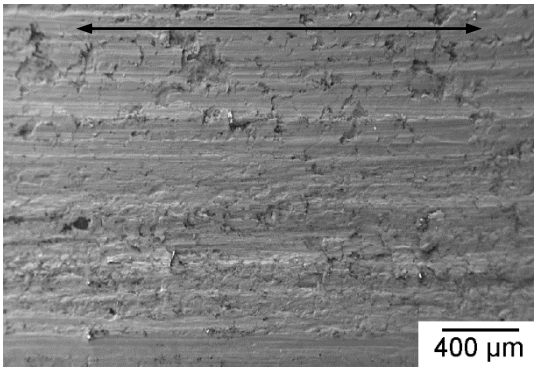

b)

Figure 5.31. Secondary electron images of the two morphologies on the intermediate scuff surface a) platelets joined into sheets 50 µm across b) adhesive wear craters remaining after material transferred to counter face.

5.5.2.2 Focused ion beam analysis

In order to further investigate the mechanisms responsible for intermediate scuffing of the nodular cast iron surface, two FIB cross sections were made transverse and parallel to the reciprocating sliding direction of the NIS1 surface. The area of interest for the traverse section was initially coated in a deposition of carbon to facilitate optimal polishing, Figure 5.32 a).

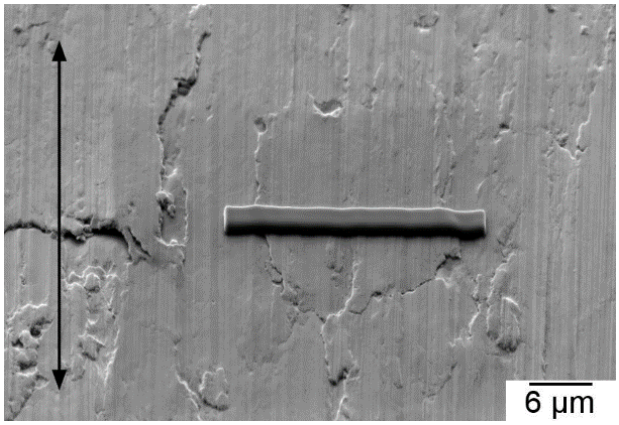

a)

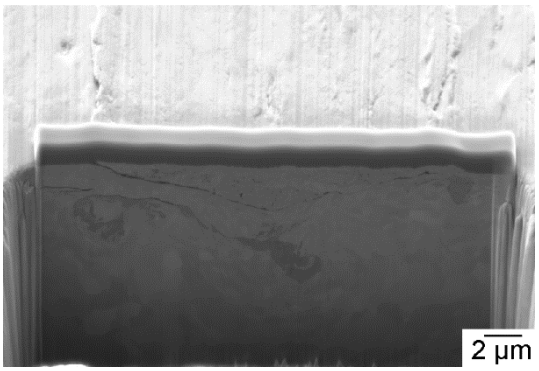

b)

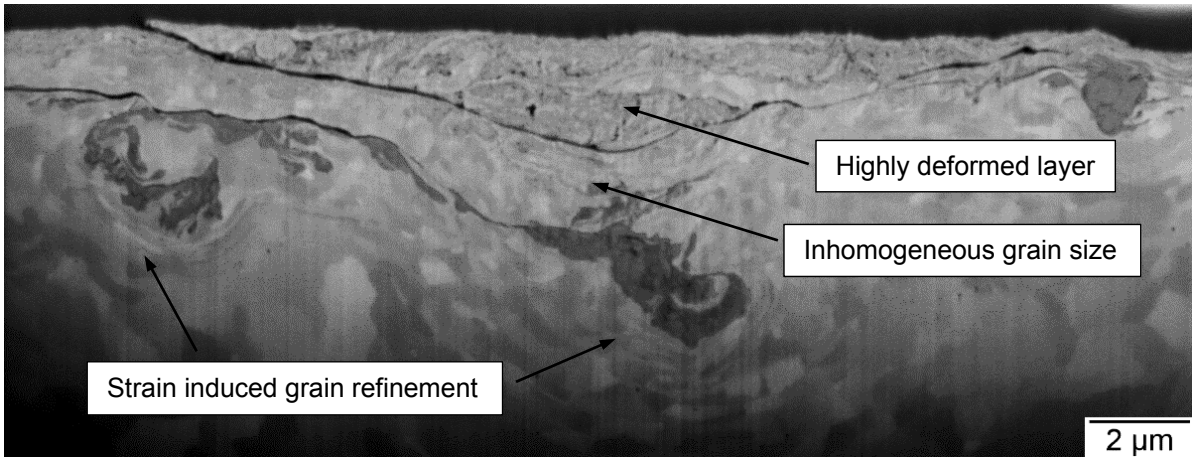

c)

Figure 5.32: Secondary electron image of (a) the area of interest for transverse cross-section on transition-scuffed surface from test NTS1. Secondary electron (b) and ion (c) images of the sub-surface microstructure.

The sub-surface microstructure, Figure 5.32 b) and c), revealed two cracks associated with the surface platelet. The upper crack at the top of the image separated a heavily deformed region of material, up to 2 µm in depth, which had a highly refined microstructure compared to the bulk matrix. The second crack arrested in the middle of the image at a region of high contrast. There were several regions of low contrast adjacent to the crack and these were surrounded by deformed matrix material. The microstructure in between the two cracks exhibited an inhomogeneous grain size, although there was distinct strain patterns around the regions of dark contrast.

A longitudinal FIB cross-section, parallel to the direction of sliding was performed in a region of the wear scar away from the stroke reversal position, as shown in Figure 5.33 a). Again, surface platelet boundaries appeared to associated with sub-surface cracks, themselves connected to

two microstructural features of low contrast, Figure 5.33 b) and c), smaller than the nodular graphite colony size, Figure 5.1. Similarly to the transverse cross section, these features appeared to have significant matrix strain around them arising from deformation induced by the sliding contact. There were no cracks present in the matrix away from these features. The undeformed bulk matrix exhibited no pearlitic grains, consistent with the microstructural observations in Section 5.1, above that the microstructure was mainly composed of ferrite. The main point arising from these FIB cross sections was that the platelets and sub-surface cracks appeared to be associated with particles that did not resemble the size or morphology of nodular graphite particles, suggesting a different material failure mechanism.

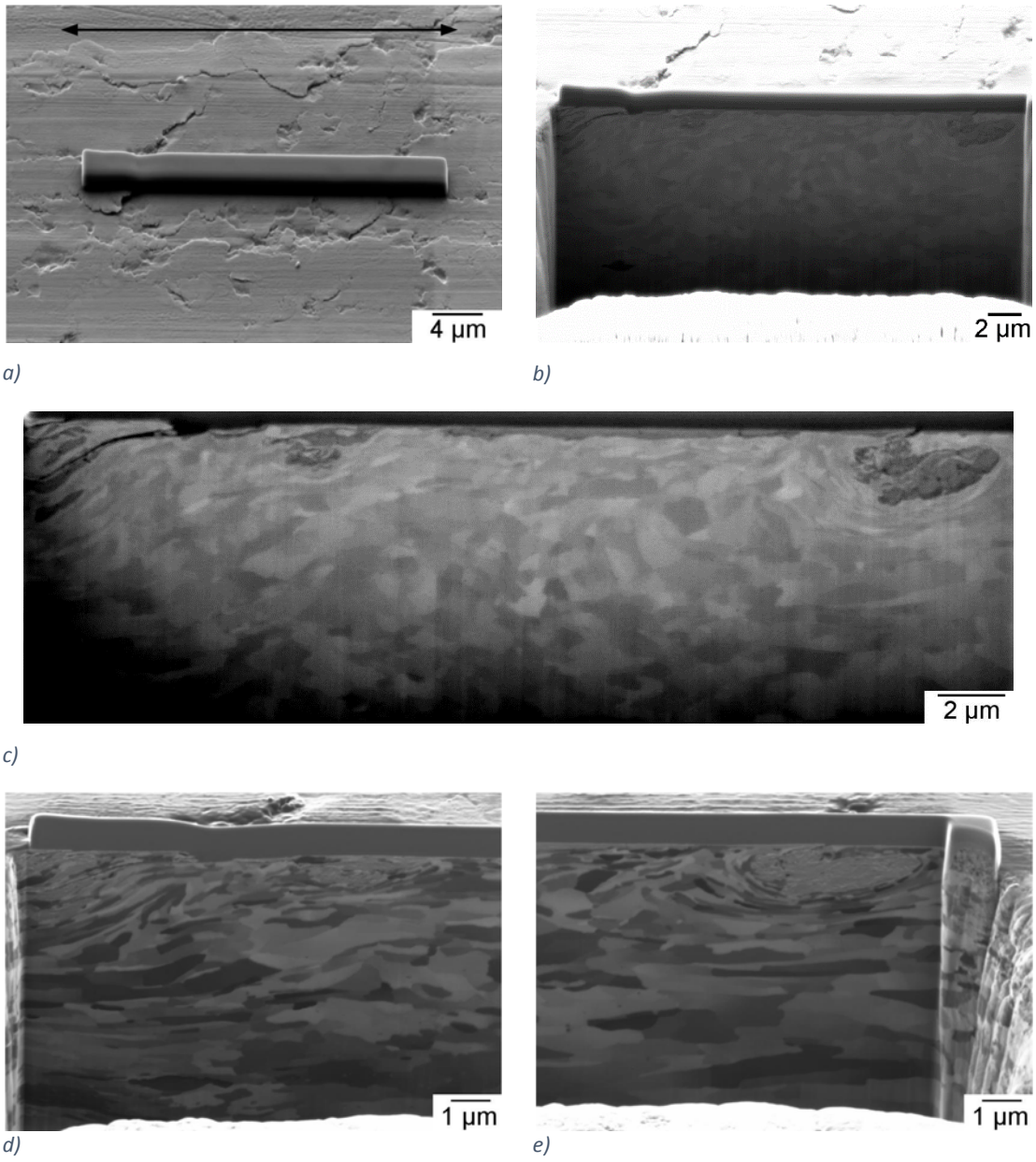

a) *b)* *c)* *d)* *e)*

Figure 5.33: Secondary electron image of (a) the area of interest on transition-scuffed surface for longitudinal cross-section from NIS1. Secondary electron (b) and ion (c) images of the sub-surface microstructure. Higher magnification secondary ion images of the left and right cross-section boundaries are shown in d) and e), respectively.

To elaborate on whether this was a valid hypothesis, a third FIB cross section was performed in the transverse direction from the surface of NIS2 (150 ^{o}C, 1 ml/h), Figure 5.34 a). The sub-surface microstructure again revealed a crack network associated with surface platelet formation, Figure 5.34 b), and once again the cracks appeared to be associated with a surface particle different in contrast, size and morphology from the larger nodular graphite particles which can be seen at the bottom of the image. The cracks propagated through the ferrite matrix, extending to the graphite phases, but arrested at the interface. There was no evidence of de-cohesion between the graphite and the ferrite, Figure 5.34 c). The upper few microns of the ferrite matrix presented a highly deformed surface, consistent with previous observations.

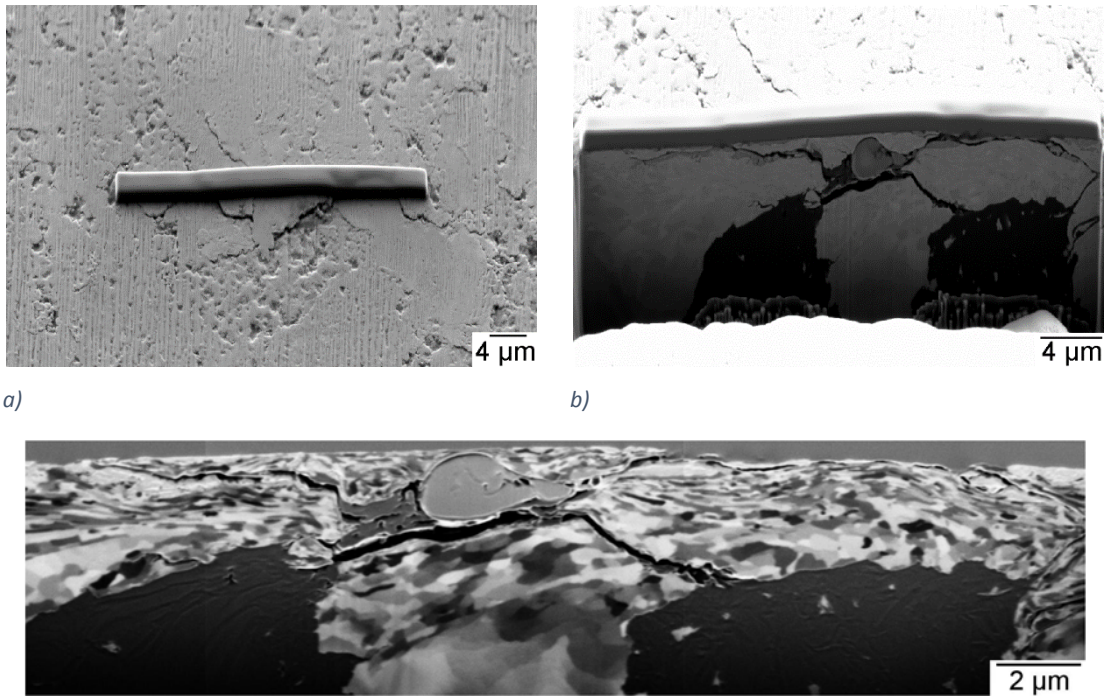

a) *b)*

c)

Figure 5.34: Secondary electron images of the FIB cross section area of interest (a) from the surface of NIS2 and the sub-surface cross section (b). Secondary ion image (c) shows deformed microstructure.

In order to identify the composition of the non-graphite phases in the FIB cross sections above, EDX analysis was attempted on the cross sections themselves, Figure 5.35 and Table 5.7. This proved challenging as the emitted X-Ray signal count was low due to the interaction volume of the species below the surface. In order to verify if this was correct, a polished cross section of the un-deformed GJS400-15 material was further analysed for similar features.

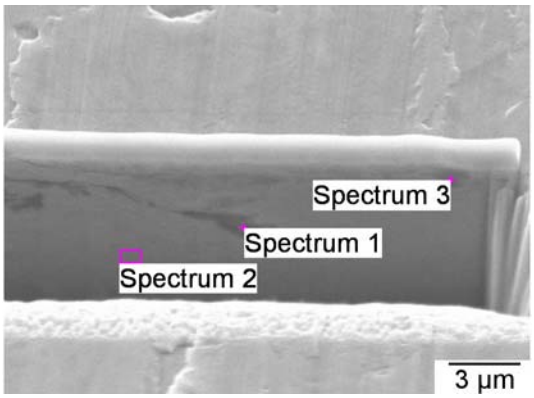

Figure 5.35: EDX analysis of FIB cross section in Figure 5.32

Table 5.7: Weight % composition of EDX spectra in Figure 5.35.

Spectrum	C	O	Si	Fe
1	16.53	10.00	1.60	71.88
2	11.99	-	1.58	86.43
3	15.75	11.37	1.71	71.17

Quantitative EDX analysis, Table 5.8, revealed a high concentration of carbon, oxygen and magnesium, suggesting these features were dross inclusions formed during the casting process [156,157], where incomplete nodularisation of the graphite had led to stringers resembling more of a flake structure. The features themselves appeared to have resisted plastic deformation induced by the normal load and shear forces from the reciprocating counter face, but facilitated plastic shear and cracking within the ferritic matrix at their interface, Figure 5.32 and Figure 5.33. This was significant as it suggested that the onset of severe scuffing in nodular cast irons was similar to that observed in flake cast iron, where platelet formation and ultimately severe adhesive wear occurred by decohesion of a pearlitic matrix along flake graphite interfaces [132]. Features observed in the longitudinal cross section that were spherical appeared to avoid crack initiation, resulting rather in deformation of the ferritic matrix and a reduction in grain size. Thus the enhanced ductility of nodular cast iron for cylinder liner applications benefits scuffing resistance to the extent that the casting process has been controlled to avoid dross inclusions that compromise severe scuffing resistance. Whilst the EDX analysis has identified these as dross inclusions, it has been reported that graphite nodules deformed due to the sliding shear stress also act as crack initiation sites [51,52,106]. The nodules of graphite where not observed to have deformed during these experiments and this is thought to be due to the reduced contact pressure achieved by using a line contact geometry which more accuracy reproduces the conditions of the ring liner interface.

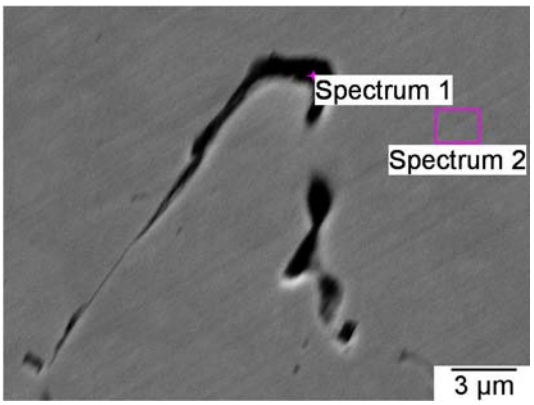

Figure 5.36: EDX analysis of nodular cast iron dross inclusions.

Table 5.8: Weight % composition of EDX spectra in Figure 5.36.

Spectrum	C	O	Mg	Si	P	S	Mn	Fe
1	32.57	12.85	7.20	0.53	0.44	0.49	0.50	45.42
2	3.78	0.54	0.00	2.53	0.10	0.00	0.41	92.72

5.5.3 Severe scuffed surface topography

a)

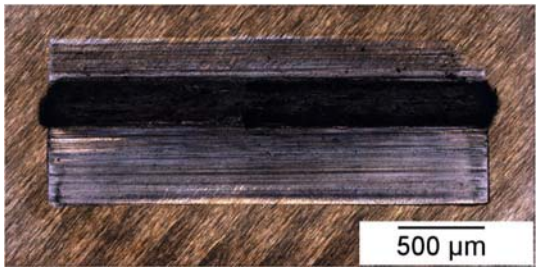

b)

Figure 5.37: Optical images of severely scuffed nodular cast iron surfaces (a) NS3 and (b) NS4

The rectangular wear scars on the NS3 and NS4 nodular cast iron samples, shown in Figure 5.37, had light and dark regions which corresponded to the intermediate and severe scuffed regions, respectively. Longitudinal profiles of the severe scuffed regions of cast iron are shown in Figure 5.39 and Appendix nodular Figure 11.5. The severe wear scar profiles had a high apparent roughness and a wear scar depth approximately three times deeper than the mild scar. The corresponding material agglomerations outside the wear scar were several orders of magnitude larger than in the mild case.

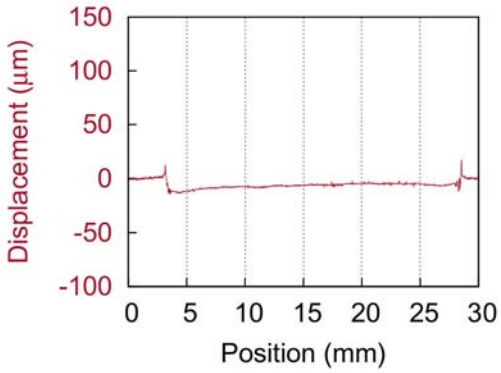

Figure 5.38: Longitudinal profile of the intermediate scuffed area of the cast iron wear scar from test NS1.

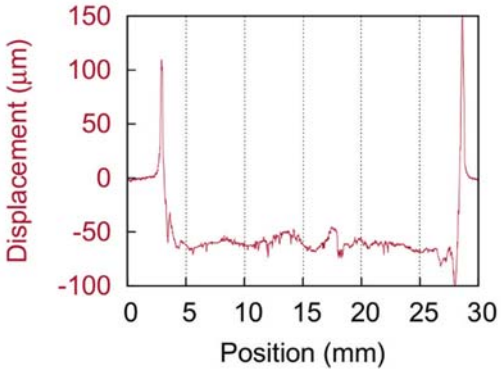

Figure 5.39: Longitudinal profile of the severe scuffed area of the cast iron wear scar from test NS1.

The intermediately scuffed surface was formed of platelets which had structures observable at the millimetre and micron length scales, as shown for NS2 in Figure 5.40 and Figure 5.41. The intermediate wear scar profiles from both NS1 and NS2 tests had a low apparent roughness and shallow wear scar depth, 15-20 µm for NS2 and 20-30 µm for NS1, Appendix nodular Figure 11.4. Agglomerated material was found on the ground surfaces outside the ends of each wear scar. The ends of the wear scar were rougher than the rest of the scar. There were three instances of platelets which were in the process of being removed and had been folded back on to the material surface. In contrast, the severely scuffed surfaces had much greater topographical relief with surface craters up to 40 µm in depth overlaid with wear tracks in the direction of sliding, as shown in Figure 5.42, Figure 5.43 and Appendix nodular Figure 11.6.

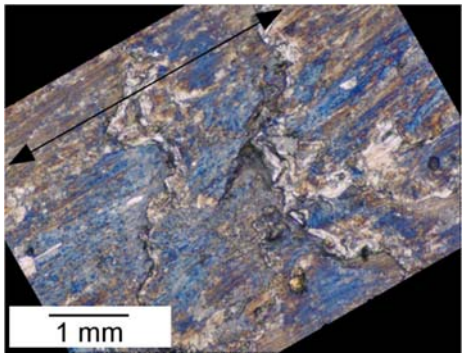

Figure 5.40: Optical image of cast iron transition scuff.

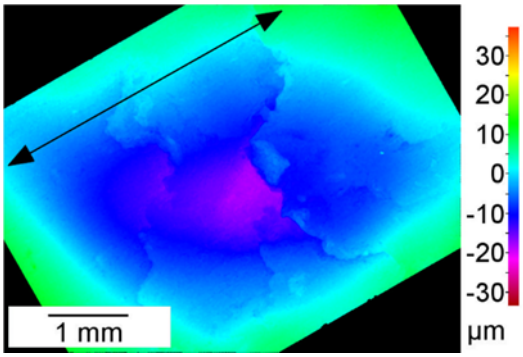

Figure 5.41: 3D colour map of cast iron transition scuff.

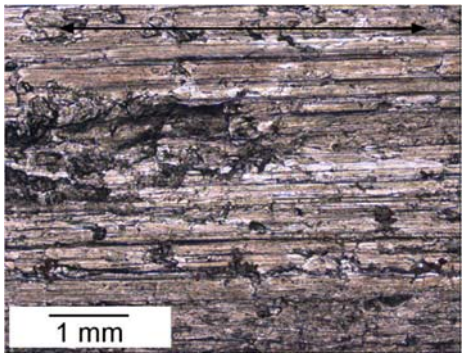

Figure 5.42: Optical image of cast iron severe-scuff.

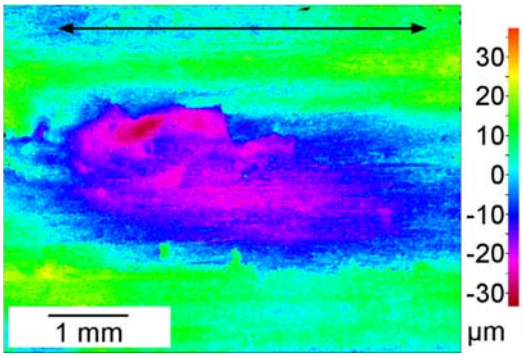

Figure 5.43: 3D colour map of cast iron severe-scuff.

5.6 Summary of nodular cast iron scuffing mechanisms

The ground nodular cast iron surface roughness, Figure 5.44, was reduced during running-in as asperities were worn down in the presence of a partial lubricant film Figure 5.45. The increased contact pressure plastically deformed the ferritic matrix observed by FIB in Figure 5.32, which starved the contact of lubricant facilitating the onset of adhesive wear at the at the stroke reversal positions, Figure 5.28. In the absence of lubricant the asperity temperature increased forming a thin oxide layer (EDX, Figure 5.23), Figure 5.46. From the analysis it appeared that the surface was composed of highly deformed matrix this might be expected because of the lower hardness of the ferritic rather than the pearlitic matrix.

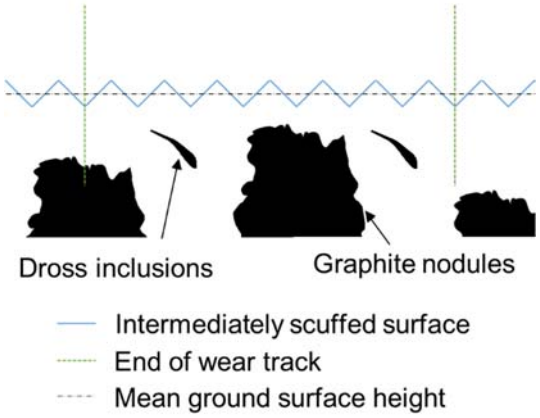

Figure 5.44: Ground nodular cast iron suface schematic.

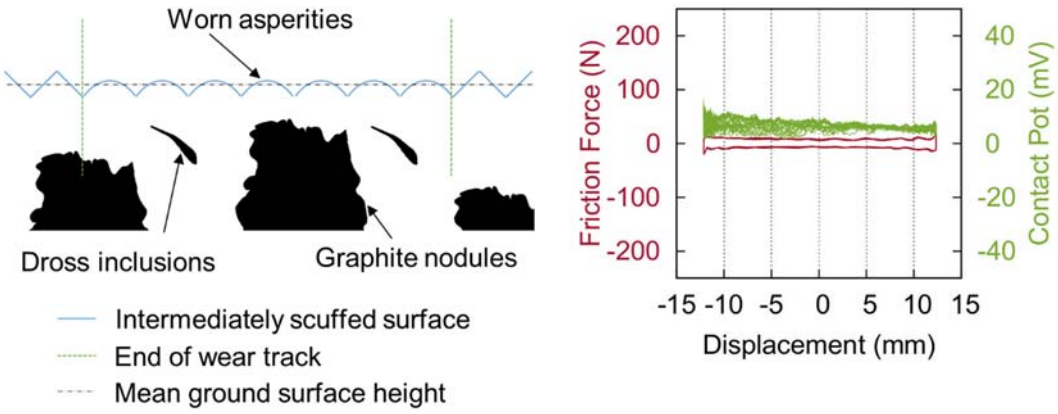

Figure 5.45: Nodular cast iron run-in surface schematic and associated high speed data.

During mild scuffing the ferritic microstructure exceeded its stain hardening limit due to the continued reciprocation of the countersurface in starved lubrication conditions and two body abrasive wear debris consisting of a refined ferrite matrix and oxide were liberated form the surface. These two body abrasive particles significantly increased the wear rate and prevented formation of the lubricant degraded tribolayer evidenced by a lack in increase in contact potential throughout the test. This was consistent with the mass loss data in Table 5.9 and Table 4.5 which showed that the nodular had an order of magnitude higher mass loss compared with the flake cast iron. Instead asperity flash temperatures led to formation of a more

comprehensive surface oxide layer, theorised by Batchelor and Stachowiak [93], although again this was of nanometre thickness shown by the lack of any distinct layer in the FIB crossections. The oxide film was unable to prevent the stop the subsequent progression to severe scuffing, contrary to Summers-Smith [77], and was removed from the surface which Ludema considered to be the initiation of scuffing [75].

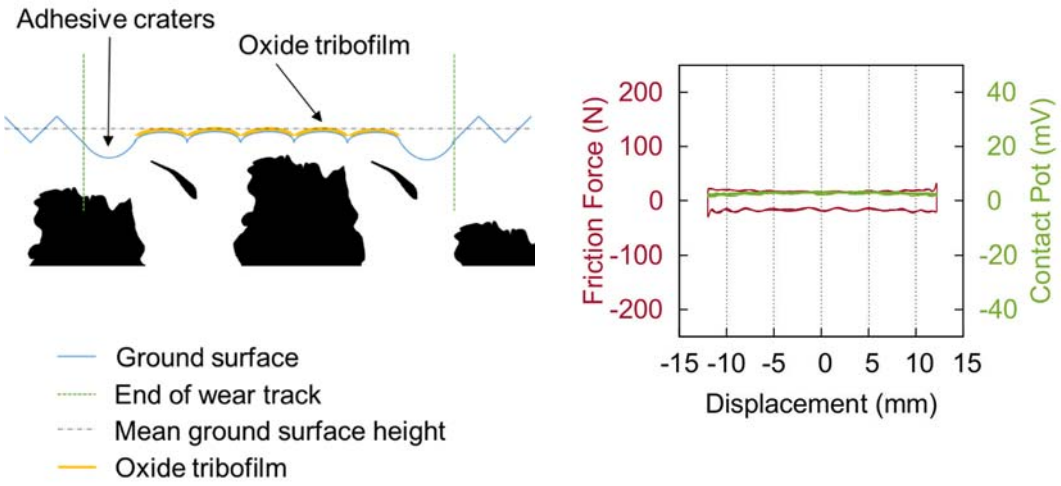

Figure 5.46: Nodular cast iron mildly scuffed surface schematic and associated high speed data.

The damage to the ferrite phase progressed until flake like dross inclusion caused initiation and propagation of sub-surface cracks, leading to formation of platelets on the surface, Figure 5.47. The increased amount of wear debris produced by two body abrasive wear mechanism were trapped between the edge of the wear scar and reciprocating counter face and plastically deformed, Figure 5.29. This was called intermediate scuffing which was defined by an increase in friction force in the decelerating direction at the stroke reversal positions which manifest in an increase in friction noise.

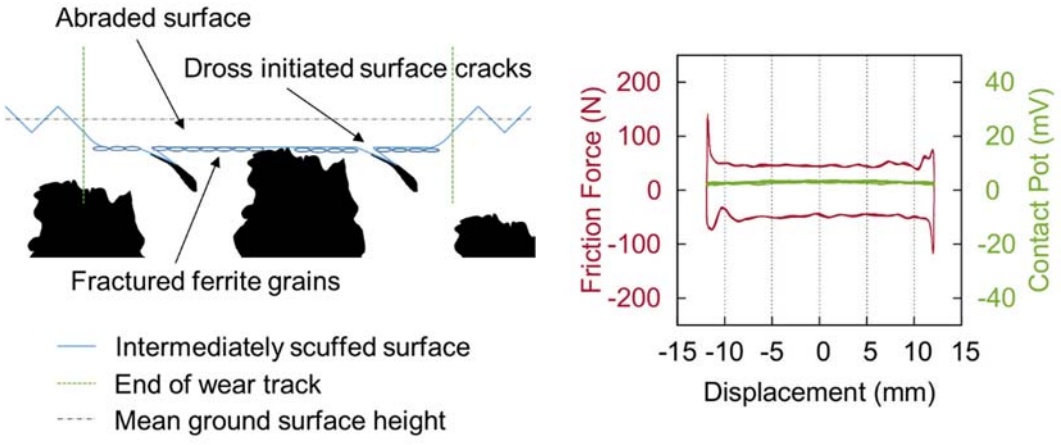

Figure 5.47: Nodular cast iron Intermediately scuffed surface schematic and associated high speed data.

During the transition to severe scuffing the friction force doubled at the stroke reversal positions in both the accelerating and decelerating directions and then at many of the locations throughout the stroke Figure 5.48. This was due to the extenuation of the severe contact

conditions at the stroke reversal positions resulting in higher energy asperity contact causing adhesive wear. The increase initially occurred at the opposite end to the lubrication feed where the contact conditions were most severe but subsequently propagated across the stroke as wear debris entrained in the contact disrupted the lubricant supply and caused locally high pressures to develop. The damage was most severe in the accelerating direction at the opposite end to the lubricant feed, due to the onset of adhesive wear. The contact potential remained close to zero during the scuffing transition as the surfaces were in continuous contact.

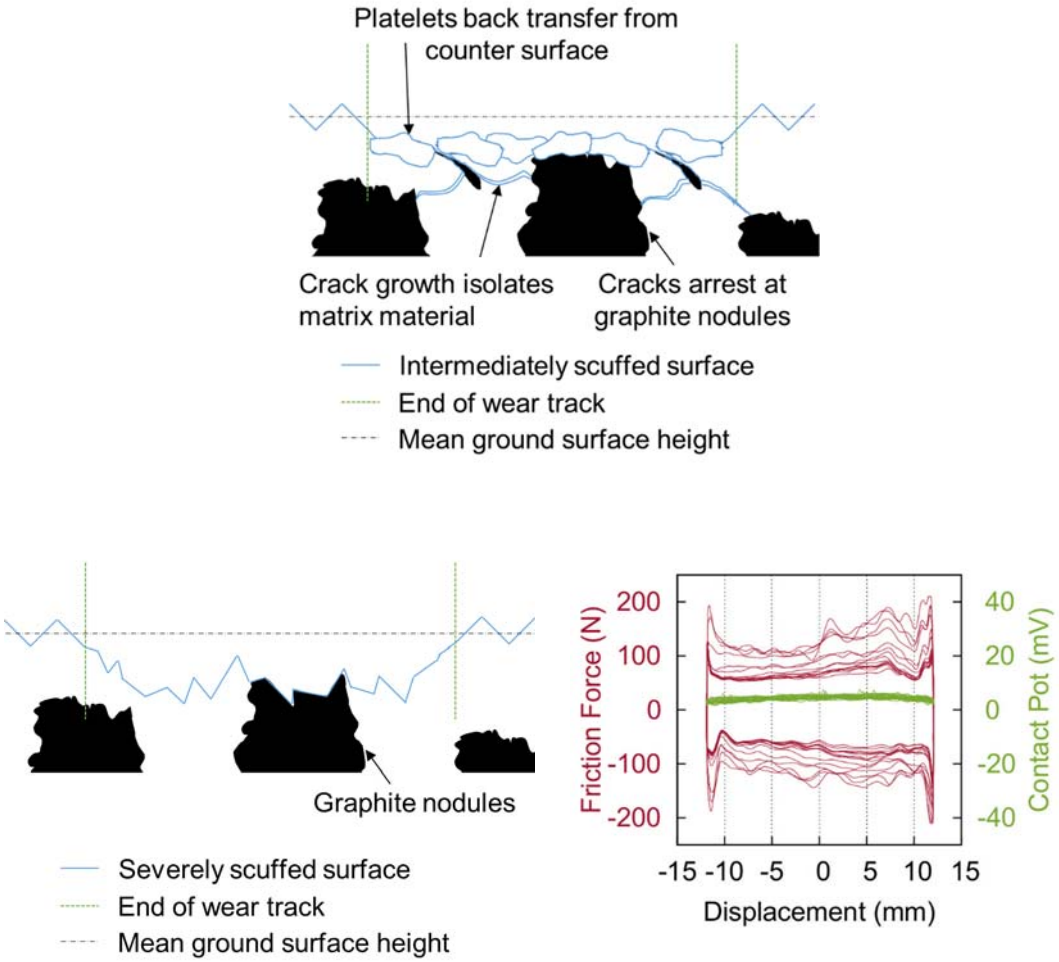

Figure 5.48: Nodular cast iron severely scuffed surface schematic and associated high speed data.

Cracks which had initially formed around dross inclusions are likely to have subsequently grown through the matrix due to the high degree of plastic deformation, also reported by Abedi et al [52]. The extensive crack networks facilitated cast iron liner material to be removed in large sections up to 40 µm deep by adhesive wear, which was similarly observed by Wojciechowski et al [51]. The severity of the adhesive wear produced an order of magnitude increase in surface roughness across the wear scar, R_a=3.347 ± 0.324 µm, Table 5.6. Large pieces of material which were entrained into the contact work hardened and caused scoring [54], [104], which prevented the lubricant film from recovering and resulted in increased scuffing wear. The severity of

adhesive scuffing was clearly demonstrated by the doubling of the cast iron mass loss of NS3 compared to NS4 given that the failure load of the former only 100 N greater, Table 5.9.

Table 5.9: Mass loss for tests NMS1 &2, NIS1, NS3 & 4 (standard deviator error, σ).

Sample	Scuffing failure load (N)	Cast iron mass loss (mg)	σ	52100 mass loss (mg)	σ
NMS1	200	1.42	0.10	0.11	0.14
NMS2	200	2.27	0.09	0.00	0.00
NIS1	500	7.85	0.16	0.01	0.12
NS3	700	40.60	0.15	-0.07	0.02
NS4	600	17.42	0.11	-0.13	0.02

Mild scuffing was detected by the scuff detection software at 200 N load, the same load as the flake cast iron, despite the increase in material ductility. There is some evidence in the literature that nodular cast iron does indeed exhibit poorer scuffing performance due to extrusion and smearing of the graphite spheroids across the surface. Once this lubricious film is compromised, adhesive wear can then progress [105]. This was not observed in the present work and is thought to be due to the reduced subsurface shear stress as a consequence of the lower contact pressures arising from the line contact geometry used in these tests.

The onset of scuffing has also been measured as increased blow-by during engine testing [81,159] although this work suggests that this is caused by the change in geometrical tolerance caused by the increase wear rate during the intermediate scuffing. It is perhaps unsurprising that blow-by did not detect the onset of scuffing as it was very difficult to detect using the average coefficient of friction, however the scuffing detection software appeared reliable in capturing the initiation phase of the failure. The nodular cast iron mild scuffing tests were repeatable within 2 % sliding distance. These results show that the assumed stochastic distribution of scuffing tests frequently reported in literature could be a product of aggressive tests which poorly control the energy dissipated in the contact.

Although the nodular cast iron had a bulk hardness 37 Hv less than the flake cast iron, the failure load for severe scuffing was 400 N more. Thus the onset of scuffing failure in nodular cast iron appears to occur at the same rate compared to flake graphite cast iron, yet the ability of the surface to resist the transition to severe scuffing was superior compared to flake graphite cast iron. This was indicative of the cumulative wear process involved. It appeared that the dross particles in nodular cast iron would facilitate the early onset of scuffing failure by adhesive wear. Yet as there are less dross particles compared to a microstructure composed entirely of flake graphite, the progression to severe scuffing would require significantly more time to accumulate the level of surface damage and sub-surface cracking required to transfer an adequate amount of ferrite to the countersurface to facilitate catastrophic adhesive wear. This process appears to

be resisted in flake graphite to a certain degree, perhaps due to the flake structure initially providing superior solid lubricant properties to a point, after which sub-surface cracking proceeds rapidly to adhesive scuffing failure.

Previous work on nodular cast iron scuffing failure has been focused on the role of graphite spheroids in the formation of a subsurface crack network, which permits material to be easily removed disrupting the lubricated contact causing scuffing [105,52]. This work supports the growth of subsurface cracks as the mechanism for severe scuffing. However, through the use of focused ion beam cross-sectioning it has been possible to determine that cracks develop around dross stringers, resembling flake graphite, earlier in the wear process during intermediate scuffing. Thus the scuffing resistance of cast iron has been proved to be intrinsically linked to the microstructure and in the case of nodular cast iron, the quality of the nodularisation and casting process to avoid dross inclusions.

6 Scuffing mechanisms of flake graphite cast iron cylinder liners

6.1 Comparison between line and conformal ring-liner geometry.

Development of a laboratory scuffing detection technique based on instantaneous friction force for materials used in fired diesel engines was shown in the previous sections to be suitable for detecting the onset of scuffing using an idealised line contact to represent the ring-liner interface. The methodology was extended to assess whether the same scuffing detection techniques and stepped load test methodology could be applied to a piston ring on cylinder liner component geometry. This would represent an increase in the complexity of the test to be representative of the contact geometry of an internal combustion engine and would be a step towards component and engine scuffing tests. For heavy duty diesel engines, engine scuffing and lubricant performance tests according to ASTM D8074 are often performed on a Detroit Diesel 13 (DD13). In order to develop the present techniques as a bridge between laboratory line contact tests and heavy duty diesel scuffing engine tests, components from a DD13 engine were used as the ring and liner materials. The DD13 is a heavy duty in-line 6 diesel engine with a displacement of 12.8 litres and a horsepower range of 350-505 HP [142].

Compared with the parallel geometry of the cylinder on flat contact, the addition of the ring and liner curvature further constrained the component orientation. If the ring and liner were not collinearly aligned then the ring would ride across the curvature of the liner causing a high friction force to be generated. In this case the resulting coefficient of friction and scuffing load would not be representative of the tribocontact being reproduced. The implications of the same misalignment for the roller on flat geometry was less severe as it did not result in geometric interference. It did however change the incident angle of the honing marks, while this is known to have an effect on the friction force and film formation [160,161], small angles of misalignment were considered to have a negligible effect, especially when operating in the boundary lubrication regime.

The roller bearing element used in the line contact tests had a uniform curvature around its 6 mm diameter and did not require to be rotated to align with the plate. The piston ring from a DD13 engine however had a symmetric barrelled face with a varied curvature, a standard design [62,150]. Therefore it was rotated such that the axial centre of the ring made a line contact with the liner. This ensured that contact curvature on the inlet and outlet of the contact were equal, and therefore any dynamic lubricant film formed by the geometry was not directional. As the piston ring had a keystone profile it was difficult to clamp the ring in the holder in the correct position at the first attempt. Correct alignment could be achieved by observing the oil film transferred to the ring after it had been in contact with the lubricated liner.

The piston ring and the cylinder liner were required to have the same diameters as mismatched diameters would not have resulted in a conformal contact. If the ring radius was smaller than the liner then an elliptical contact would have developed, increasing the contact pressure at a given load. This effect could also have been achieved if the ring radius was larger than the liner, in which case the edges of the ring would load against the top edges of the liner. These effects were minimised by using oversized piston rings which in their relaxed state formed a conformal contact with the liner samples.

6.2 Microstructure and hardness

The microstructure of the DD-13 liner was flake graphite cast iron as shown in Figure 6.1 and was form I, distribution C, size 6 according to BS EN ISO 945-1-2008 standard [59]. This was very similar to the cast iron microstructure of the Grade 250 plates discussed in Section 4 and therefore would make a good comparison of the detection techniques between idealised line contacts and conformal ring liner contacts. The Vickers hardness H_v of the liner and ring were 216 ± 2 H_v and 363 ± 2 H_v respectively.

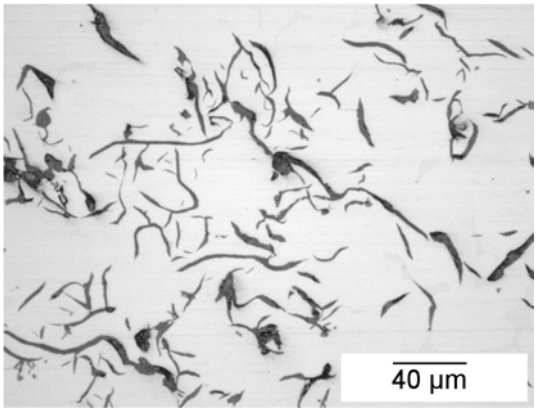

Figure 6.1: Optical micrograph of the DD 13 flake graphite cast iron liner.

6.3 Severe scuffing test

The test conditions for the scuffing of the DD13 ring-liner contact were purposefully set to be similar to the liner contact tests. A stroke length of 25 mm was used to reciprocate the ring at a frequency of 15 Hz. The normal load of the test was again ramped to 100 N over a period of 300 s followed by a running-in period up to 1200 s. This was concurrent with an increase in the test temperature to 180 ˚C. The same unformulated PAO lubricant was used and scuffing induced by incrementing the normal load at 100 N steps over 5 minute periods.

The first severe scuffing test RLS1 was terminated when the friction coefficient exceed 0.2 which occurred at 1000 N. Instantaneous friction force and contact potential data, Figure 6.4, suggested the lubricant film collapsed during severe scuffing causing the friction force to be velocity independent. The average coefficient of friction decreased from approximately 0.14 at the end of the running-in stage to 0.09 during the 400 N load step, although the fluctuations in

average coefficient of friction and contact potential appeared less sensitive to incremental increases in normal load.

It appeared that boundary lubrication conditions were temporarily achieved during the 400 N load step before the lubricant film recovered, indicated by the contact potential increasing from 2 to 6 mV in Figure 6.2. The friction noise increased from 5 % to 8 % during the film recovery which was due to a decrease in friction force that occurred as a function of velocity caused by the hydrodynamic effects of the lubricant shown in Figure 6.2. The asymmetric contact potential is consistent with the formation of a squeeze film in the decelerating direction at the stroke reversal positions [162], Figure 6.3. The friction noise, friction coefficient and lubricant film appeared to stabilise until the onset of mild scuffing whereupon the friction noise gradually descended to 5 % and then dropped to 3 % just prior to severe scuffing. Whilst the final drop in this value was consistent with the repeat severe test RLS2, the oscillatory behaviour observed in Figure 6.5 between mild and severe scuff was not observed, perhaps suggesting some localised differences in the surface damage arising from the mild scuffing transition.

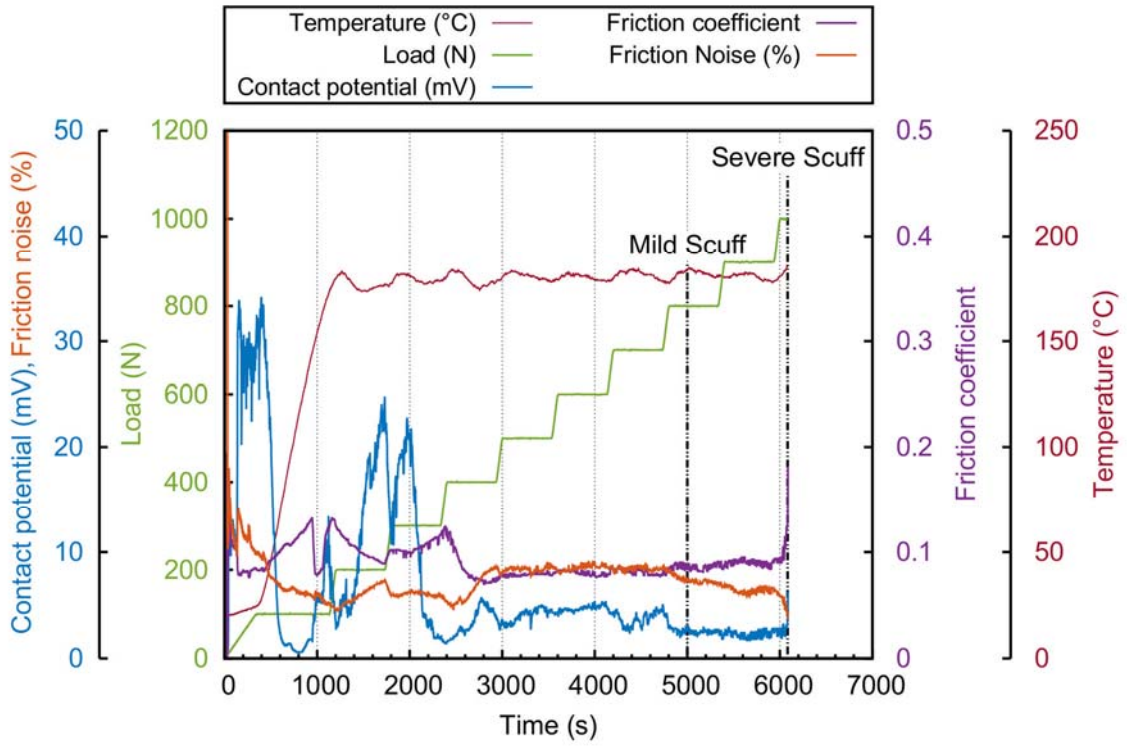

Figure 6.2: Average friction, normal load, temperature and contact potential plotted against time RLS1.

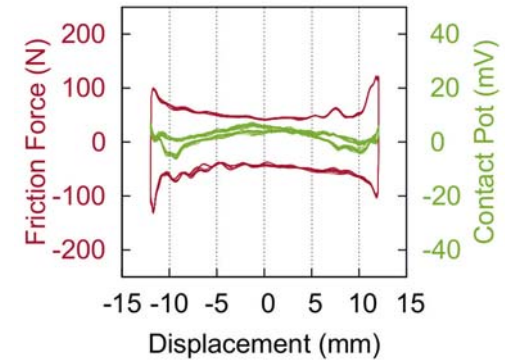

Figure 6.3: Friction force and contact potential data during mild scuffing RLS1.

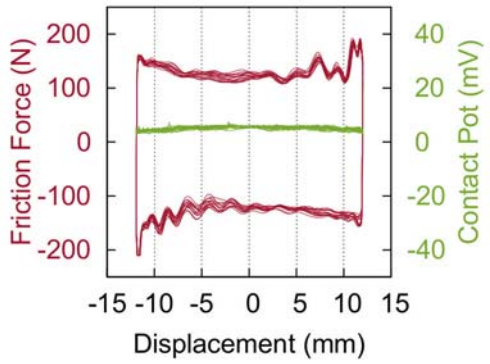

Figure 6.4: Friction force and contact potential data during severe scuffing failure RLS1.

Severe scuffing occurred at 900 N, 100 N less than RLS1, for the second severe scuffing ring on liner test RLS2, Figure 6.5. During the running in period and the early part of the load ramp, the average coefficient of friction generally decreased from approximately 0.15 at the beginning of the test to 0.09 at the onset of mild scuffing. This decrease was also accompanied by fluctuations in the contact potential signal. Towards the end of several load steps, the contact potential appeared to increase from 2-3 mV to 9-10 mV. The friction noise also followed the same general trend as the contact potential. Conversely, the average friction coefficient would see a small increase during the beginning of a load step, before continuing the gradual trend downwards. This behaviour was thought to be linked to increased wear of the surface at the beginning of a load increment, leading to a more conformal contact which subsequently enhanced lubrication towards the end of a load step. The enhanced lubrication resulted in the friction force developing a velocity dependence, increasing the deviation from the RMS value and consequently increase the friction noise. The cumulative effect of each load step ultimately led to the observed negative gradient for the average coefficient of friction. Prior to severe scuffing the friction noise decreased to its lowest value as mild scuffing spread across the stroke which increased the friction force across the stroke. At the beginning of the 900 N load step severe scuffing occurred indicated by a rapid rise in the average coefficient of friction above 0.2. During severe scuffing for both severe scuff tests RLS1 and RLS2 the lubricant film completely collapsed and adhesive wear occurred across the stroke resulting in a velocity independent friction force and very low contact potential, Figure 6.4 and Appendix cylinder liner Figure 12.3.

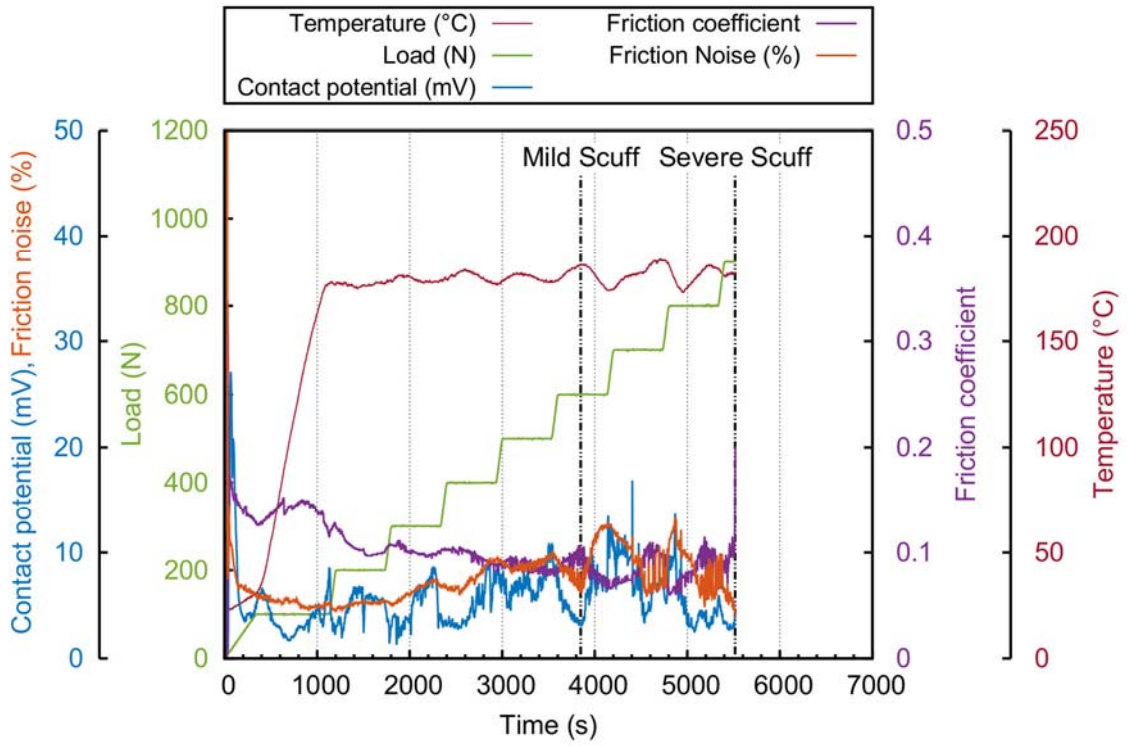

Figure 6.5: Average friction, normal load, temperature and contact potential plotted against time RLS2.

Despite this difference, the severe scuffing loads were within 560 s of each other. A further observation from both tests was that the temperature appeared to oscillate with each load step, which was not observed for the line contact tests. This was again more pronounced for the severe scuffing test RLS2 (approximately 20 ˚C during the latter stages of the test) and was due to the closed loop temperature feedback control which would attempt to maintain a test temperature of 180 ˚C even with an increase of frictional energy input. This was one of the reasons that the ring-liner tests failed at high loads of 900 N and 1000 N compared to line contact tests.

6.4 Detecting scuffing transition for ring on liner geometry

6.4.1 Friction force and friction noise

Whilst severe scuffing had been effectively replicated using a ring on liner geometry, the onset of mild scuffing was initially difficult to determine compared to the line contact experiments. This was due to velocity dependent friction behaviour observed during the ring-liner tests. When the scuff detection software was designed it was assumed that the contact needed to be operating in the boundary lubrication regime for scuffing to occur. In this regime the spatially resolved friction force was independent of sliding velocity and local increases in friction force indicating adhesive wear events were readily identifiable.

The ring on liner line contact length was 30 mm, 20 mm longer than the roller on flat contact. This decreased the contact pressure for a given load, consequently the maximum load supported by the lubricant film increased. This extended the duration of the run-in period for the ring on

liner contact as the length of the load steps were the same for both geometries. It also resulted in smaller pressure increments between each load step. This increased the resolution of the ring on liner tests and allowed the contact to operate at a pressure at which mild scuffing was recoverable.

The surface recovered from mild scuffing when the decrease in roughness caused by the mild scuffing process allowed the remaining surface asperities to be separated by the lubricant film thickness permitted at that load. This created a problem as when the surfaces were separated by a lubricant film, the friction force was never fully independent of sliding velocity when the onset of scuffing occurred. Consequently the velocity dependence of the spatially resolved friction force masked local increase at stroke reversal positions. This was compounded by the effect of a squeeze film at the reversal positions which also resulted in an increase in friction force [162]. These effects required that the criteria and threshold for mild scuffing used in the roller on flat tests had to be recalibrated for the ring on liner tests.

Friction force fluctuations inside the stroke rather that at the stroke reversal positions were used as a more robust indicator that mild scuffing was occurring for the ring on liner tests. However the fluctuations occurred rapidly and the contact quickly recovered. This made specifying an effective high speed data criteria difficult as the software only analysed the first 0.06 s of every two seconds.

The friction noise parameter however was able to indicate that these fluctuations were occurring, as it provided a continuous measure of signal disorder and had a high sensitivity to rate of change of friction force. In the line contact tests the friction noise changed approximately 2 % to produce a local maximum during mild scuffing detected by the scuffing software. Consequently mild scuffing could be detected by identifying the presence of a local maximum. The physical process that caused this is was a temporary increase in friction force at a local stroke position relative to the RMS value due to a scuffing event. When the mild scuffing recovered the local increase in friction force reduced to the RMS value. These observations support the use friction noise to identify mild scuffing for the ring on liner contact, however to be certain that the increase in friction noise is due to scuffing it must be compared with the RMS friction coefficient and the contact potential.

6.4.2 Contact potential measurement

When there was direct contact between the piston ring and cylinder liner then the resistance was very low or non-existent and in this case the contact potential was 0 mV. Separation of the metallic surfaces caused the resistance and consequently the contact potential to increase. There were three possible mechanisms which could have caused an insulating film to form:

hydrodynamic lubricant film, physical absorption of chemical species and chemical reaction [141].

The oil used in all the tests was a PAO base oil which did not contain any additives, therefore it was unlikely that an insulating film formed by physical absorption of polar molecules [163]. It was possible however for the surface to be separated by a hydrodynamic film or oxide layer. The high speed friction data was compared with the contact potential data to determine which film was separating the contact.

When a full hydrodynamic film separated the surfaces the contact potential was independent of sliding velocity. This occurred at the beginning of the tests, where the contact operated at low loads and temperatures but at maximum frequency, 15 Hz. However, the contact potential exhibited a velocity dependence when the film was reduced to the height of the surface asperities, caused by the increased temperature and load. This was caused by the velocity profile across the stroke changing the film thickness and the number asperity interactions between the surfaces. Consequently the contact potential and reciprocal friction force were proportional to sliding velocity in the mixed lubrication regime.

The high acceleration at the stroke reversal positions resulted in the film being modified by squeeze effects. This was because the time for the counterface to change of direction was of the same order as the time for the lubricant to be squeezed out of the contact, consequently there was a delay between the change in entrainment speed and reduction in film thickness. This only occurred in the decelerating direction as the film had to be first formed before it could collapse, which occurred over the central part of the stroke due to the high entrainment velocities. Therefore the resulting lubricant film was asymmetric, however its general trend over the stroke was that of velocity dependence [162]. Consequently the friction force at the stroke reversal positions was also asymmetric.

The friction force was independent of sliding velocity when operating in the boundary regime. On transition to this regime the contact potential reduced to zero as the asperities from both surfaces came into contact. However as the surface topography and microstructure was altered by mild scuffing the contact potential increased. This is likely to be caused by the growth of very thin oxide films that formed due to the increased energy dissipated in the contact however presence of mild scuffing quickly removed the film preventing it from growing.

As well as the shape of the high speed contact potential data, the absolute value is also of interest. The resistance of thin lubricant films or tribolayers are qualitatively linked to their thickness. Attempts have been made to calibrate these measurements to produce a quantitative measure of thickness, although it usually concluded that the measurements are only qualitative.

However it can be seen from the information summarised in Table 6.1 that a considerable amount of information is obtained by this rudimentary technique.

Table 6.1: Relationship between friction force, contact potential and lubricant film.

Friction force velocity dependence	Contact potential velocity dependence	Lubricant film
independent	independent	Oxide
dependent	independent	Hydrodynamic lubrication
dependent	dependent	Mixed lubrication regime

For the purpose of the scuffing tests the time averaged and high speed contact potential measurements were used to determine when the contact had entered the boundary lubrication regime. This indicated the point in the tests when the scuffing software could be used to detect mild scuffing. The lubricant film collapsed only once during each roller on flat test providing a single point from which the software could be used for the rest of the test. However because the transition from mixed to be boundary lubrication was reversible for the ring on liner contact adjustments to the scuffing detection technique were required. After a mild scuffing event the ring on liner contact recovered and the contact potential increased, this behaviour was also observed during the severe flake cast iron tests S1 & S2. The contact repeatedly recovered during the severe ring on liner test (RLS1). On each occasion a lubricant film formed separating the contact and substantially reduced the friction coefficient. Following these observations the mild scuffing criteria was specified as a simultaneous local friction coefficient and friction noise maximum and contact potential minimum.

As the criteria specified a local inflection point it was necessary for the test to be stopped a short time after the mild scuffing event had occurred. Consequently this criteria was not able to stop the test as quickly after the onset of mild scuffing as the scuffing detection software used for the roller on flat geometry. However as the mild scuffing events recovered several times before the onset of severe scuffing it provided adequate sensitivity to stop a test with the mild scuffed surfaces intact.

Applying these criteria to the two severe ring-liner tests above resulted in mild scuffing occurring for the RLS1 test at 3848 s and 5000 s for the RLS2 test, Figure 6.2 and Figure 6.5, Table 6.2. The high speed friction force and contact potential traces in Figure 6.3 both exhibited the velocity dependent frictional response as described above. Normal loads for the onset of mild scuffing in these two tests were 800 N and 600 N, respectively, suggesting the differences in the friction noise and contact potential between the two tests had influenced the onset of mild scuffing, although the progression to severe scuffing was closer. Indeed it was observed that RLS2 was still operating in the mixed lubrication regime mid-stroke when the conditions for mild scuffing

were met at the stroke reversal positions. To investigate whether the criteria were able to detect and interrupt the test at the onset of mild scuffing required further testing as detailed below.

Table 6.2: Comparison of test duration and failure loads for ring on liner scuffing tests.

Test Name	Mild		Severe scuffing	
	Test time (s)	Load (N)	Test time (s)	Load (N)
RLS1	3840	600	5520	900
RLS2	5000	800	6080	1000
RLMS1	3820	600		
Max absolute Deviation	780	133	280	50
Max absolute Deviation (%)	18	20	5	5

6.4.3 Mild scuffing test

The mild scuffing ring on liner test (RLMS1) ran until the mild scuffing criteria from the severe scuffing tests outlined above was achieved. The ring on liner tests behaved in a similar manner to the roller on flat tests, Figure 6.6. At the start of the tests a lubricant film separated the surfaces, indicated by a positive contact potential and the instantaneous friction force inversely proportional to the sliding velocity. This film decreased in thickness as the load increased to 100 N. The film thickness further decreased with increasing temperature due to the associated decrease in viscosity. The decreasing film thickness resulted in greater asperity interaction which increased the coefficient of friction to 0.15, again similar in behaviour to the two previous severe scuffing tests. Consequently the asperities wore to form a conformal contact which decreased the friction coefficient. The worn surfaces had a reduced roughness which was able to be separated by a thinner lubricant film which resulted in an increase in contact potential.

The contact load continued to increase which reduced the thickness of the film. The contact was then operating in the mixed lubrication regime as the friction force exhibited a velocity dependent profile. The friction coefficient (0.11), contact potential (2-3mV) and friction noise (4 %) reached steady state during the 400 N load step, consistent with both severe scuffing tests. The contact exhibited mild scuffing behaviour during the 600 N load step, consistent with the RLS1 test, when the average friction coefficient decreased to 0.09, Table 6.2. The friction noise and the contact potential increased slightly at this point just prior to test termination.

The mild scuffing criteria corresponded with an increase in friction force magnitude at the stroke reversal positions in both directions. It also increased the friction force inside the reversal positions dissipating 46 W of frictional energy, Figure 6.7. After the mild scuffing event the surface recovered and reduced the dissipated friction energy to 28 W, illustrated by the decrease in area enclosed by the friction loop, Figure 6.8. The friction force was again symmetric and the lubricant film increased across the stroke and notably at the reversal positions.

As can be seen in Table 6.2 the onset of mild scuffing in severe scuffing test RLS2 and mild scuffing test RLMS1 were detected within 20 s of each other, again highlighting the potential of the developed techniques to accurately reproduce and identify scuffing transitions. However as can be seen from RLS1, the onset of mild scuffing was delayed such that the overall maximum absolute deviation for this series of tests was again 18 %, comparable to both the flake and nodular line contact tests discussed above. Such deviations may be attributed to a number of variables including localised difference in the liner microstructure or stochastic events related to the local lubrication. Regardless, the present work suggests that the onset of mild scuffing can be detected within less than 20 % of the mean absolute deviation for all tests conducted and represents a significant improvement in repeatable detection of scuffing compared to existing literature, [10,128,146].

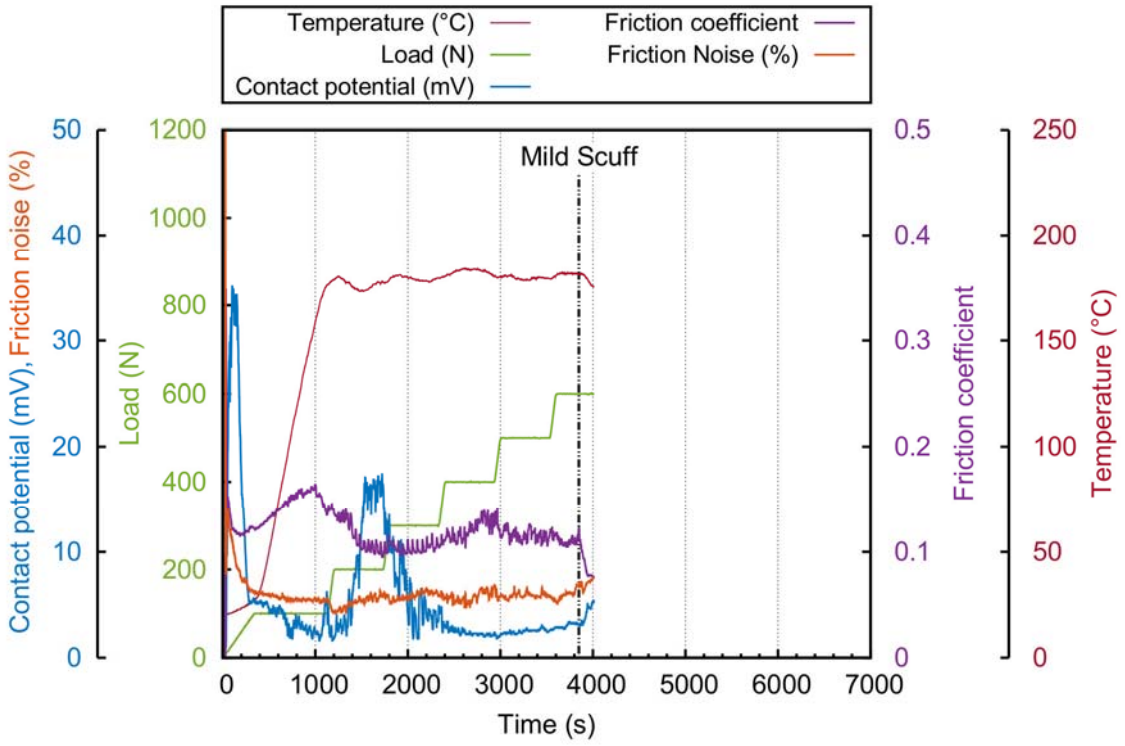

Figure 6.6: Average friction, normal load, temperature and contact potential plotted against time RLMS1.

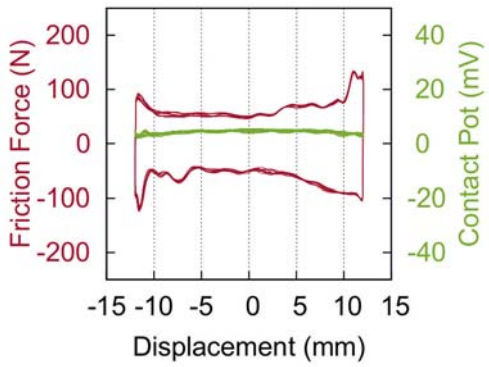

Figure 6.7: Friction force and contact potential data during mild scuffing RLMS1.

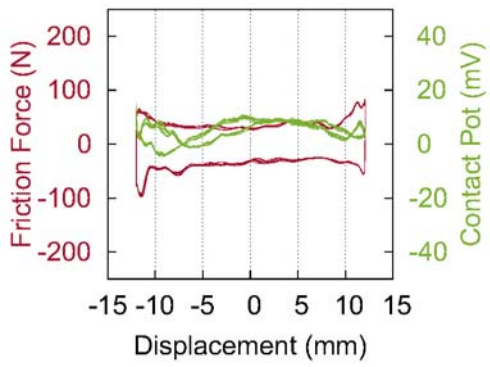

Figure 6.8: Friction force and contact potential data before test termination RLMS1.

6.5 Surface analysis

6.5.1 Mild scuffed surface topography

The contact between the ring and liner resulted in a worn region which extended across the liner sample, Appendix cylinder liner Figure 12.1. Whilst wear tracks parallel to the reciprocating direction were observed, the honing pattern largely remained visible. The colour map of the worn area, Figure 6.9 (horizontal reciprocating direction), showed very little directionality which has occurred due to the smoothing of the surface during mild scuffing which was similarly observed by Papadopoulos et al [101]. Close examination revealed the honing marks to have been filled with wear debris. Plastic deformation of asperities into the honing marks was also observed. These observations were in close agreement with the mild scuffing mechanism for the cylinder on flat geometry.

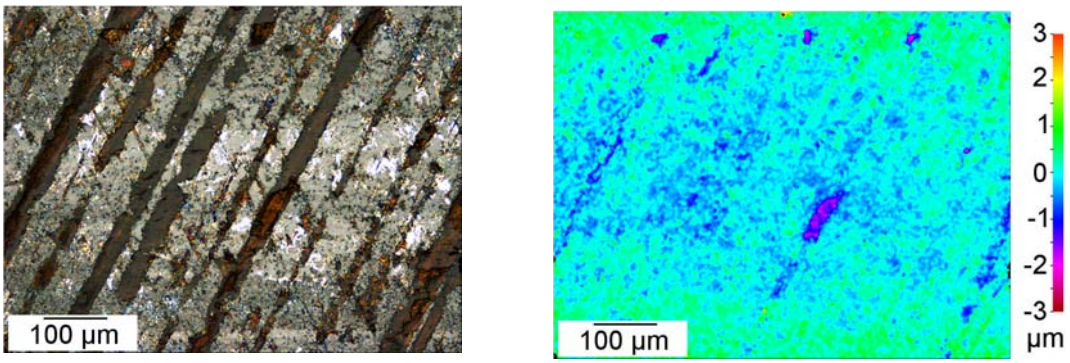

a) b)

Figure 6.9: Optical image of mild scuff RLSM1 cast iron showing plastic deformation of asperities into grinding marks (a) and 3D colour map (b).

Figure 6.10 (horizontal reciprocating direction) showed the wear scar in the centre of the piston ring, Appendix cylinder liner Figure 12.2. Two different wear scar characteristics were present. In the centre of the ring which corresponded to the worn area of the liner sample a lubricant tribolayer 4 µm thick was present. This observation suggested that the ring on liner geometry scuffed with a similar mechanism to the flake cast iron line contact tests, which also required the transfer of cast iron material to the countersurface for severe scuffing to occur.

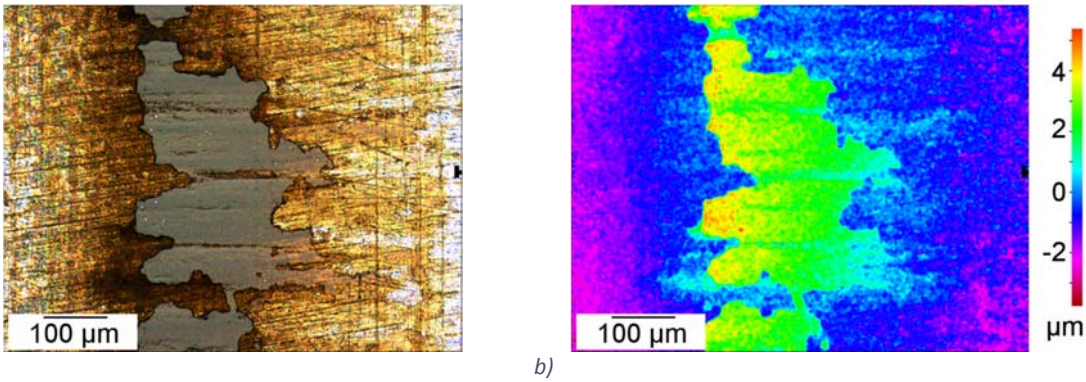

a) b)

Figure 6.10: Optical image of the RLSM1 52100 roller element showing cast iron transfer (a) and 3D colour map (b).

Secondary electron images of the mild scuffed RLMS1 test are shown in Figure 6.11 and indicate a disruption to the honing pattern where the mild scuff has occurred, Figure 6.11 a). Higher magnification images in Figure 6.11 b) and Figure 6.11 c) exhibit evidence of torn and folded metal but also platelet formation. The EDX spectra in Figure 6.11 d) was of the central particle in Figure 6.11 c) and exhibited a high carbon peak suggesting adhesive material removal from cracks initiating at flake graphite- matrix boundaries. This mechanism was wholly consistent with both the flake graphite line contact experiments, Section 4, but also the scuffed engine liners shown in Figure 2.18 in Section 2.13. This is important as it shows the development of the scuffing detection techniques in this project from an idealised line contact (level E test) to a conformal ring liner component test (level D test) and its mechanistic validation against a fired engine scuffing test (level B test).

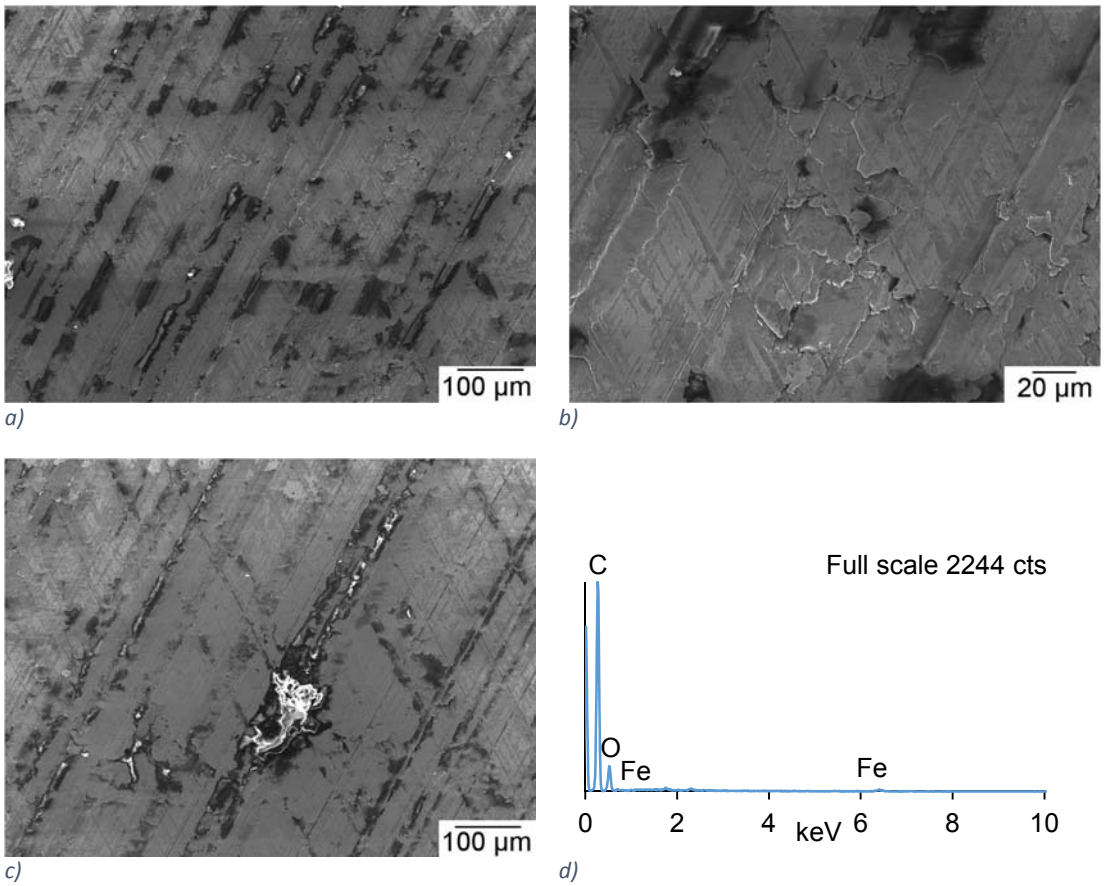

Figure 6.11: Secondary electron images (a-c) of mild scuffed region from ring on liner test RLMS1. EDX spectrum (d) from the central particle in c).

6.5.2 Severe scuffing surface topography

The RLS2 test presented with a dark scuffing band across the length of the liner wear scar, Figure 6.12. The wear band initially resembled the onset of mild scuffing observed in the flake cast iron roller on flat tests. However closer inspection of the bands revealed two wear morphologies; the first was a smooth surface between honing valleys, the second was a smooth surface which had adhesive wear craters.

The reduction in roughness of the honing marks had occurred at both ends of the wear scar and spread across the width of the wear scar, consistent with the severe scuffing progression observed in the line contact experiments, Figure 6.16. Adhesive wear craters were distinguished from the honing marks by their shape, Figure 6.17. They were parallel to the reciprocating sliding direction and were oval in shape, in contrast to features in the two honing directions which had a rectangular shape. Platelets which had been back transferred were observed in the vicinity of this area. This illustrated that the progression to severe scuffing occurred by back transfer of adhesive wear particles in a similar manner to that observed for the roller on flat geometry.

Figure 6.12: Optical images of the RLS2 cast iron wear scar.

Figure 6.13: Optical images of the RLS1 cast iron wear scar.

Figure 6.14: Optical image of the RLS2 piston ring wear scar.

Figure 6.15: Optical image of the RLS1 piston ring wear scar.

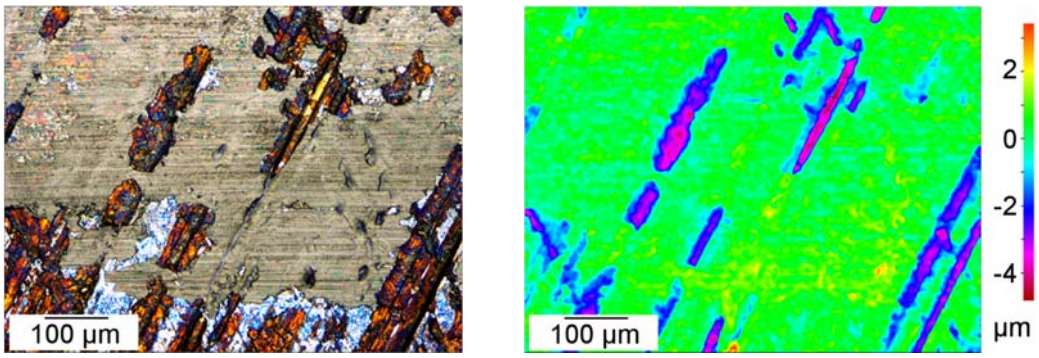

a) b)

Figure 6.16: Optical image of severe scuff on RLS2 cast iron wear scar showing the initial formation of platelets and plastic deformation of asperities (a) and 3D colour map (b).

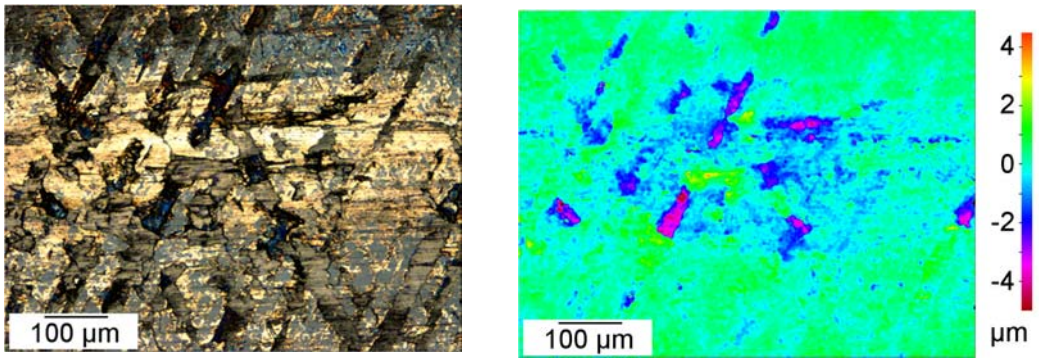

a) b)

Figure 6.17: Optical image of severe scuff on RLS2 cast iron showing well defined platelets and scoring (a) and 3D colour map (b).

The wear scar on the ring surface from the RLS2 test, Figure 6.14, indicated that a good conformal alignment of the ring with the liner was achieved as there was an even wear scar along almost 30 mm of the ring surface. The central portion of the ring wear scar was wider and corresponded to the portion of the wear track on the liner where severe scuffing had occurred, Figure 6.12.

The surface of the liner from the severe scuffing test RLS1 test was shown in Figure 6.13 and whilst the dimensions of the wear scar where similar to the liner form the severe scuffing test RLS2 test, the severely scuffed region was located in the bottom portion of the image. This may have suggested mis-alignment of the ring, however, inspection of the optical image from the worn RLS1 ring surface, Figure 6.15, again indicated a wear scar approximately 30 mm in length, suggesting no mis-alignment. Indeed the wear scar of the ring was similar for both tests, with a wider scar width in the central region of contact. The only difference was the presence of transferred debris either side of the central position, which had clearly led to severe adhesion, especially in the bottom third of the liner image.

Higher magnification images and corresponding 3D colour depth maps of the mild scuffed region, Figure 6.18, revealed the onset of adhesive wear craters on the cast iron surface inside the stroke reversal positions. Adhesive wear particles were observed at the ends of grooves in

the direction of sliding on the surface. It is proposed that the wear particles were formed by asperity adhesion which grew into larger wear particles which then re-adhered to the surface, which was consistent with the mechanism observed for the line contact flake graphite cast iron tests. As these wear particles were 4 µm proud of the surround surface this mechanism is thought to occur during severe scuffing at the end of the test. These occurred in areas where the peaks of the honing topography had been smoothed and exhibited both relief from the surrounding surface as well as two body abrasion. This lends weight to the mechanism of cumulative adhesive transfer of material from the liner to the ring surface, as observed in the line contact tests. This results in further surface damage, platelet formation and continuing adhesive transfer until sufficient material from the liner is present on the ring leading to catastrophic adhesive wear and severe scuffing of the liner surface. Evidence of this was shown Figure 6.19, where the honed topography was completely replaced by an adhesive wear track with craters up to 12 µm deep, again similar to the features observed for the roller on flat flake cast iron. As previously discussed the size of the wear craters in the roller on flat tests were controlled by the flake graphite structures, suggesting that the similar size craters observed in this test were caused by the same scuffing mechanism.

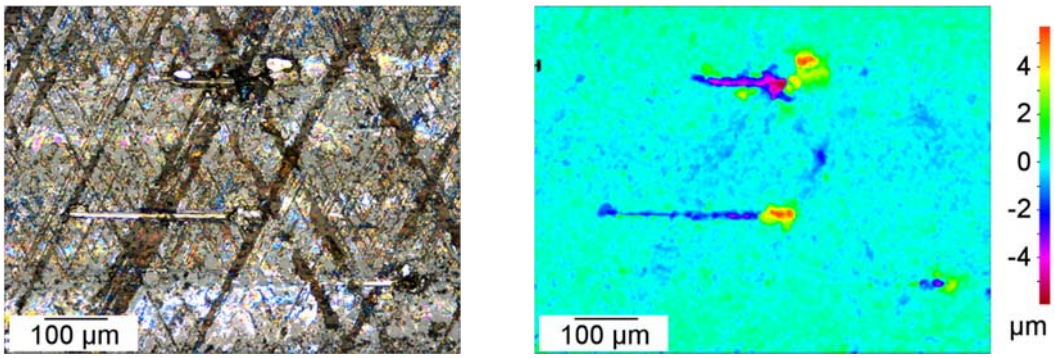

a) b)

Figure 6.18: Optical image of adhesive wear particles leaving scoring marks on the RLS1 cast iron wear track (a) and 3D colour map (b).

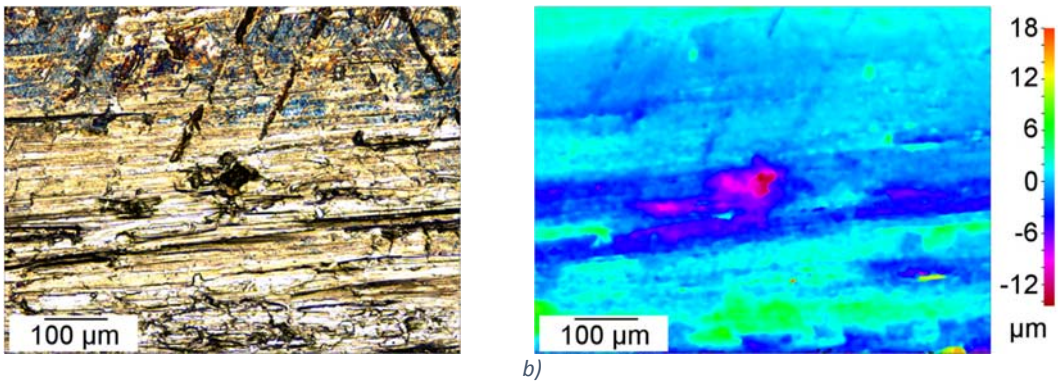

a) b)

Figure 6.19: Optical image of adhesive wear crater on surface for the RLS1 cast iron wear track (a) and 3D colour map (b).

Validation that these tests were representative of engine scuffing was provided by comparison with flake graphite liners taken from a scuffing test performed on a V6 gasoline engine (the liners were kindly provided by a third party). The engine was lubricated with a fully formulated factory fill oil and run at open throttle, failure was measured by a number of metrics including the level of blow-by exhaust gas escaping from the crank housing. Figure 2.18 shows electron microscopy images from the failed liner oriented with a vertical reciprocating direction. Figure 2.18 a) shows a low magnification SEM image of the liner which exhibited three distinct topographies. Grooves at ± 60^{o} to the direction of reciprocation created by the honing process were visible particularly on the left side. Areas which had been mildly scuffed were identified by an absence of honing marks and appeared smooth. Darker vertical lines in the direction of sliding were also present indicating severe scuffing in these regions.

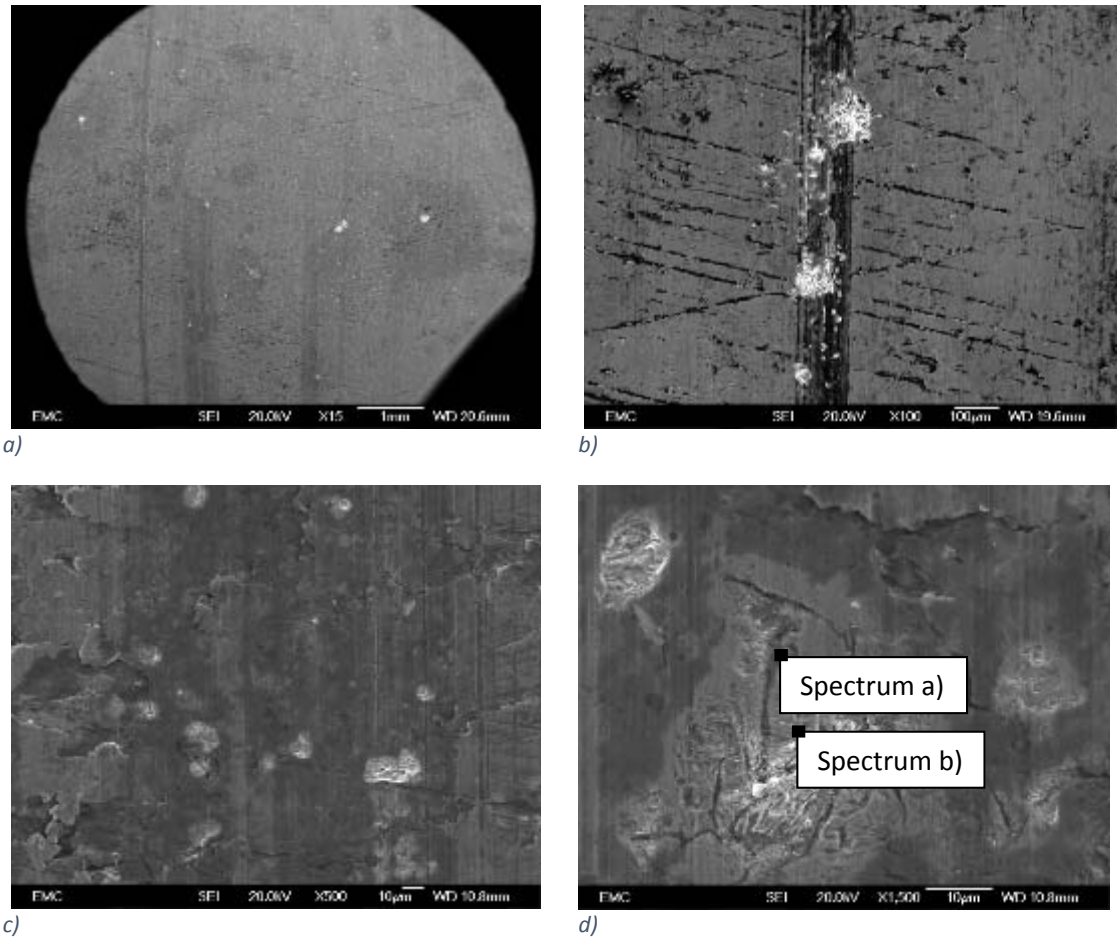

a) *b)* *c)* *d)*

Figure 2.20: Secondary electron images of flake cast iron cylinder liner showing a region exhibiting mild and severe scuffing at a) low magnification, b) high magnification, c) high magnification of the mild scuffed, d) high magnification of the severe scuffing.

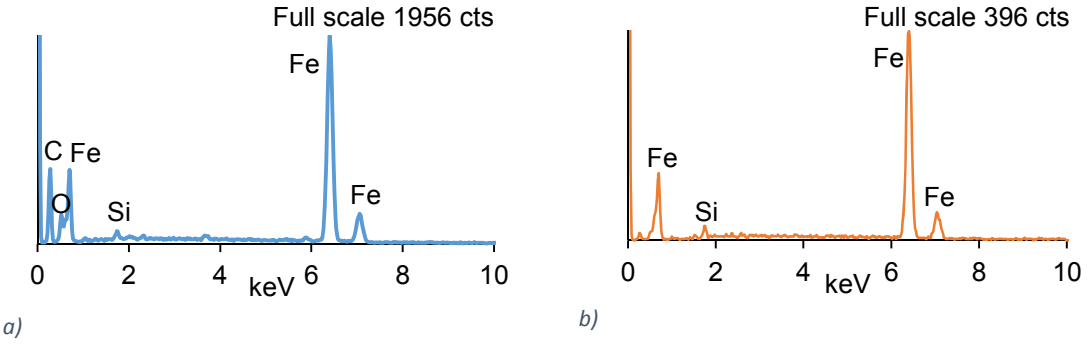

Figure 2.21: EDX spectra of the a) flake graphite and b) iron matrix in Figure 2.18b.

A higher magnification image of the interface between the mild and severe scuffed regions is shown in Figure 2.18 b). Honing marks are present on each side of the vertical wear track in the centre of the image which has been severely scuffed. In the mildly scuffed areas the honing marks appear to have been worn away, this can be seen extensively on the right of the image. There are also small vertical grooves which appear to have originated at the interface between the honing marks and the smoothed topography, on both the left and right of the image. A higher magnification image, Figure 2.18 c), of the mildly scuffed surface revealed plastic deformation of liner material into the honing grooves (centre) and the formation of surface platelets (left). Shallow vertical grooves (right), were in the vicinity of a high contrast crater in the surface. This mechanism was also observed for the ring-liner tests shown in Figure 6.11a and 6.16.

Severe scuffing had occurred inside an area which had been mildly scuffed, exhibiting grooves and smeared material in the direction of sliding, and two large high contrast craters, features of two body abrasion and adhesive wear, Figure 2.18 b). These features were was also observed for the severely scuffed ring-liner tests shown in Figure 6.18. The craters had exposed the morphology of the flake graphite in the cast iron liner, Figure 2.18 d) suggesting that the material had failed at the interface between the iron matrix and graphite flakes. This was confirmed by the significantly higher carbon content of the spectrum in Figure 2.19 a) located on a graphite flake compared with spectrum in Figure 2.19 b) located on the iron matrix. The close vicinity of the groves to the craters indicated that they were caused by adhesive wear particles which had transferred to the ring surface.

The ring-liner tests and the fired engine tests surfaces both exhibited adhesive and abrasive failure mechanisms caused by the similar microstructural features. This evidence was wholly consistent with what had been observed in the ring-liner tests in the present work and gave confidence about the applicability of the technique for detecting the onset of scuffing.

6.6 Summary of flake graphite cast iron cylinder liner scuffing mechanisms

The high speed friction force scuffing detection software was applied to the ring on liner tests which used the same load step increments as the line contact tests. However the increased contact area of the ring on liner contact compared with the line contact reduced the contact pressure and therefore the contact was not forced to operate in the boundary lubrication regime. The mild scuffing detection technique used previously assumed the contact was operating in the boundary regime and consequently had to be recalibrated for the ring on liner tests.

The friction noise, RMS friction coefficient and RMS contact potential were used to identify the onset of mild scuffing which was confirmed by analysing the surface topography which was consistent with the mild scuffed line contact tests surfaces. The recalibrated technique detected mild scuffing with an 18 % maximum absolute deviation in test time which was comparable with the scuff detection software for the flake and nodular that achieved maximum absolute deviation of 18 % and 17 % respectively.

The scuffing mechanism observed for the flake cylinder liner was similar to that observed for the flake cast iron line contact tests and importantly the fired engine dynamometer tests. Plastic deformation and smearing of asperities into honing marks were observed during mild scuffing, consistent with the mechanisms observed for the flake and nodular cast iron and by Papadopoulos et al [101]. Local adhesive wear resulted in two body abrasion as adhesive transfer particles ploughed the surface during the transition to severe scuffing. The presence of adhesive and abrasive wear is in agreement with Neale's description of scuffing [96] and observations by Carver and Johnson [99]. Adhesive wear craters were found to contain flake graphite which was consistent with the wear mechanism observed for the flake graphite line contact tests, Section 4 and the engine tests in Section 2.13 . Adhesive transfer of material from the liner to the piston ring indicated severe scuffing which resulted in roughening of the surface topography.

The close agreement of these tests shows correlation between level E (coupon), level D (component) and level C (assembly) tests, indicating that the developed methodology and detection techniques accuracy reproduced and differentiated scuffing mechanisms observed in an engine using a laboratory tribometer. This confirmed that accelerated tribometer test methodology which used higher contact loads than those seen in fired engines successfully reproduced similar scuffing mechanisms observed in a fired combustion engine in under two hours. This shows the potential of the methodology to decrease cost and time required to evaluate the scuffing performance of material pairs for the piston ring on liner contact.

6.7 Comparison between friction noise and scuffing detection software

The two techniques, friction noise and scuffing detection software, were developed to detect the onset of scuffing as this could not be achieved using RMS friction force. The scuffing detection software performed a highly prescribed analysis of local friction force variation directly attributed to a physical wear process, adhesive wear. In contrast friction noise was sensitive to variations in the friction force arising across the entire stoke length from various physical mechanisms. It was particularly sensitive to rapid changes in friction force and was consequently able to detect the change from adhesive to abrasive wear which occurred during intermediate scuffing of nodular cast iron, and the recoverable scuffing which occurred in the ring on liner contact.

The accuracy of each detection technique could be evaluated as scuffing was precisely produced by the test method. This was validated by observing comparable surface morphology on cast iron samples which had experienced similar conditions. The test methodology ensured that the line contact tests operated in steady state boundary lubrication conditions until severe scuffing occurred. This permitted the scuffing detection software to detect small local changes in friction force attributed to the onset of scuffing, validated by optical microscopy. The software was highly successful as each mild scuff detected by the software corresponded to mild scuffing on the cast iron surface.

Friction noise did not have the required sensitivity to detect the small local changes in friction force and therefore could not detect the onset of scuffing for the line contact tests. However, it did identify a change in instantaneous friction force which accompanied intermediate scuffing in the case of nodular cast iron. This was the transition from adhesive to abrasive wear which was not detected by either the scuffing detection software or the RMS friction force. The RMS friction force was calculated over a time of 1.4 s which meant it did not have the sensitivity required to measure the highly localised changes. In contrast the threshold used by the software to indicate mild scuffing had already been met earlier in the tests, so the large fluctuations during intermediate scuffing were not detected. This illustrated that whilst the friction noise parameter was not successful in detecting mild scuffing it was still an insightful metric into the contact behaviour.

The software was able to detect scuffing almost as soon as it had occurred. It determined the occurrence of scuffing using numerical thresholds which resulted in accurate and precise detection. The same thresholds were applied to both the flake and nodular cast iron tests and yielded similar surface topographies indicating that the mild scuffing detection was independent of microstructure but not of mechanism. In the case of flake cast iron mild scuffing was identified within 18 % total test time deviation, and 16 % for the nodular cast iron,

which was a significant improvement in repeatable detection of scuffing compared to existing literature [10,128,146]. The variation was attributed to local differences in microstructure on the cast iron sample surface. Although the detection software was key to this improvement, the specimen preparation and test methodology were also critical. This was evident as severe scuffing which was detected using the standard method from literature, a rapid increase in friction coefficient, also showed a marked improvement in repeatability. The flake tests had a total test time deviation of 6 % compared with 8 % for nodular cast iron.

When the same methodology was applied the ring on liner contact, the software was not able to detect the onset of scuffing. The ring on liner geometry had a larger contact area than the line contact and consequently each load step resulted in only a small increase in contact pressure. This was not sufficient to ensure that the contact was running in boundary lubrication after the running in period and also permitted the lubricant film to reform after mild scuffing events. The presence of a lubricant film prevented the software from successfully detecting the onset of scuffing, as it required the friction force to be independent of sliding velocity to detect local friction force variation caused by adhesive wear. This illustrated that the confidence in the scuffing software was highly dependent on the test program forcing the contact to operate in the boundary lubrication regime.

Friction noise was able to detect the onset of scuffing in the ring on liner contact as it was sensitive to rapid changes in friction force which occurred during these mild scuffing events. It had a slower response time compared to the software, however as mild scuffing was recoverable it was sufficient to stop the tests with the mildly scuffed surface intact. Friction noise identified mild scuffing within 18 % of the tests sliding distances. Although this appeared comparable with the distribution of the line contact tests it represented a wider range of dissipated energy, 11 % compared with 2 % for flake and 4 % for nodular line contact tests. The increased deviation in dissipated energy was partly due to the lower sensitively of friction noise but also due to stochastic events related to local lubricant film collapse during the recovery of mild scuffing, which occurred exclusively during the ring on liner tests.

The success of each technique to detect mild scuffing was dependant on the ability of the test method to control the lubricant regime in the contact, consequently the software was suited to the line contact tests and friction noise to the ring on liner tests. Both techniques were able to identify mild scuffing sufficiently quickly for the intact mildly scuffed surfaces to be examined. The scuffing detection software identified mild scuffing more precisely than friction noise in terms of dissipated energy, although it is difficult directly compare the accuracy and precision of the two techniques as the variability may have arisen from the different test geometries rather than from the detection techniques. Whilst the software was more precise

it required prior knowledge of the scuffing mechanism to determine the mild scuffing thresholds. On the contrary, friction noise did not require prior knowledge as it continuously analysed the friction force across the entire stroke. It therefore had the capability to identify unexpected changes in friction force.

The two techniques offered complimentary information about the wear mechanisms occurring in the contact which helped to understand the stages of scuffing pertaining to the different cast iron materials. Friction noise was well suited to investigation of scuffing mechanisms, as shown by the identification of intermediate scuffing, whereas the software was an effective tool for precisely and repeatedly detecting mild scuffing.

7 Conclusions

7.1 Scuffing detection techniques

- Two new scuff detection methods have been developed to investigate the scuffing mechanisms of cast iron cylinder liner materials. The high speed friction data scuff detection software was found to successfully detect the onset of mild and severe scuffing for the line contact tests using local increases in friction force at the stroke reversal position.

- The incremental load methodology developed allowed scuffing repeatability to within an 8 % sliding distance for severe scuffing and 18 % maximum absolute deviation for mild scuffing. This is a significant improvement compared to previous studies in the literature and has shown that the distribution of scuffing test results is perhaps not inherent to the mechanism but is in fact a system response to the test methodology.

- Comparing the cast iron wear scars between repeat scuffing tests showed that the technique consistently identified surfaces with similar scuffed topography.

- The friction noise parameter was found to be not sensitive enough to detect the transition to mild scuffing, as the maximum friction noise occurred during the transition from intermediate to severe scuffing. The rate of change of friction noise which occurred immediately before the rapid rise in RMS friction coefficient was a repeatable characteristic and could potentially be used as an alternative measure to detect imminent severe scuffing failure.

- Despite the failure of the friction noise parameter to detect mild scuffing it did indicate transitions in wear mechanisms and therefore has the potential to be used to assist in differentiating between different wear mechanism transitions, for example running in, abrasive and adhesive wear.

- For conformal ring on liner contacts, the presence of squeeze films and recoverable mild scuffing events reduced the effectiveness of the software technique to identify mild scuffing because the lubricant film was repeatedly forming and collapsing. The RMS friction coefficient, contact potential and friction noise signals were subsequently used

to determine mild scuffing when the local friction coefficient and friction noise was at a maximum and contact potential were at a minimum.

- The onset and progression to severe scuffing was found to be dependent on the energy dissipated in the contact. Scuffing failure occurred at the same load despite doubling the duration of each load step which indicated that a critical energy was required for scuffing to occur.

- To avoid compensation for increases in dissipated friction energy arising from scuffing, open loop heat energy input is recommended to facilitate scuffing in benchtop tribometer tests.

7.2 Cast iron scuffing failure mechanisms

- The results of this study show that the scuffing failure of flake graphite cast iron in lubricated reciprocating line contacts is a multistage process that initiates upon thermally induced lubricant degradation. This facilitated the onset of mild scuffing which was characterised by the removal of lubricant and oxide tribofilms and the development of a crack network at the graphite-pearlite interface. Continued increase in the contact pressure caused transition to severe scuffing characterised by removal of surface platelets by adhesive wear and back transfer to the cast iron surface.

- Nodular cast iron scuffing failure undergoes three distinct stages: mild, intermediate and severe scuffing. Mild scuffing was characterised by the formation of an oxide tribolayer and the fracture of the ferritic matrix leading to a two body abrasive mechanism. Further increases in contact pressure initiated a transition to intermediate scuffing which was characterised by formation of surface platelets associated with dross inclusions from the casting process the cumulative adhesive transfer of these platelets ultimately led to severe scuffing of the surface.

- Scuffing detection software thresholds to identified mild and severe scuffing for both flake and nodular cast iron tests which were based on increases in the friction force at the stroke reversal positions. An increase of 140 % in the accelerating direction was associated with adhesive wear during the change of stroke direction and an increase of 110 % in the decelerating direction was associated with the deformation of wear debris.

- Despite the differences between the two cast iron microstructures both materials exhibited similar features to those observed in the literature for scuffing, showing that the detection techniques were independent of the material microstructure.

- Scuffing of a flake graphite ring liner conformal contact was achieved using a benchtop configuration. Scuffing initiated by the degradation of the lubricant into a tribolayer which was removed by the ring counter face. During mild scuffing asperities were deformed into the honing marks. The transition to severe scuffing was characterised by the formation of platelets and fractures at graphite interfaces. Whilst similar to the flake line contact tests the occurrence of severe adhesive wear was less prolific due to the lubricant squeeze film effect and lower contact pressures which enabled recovery from mild scuffing.

- This thesis has shown the development of scuffing detection techniques for a laboratory benchtop tribometer which successfully differentiated between distinct stages of scuffing for coupon (level E) and part (level D) tests. Similar scuffing mechanisms were observed for both test levels and were in agreement with tests from a fired engine dynamometer (level B). The repeatable correlation of scuffing mechanisms between level E and level B tests was a breakthrough in the understanding of automotive scuffing. The new knowledge of scuffing mechanisms and detection techniques have been of immediate interest and use to the automotive industry.

8 Future work

8.1 Recommendation for a scuffing test standard

When prescribing the load increment scuffing test parameters for a particular material pair it is important to establish the test temperature. Typically this is the temperature range expected inside the fired engine that the components will be used in. To determine the specific contact temperature the test will run at a temperature ramp will be performed at the run-in contact load. This establishes the system energy input required for scuffing. By reducing the temperature, failure may be induced by increasing the load allowing the scuffing mechanism to be characterised by contact pressure. This is advantageous as the control feedback occurs rapidly, it also means that the test does not become a lubricant starvation test which introduces a great deal of variability [128].

A load increment scuffing test is then performed at the test temperature. The duration of the load steps is typically 5 minutes however this may be increased to 10 minutes if the run in response of the contact is particularly lengthy.

Increasing the bulk contact temperature is achieved using resistance heaters. The temperature is measured using a thermocouple and the heaters controlled using feedback from a PID controller. Consequently the temperature rise associated with additional friction energy dissipation from an increased contact pressure may be offset by the PID control loop. This had little effect on the line contact scuffing tests, as the temperature control was damped by the heat capacity of the contact assembly consequently rapid rises in contact temperature such as during scuffing were not offset.

However incremental increases in energy dissipation that lead to scuffing were compensated for by the PID controller in the ring on liner contact. Therefore it is proposed that incremental scuffing tests are conducted not at a constant temperature but at a constant rate of thermal energy input to the system. In this methodology the pulse width of the heater controller is adjusted so that in the absence of sliding, the contact reaches a steady state at the desired temperature. Due to this open loop control method, it can take a considerable period of time to ensure steady state conditions have been achieved. The contact must be fully assembled during this period as the reciprocating assembly and counter face increases the thermal capacity of the system and affects the heat transfer characteristics. This proposed method precisely controls the energy dissipated in the contact and should therefore result in increased scuffing repeatability.

Depending on the type of scuffing mechanism occurring the friction noise parameter or the scuffing detection software can be used to repeatedly detect the onset of mild scuffing aiding in

the investigation of the failure mechanism. The friction coefficient rate of change or magnitude threshold method can be used to stop tests when severe scuffing occurs.

8.2 Expanding ring on liner detection

The majority of the investigation into scuffing used a line contact which was chosen for its repeatability and ease of use. This provided a reliable experiment platform that facilitated the development of the scuff detection techniques previously explained. Several challenges were encountered when the techniques were applied to a ring on liner contact, however these have met by changes to the detection techniques and the test methodology. Further refinement of the synergistic interplay between instantaneous friction force, contact potential and disorderly friction would make the methodology and techniques readily accessible for assessing the scuffing performance of production engine.

8.3 White etched surface layers.

The scuffing literature has referred to the formation of white etched surface layers [164]. These layers have been reported to be very hard and consist of a nano-crystaline structure white etch white using nitial solution. The transformation of the bulk material to the white etching layer has been reported as a transition between run-in and scuffing called first transition scuffing. The formation of these layers is thought to occur during frictional heating of the surface, it is therefore hypothesised that the use of a formulated oil would assist in a higher energy dissipation at failure due to the boundary additive protection of surface asperities. It is proposed to use a fully formulated oil in the current scuffing test to form white etched layers on cast iron. A focused ion beam could then mill a cross section through the white layer and bulk material interface to create a thin lamellar suitable for transmission electron microscopy. TEM analysis would identify the crystal structure of the white layer which has been reported as potentially having a martensitic structure [14,165,166] although this is disputed [81,164]. The analysis would also show the transformation of grain size and their orientation. This information could then be used to confirm the mechanism of crack growth proposed in this research.

8.4 Influence of additives

Friction modifiers are known to affect the friction performance of tribological contacts, and in Cooper et al [86] friction modifiers were seen to completely remove adhesive wear peaks at the reversal positions. The additive chemistry may prevent adhesive wear events from causing distinct local increases in friction force. However it may be possible to detect them using friction noise because increases in friction force disorder across the mid-stroke may occur due to the interaction of adhesive wear particles with the rest of the wear scar.

8.5 Expand the scuffing detection techniques to recently developed surface coatings

Whilst the developed techniques have been successful in identifying and discriminating scuffing failure in cast iron, the universal applicability of the techniques to other materials has yet to be established.

An alternative strategy for reducing emissions is engine light weighting. This can be achieved by using engine blocks made from aluminium instead of cast iron, however the cylinder liner requires a hard low friction coating to provide acceptable tribological performance. Diamond like carbon (DLC) coatings offer wear resistance and low friction properties however the thin coatings have high residual stress [167] and may exhibit surface adhesion issues depending on the substrate.

Measuring scuffing of a DLC surface however, is a challenge using traditional techniques as the inherently low friction properties of the coating could mask the failure which is consequently only detected when severe surface damage has occurred. This can potentially result in a product failure in service, which is catastrophic for industry and the consumer.

The scuffing test developed as part of this work has been design to encourage the progressive failure of the lubricate film resulting in adhesive failure at the stroke reversal positions. Consequently it's hoped that coating test will be encouraged to fail by an adhesive mechanisms. However depending on the sliding conditions coatings testing has the potential for other failure modes besides adhesion to occur. In particular spalling failure of the coating, where due to high pressures cracks initiate at the interface between the coating and bulk material and propagate towards the surface. In some instances the use of electrical contact resistance maybe used to indicate the absence of an insulating coating. However this does not indicate the mechanism which has resulted in coating failure. It is therefore important to verify that the scuffing detection criteria only identify scuffing failure but that new analysis using the same techniques can result in criteria which can discriminate other types of failure such as abrasive and spalling failure.

8.6 Integrating in-situ measurement of surface profiles

The experiments presented have shown how evolution of the surface topography results in mild and severe scuffing failure. Calculating the lubricant film thickness during the scuffing process would greatly assist in describing the wear mechanisms occurring. Calculation however relies on knowledge of the composite surface roughness which has been demonstrated to change by nearly an order of magnitude during scuffing. Therefore measurements of the surface topography during the experiment are required to enable the lubricant film thickness to be

calculated. Samples have to be removed from the tribometer to be measured using a conventional profilometer, however this presents the problem of re-aligning samples in the machine. Whilst some geometries can be readily aligned others, such ring on liner contacts, cannot.

As part of a knowledge transfer internship during the PhD program, an in situ profilometer for the TE-77 reciprocating tribometer was developed to remove the need for specimen realignment Figure 8.1 and Figure 8.2 [168]. The measurement system was fully integrated into the tribometer control software to enable autonomous profile measurements during a test. In addition to measuring the surface at regular intervals, the measurements will be able to be triggered when specific friction events occur. This reactive measurement system has the potential to reveal more detail about surface topography evolution during changes in wear mechanism. The in situ profilometer could be applied to a broad range of tests beyond the scope of this research by providing wear measurement during experiments to challenge the often presumed, linear wear rate assumption.

It is proposed that the stylus profilometer be used when investigating ring on line geometry and DLC failure discussed previously. Changes in surface topography measured by the profilometer can be correlated to characteristic friction force and friction noise behaviours. Consequently the stylus profilometer provides an online validation method to enable the scuffing detection techniques to be calibrated to the wear mechanism. Using the insitu profilometer enables the evolution of the surface to be obtained from a single experiment, potentially saving a considerable amount of time. However it is not known how interrupting the test will affect the progression of scuffing as the frictional energy dissipated in the contact is removed during measurement. It is possible therefore that the onset of scuffing may be delayed or perhaps accelerated due to the change in lubrication experienced during stopping and starting. The effects of stop start on scuffing is another avenue of research which would be well supported by the stylus profilometer and scuffing techniques and warrants further investigation.

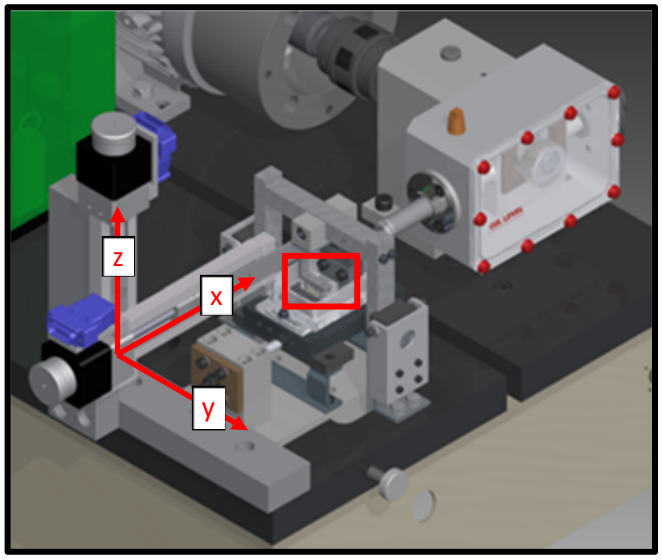

Figure 8.1: In situ profilometer attached to a TE-77 high frequency reciprocating tribometer.

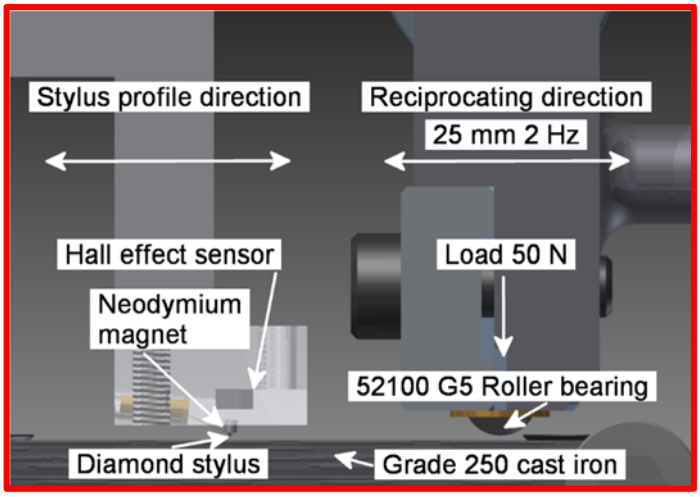

Figure 8.2: Cross section of the tribometer configuration for line contact dry sliding with the stylus measurement assembly in the measurement position.

8.7 Running in

It is clear from the literature that the contact surfaces are conditioned before the contact is stressed to failure. This is an important requirement to ensure that a conformal contact has been achieved at the start of every test which increases test repeatability. This conditioning usually occurs at steady state conditions until the friction coefficient has also reach steady state conditions. The actual duration is determined experimentally for each tribosystem but remains constant between repeat tests to ensure that the sliding distance is the same. This methodology was the approached adopted for the scuffing test developed for this investigation.

However, the ASTM reciprocating sliding standard G181 details run-in procedure which consists of a series of a stepped load increment cycle, where each step can only advance once the friction force reaches steady state. After each loading cycle the friction force on the ascending and descending side for each load step is compared. This method does not have a fixed duration so the sliding distance may vary depending on each test. This variability in sliding distance may

produce more variability in test results. This method is also more complex to implement and on many tribometers would require a manual process. Consequently it is not widely used. However the advantage of this technique is that it removes running in effects from the beginning of each load step. In the case of a scuffing test the loading cycle cannot increase to the scuffing load so the running in standard can only be used to a lower load. It is of course possible not to use this providing investigators acknowledge the presence of running in effects at the being of each load step. Investigation of the effect of the each run-in methodology on the performance of the contact should be investigated in the context of the disorderly friction signal, which from the present work exhibits significant changes during the running in period and potentially could be used as an alternative measure of when running in has concluded.

9 Publications and presentations

9.1 Poster presentations

- **Society of Tribologists and Lubricant Engineers Annual Meeting, Dallas, USA, May 2015**
  Assessing running-in behaviour using in situ profilometry.

- **Gordon Research Conference on Tribology, Massachusetts, USA, July 2014**
  Detecting scuffing of cast iron using high speed friction data.

- **Society of Tribologists and Lubricant Engineers Annual Meeting, Florida, USA, May 2014**
  Detecting scuffing of cast iron using high speed friction data.

9.2 Oral presentations

- **Wear of Materials, Long beach, California, USA, March 2017**
  1. Tribological behaviour of an electrochemical jet machined textured Al-SI automotive cylinder liner material.
  2. Scuffing mechanisms of EN-GJS 400-15 spheroidal graphite cast iron against a 52100 bearing steel in a PAO lubricated reciprocating contact.

- **Society of Tribologists and Lubricant Engineers Annual Meeting, Las Vegas, USA, May 2016**
  1. Theoretical analysis of stroke length versus scuffing in reciprocating rigs.
  2. Challenging the linear wear rate assumption: An in-situ stylus profilometer for a reciprocating tribometer.

- **Mission of Tribology, Institute of Mechanical Engineers, London, December 2015**
  Disorderly friction and its role in detecting scuffing.

- **Society of Tribologists and Lubricant Engineers Annual Meeting, Dallas, USA, May 2015**
  The measurement of disorderly friction and its use in the detection of scuffing.

- **Wear of Materials, Toronto, Canada, April 2015**
  Reproducing automotive engine scuffing using a boundary lubricated reciprocating contact.

- **TriboUK, Sheffield, April 2014**

  Scuffing in piston assembly and liner of fired combustion engines.

9.3 Directly related journal publications

- Kamps, T.J., Walker, J.C., Wood, R.J., Lee, P.M., Plint, A.G., Reproducing automotive engine scuffing using a lubricated reciprocating contact, Wear, 332, 2014, 1193-1199 Cited: 5.

- Kamps, T.J., Walker, J.C., Wood, R.J., Lee, P.M., Plint, A.G., Scuffing mechanisms of EN-GJS 400-15 spheroidal graphite cast iron against a 52100 bearing steel in a PAO lubricated reciprocating contact, Wear, 376-377, 2017, 1542-1551 .

9.4 Indirectly related journal publications

- Walker, J.C., Kamps, T.J., Wood, R.J., The influence of start-stop transient velocity on the friction and wear behaviour of a hyper-eutectic Al-Si automotive alloy, Wear, 306, 2012, 209-218 Cited: 8.

- Walker, J.C., Kamps, T.J., Lam, J.W., Mitchell-Smith, J., Clare, A.T., Tribological behaviour of an EJM textured AL-SI automotive cylinder liner material, Wear, 376-377, 2017, 1611-1621.

- Kamps, T.J., Walker, J.C., Wood, R.J., Plint, A.G., In situ stylus profilometer for a high frequency reciprocating tribometer, Surface Topography: Metrology and Properties, 5, 2017, 34004.

9.5 Awards

- Tribology Trust Bronze Medal, Institute of Mechanical Engineers, December 2015

  “The Tribology Bronze Medal is an encouragement award for engineers and scientists working in the fields of friction, lubrication and wear, ie tribologists both those working or studying full-time who haven’t yet completed their formal education and training." IMechE

- Doctoral Prize Award, Engineering and Physical Sciences Research Council, March 2017

  1 year of funding to support to investigate scuffing of DLC cylinder liner materials using the scuffing detection techniques and understanding detailed in this thesis.

- Named researcher on EPSRC grant EP/P024475/1 In-situ profilometry for transient testing of automotive materials.

10 Appendix flake

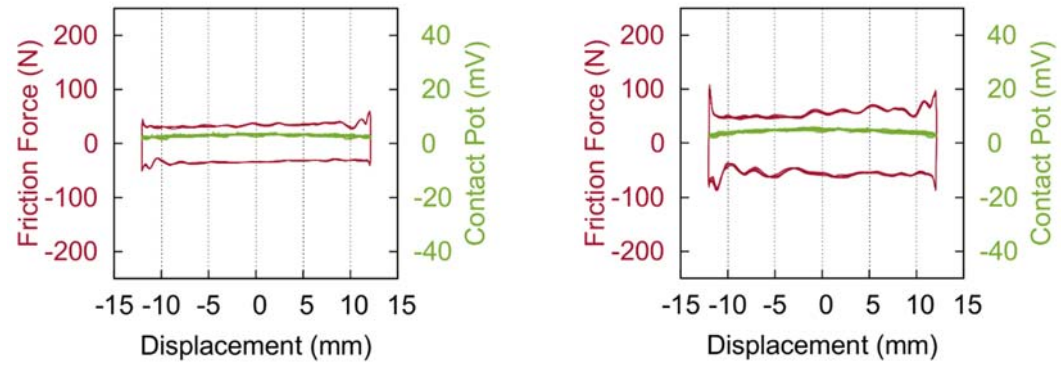

(a) *(b)*

Figure 10.1: High speed friction and contact potential data from (a) mild and (b) severe scuffing flake test S2.

11 Appendix nodular

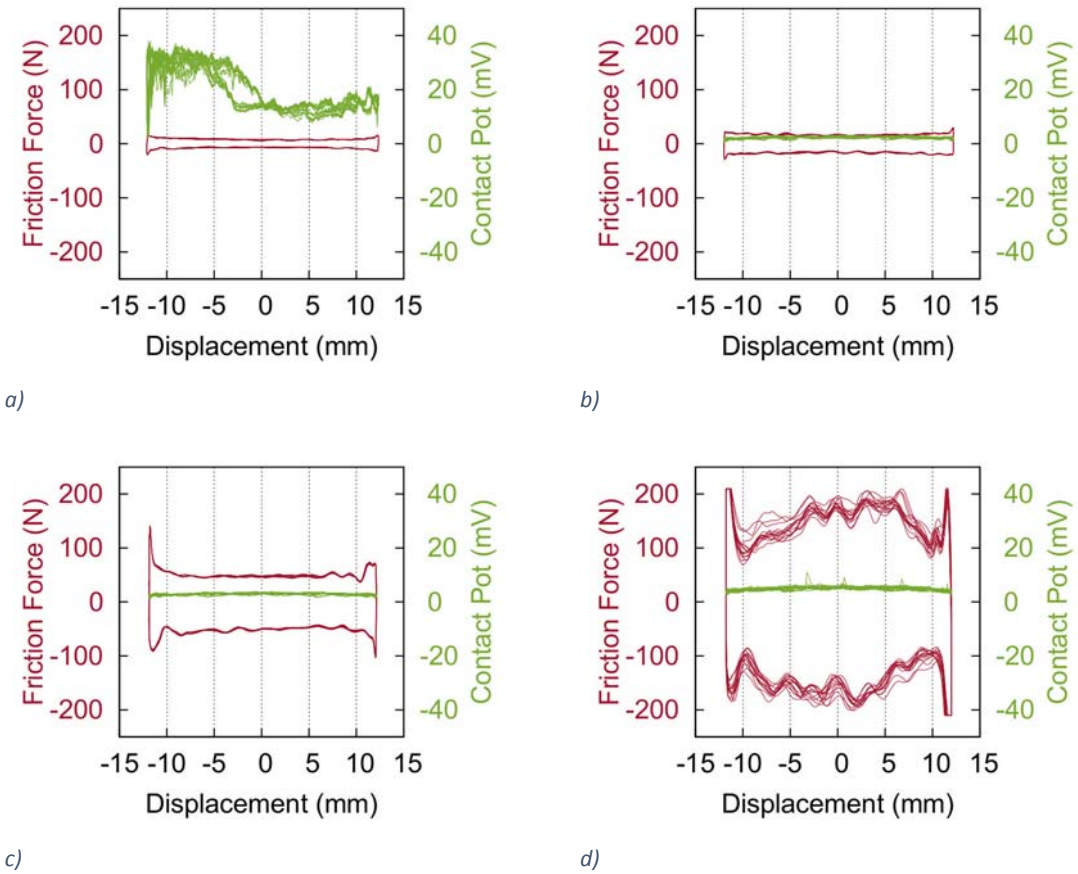

Figure 11.1: Friction force and contact potential data for (a) HS1: running-in, (b) HS2: mild scuffing, (c) HS3: intermediate scuffing, (d) HS4: severe scuffing.

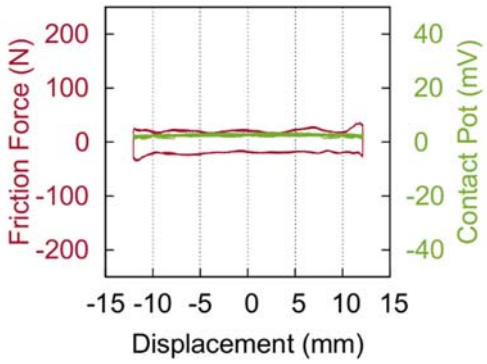

Figure 11.2: Friction force and contact potential data during mild scuffing NS4.

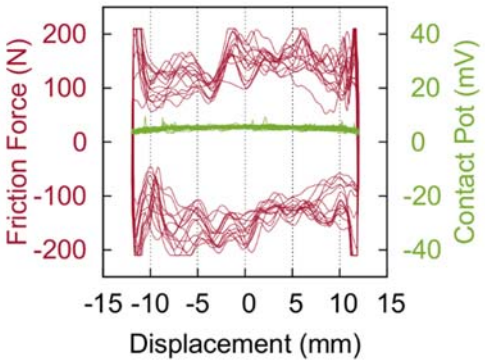

Figure 11.3: Friction force and contact potential data during severe scuffing failure NS4.

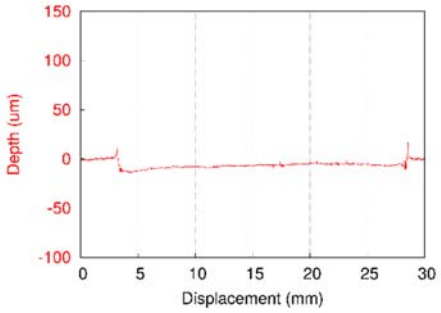

Figure 11.4: Longitudinal profile of the intermediate scuffed wear scar NS2.

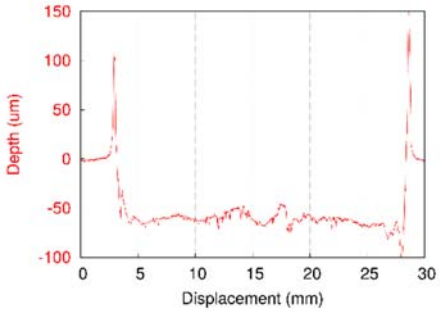

Figure 11.5: Longitudinal profile of the severe scuffed wear scar NS2.

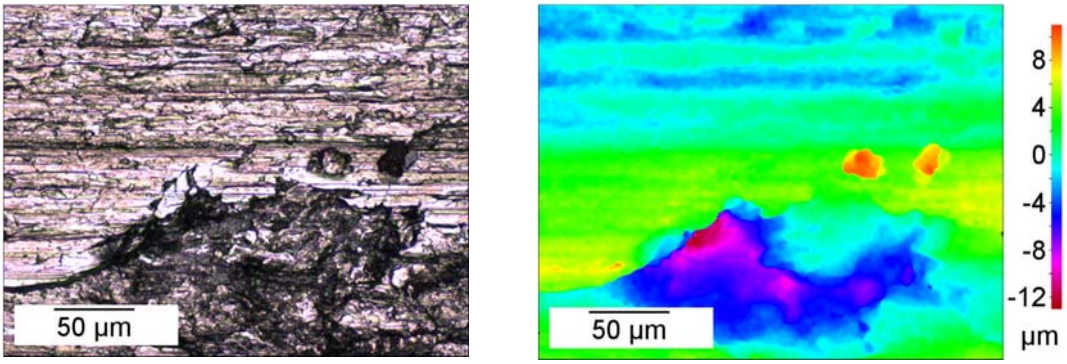

a) *b)*

Figure 11.6: Optical image of the severely scuffed nodular cast iron wear scar NS3, showing wear debris produced by severe adhesive wear a) and 3D colour map b).

12 Appendix cylinder liner

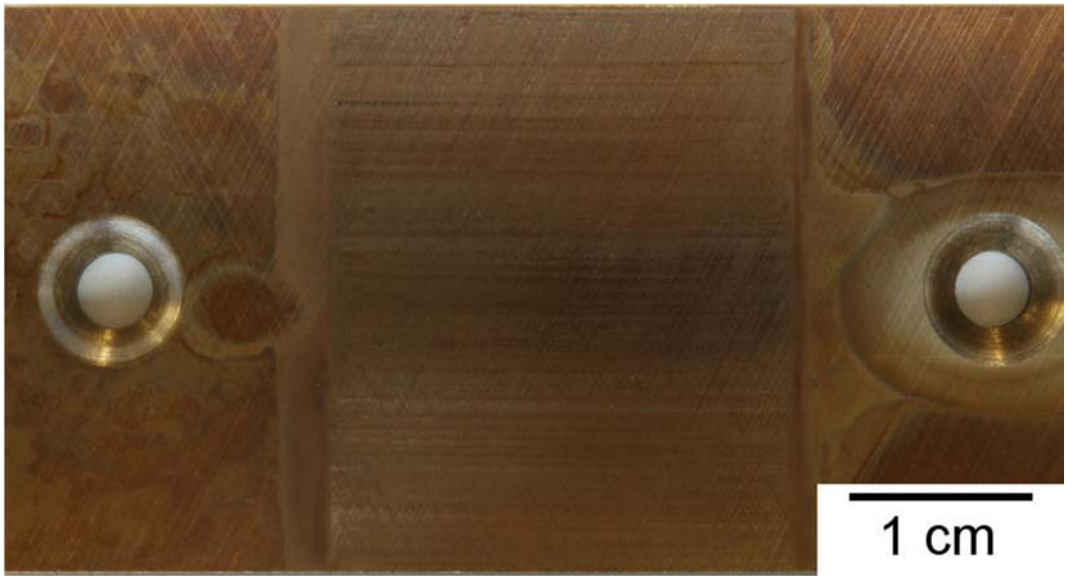

Figure 12.1: Optical images of the RLMS1 cast iron wear scar.

Figure 12.2: Optical images of the RLMS1 and piston ring wear scar.

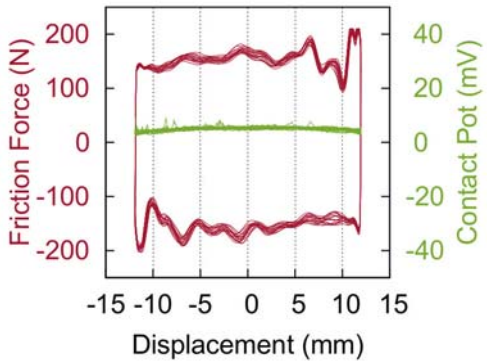

Figure 12.3: (HS2) Friction force and contact potential data during severe scuffing failure RLS2.

13 References

[1] Greenhouse gas emissions standards and fuel efficiency standards for medium- and heavy-duty engines and vehicles, Final Rule, Federal Register. 76 (2011) 57140.

[2] D.E. Richardson, Review of Power Cylinder Friction for Diesel Engines, Journal of Engineering for Gas Turbines and Power. 122 (2000) 506–519.

[3] K. Holmberg, P. Andersson, A. Erdemir, Global energy consumption due to friction in passenger cars, Tribology International. 47 (2012) 221–234.

[4] M. Priest, C.M. Taylor, Automobile engine tribology - approaching the surface, Wear. 241 (2000) 193–203.

[5] Y. Tateishi, Tribological issues in reducing piston ring friction losses, Tribology International. 27 (1994) 17–23.

[6] ASTM G40-15, Standard terminology relating to wear and erosion, ASTM International, West Conshohocken, PA, 2015.

[7] G.C. Barber, K.C. Ludema, The break-in stage of cylinder-ring wear: a correlation between fired engines and a laboratory simulator, Wear. 118 (1987) 57–75.

[8] J.E. Booth, T.J. Harvey, R.J.K. Wood, H.E.G. Powrie, Scuffing detection of TU3 cam–follower contacts by electrostatic charge condition monitoring, Tribol. Int. 43 (2010) 113–128.

[9] H. Rahnejat, ed., Tribology and dynamics of engine and powertrain: Fundamental, applications and future trends, Woodhead Publishing Limited, Cambridge, 2010.

[10] F. Saeidi, S.A. Shevchik, K. Wasmer, Automatic detection of scuffing using acoustic emission, Tribology International. 94 (2016) 112–117.

[11] M. Shuster, D. Combs, K. Karrip, D. Burke, Piston ring cylinder liner scuffing phenomenon studies using acoustic emission technique, SAE Paper 2000-01-1782. (2000).

[12] M. Shuster, T. Stong, M.C. Deis, D.C. Burke, Piston ring cylinder liner scuffing phenomenon: Investigation, simulation and prevention, SAE Paper 1999-01-1219. (1999).

[13] O.D. Tasbaz, R.J.K. Wood, M. Browne, H.E.G. Powrie, G. Denuault, Electrostatic monitoring of oil lubricated sliding point contacts for early detection of scuffing, Wear. 230 (1999) 86–97.

[14] S. Morris, R.J.K. Wood, T.J. Harvey, H.E.G. Powrie, Use of electrostatic charge monitoring for early detection of adhesive wear in oil lubricated contacts, J. Tribol. 124 (2002) 288–296.

[15] J. Qu, J.J. Truhan, P.J. Blau, Detecting the onset of localized scuffing in a pin-on-twin fuel-lubricated test for heavy-duty diesel fuel injectors, International Journal of Engine Research. 6 (2005) 1–9.

[16] I. Hutchings, Tribology: friction and wear of engineering materials, Butterworth-Heinenmann, Oxford, 2001.

[17] B. Bhushan, Introduction to Tribology, John Wiley & Sons, New York, 2002.

[18] British standards institution, BS EN ISO 13565-2: Geometric product specifications (GPS): profile method- surfaces having stratified function properties-part 2: height characterization using linear material ratio curve, British standards institution, 1998.

[19] Michael Neale and Associates, Piston ring design: a survey of information from research on piston rings and its application to design, 1973.

[20] P. Andersson, J. Tamminen, C.-E. Sandström, Piston ring tribology - a literature survey, Finland, 2002.

[21] A. van Beek, Advanced engineering design Lifetime performance and reliability, TU Delft, Delft, 2012.

[22] A. Isaacs, ed., A Dictionary of Physics, Fourth, Oxford University Press, Oxford, 2000.

[23] L. da Vinci, Codex Arundel 263, British Library, London, 1478.

[24] L. da Vinci, Codex Atlanticus, Biblioteca Ambrosiana, Milan, 1478.

[25] G. Stachowiak, A. Batchelor, Engineering Tribology, Butterworth-Heinemann, 2005.

[26] M.B. Peterson, W.O. Winer, Archard, J.F. Wear theory and mechanisms, in Wear control handbook, ASME, New York, 1980.

[27] F.P. Bowden, D. Tabor, The friction and lubrication of solids, Oxford University Press, Oxford, 1950.

[28] T. Butlin, J. Woodhouse, Friction-induced vibration : Model development and comparison with large-scale experimental tests, Journal of Sound and Vibration. 332 (2013) 5302–5321.

[29] R.G. Bayer, Effects of Mechanical Stiffness and Vibration on Wear, STP 1247, ASTM,

1995.

[30] P.J. Blau, Mechanism for transitional friction and wear behaviour of sliding metals, Wear. 72 (1981) 55–66.

[31] B. Bhushan, Principles and applications of tribology, John Wiley & Sons, 1999.

[32] E.H. Smith, ed., Mechanical Engineer's Reference Book (12th Edition), Elsevier, 1998.

[33] H. Czichos, Tribology: a systems approach to the science and technology of friction, lubrication and wear, Elsevier, Amsterdam, 1979.

[34] D. Dowson, Elastohydrodynamic and micro-elastohydrodynamic lubrication, 190 (1995) 125–138.

[35] C.M. Taylor, Engine Tribology, Elsevier B.V., 1993.

[36] R. Stribek, Die Wesentlichen Eigenschaften der Gleit-und Rollenlager, Zeitschrift Des Vereines Deutscher Ingenieure. (1902).

[37] M. Woydt, R. Wäsche, The history of the Stribeck curve and ball bearing steels: The role of Adolf Martens, Wear. 268 (2010) 1542–1546.

[38] A. Caines, R. Haycock, Automotive Lubricants Reference Book, Mechanical Engineering Publications Ltd, UK, 1996.

[39] L. Gümbel, Das Problem der Lagerreibung (The problem with the bearing friction), Mitteilungsblatt Des Berliner Bezirksvereins Deutscher Ingenieure (VDI). (1914) 87–104, 109–120.

[40] M.D. Hersey, The laws of lubrication of horizontal journal bearings, J. Wash. Acad. Sci. 4 (1914) 542–552.

[41] D. Dowson, History of Tribology, Professional Engineering Publishing, London, 1998.

[42] M.J. Neale, ed., Tribology Handbook, 2nd ed., Elsevier, 1995.

[43] J. Williams, Engineering Tribology, Cambridge University Press, 1994.

[44] J.S. McFarlane, D. Tabor, Relation between friction and adhesion, Proc. Roy. Soc. 202 (1950) 244–253.

[45] A. Kapoor, K.L. Johnson, Plastic Ratchetting as a Mechanism of Metallic Wear, Proceedings of the Royal Society of London. Series A: Mathematical and Physical Sciences. 445 (1994) 367 LP-384.

[46] J. Wang, Y. Chung, eds., Encyclopedia of tribology, Springer, 1991.

[47] P. Obert, T. Müller, H.J. Füßer, D. Bartel, The influence of oil supply and cylinder liner temperature on friction, wear and scuffing behavior of piston ring cylinder liner contacts - A new model test, Tribology International. 94 (2016) 306–314.

[48] W.D. Callister, Materials science and engineering an introduction, 7th ed., John Wiley & Sons, New York, 2007.

[49] A.R. Riahi, A.T. Alpas, Wear map for grey cast iron, Wear. 255 (2003) 401–409.

[50] E.D. Rejowski, E. Soares, I. Roth, S. Rudolph, Cylinder Liner in Ductile Cast Iron for High Loaded Combustion Diesel Engines, Journal of Engineering for Gas Turbines and Power. 134 (2012) 72807.

[51] Ł. Wojciechowski, S. Eymard, Z. Ignaszak, T.G. Mathia, Fundamentals of ductile cast iron scuffing at the boundary lubrication regime, Tribology International. 90 (2015) 445–454.

[52] H.R. Abedi, A. Fareghi, H. Saghafian, S.H. Kheirandish, Sliding wear behavior of a ferritic-pearlitic ductile cast iron with different nodule count, Wear. 268 (2010) 622–628.

[53] D. Stickel, A. Fischer, The influence of topography on the specific dissipated friction power in ultra-mild sliding wear: Experiment and simulation, Tribology International. 91 (2015) 48–59.

[54] B.K. Prasad, Sliding wear response of cast iron as influenced by microstructural features and test condition, Materials Science and Engineering A. 456 (2007) 373–385.

[55] H. Yamagata, The science and technology of materials in automotive engines, Woodhead Publishing Limited, Cambridge, 2005.

[56] British standards institution BS EN 1561 : 2011, Founding — Grey cast irons, BSI, London, 2011.

[57] E.C. Rollason, Metallurgy for engineers, Third, Edward Arnold Ltd, London, 1961.

[58] British standards institution BS EN 1563 : 2011, Founding — Spheroidal graphite cast irons, BSI, London, 2011.

[59] British standards institution BS EN ISO 945-1:2008, Microstructure of cast irons, BSI, London, 2008.

[60] E. Tomanik, C. Cia, F.D.E. Peças, Nitrided Piston Ring Pack for Diesel Engines, SAE Technical Paper 952249. (1995).

[61] E. Tomanik, J. Vatavuk, Nitrited Steel Piston Rings for Internal Combustion Engines, SAE Technical Paper 942394. (1994).

[62] J.A. Cullen, G.M. Frodsham, Reduced Cross Section Compression Rings for Diesel Engines, SAE Technical Paper 971146. (1997).

[63] A. Ferrarese, J. Bieneman, D.J. Domanchuk, T. Smith, T. Stong, P. Einberger, Piston Ring Solutions on Side Wear to the Next Generation of Truck Engines, (2011) 3–8.

[64] GOETZE, Piston rings and piston ring elements steels, http://korihandbook.federalmogul.com/en/pdf/section_66_en.pdf (accessed July 3, 2017).

[65] British standards institution BS 5341-6.3:1992, Piston rings up to 200 mm diameter for reciprocating internal combustion engines : Specification for rectangular rings with narrow ring width, (1992).

[66] H.R. Ricardo, Some recent research work on the I.C. engine, Auto. Engr. 12 (1922) (Sep.), 265; (Oct.), 299; (Nov.), 329.

[67] K. Holmberg, A. Erdemir, Global impact of friction on energy consumption, economy and environment, FME Transactions. 43 (2015) 181–185.

[68] M.O. Teetor, The reduction of piston ring and cylinder wear, S.A.E. Transactions. 33 (1938) 137.

[69] Department For Education and Science, Lubrication (tribology) education and research, (Jost Report), London, 1966.

[70] Organisation for Economic Co-operation and Development, Glossary of terms and definitions in the field of friction, wear and lubrication, Paris, 1969.

[71] T.S. Eyre, K.K. Dutta, Some metallurgical aspects of scuffing, in: Piston Ring Scuffing, Mechanical Engineering Publications Ltd, 1975: pp. 125–140.

[72] K.G. Budinski, Guide to friction, wear and erosion testing: (MNL 56), ASTM International, 2007.

[73] E.J. Murray, A survey of scuffing in spark ignition engines, in: Piston Ring Scuffing, Mechanical Engineering Publications Ltd, 1975: pp. 157–164.

[74] D. Nilsson, P. Isaksson, B. Prakash, Effects of area ratio and nature of surfaces on scuffing in lubricated contacts, in: Proceedings of the Institution of Mechanical Engineers, Part J: Journal of Engineering Tribology, 2009: pp. 223–455.

[75] K.C. Ludema, A review of scuffing and running-in of lubricated surfaces, with asperities and oxides in perspective, Wear. 100 (1984) 315–331.

[76] P.I. Lacey, R.T. Stockwell, Development of a methodology to predict cylinder liner scuffing in the 6V92TA engine lubricant test, Tribol. Trans. 42 (1999) 192–201.

[77] D. Summers-Smith, An introduction to tribology in industry, The machinery publishing company Ltd, 1969.

[78] R. Munro, Diesel engine ring scuff - is there a major problem?, in: Piston Ring Scuffing, Inst. Mech. Eng. Conference, Mechanical Engineering Publications Ltd, London, 1975: pp. 9–14.

[79] G.K. Aue, Piston Ring Scuffing - General Review, in: Piston Ring Scuffing, Mechanical Engineering Publications Ltd, 1975: pp. 1–5.

[80] W.F. Bowman, G.W. Stachowiak, A review of scuffing models, Tribol. Lett. 2 (1996) 113–131.

[81] A. Dyson, Scuffing - a review, Tribol. Int. 8 (1975) 77–87.

[82] A. Dyson, Scuffing - a review: Part 2: The mechanism of scuffing, Tribology International. 8 (1975) 117–122.

[83] J.R. Davis, ed., Gear Materials, Properties, and Manufacture, ASM International, 2005.

[84] H.E. Staph, P.M. Ku, H.J. Carper, Effect of surface roughness and surface texture on scuffing, Mechanism and Machine Theory. 8 (1973) 197–208.

[85] A.F. Alliston-Greiner, A.G. Plint, M.A. Plint, Testing extreme pressure and anti-wear performance of crankcase and gearbox lubricants, in: ASTM Special Technical Publication, Seatlle, WA, United States, 2001: pp. 140–152.

[86] D. Cooper, A.J. Moore, The influence of boundary films on lubricant anti-scuff performance, Lubricants and Lubrication. (1995) 617–633.

[87] S.C. Lee, H.S. Cheng, Correlation of scuffing experiments with EHL analysis of rough surfaces, Journal of Tribology. 113 (1991) 318–326.

[88] O.O. Ajayi, J.G. Hersberger, J. Zhang, H. Yoon, G.R. Fenske, Microstructural evolution during scuffing of hardened 4340 steel - implication for scuffing mechanism, Tribology International. 38 (2005) 277–282.

[89] S.C. Lee, H. Chen, Experimental validation of critical temperature-pressure theory of scuffing, Tribology Transactions. 38 (1995) 738–742.

[90] R.M. Matveevsky, Evaluation of temperature stability of a lubricant film on rubbing surfaces, Wear. 12 (1968) 300.

[91] W.J.S. Grew, A. Cameron, Thermodynamics of boundary lubrication and scuffing, Proceedings of the Royal Society of London. A. Mathematical and Physical Sciences. 327 (1972) 47–59.

[92] S.M. Hsu, M.C. Shen, E.E. Klaus, H.S. Cheng, P.I. Lacey, Mechano-chemical contact model : reaction temperatures in a concentrated contact, Wear. 175 (1994) 209–218.

[93] A.W. Batchelor, W. Stachowiak, Some kinetic aspects of extreme pressure lubrication, Wear. 108 (1986) 185–199.

[94] E.C. Cutiongco, Y.-W. Chung, Prediction of scuffing failure based on competitive kinetics of oxide formation and removal: Application to lubricated sliding of AISI 52100 steel on steel, Tribology Transactions. 37 (1994) 622–628.

[95] A.W. Batchelor, G.W. Stachowiak, Model of scuffing based on the vulnerability of an elastohydrodynamic oil film to chemical degradation catalyzed by the contacting surfaces, Tribology Letters. 1 (1995) 349–365.

[96] M.J. Neale, Piston ring scuffing - a broad survey of problems and practice, in: Proc. Inst. Mech. Eng., 1970: pp. 21–32.

[97] D.M. Hesling, A study of typical bore finishes and their effect on engine performance, Lubrication Engineering. 19 (1963) 414–422.

[98] P.S. Gupte, Y. Wang, W. Miller, G.C. Barber, C. Yao, B. Zhou, Q. Zou, A study of torn and folded metal (TFM) on honed cylinder bore surfaces, Tribol. Trans. 51 (2008) 784–789.

[99] D.P. Carver, K.A. Johnson, The effect of bore finish on piston ring scuffing, in: Piston Ring Scuffing, Mechanical Engineering Publications Ltd, London, 1975: pp. 165–202.

[100] Ł. Wojciechowski, T.G. Mathia, Proposal of invariant precursors for boundary lubricated scuffing, Wear. 340–341 (2015) 53–62.

[101] P. Papadopoulos, M. Priest, W.M. Rainforth, Investigation of fundamental wear mechanisms at the piston ring and cylinder wall interface in internal combustion engines, Proceedings of the Institution of Mechanical Engineers, Part J: Journal of Engineering Tribology. 221 (2007) 333–343.

[102] M.F. Jensen, J. Bøttiger, H.H. Reitz, M.E. Benzon, Simulation of wear characteristics of engine cylinders, 253 (2002) 1044–1056.

[103] J. Sugishita, S. Fujiyoshi, The effect of cast iron graphites on friction and wear performance I: Graphite film formation on grey cast iron surfaces, Wear. 66 (1981) 209–221.

[104] B.K. Prasad, Sliding wear behaviour of a cast iron as affected by test environment and applied load, Industrial Lubrication and Tribology. 61 (2014) 161–172.

[105] R.S. Montgomery, The mild wear mechanism of nodular iron, Wear. 13 (1969) 337–343.

[106] J. Han, G. Barber, Q. Zou, X. Sun, P. Seaton, Effect of material microstructure on scuffing behavior of ferrous alloys, SAE 2011 World Congress and Exhibition. (2011).

[107] J.M. Han, R. Zhang, O.O. Ajayi, G.C. Barber, Q. Zou, L. Guessous, D. Schall, S. Alnabulsi, Scuffing behavior of gray iron and 1080 steel in reciprocating and rotational sliding, Wear. 271 (2011) 1854–1861.

[108] F. Saeidi, A.A. Taylor, B. Meylan, P. Hoffmann, K. Wasmer, Origin of scuffing in grey cast iron-steel tribo-system, Materials and Design. 116 (2017) 622–630.

[109] P.J. Blau, A Review of Sub-Scale Test Methods to Evaluate the Friction and Wear of Ring and Liner Materials for Spark and Compression Ignition Engines November 2001, 2001.

[110] DIN Deutsches Institut für Normung e.V, DIN-50322: Wear, wear testing categories, Berlin, 1986.

[111] M. Woydt, N. Kelling, Testing the tribological properties of lubricants and materials for the system “piston ring/cylinder liner” outside of engines, Industrial Lubrication and Tribology. 55 (2003) 213–222.

[112] ASTM International, ASTM D6750 - 13 Standard test methods for evaluation of engine oils in a high-speed, single-cylinder diesel engine—1K procedure (0.4% fuel sulfur) and 1N procedure (0.04% fuel sulfur), 2013.

[113] ASTM International, ASTM D6681 - 13 Standard test method for evaluation of engine oils in a high speed, single-cylinder diesel engine - Caterpillar 1P test procedure, 2013.

[114] API, API Engine oil classifications for service fill oils, 2008.

[115] Y. Wang, S.C. Tung, Scuffing and wear behavior of aluminum piston skirt coatings against aluminum cylinder bore, Wear. 225–229 (1999) 1100–1108.

[116] P.M. Lee, R.J. Chittenden, Consideration of Test Parameters in Reciprocating Tribometers Used to Replicate Ring-On-Liner Contact, Tribology Letters. (2010) 81–89.

[117] M. Priest, The wear and lubrication of piston rings, Thesis, University of Leeds, 1996.

[118] R. Evans, N. Tawil, J. Owen, Honing of parent metal cylinder bores for automotive deisel engines, in: Tribology of Reciprocating Engines, Leeds-Lyon Symposium, 1982.

[119] G. Hamilton, S. Moore, Measurement of piston ring profile during running-in, in: Piston Ring Scuffing, Inst. Mech. Eng., 1975.

[120] K. Liu, X.J. Liu, C.L. Gui, Scuffing failure analysis and experimental simulation of piston ring – cylinder liner, Tribol. Lett. 5 (1998) 309–312.

[121] J. Dearlove, W.K. Cheng, Simultaneous piston ring friction and oil film thickness measurements in a reciprocating test rig, SAE Trans., J. Fuels & Lubr. 104 (1995) 1452–1462.

[122] S. Hartfield-Wunsch, S. Tung, C. Rivard, Development of a Bench Wear Test for the Evaluation of Engine Cylinder Components and the Correlation with Engine Test Results, SAE Paper 932693. (1993).

[123] D.J. Patterson, S.H. Hill, S.C. Tung, Bench wear testing of engine power cylinder components, Lubr. Eng. 49 (1993) 89–95.

[124] R.W. Bruce, A high temperature tribotest for lubricated contacts of aluminium against steel, Lubr. Eng. 41 (1985) 430–433.

[125] D. Dowson, Engine Tribology, Elsevier B.V., 1993.

[126] M.G. El-Sherbiny, Cylinder liner wear, in: Proceedings of the 9th Leeds-Lyon Symposium on Tribology, 1982: pp. 132–136.

[127] Y. Wang, K. Brogan, S.C. Tung, Wear and scuffing characteristics of composite polymer and nickel/ceramic composite coated piston skirts against aluminum and cast iron cylinder bores, Wear. 250 (2001) 706–717.

[128] P. Olander, S.S. Eskildsen, J.W. Fogh, P. Hollman, S. Jacobson, Testing scuffing resistance of materials for marine 2-stroke engines - Difficulties with lab scale testing of a complex phenomenon, Wear. 340–341 (2015) 9–18.

[129] A.F. Alliston-Greiner, Testing extreme pressure and anti-wear performance of gear lubricants, in: Proceedings of the Institution of Mechanical Engineers, 1991: pp. 89–101.

[130] J. Zhang, B.W. Drinkwater, R.S. Dwyer-Joyce, Calibration of the ultrasonic lubricant-film thickness measurement technique, Measurement Science and Technology. 16 (2005) 1784–1791.

[131] B. Clarke, M. Fazio, D. Scott, AN-268 RMS-to-DC Converters Ease Measurement Tasks,

http://www.analog.com/media/en/technical-documentation/application-notes/AN-268.pdf (accessed April 19, 2017).

[132] T.J. Kamps, J.C. Walker, R.J. Wood, P.M. Lee, A.G. Plint, Reproducing automotive engine scuffing using a lubricated reciprocating contact, Wear. 332–333 (2015) 1193–1199.

[133] J. Hershberger, O. Ajayi, J. Zhang, H. Yoon, G.. Fenske, Formation of austenite during scuffing failure of SAE 4340 steel, Wear. 256 (2004) 159–167.

[134] J. Keller, V. Fridrici, P. Kapsa, J.F. Huard, Surface topography and tribology of cast iron in boundary lubrication, Tribology International. 42 (2009) 1011–1018.

[135] P.N. Suh, The delamination theory of wear, Wear. 25 (1973) 111–124.

[136] Phoenix Tribology Ltd, TE-77 High frequency friction machine, http://www.phoenix-tribology.com/cat/at2/leaflet/te77.htm (accessed May 20, 2013).

[137] Kistler Holding AG, Quartz force sensor type 9203, https://kistler-embedded.partcommunity.com/3d-cad-models/FileService/File/kistler/02_force/01_single_component_force_sensors_compression/01_sensors/9203_english.pdf/ (accessed April 19, 2017).

[138] Kistler Holding AG, Piezoelectric Theory and Applications, https://www.kistler.com/?type=669&fid=92&model=download (accessed April 12, 2017).

[139] Phoenix Tribology Ltd, Operating instructions: TE 77 High frequency friction machine, (2009) 8.

[140] G. Plint, Guidance notes on lubricated wear testing, http://www.phoenix-tribology.com/wp-content/uploads/guidance/Guidance-Lubricated-Testing.pdf (accessed July 29, 2017).

[141] R.J. Smalley, A. Cameron, The Role of Boundaiy Lubrication in Scuffing Reactions, Elastohydrodynamics - ’96 Fundamentals and Applications in Lubrication and Traction, Proceedings of the 23rd Leeds-Lyon Symposium on Tribology Held in the Institute of Tribology, Department of Mechanical Engineering. Volume 32 (1997) 501–507.

[142] Daimler, Detroit DD13 technical specifications, https://detroitads.azureedge.net/9276-detroit_dd13_ghg17_product_ove-2017-04-20.pdf (accessed July 22, 2017).

[143] ASTM International, ASTM D8074-16, Standard test method for evaluation of diesel engine oils in DD13 D diesel engine, (2016).

[144] L.A. Giannuyi, F.A. Stevie, Introduction to Focused Ion Beams, Springer US, New York, 2005.

[145] West Yorkshire Steel, BS1452 Grade 250 Cast Iron Datasheet, https://www.westyorkssteel.com/files/bs1452-grade-250.pdf (accessed July 3, 2017).

[146] O.O. Ajayi, C. Lorenzo-Martin, R.A. Erck, G.R. Fenske, Scuffing mechanism of near-surface material during lubricated severe sliding contact, Wear. 271 (2011) 1750–1753.

[147] Y. Kimura, Influence of surface roughness on friction and scuffing behaviour of cast iron under sparse lubrication, 29 (1996).

[148] J. Galligan, A.A. Torrance, G. Liraut, A scuffing test for piston ringrbore combinations Part I. Stearic acid lubrication, Wear. 236 (1999) 199–209.

[149] M. Wasim Akram, A.A. Polycarpou, Wear Mechanisms of Gray Cast Iron in the Presence of Environmentally Friendly Hydrofluoroolefin-Based Refrigerant and the Effect of Tribofilm Formation, Journal of Tribology. 137 (2015) 41602.

[150] S. Wan, D. Li, G. Zhang, A.K. Tieu, B. Zhang, Comparison of the scuffing behaviour and wear resistance of candidate engineered coatings for automotive piston rings, Tribology International. 106 (2017) 10–22.

[151] J. Qu, J.J. Truhan, P.J. Blau, Investigation of the scuffing characteristics of candidate materials for heavy duty diesel fuel injectors, Tribol. Int. 38 (2005) 381–390.

[152] M.A. Islam, A.S.M.A. Haseeb, A.S.W. Kurny, Study of wear of as-cast and heat-treated spheroidal graphite cast iron under dry sliding conditions, Wear. 188 (1995) 61–65.

[153] C.A. Schneider, W.S. Rasband, K.W. Eliceiri, NIH Image to ImageJ: 25 years of image analysis, Nature Methods. 9 (2012) 671–675.

[154] West Yorkshire Steel, BS2789 Grade 400-15 SG Iron Datasheet, https://www.westyorkssteel.com/files/400-15.pdf (accessed March 21, 2017).

[155] T. Akagaki, K. Kato, Plastic flow process of surface layers in flow wear under boundary lubricated conditions, Wear. 117 (1987) 179–196.

[156] G.M. Goodrich, Cast Iron Microstructure Anomalies and Their Causes, AFS Transactions. (1997) 669–683.

[157] M. Gagné, M. Paquin, P. Cabanne, Dross in Ductile Iron : Source , Formation and Explanation, Foundry Trade Journal. (2009) 276–280.

[158] A.Y. Suh, A.A. Polycarpou, T.F. Conry, Detailed surface roughness characterization of

engineering surfaces undergoing tribological testing leading to scuffing, Wear. 255 (2003) 556–568.

[159] A. Moosavian, G. Najafi, B. Ghobadian, M. Mirsalim, S.M. Jafari, P. Sharghi, Piston scuffing fault and its identification in an IC engine by vibration analysis, Applied Acoustics. 102 (2016) 40–48.

[160] S. Mezghani, I. Demirci, H. Zahouani, M. El Mansori, The effect of groove texture patterns on piston-ring pack friction, Precision Engineering. 36 (2012) 210–217.

[161] A. Spencer, A. Almqvist, R. Larsson, A numerical model to investigate the effect of honing angle on the hydrodynamic lubrication between a combustion engine piston ring and cylinder liner, Proceedings of the Institution of Mechanical Engineers, Part J: Journal of Engineering Tribology. 225 (2011) 683–689.

[162] R. Taylor, Squeeze film lubrication in piston rings and reciprocating contacts, Proceedings of the Institution of Mechanical Engineers, Part J: Journal of Engineering Tribology. 229 (2015) 1–12.

[163] A. Cameron, Lubricant chemistry and tribology chemistry - boundary and extreme pressure lubrication, Proceedings of the Institution of Mechanical Engineers (London). C250 (1987) 355–364.

[164] T.S. Eyre, A. Baxter, The formation of white layers at rubbing surfaces, Tribology. (1972) 256–261.

[165] Y.Y. Yang, H.S. Fang, W.G. Huang, A study on wear the white layer resistance of, Tribology International. 29 (1996) 425–428.

[166] D. Scott, A.I. Smith, J. Tait, G.R. Tremain, Materials and metallurgical aspects of piston ring scuffing - a literature survey, Wear. 33 (1975) 293–315.

[167] K. Holmberg, H. Ronkainen, A. Laukkanen, K. Wallin, S. Hogmark, S. Jacobson, U. Wiklund, R.M. Souza, P. Ståhle, Residual stresses in TiN, DLC and MoS2 coated surfaces with regard to their tribological fracture behaviour, Wear. 267 (2009) 2142–2156.

[168] T.J. Kamps, J.C. Walker, A.G. Plint, In situ stylus profilometer for a high frequency reciprocating tribometer, Surface Topography: Metrology and Properties. 5 (2017) 34004.